Nuclear matter distribution of ^{56}Ni measured with EXL

TECHNISCHE
UNIVERSITÄT
DARMSTADT

Fachbereich Physik
Institut für Kernphysik
AG Kröll

Nuclear matter distribution of ^{56}Ni measured with EXL
Kerndichteverteilung von ^{56}Ni gemessen mit EXL

Genehmigte Dissertation von Mirko von Schmid M.Sc. aus Fulda

1. Gutachten: Prof. Dr. Thorsten Kröll
2. Gutachten: Prof. Dr. Thomas Aumann

Tag der Einreichung: 14.07.2015
Tag der Prüfung: 03.08.2015

Darmstadt — D 17
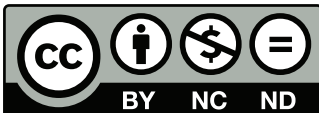
Erklärung zur Dissertation

Hiermit versichere ich, die vorliegende Dissertation ohne Hilfe Dritter nur mit den angegebenen Quellen und Hilfsmitteln angefertigt zu haben. Alle Stellen, die aus Quellen entnommen wurden, sind als solche kenntlich gemacht. Diese Arbeit hat in gleicher oder ähnlicher Form noch keiner Prüfungsbehörde vorgelegen.

Darmstadt, den 14.07.2015

_____

(Mirko von Schmid)

Abstract

In the present work, the nuclear matter distribution and the RMS matter radius of ^{56}Ni were successfully measured for the first time by exploiting elastic proton scattering. Being a doubly magic nucleus with an equal number of protons and neutrons, ^{56}Ni is of particular physical interest. Since it is also a radioactive nucleus, the experiment has to be performed in inverse kinematics. Hence, the experiment was conducted at the ESR (**E**xperimental **S**torage **R**ing) at the GSI Helmholtzzentrum für Schwerionenforschung as part of the first experimental campaign of EXL (**EX**otic nuclei studied in **L**ight-ion induced reactions). The beam of ^{56}Ni, which was produced by in-flight fragmentation of a ^{58}Ni beam and selected by the **FR**agment **S**eparator (FRS), was injected into the ESR and interacted with the internal hydrogen target. The demanding vacuum conditions of a storage ring made it necessary to develop a novel detector system. This had to be ultra-high vacuum (UHV) compatible and, at the same time, feature an energy threshold as low as possible to enable the measurement of particles scattered at low momentum transfer. To equally fulfil both conditions, a windowless detector system was developed in which the UHV is separated from an auxiliary vacuum by a silicon strip detector. In the auxiliary vacuum, additional detectors as well as other non-UHV compatible components may be placed. This way, a telescope based on silicon detectors was set up which makes the measurement of protons in an energy range starting at few hundreds of keV up to about 50 MeV possible. In the course of the present work the employed detectors were tested and further developed by extensive laboratory tests as well as in-beam experiments.

The differential cross section for elastic proton scattering was deduced from the measured angular distribution of the detected recoil protons. For this, comprehensive Monte-Carlo simulations of the setup have been performed. Then, the nuclear matter distribution was extracted from the cross section with the help of the Glauber multiple-scattering theory. For this purpose, the density distribution was parametrised by a phenomenological distribution for which a symmetrised Fermi distribution and the model-independent **S**um-**O**f-**G**aussians (SOG) method was used. The latter allows to determine theory-dependent contributions to the systematic error. Eventually, the RMS matter radius of ^{56}Ni was calculated from the matter distributions to be (3.76 ± 0.08) fm which is in agreement with predictions by HFB and HF+BCS calculations. The correctness of the whole method, i. e. the measurement in inverse kinematics and the applied analysis procedure, was proven in comparison to an already known nuclear matter distribution of ^{58}Ni of which the results are in a good agreement with the literature values.

Zusammenfassung

In der vorliegenden Arbeit ist es erstmalig gelungen die Kerndichteverteilung und den Materieradius des exotischen Kerns ^{56}Ni mittels elastischer Protonenstreuung experimentell zu bestimmen. Aufgrund seiner Eigenschaft als doppelt magischer Kern, mit darüber hinaus gleicher Anzahl an Protonen und Neutronen, ist der untersuchte Kern von besonderem physikalischen Interesse. Da es sich dabei allerdings um einen radioaktiven Kern handelt, muss eine solche Messung in inverser Kinematik durchgeführt werden. Das Experiment wurde daher am ESR (**E**xperimental **S**torage **R**ing) des GSI Helmholtzzentrums für Schwerionenforschung im Rahmen der ersten experimentellen Kampagne des EXL-Projekts (**EX**otic nuclei studied in **L**ight-ion induced reactions) durchgeführt. Der ^{56}Ni Ionenstrahl wurde durch Fragmentation eines ^{58}Ni Strahls erzeugt, im FRS (**FR**agment **S**eparator) selektiert und schließlich in den ESR injiziert, wo er mit dem internen Wasserstofftarget des ESR wechselwirkte. Die anspruchsvollen Vakuumbedingungen eines Speicherrings machten es dabei notwendig ein neuartiges Detektorsystem zu entwickeln. Dieses musste zum einen den Bedingungen des im Inneren des Speicherring herrschenden Ultrahochvakuums (UHV) genügen und zum anderen gleichzeitig über eine besonders niedrige Energieschwelle verfügen, um die Messung von Teilchen zu ermöglichen, die bei niedrigen Impulsüberträgen gestreut werden. Um beiden Bedingungen gleichermaßen gerecht zu werden, wurde ein fensterloses Detektorsystem entwickelt, bei dem das UHV mittels eines Siliziumstreifendetektors von einem Hilfsvakuum getrennt wird, das weitere, nicht UHV-kompatible, Detektoren und Komponenten aufnimmt. Auf diese Weise konnte ein aus Siliziumdetektoren aufgebautes Detektorteleskop zur Messung der rückgestreuten Protonen in einem Energiebereich von wenigen hundert keV bis hin zu ungefähr 50 MeV realisiert werden. Die dazu verwendeten Detektoren wurden im Rahmen dieser Arbeit in zahlreichen Labortests als auch in Strahlexperimenten getestet und weiter entwickelt.

Aus der gemessenen Winkelverteilung der elastisch gestreuten Protonen wurde zunächst der differentielle Wirkungsquerschnitt bestimmt. Hierfür wurden umfangreiche Monte-Carlo Simulationen des experimentellen Aufbaus durchgeführt. Unter Zuhilfenahme der Glauber-Vielteilchenstreutheorie wurde die Dichteverteilung der Kernmaterie dann aus diesen Wirkungsquerschnitten bestimmt. Die Dichteverteilung muss dafür über eine phänomenologische Parametrisierung beschrieben werden. Im vorliegenden Fall wurde dafür sowohl die symmetrisierte Fermiverteilung als auch der modellunabhängige **S**um-**O**f-**G**aussians (SOG) Ansatz gewählt. Letzterer ermöglicht insbesondere die Bestimmung theorieabhängiger Beiträge zur sys-

tematischen Unsicherheit. Aus der Dichteverteilung konnte schließlich für ^{56}Ni ein mittlerer Materieradius von $(3.76 \pm 0.08)\,\mathrm{fm}$ bestimmt werden, was mit theoretischen Vorhersagen aus HFB und HF+BCS Rechnungen übereinstimmt. In einer ebenfalls durchgeführten Messung der schon bekannten Kerndichteverteilung von ^{58}Ni konnte diese erfolgreich bestätigt werden, was die Korrektheit der angewandten Methodik (Experiment und Analyse) bestätigt.

Contents

1 Introduction

The investigation of light-ion induced direct reactions, like elastic and inelastic scattering, transfer and charge exchange reactions, yields important information about nuclear structure and astrophysics. Especially the spin-isospin selectivity is a clear advantage in these types of reactions. Much of what is currently known about nuclei has been obtained from light-ion induced direct reactions. In fact, it even goes back to the discovery of the nucleus by elastic scattering of α-particles in the Rutherford experiment more than hundred years ago.

Before radioactive beams became available, the experiments were mostly performed in direct kinematics where the light-ion beam was shot on a target made of the nucleus of interest. Obviously, the experiments are limited to stable or very long lived isotopes from which targets can be made. With radioactive beams, such experiments can be carried out in *inverse kinematics*, i.e. with the nucleus of interest being shot on a light target.

The important physics is often extracted from high-resolution measurements at low momentum transfer. There, for example, information about the matter distribution in nuclei can be obtained by elastic proton scattering experiments. Collective modes can be studied using inelastic proton or alpha scattering and the strength of Gamow–Teller resonances can be investigated in charge exchange reactions. As a consequence of the inverse kinematics the region of low momentum transfer results in large scattering angles and low energies of the target-like recoils in the laboratory frame. The latter mandates the use of thin targets which comes at the cost of drastically reduced rates. Hence, experiments with exotic beams impinging on thick targets are usually limited to higher momentum transfer. Performing these kinds of experiments with the ions injected and stored in a ring offers a complementary way of studying reactions and has several advantages over the former:

- high luminosity because of beam recirculation frequencies of in the order of MHz and continuous beam accumulation;

- low background due to pure, windowless targets like for example H_2 or ^{4}He gas-jets;

- high resolution measurement of low-energy recoils possible due to beam cooling techniques and the use of thin targets;

- reduction of beam contaminants or isomeric states in the storage ring.
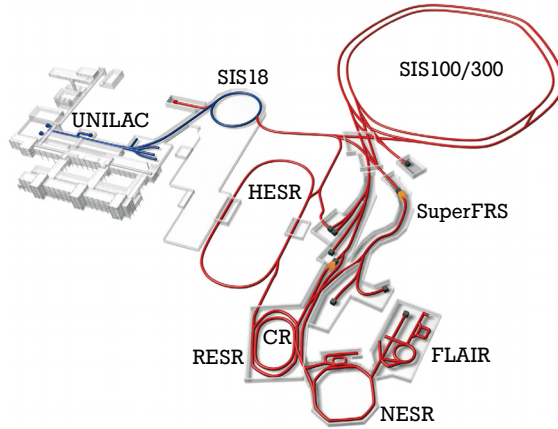
Figure 1.1.: Schematic view of the future FAIR facility (*red*) extending the present GSI facility (*blue*). (*adapted from* [1])

The EXL project is set out to implement this technique at the future **F**acility for **A**nti-proton and **I**on **R**esearch (FAIR) [1]. However, first experiments can be performed at the existing GSI facility already.

Exotic nuclei studied in light-ion induced reactions at storage rings

The EXL project (**EX**otic nuclei studied in **L**ight-ion induced reactions at storage rings) is a project within NUSTAR (**N**uclear **S**tructure, **A**strophysics and **R**eactions) at the upcoming FAIR facility (see figure 1.1) and will study light-ion induced reactions originally planned for the **N**ew **E**xperimental **S**torage **R**ing (NESR) [1]. EXL will consist of several detector systems to allow a kinematically complete measurement of a broad range of reactions complementary to experiments using external targets like for example R^{3}B (**R**eactions with **R**elativistic **R**adioactive **B**eams) [1]. The central component of EXL will be the **EXL S**ilicon **P**article **A**rray (ESPA) which is designed as a universal recoil-detector for the target-like recoils. It will be build as a sphere consisting of several layers of segmented silicon detectors (see figure 1.2). The detectors of ESPA will be arranged with respect to the kinematical properties of the different reaction types as sketched in figure 1.3. For example, in case of elastic scattering the energy of the recoil is effectively zero at an angle of 90° with respect to the beam axis and then quickly rises to several tens of MeV in a few degrees. Hence, a telescope of silicon detectors is planned for this angular region. The array will be surrounded by a calorimeter made of CsI crystals for the detection of gamma rays and punch-through charged particles, i. e. the **EXL G**amma & **P**article **A**rray (EGPA). In the proximity of the recoil detector, the **EXL L**ow **E**nergy **N**eutron
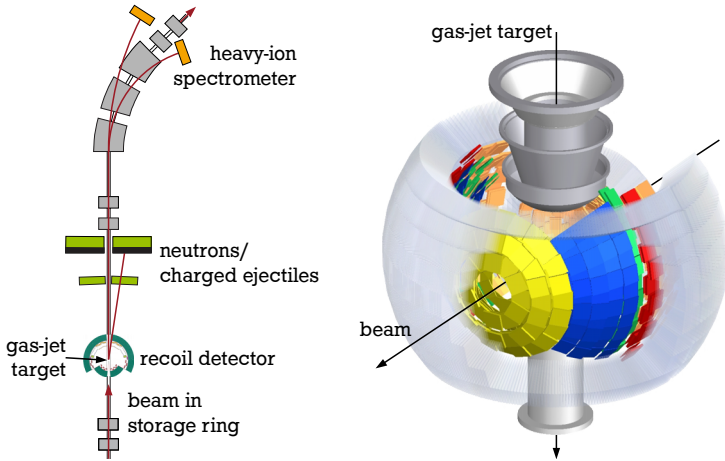
Figure 1.2.: Schematic view of the EXL detection systems. *Left*: Setup built into the NESR storage ring; *Right*: Target-recoil detector surrounding the gas-jet target. (*adapted from* [1])

Array (ELENA) is intended to detect slow neutrons. In the forward direction, a detector for fast ejectiles, i. e. protons, neutrons and light clusters like α-particles, is planned to be installed. Eventually, an in-ring heavy-ion spectrometer is intended for the detection of beam-like ejectiles. A schematic overview of the whole system is showed in figure 1.2.

Technically, the most challenging part of the project is certainly the recoil detector and especially ESPA. First and foremost, the ultra-high vacuum (UHV) conditions in the storage ring demand the exclusive use of low-outgassing materials which withstand the bake-out of the ring at temperatures of at least 150 °C. At the same time, the low energy threshold mandatory for the measurement of recoils at low momentum transfer excludes the use of vacuum windows as they would prevent the detection of low-energy recoils.

Measuring the size of a nucleus

As outlined, one of the physics interests of EXL is the measurement of nuclear matter distributions and matter radii. The method of choice for this will be elastic proton scattering at intermediate energies which has proven to be an excellent tool for the study of matter distributions of stable nuclei [2, 3]. More recently, the method was also applied to light exotic nuclei in inverse kinematics using an active target [4, 5, 6]. By taking into account the charge distributions measured in electron scattering experiments it is also possible to extract the neutron
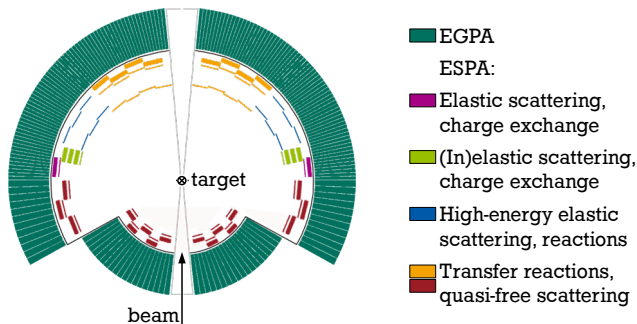
Figure 1.3.: Cross section through the mid plane of the EXL recoil and gamma array. (*adapted from* [1])

distributions from the measured differential cross sections for elastic proton scattering [7, 8, 9, 10]. However, in the case of exotic nuclei, classic electron scattering experiments with external targets are not possible. To apply this powerful method also to exotic nuclei, an electron-ion collider is envisaged at the NESR by the ELISe collaboration (**EL**ectron **I**on **S**cattering at the NESR) [1]. Together with EXL, this will allow to deduce proton and neutron densities for a vast range of exotic nuclei. Charge radii of exotic nuclei can also be obtained by measuring the hyperfine splitting or isotopic shifts using collinear laser spectroscopy [11].

There are also other methods which are sensitive to the RMS radius of nuclear matter or the difference between both radii, i. e. the neutron-skin thickness. For example, the total matter radius can be determined from total interaction cross-sections [12]. It is also known that the cross section for the excitation of the giant dipole resonance (GDR) and the spin dipole resonance (SDR) depend on the neutron-skin thickness [13]. Another way to determine the neutron-skin thickness is via the electric dipole polarisability which can be measured using Coulomb excitation [14].

Antiprotons can be used to deduce nuclear radii, as well. The difference between proton and neutron radius at larger radii can be probed either by decay spectroscopy analysis of the $A-1$ antiproton annihilation residues and by obtaining level shifts and widths from antiprotonic x-rays [15]. Currently, this method is only applicable to stable nuclei but an extension to exotic nuclei is envisaged [16]. Another method using antiprotons is proposed for the FAIR facility. The **A**ntiproton-**I**on-**C**ollider (AIC) [1] situated at the NESR aims for the measurement with both stored and cooled exotic nuclei and antiprotons. By measuring the total antiproton-absorption cross section and cross sections for antiproton annihilation on protons and neutrons the RMS radii of the proton and neutron distributions can be ob-
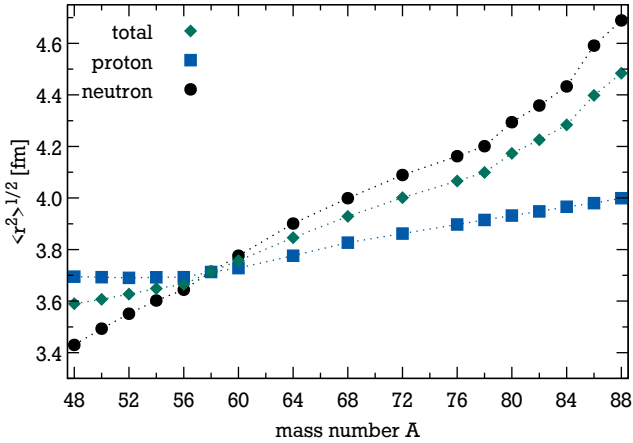
Figure 1.4.: Evolution of the RMS radii in nickel isotopes. HFB calculations for protons (*squares*), neutrons (*circles*) and total matter (*diamonds*) assuming point-like nucleons. The lines serve as guides to the eye. (*data taken from* [18])

tained in one measurement and with one method [17, 18]. The realisation of the AIC project, however, will come only as a FAIR upgrade in the far future.

Since electrons interact with neutrons via the electroweak force, the measurement of the parity-violating asymmetry by elastic scattering of polarised electrons allows to determine the neutron radius of a nucleus [19]. It is also possible to determine the matter radius by measuring the coherent π^0-photoproduction cross sections [20]. These methods are limited to stable nuclei, however.

First EXL experiment with radioactive beam

Despite the origin of the EXL project as an experiment located at the NESR, it is not bound to this particular storage ring. The already existing **E**xperimental **S**torage **R**ing (ESR) at GSI, together with its internal gas-jet target, provides a world-wide unique opportunity to perform such experiments at present. After first feasibility measurements with the stable nuclei ^{136}Xe (2005) [21, 22] and ^{40}Ar (2011) [23], an experiment (2012, E105 [24]) with stable ^{58}Ni and radioactive ^{56}Ni beams interacting with H_2 and ^{4}He targets was performed by the EXL collaboration. Besides the commissioning of the novel detection system, the main goal of the experiment and the subject of this work was the first measurement of the nuclear matter distribution and RMS matter radius of ^{56}Ni by employing elastic proton scattering. The fact that ^{56}Ni is a self-conjugate doubly-magic nucleus

makes it very interesting from a point of view of nuclear structure. It also plays an important role in the element formation in astrophysical scenarios around mass 56 where fusion reactions at the end of the life-cycle of stars end. Hence, knowledge about the deeper structure of this nucleus is very desirable and can serve as a benchmark point for theory.

In combination with the measurement of the RMS charge radius of ^{56}Ni which is planned at ISOLDE using collinear laser spectroscopy [25] and the RMS matter radius determined in this work, it will be possible to calculate the size of the neutron distribution. This way, the predicted change from proton skins at $A \lesssim 58$ to neutron skins at larger mass numbers (see figure 1.4) can be evaluated [18].

2 Developments towards EXL

The previous chapter has shown that the realisation of the EXL project and especially of its recoil detector is technically ambitious. First and foremost, the ultra-high vacuum (UHV) conditions inside a storage ring demand the use of components which are made of low-outgassing materials and bakeable to temperatures of around 150 °C to 200 °C. The usual solution to this problem is to place the UHV incompatible components in a pocket separated from the UHV. This approach is not feasible here as the unavoidable entrance foil of the pocket would introduce an unwanted dead layer and prevent the detection of low-energy particles. However, the measurement at low momentum transfer is one of the key goals of EXL. Additionally, the recoil detection system has to cover a large dynamic range of energy. The fact that the reactions are studied in inverse kinematics means that the energy of the recoil starts from effectively zero at 90° and quickly rises to hundreds of MeV within a few degrees of laboratory angle. Thus, it has to be shown that it is feasible to measure target recoils with energies ranging from as low as 100 keV to hundreds of MeV with the proposed setup of silicon-detector telescopes.

The following sections will give an overview of preparative experiments and technical developments undertaken by the EXL collaboration in order to build the detector setup for the first EXL physics campaign with radioactive beams at the ESR.

2.1 In-beam tests with the EXL demonstrator

The EXL demonstrator resembles a segment of the sphere of the EXL recoil detector. Consequently, it is set up as a telescope composed of up to two DSSDs (**D**ouble-sided **S**ilicon **S**trip **D**etector, section 2.1.1), two Si(Li)s (**Li**thium-drifted **Si**licon detector, section 2.1.2) and two CsI scintillators (section 2.1.3). With different configurations of these detectors three in-beam experiments with proton beams of different energies were performed. The aim was to study the response of the individual detector systems and the precision of the energy reconstruction. In the first test, conducted 2009 with a 50 MeV proton beam at KVI, two DSSD and two Si(Li) detectors were used. A brief summary of this test can be found in [26, 27]. Later in the same year, a second test with 100 MeV and 150 MeV protons was performed at GSI. This time, only one DSSD was used and a double CsI scintillator was also added to the demonstrator. The most recent test of the EXL demonstrator was done with a 133 MeV proton beam at KVI in 2010. In this

test, the second DSSD was added again but placed in between the last Si(Li) and the CsI crystal. The detailed setup and the results of this test will be discussed in section 2.1.4.

2.1.1 First generation DSSD for EXL
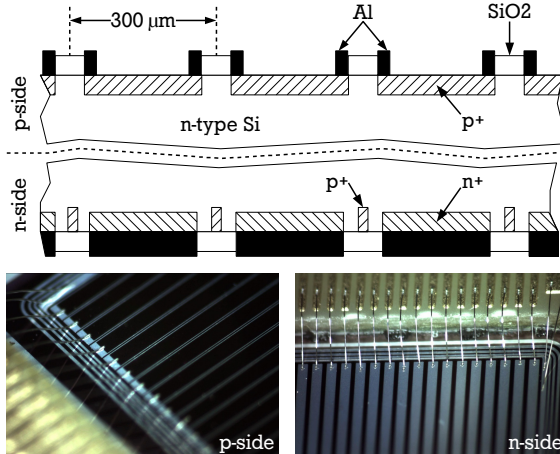
Figure 2.1.: Schematic drawing [28] and photos [29] of the first generation of DSSD prototypes for EXL.

A first generation of DSSDs for the EXL project was developed by PTI, St. Petersburg. The detectors, with a thickness of 280 μm, were produced in several sizes and strip pitch configurations but share the same design (see figure 2.1) [31]. The DSSDs used in the EXL demonstrator had an active area of approximately (2×2) cm^2 and were segmented into 64 strips on the front side (p-side) and – perpendicular to the p-side – 64(16) strips on the back side (n-side). This results in a strip pitch of 300 (1200) μm. The speciality of these DSSDs is the small interstrip gap of only 15 μm and their thin-window design [28]. In order to keep the dead layers and the consequent energy losses as low as possible, the electrical coupling of the p-side strips is provided only by a thin frame of aluminium surrounding each strip. The strip itself remains uncovered except for an unavoidable layer of oxidised silicon. On the n-side, the strips are fully covered with aluminium.

Laboratory tests with α-sources have shown a good energy resolution of typically 18 keV (FWHM) for the p-side strips and 20 keV (FWHM) for the n-side strips but have also revealed some drawbacks of the detector design. As the aluminium ring around the p-side strips is about 0.8 μm thick, low-energy ions already face a
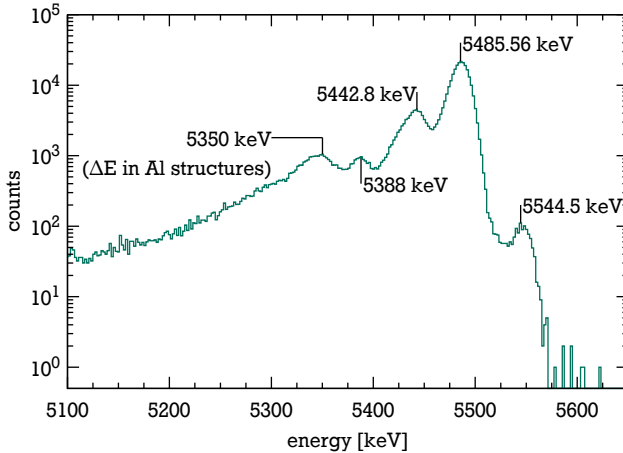
Figure 2.2.: Typical energy spectrum of an ^{241}Am α-source recorded with a p-side strip of a first generation DSSD for EXL. Indicated are the prominent α-energies of ^{241}Am (see also table 4.3 and [30]). The peak at 5350 keV is due to an energy loss in the aluminium structures surrounding each p-side strip.

significant energy loss when passing through this dead layer. A 5.5 MeV α-particle loses about 120 keV in this dead layer which is already so high that particles passing through it appear in the energy spectrum as a separate peak at lower energies. The energy spectrum of an ^{241}Am α-source, which is plotted in figure 2.2, shows this peak at an energy of 5350 keV, which is very close to the expected value. More details on the laboratory tests of these detectors can be found in [27].

The detectors have a depletion voltage of approximately 50 V but are typically operated at bias voltages of 80 V. Typical dark currents are then in the order of a few nA (16 × 16 type) or a few tens of nA (64 × 64 type).

It should be mentioned that the same type of detector was also used to explore the possibility of particle identification by means of **p**ulse-**s**hape **a**nalysis (PSA) with highly-segmented silicon detectors for the first time [32, 33]. Compared to traditional particle-identification techniques based on, for example ΔE-E detector arrays, where the particles have to punch through the first layer of detectors at least, the PSA allows particle-identification already in the first layer. In the case of the future **EXL S**ilicon **P**article **A**rray (ESPA), a first layer of 100 μm thick DSSDs is envisaged. In this first layer, protons of up to about 3.2 MeV and α-particles of up to about 12.7 MeV would be stopped. By applying PSA techniques to the DSSDs these thresholds for particle identification could be potentially lowered.
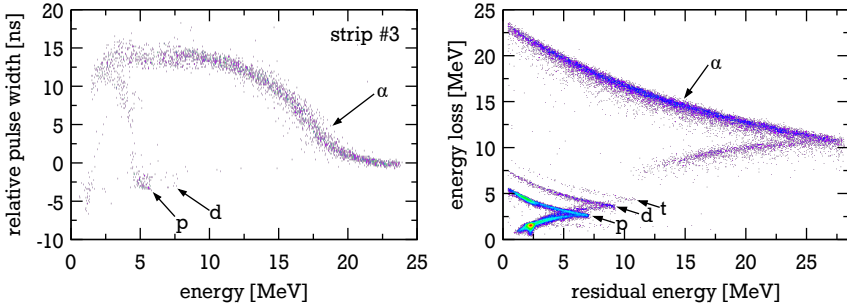
Figure 2.3.: Particle identification with a first generation DSSD for EXL [32, 33].
Left: pulse-shape analysis; *right*: energy loss measurement.

To demonstrate the feasibility of the PSA a 16×16 DSSD with 300 μm strip pitch was used in an in-beam experiment at the Maier-Leibnitz-Laboratorium, Garching. A 70 MeV ^{12}C beam impinged on a Mylar target and the light reaction products up to ^{4}He were detected in the DSSD and a subsequent PIN-diode detector. The PSA was implemented for the 16 p-side strips of the DSSD using analogue electronics. By measuring the amplitude and the width of the pre-amplified current signal at the same time, a particle discrimination is possible by looking at the correlation between both magnitudes. Further details on the experimental setup and the principle of PSA can be found in [32, 33] and references therein. Figure 2.3 (left side) shows a typical particle-identification plot for an exemplary p-side strip of the DSSD. By excluding punch-through events with a veto on the PIN-diode as well as interstrip events in the DSSD, i. e. events where the charge was shared between two strips, a good separation of protons and α-particles has been obtained down to 3 MeV already in this first approach. For punch-through particles the particle identification can be achieved by a ΔE-E measurement together with the subsequent detector which is demonstrated in figure 2.3 on the right side.

2.1.2 Si(Li) detectors for EXL

The Si(Li) detectors used in the EXL demonstrator and later on in the first EXL campaign with radioactive beam were manufactured by Semikon Detector GmbH, Jülich [34]. They were originally developed as transmission detectors for the MUST2 experiment [35]. For a transmission detector, i. e. a detector for the energy-loss measurement as a part of a telecsope setup, it is favourable to not only have a thin dead layer at the entrance side but also at the back side. The boron-implanted p$^+$-contact on the front side of this detector is covered with a layer of evaporated
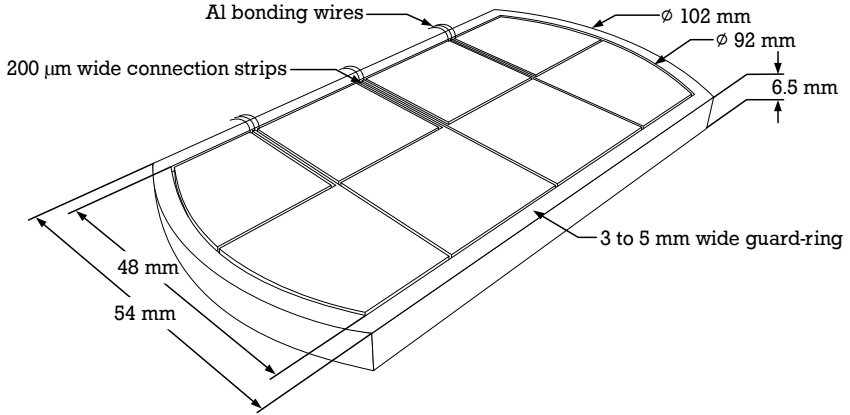
Figure 2.4.: Schematical drawing of the EXL Si(Li)-detectors. (*adapted from* [36])

1st Si(Li)
ST9-23

2nd Si(Li)
ST9-21
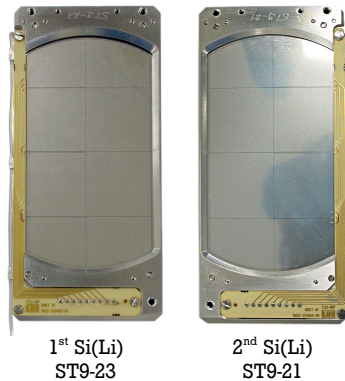
Figure 2.5.: Pictures of the two Si(Li) detectors *ST9-21* (*left*) and *ST9-23* (*right*).

aluminium and has a total thickness below $1\,\mu m$. On the back side, the Li-diffused n-contact is thinned so that an effective thickness (including the evaporated aluminium layer) below $5\,\mu m$ is reached [36, 37]. With these properties, the detector is well suited to be used in a detector telescope within the EXL recoil detector as well. Two such detectors with the serial numbers *ST9-21* and *ST9-23* are available (see figure 2.5). On the front side, each of these detectors is segmented into eight pads of approximately $(24 \times 24)\,mm^2$ each (see figure 2.4). The segmentation is realised by plasma etched $60\,\mu m$ wide and $15\,\mu m$ deep grooves [36]. All eight segments can be read out independently while the back-side is not segmented and is

not read out. During operation, the 6.5 mm thick detectors must be cooled down to temperatures of around −10 °C. At such temperatures, the dark current lies between 1 mA to 1.5 mA for a typical bias voltage of around 800 V which is needed for full depletion.

2.1.3 CsI(Tl) scintillators for EXL
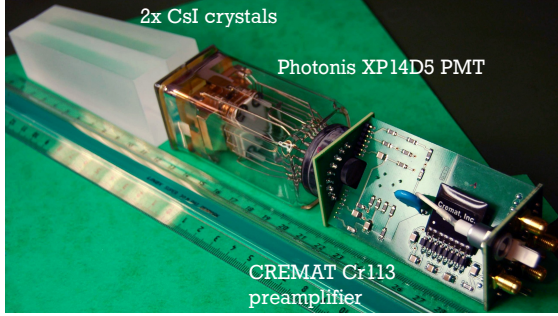
Figure 2.6.: Parts of the CsI(Tl) detector used in the EXL demonstrator tests. *From left to right*: two CsI(Tl) scintillator crystals, *Photonis XP14D5* PMT and *CREMAT Cr113* based preamplifier. (*adapted from* [38])

For the future EXL recoil detector, an outer shell of CsI(Tl) scintillators forming the **EXL G**amma and **P**article **A**rray (EGPA) is envisaged as a calorimeter for high energy recoils as well as γ-rays. Since the demands of this detector are very similar to the ones of the CALIFA barrel detector [1, 39, 40] of the R^{3}B project [1], the development of both detector projects started in cooperation. Therefore, the CsI(Tl) crystals used in the EXL demonstrator tests share similar dimensions with early prototypes for CALIFA. The CsI(Tl) crystals are made by *Amcrys* and are roughly 110 mm long with a tapered shape that expands from (10×20) mm^2 at the front to (19×38) mm^2 at the back. Two of these crystals are read out together by a *Photonis XP14D5* dual channel photomultiplier tube (PMT), in which two independent PMTs are housed and coupled to the scintillator by a common entrance window (see figure 2.6). The PMT bases are equipped with charge sensitive preamplifiers (*CREMAT Cr113*) to allow the use of conventional shaping amplifiers and peak-sensing ADCs.

Figure 2.7.: Schematics of the EXL demonstrator for the third test with 133 MeV proton beam at KVI. (*based on drawings by* [29])

Of the three EXL demonstrator tests, only the last one with a 133 MeV proton beam will be discussed in more detail here (the first test at KVI is briefly summarised in [26]). As shown in figure 2.7, the EXL demonstrator in this test was composed out of a 64×64 DSSD, two Si(Li) detectors, a second DSSD with 64×16 strips and a double CsI(Tl) crystal. All silicon detectors were placed in vacuum and the CsI(Tl) crystals were positioned behind a $75\,\mu m$ thin stainless steal window in air.

For each DSSD only 32 channels of electronics were available. By coupling four strips together it was possible to make use of the whole sensitive area of both DSSDs. Consequently, the strip pitch was increased to effectively $1.2\,mm$ for both detectors on both sides. The first Si(Li) detector was positioned such that the beam hit the detector in the centre between four pads. The four remaining pads at the edge of the detector were not covered by the beam spot and not read out. The second Si(Li) was slightly shifted so that the beam spot was centred on one single pad. Therefore, only this single segment was read out. The CsI(Tl) detector was placed centred with respect to the beam and both channels were read out independently.

Spectra from the individual detectors

Figures 2.8, 2.9 and 2.10 show exemplary energy spectra from the different detectors of the EXL demonstrator. The energy calibration of the DSSDs and Si(Li)s was established by a calibration of the electronics using a pulser and a gain match
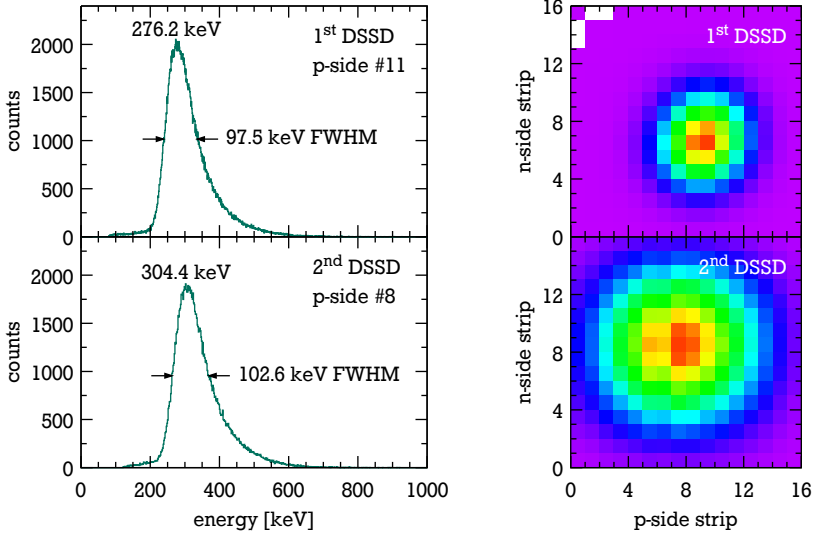
Figure 2.8.: Exemplary energy spectra of the two DSSDs of the EXL demonstrator (*left*) and the beam spot visible in the hit pattern (*right*).
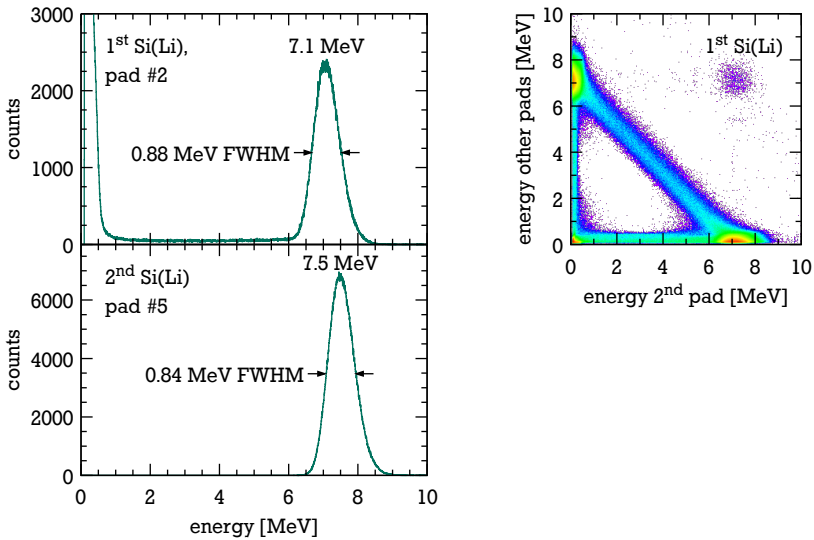
Figure 2.9.: Exemplary energy spectra of the two Si(Li)s of the EXL demonstrator (*left*) and charge sharing observed in the first Si(Li) (*right*).

2. Developments towards EXL

CsI sum   116.2 MeV

1.6 MeV FWHM

counts — energy [MeV]

energy 2nd CsI [MeV] — energy 1st CsI [MeV]
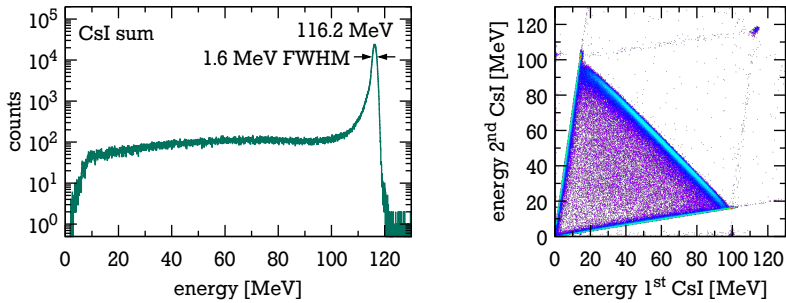
Figure 2.10.: Reconstructed energy spectrum as measured with the CsI scintillator of the EXL demonstrator (*left*) and the correlations between the two signals of the individual channels (*right*).

layer	material	thickness	energy loss calculated	measured	figure
vacuum window	Mylar	75 μm	0.058 MeV	—	
	air	1.02 m	0.640 MeV	—	
vacuum window	Mylar	75 μm	0.058 MeV	—	
1st DSSD	Si	280 μm	0.311 MeV	0.276 MeV	2.8
1st Si(Li)	Si	6.5 mm	7.379 MeV	7.1 MeV	2.9
2nd Si(Li)	Si	6.5 mm	7.702 MeV	7.5 MeV	2.9
2nd DSSD	Si	280 μm	0.340 MeV	0.304 MeV	2.8
vacuum window	stainless steel	75 μm	0.273 MeV	—	
	air	50 mm	0.007 MeV	—	
CsI scintillator	CsI	115 mm	116.23 MeV	116.2 MeV (*fixed*)	2.10
sum			133 MeV	131.8 MeV	
sum (detectors only)			131.96 MeV	131.8 MeV	2.11

Table 2.1.: Expected and measured energy losses. The energy losses were calculated with *LISE++* v.9.8.37 [41] for a 133 MeV proton beam.

with α-sources (the general procedure is described in more detail in section 4.2). Despite the fact that the energy of the α-particles used for the calibration is about 20 times higher than the expected energy loss of the protons in the DSSDs (as summarised in table 2.1), the measured energies are in good agreement with the expectations. The same is true for the energy loss in the Si(Li) detectors.

Since the beam was centred on the first Si(Li) detector at the intersection of four of its segments, there is a non-negligible probability for charge sharing between the segments. The resulting anti-correlation is plotted in figure 2.9. It is the main source of the background which is visible in the energy spectra.
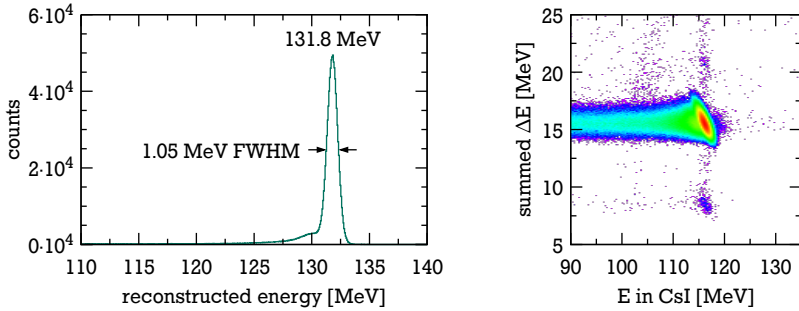
Figure 2.11.: Total energy reconstructed with the EXL demonstrator (*left*) and correlation between the energy in the CsI(Tl) and the summed ΔE signals.

The energy response of the CsI(Tl) detector shows a certain peculiarity which is revealed in the correlation plot of the two individual channels as shown in figure 2.10. For two scintillators so close to each other it is foreseeable that some of the high-energy protons get scattered from one crystal into the other. This "proton leakage" can be observed in figure 2.10 as an anti-correlated band, i. e. if the proton deposits more energy in one crystal, it deposits less in the other. Additionally, figure 2.10 reveals a correlation between the two signals: For every event about 12 % of the energy is shared with the other channel. This "light leakage" is caused by the common window with which the two crystals are coupled to the two PMTs. The effect was further studied and qualitatively confirmed by comparison with simulations in [42]. By summing the two channels on an event-by-event basis, both "leakages" can be restored as shown in figure 2.10. The remaining background in the energy spectrum can be attributed mostly to hadronic reactions in the crystal [42]. Since the CsI(Tl) scintillator cannot be reasonably calibrated with a radiation source, its energy was fixed to the simulated energy value as listed in table 2.1.

The total energy was reconstructed by adding up all signals from the individual detectors (see figure 2.11). The only condition applied to the data was that all detectors had a coincident signal above their individual noise threshold. Since the total energy is dominated by the energy deposit in the CsI(Tl), which had to be fixed to the nominal value, the actual reconstructed proton energy of 131.8 MeV is very close to the expected energy loss in all detectors. With a resolution of about 0.8 % (FWHM) the feasibility of the energy reconstruction in the EXL detector telescopes was successfully proven.
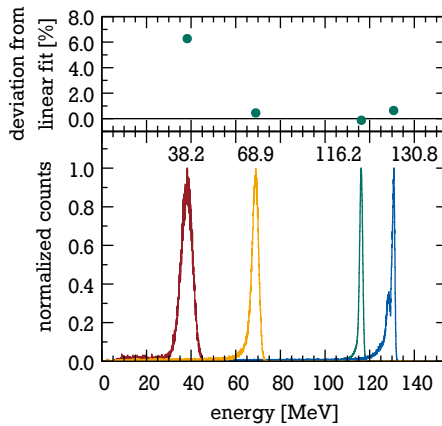
Figure 2.12.: Energy spectra of the four proton energies measured with the CsI(Tl) scintillator of the EXL demonstrator (*bottom*). Deviation of the measured energy from a linear fit (*top*).

Another goal of this demonstrator test was to get an estimate of the linearity of CsI(Tl) for high proton energies. Therefore, additional measurements with different beam energies were conducted. Since it was technically problematic to change the beam energy, a 42.6 mm thick aluminium block was placed in front of the EXL demonstrator in order to reduce the beam energy. This way and by placing the CsI(Tl) detector directly in the beam (with and without the absorber), four measurements with calculated beam energies of 36.33 MeV, 66.61 MeV, 116.22 MeV and 132.55 MeV were performed. The resulting energy spectra are shown in figure 2.12. A first impression of the linearity is given by a linear fit and by evaluating the deviations of the measured data from the fit (see figure 2.12 at the top). At first glance the linearity seems good except for the lowest data point. However, the fact that the beam energy was not measured independently but calculated from energy-loss measurements limits the significance of this measurement.

These results contributed to the TDR (**T**echnical **D**esign **R**eport) for the CALIFA barrel which was approved by FAIR [40].
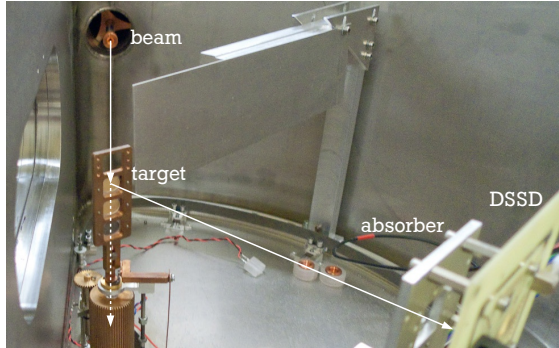
Figure 2.13.: Experimental setup at the Rosenau laboratory.

As already outlined before, the measurement of light ions with low energy is a key demand for the ESPA. Therefore, tests were performed at the 3 MV Van-de-Graaf accelerator of the Rosenau laboratory in Tübingen using a small DSSD of the first generation with 16×16 strips and 300 μm pitch (see section 2.1.1). All channels of the DSSD were read out individually and connected to standard electronics, i. e. *Mesytec MPR-16* preamplifier, *Mesytec MSCF-16* shaping amplifier and *Mesytec MADC-32* ADC. The DAQ was triggered by a logic OR of all p-side strips. For the tests, proton and H_2^+ beams were accelerated at different terminal voltages between 818 kV and 1508 kV. As shown in figure 2.13, the DSSD was not exposed to the beam directly. Instead, the beam first scattered off a carbon target with a thickness of 32 μg/cm^2 before it hit the DSSD which was placed at a distance of 208 mm to the target and at an angle of about 40° with respect to the beam axis. With additional Mylar absorbers right in front of the DSSD the proton energies were further reduced to below 100 keV. Two exemplary spectra, each from the p-side strip #12, are shown in figure 2.14 for the highest proton energy of 1433 keV (calculated energy after the target without absorber) and the lowest energy of 97 keV (calculated energy after the target and Mylar absorber) of which the latter resulted in a measured energy of 68 keV. It should be noted that the setup was not specifically designed to reach the best possible energy resolutions. Nevertheless, the conditions allowed to successfully measure protons with energies slightly below 100 keV. Also, the peak of interest in figure 2.14 appears well separated from the noise. A trigger threshold of 30 keV seems to be reachable.
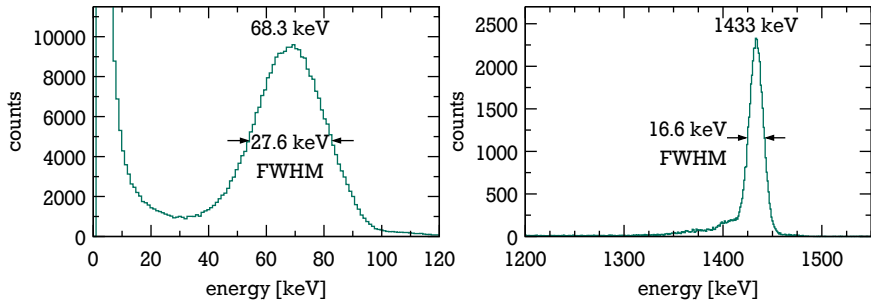
Figure 2.14.: Exemplary spectra from the low energy proton beam-time at the Rosenau laboratory in Tübingen. Shown are spectra from the DSSD p-side strip #12 for the lowest (*left*) and highest proton energies (*right*) in the test. The given FWHM include contributions from electronics noise as well as straggling in the target and the absorber in front of the DSSD.

2.3 Second generation DSSD for EXL
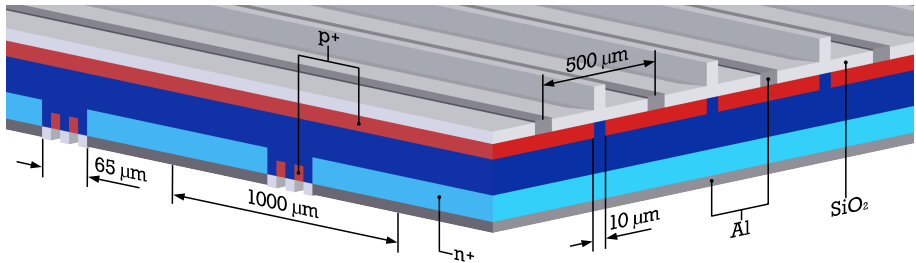
Figure 2.15.: Schematic drawing of the second generation of DSSD prototypes for EXL (not to scale) [31].

A second generation of DSSD prototypes for the EXL project was also developed by PTI, St. Petersburg. The new design was aimed to keep the benefits of the old design, i. e. small interstrip gap and thin dead layers, while improving it in certain aspects. Especially by further minimising the dead layers, the peaks which were visible in the energy spectra of the first generation detectors (see figure 2.2) are avoided. Figure 2.15 shows the new layout sketched schematically. The electrical contacts on the p-side of the detector are now realised with a central aluminium strip (600 Å thick) instead of the previous frame around the strip [31]. Also, the remaining area is now covered by a thin layer of SiO_2 (500 Å thick) [31]. The thick-
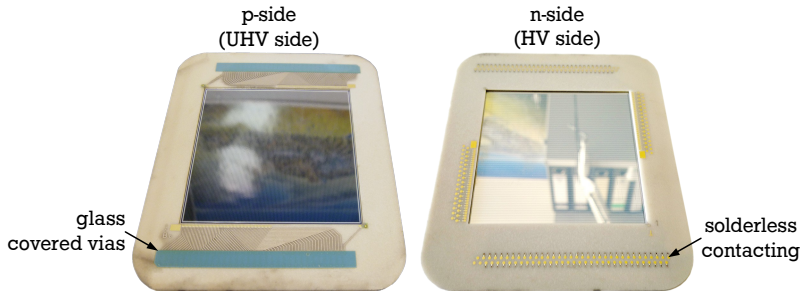
Figure 2.16.: Second generation DSSD mounted on a UHV compatible AlN PCB.

ness of both layers was optimised relatively to each other such that the energy loss of light ions with low energy is approximately the same in these layers. For example, the energy loss of an α-particle with an energy of 5.5 MeV is roughly 9.3 keV and 7.5 keV in the aluminium structure and in the oxide layer, respectively. The slight difference is indistinguishable within the typical resolution of the complete detector system and should not create any visibly shifted peaks compared to the previous design.

The DSSD has a thickness of 285 μm and an active area of (6.4×6.4) cm^2 [31]. It is segmented into 128 strips on the p-side and 64 on the n-side which results in a strip pitch of 500 μm and 1 mm on the p-side and on the n-side, respectively. In the new design, the gap between the strips was further reduced to 10 μm (p-side) and 65 μm (n-side) [31].

So far, three DSSDs were mounted on UHV compatible AlN PCBs (**P**rinted **C**ircuit **B**oard, see figure 2.16) to make them usable for experiments in the storage ring. The PCBs are further discussed in section 2.4.

Performance tests with α-sources

With these new detectors, extensive tests with α-sources were performed not only to probe their general functionality but also to determine the energy resolution, the probability for interstrip events, i. e. charge sharing between two segments, and the structure of the background in their energy spectra.

For these tests, each channel of the DSSD was read out using conventional electronics. The same modules were used also for the E105 experiment later (see section 3.5). As α-sources, ^{241}Am and ^{148}Gd were used. The latter only emits an α-particle at one single energy of 3182.69 keV [43] while ^{241}Am has several transitions with the most prominent one at an energy of 5485.56 keV [30] (see table 4.3 for details). The lower energy and the fact that the ^{148}Gd α-source has only one

line is an advantage here. The relatively low energy of the emitted α-particles causes higher energy losses in the dead layers and hence, the measurement will be more sensitive to them. Also, a single line simplifies the interpretation of the background as any additional structure in the energy spectrum would be created by the detector.

Figure 2.17 shows spectra of a measurement with the ^{148}Gd α-source illuminating the p-side of the detector. The figure shows a correlation between the energy measured on the p-side (x-axis) versus the n-side energies (y-axis), i.e. the pn-correlation. Projections of these correlations are plotted along the corresponding axes. In the two-dimensional pn-correlation plot, the diagonal line corresponds to events where both detector sides have measured the same energy and consequently no charge was shared between segments. Events outside of this diagonal result from events where a charge sharing between strips occurred at least on one side of the detector. The origin of the horizontal and vertical lines can be studied with the help of the correlation between two interstrip signals. These correlations are shown in figure 2.17 separately for the p- and the n-side. The clear anti-correlation visible in both plots is the expected characteristics of a charge sharing between two adjacent segments. By setting gates on these anti-correlations the different contributions of interstrip events can be isolated in the pn-correlation plot. This was done in figure 2.19. The vertical line in the pn-correlation can be attributed to the case where the charge sharing has happened mostly on the n-side but not on the p-side, i.e. n-interstrip events. Consequently, the horizontal line corresponds to the opposite case, i.e. p-interstrip events. The events in between these lines are due to coincident p- and n-interstrip events. Hence, the background in the energy spectrum of the p-side can be attributed mostly to p-interstrip events and vice versa for the n-side spectrum. The p-side background spectrum is also free of any shifted peaks which clearly demonstrates the progress made with the new detector design. The faint vertical line at 2.9 MeV p-side energy is too weak to become visible in the energy spectrum even in logarithmic scale. Unfortunately, its origin is currently unclear. At the same time, the small ghost peak in the n-side spectrum at around 2.8 MeV is caused by p-interstrip events. Particles which hit the interstrip region of the p-side are shifted towards lower energy as they face a higher energy loss in the thicker dead layer of the interstrip region.

Figure 2.18 shows the analogue case where the α-particles of the ^{148}Gd source were injected from the n-side of the detector. Now, the pn-correlation plot shows a drastically different structure compared to p-side injection. The vertical line which was previously attributed to n-interstrip events and the corresponding n-interstrip events in the correlation-plot are missing altogether. Instead, an additional diagonal line appeared. Its origin is not understood yet. The missing n-side interstrip
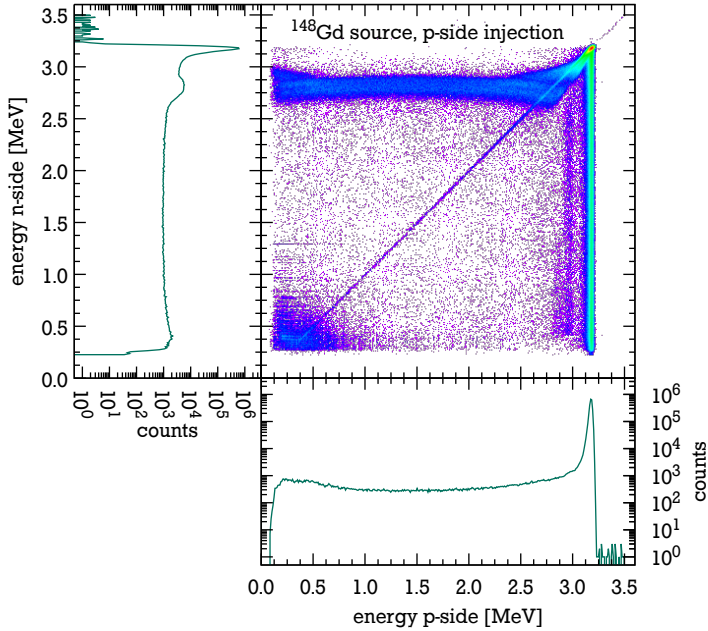
Figure 2.17.: Test of a second generation DSSD with a ^{148}Gd α-source illuminating the detector's p-side. *Top*: correlation between p- and n-side energy signals together with projected energy spectra; *bottom*: correlation of interstrip events.
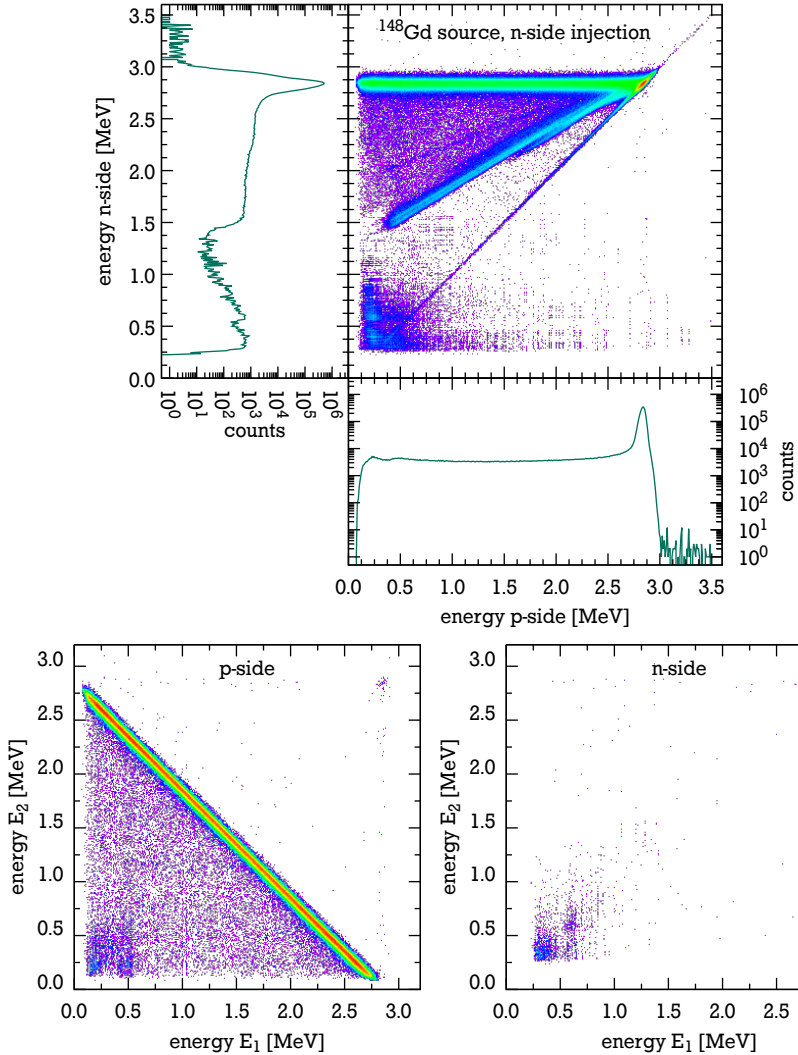
Figure 2.18.: Test of a second generation DSSD with a ^{148}Gd α-source illuminating the detector's n-side. *Top*: correlation between p- and n-side energy signals together with projected energy spectra; *bottom*: correlation of interstrip events.
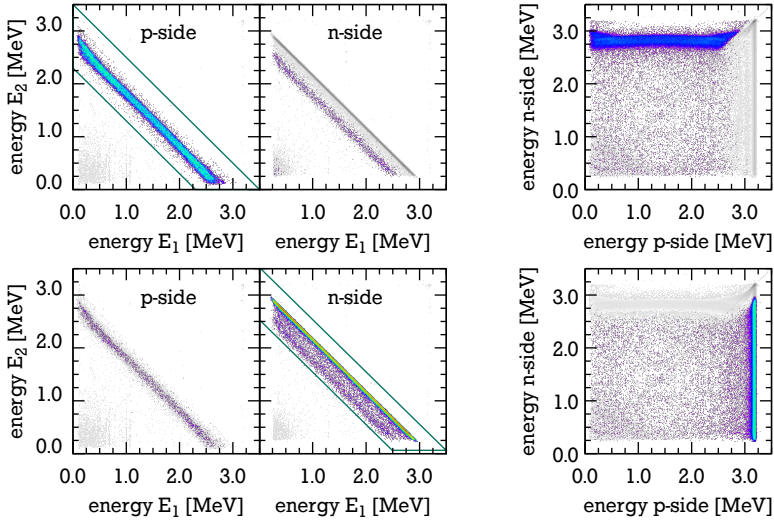
Figure 2.19.: Cuts on the interstrip correlations for ^{148}Gd α-source and p-side injection.

events, however, can be explained by the structure of the detector's n-side (figure 2.15): The n$^+$-strips are insulated with respect to each other by a p$^+$-doped structure between them. Naturally, this forms a separate p-n contact with its own depletion zone. If a particle is stopped in this region, the charge carriers created there do not drift towards the p$^+$-strips on the front side but to the p$^+$-insulation structure. Thus, the p-side does not see a signal from the particle. Since the trigger for the data acquisition was taken from the p-side only, this particular signal is not recorded and therefore not visible in this plot.

The statistical probabilities for the different interstrip signals were also analysed quantitatively for measurements with the ^{148}Gd and ^{241}Am α-sources and for both p- and n-side injection. The results are summarised in table 2.2. When compared with the geometric coverage, i.e. the ratio between the actual detector strip and the interstrip region, the values for p-side injection are in the same order of magnitude as the values expected from geometry. The probabilities extracted from the measurements with α-particles at lower energy are closer to the geometric value. In the case of a n-side injection, the p-interstrip probability is higher than for a p-side injection. The α-particles are stopped close to the back face of the detector which should be similar to a high energy particle impinging from the p-side and being stopped close to the back face. While an energy dependence of the interstrip

α-source	injection side	p-interstrip	n-interstrip
^{148}Gd	p-side	$(1.61 \pm 0.01)\,\%$	$(5.74 \pm 0.01)\,\%$
^{148}Gd	n-side	$(13.68 \pm 0.02)\,\%$	$(0.02 \pm 0.01)\,\%$
^{241}Am	p-side	$(4.13 \pm 0.01)\,\%$	$(7.98 \pm 0.01)\,\%$
^{241}Am	n-side	$(19.26 \pm 0.01)\,\%$	$(0.41 \pm 0.01)\,\%$
geometry		$2.0\,\%$	$6.5\,\%$

Table 2.2.: Probability of interstrip events in comparison to the geometry of the detector. The given error bars represent statistical uncertainties only.

probability might seem plausible, the few data points here do not allow to draw definitive conclusions. Later on, in section 4.4, the analysis of the elastic proton scattering data with continuous energy shows the dependence on the penetration depth more clearly.

Finally, the energy resolution (FWHM) of each strip was evaluated for the measurements with both α-sources. The results are summarised in figure 2.20. For the average resolution of the p-side strips, a value of 26.6 keV (FWHM for ^{148}Gd α-source) and 25.6 keV (FWHM for ^{241}Am α-source) were found. These values include a contribution from electronic noise of 19.8 keV which was determined as the FWHM of an electronic pulser signal connected to the test inputs of the pre-amplifiers (see figure 2.20). Unfolding the contribution of the electronics, the average resolution of the p-side strips is 16.2 keV (FWHM) and 17.8 keV (FWHM) for the ^{148}Gd α-source and the ^{241}Am α-source, respectively.
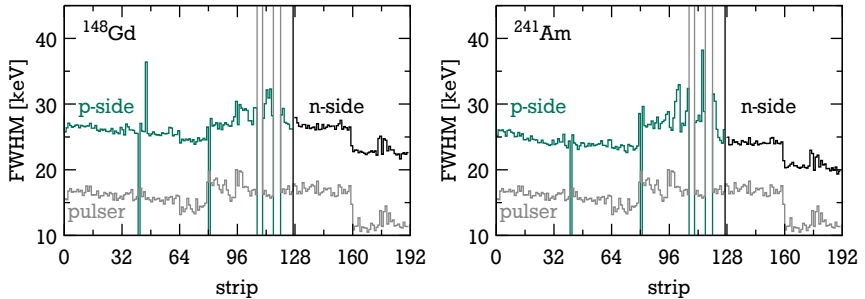
Figure 2.20.: Resolution (FWHM) of all strips of a second generation DSSD determined with ^{148}Gd (*left*) and ^{241}Am (*right*) α-sources. The resolution (FWHM) of the electronics is plotted in grey.

2.4 Vacuum concept
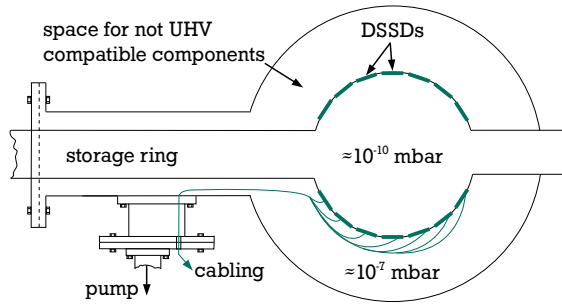
Figure 2.21.: Vacuum concept for EXL as proposed in [44].

The UHV compatibility of the EXL recoil detector is a crucial technical challenge. The ESPA will contain hundreds of silicon detectors of which some, i. e. the Si(Li)s, cannot be baked at all. Also the cabling of the detectors and potentially also parts of the readout electronics have to be placed inside the vacuum but not inside the UHV. Traditional approaches to solve this problem exist but are not favourable. One is differential pumping, where a HV in the region of the recoil detector is tolerated and separated from the UHV in the storage ring by conductance-limiting apertures. The drawback of this method is of course a degeneration of the ion beam interacting with the residual gas in the region of the particle detector. Additionally, the conductance-limiting apertures in between the vacuum sections might limit the acceptance for broad, un-cooled beams and certain beam trajectories in general. Another solution would be to enclose the recoil detector in some kind of pocket separated from the ring vacuum by a thin window. This would allow the use of standard, i. e. not UHV compatible, materials inside the pocket and avoid the need for a bakeable detector system. However, the dead layer of the window would increase the threshold for low energy recoils and, therefore, does not allow to reach the aim of EXL to measure at low momentum transfer, where recoil energies are low. For example, a 50 μm thick stainless steel foil would still stop protons with energies up to about 3.7 MeV [41].

A possible solution to this problem was proposed in [44]. By using the innermost layer of DSSDs as a vacuum barrier, the UHV of the storage ring can be separated from an auxiliary vacuum where all the non-bakeable components will be installed (see figure 2.21). An absolute tightness between the two vacua is not necessary as the auxiliary vacuum would be in the order of a high vacuum (HV) only. The idea here is again the differential-pumping approach with the difference that the

conductance between the two vacua is only given through possible leaks of the innermost sphere of DSSDs. Compared to the traditional differential-pumping scheme, the vacuum quality in the interaction area is expected to be much better and the beam dynamics are not restricted due to apertures in the beam line. Furthermore, the use of the DSSD as a vacuum barrier, hence *active vacuum window*, avoids additional dead layers and allows the detection of recoils with lower energy.

First vacuum demonstrator
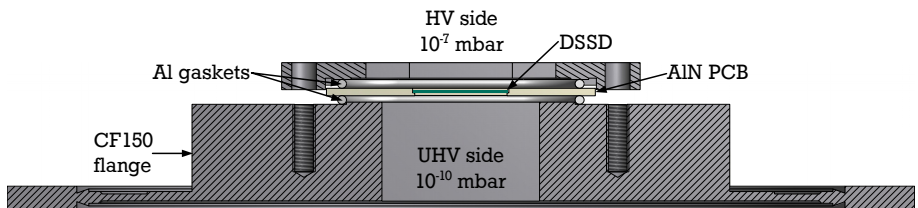
Figure 2.22.: Schematic view of the first vacuum demonstrator for EXL.

The idea was further developed within the EXL collaboration and resulted in a first vacuum demonstrator [45] which is shown in figure 2.22. With this first prototype the general feasibility of the active vacuum-window principle should be demonstrated. Also, clarification was needed whether the DSSD would survive the bake-out process without degradation of its spectroscopic properties. Therefore, one of the (2×2) cm^2 first generation DSSDs was glued to a 1.5 mm thick AlN PCB manufactured by LUST Hybrid-Technik GmbH[1] using a UHV compatible epoxy glue *EPO-TEK H77* [46]. AlN was chosen as material for the PCB since it has an expansion coefficient close to the one of silicon in order to minimise mechanical stress on the detector during baking. On the front side of the PCB, i. e. the side facing the UHV, the signal lines are routed through glas covered vias to the back side leaving the front side UHV compatible and in principle airtight. All cabling is then connected reversibly on the back side of the PCB by using spring pins housed in custom made connectors made of polyether ether ketone (PEEK) [47]. PEEK has the advantage that it can be machined easily, is mechanically stable, withstands high temperatures and can even be used in a UHV environment [48]. The choice to use low-outgassing and clean material also for the HV side was made since

---

Figure 2.23.: Vacuum block diagram used for the differential pumping tests with the first and improved vacuum demonstrators for EXL (see figures 2.22 and 2.25). (*adapted from* [45])

the leakage rate from the HV to the UHV side was not known a priori. Also, the connectors have to stand the baking of the detector which excluded most other commercially available solutions. The PCB with the detector is mounted to a CF150 flange by clamping it in between of two aluminium rings which serve as sealing gaskets (see figure 2.22). This flange is then used to intersect two different vacuum systems as shown in the block diagram in figure 2.23. Both sides are evacuated in parallel by two independent pumping systems. The UHV side is then baked for about one week and further evacuated until UHV conditions are reached. After the baking was finished, the technical limit of the test stand of $1.2 \cdot 10^{-10}$ mbar was reached on the UHV side while a vacuum of $2.2 \cdot 10^{-7}$ mbar was achieved on the HV side. The dependence between the pressures in the two sections was then systematically studied by using a needle valve on the HV side as an artificial leak that worsens the vacuum in this section. In figure 2.24 on the left side, the pressures measured in the two vacuum sections are plotted against each other. Although the pressure on the HV side was increased by four orders of magnitude, the pressure in the UHV side stayed within the 10^{-10} mbar region. Hence, the DSSD used as an active vacuum window was able to maintain a pressure difference of up to six orders of magnitude. Ultimately, the comparison of two ^{241}Am α-spectra measured before and after the vacuum test proved that the DSSD maintained its spectroscopic properties. The resolution changed only slightly from 18 keV (FWHM) before the bake-out to 21 keV (FWHM) after the bake-out [45].
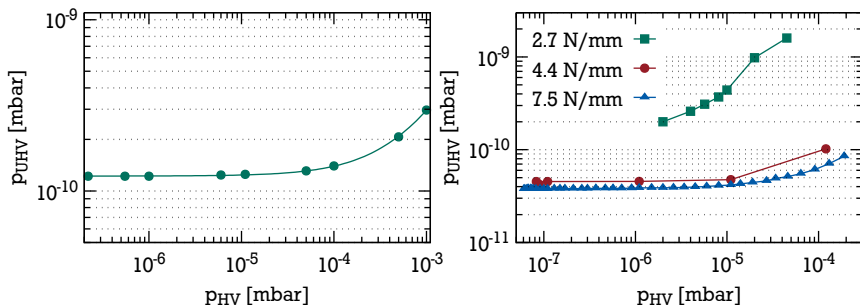
Figure 2.24.: Results of differential pumping tests using the vacuum demonstrator. *Left*: Test of the first vacuum demonstrator of figure 2.22 (*adapted from* [45]); *right*: Tests with various screw forces in N/mm wire length using the improved vacuum demonstrator setup of figure 2.25 (*data from* [29]).

Developing the vacuum demonstrator further

While the first vacuum demonstrator successfully proved the principle of using a DSSD as an differential pumping barrier, the setup had to be improved. One trial ended in a complete loss of the detector as the clamping caused hairline cracks in one PCB which eventually destroyed the detector. To reduce the risk of such problems, the system was further developed and improved within the EXL collaboration. It was also adapted for the full size DSSD of the second generation.

One problem of the first demonstrator was that too much force was needed to compress and therefore tighten the aluminium gaskets. Furthermore, the force was not distributed equally. Improvements were achieved in several ways: In order to distribute the force on the PCB more equally, a new PCB with rounded corners following the curvature of the gasket was designed. This allowed the re-designed clamp, which was now mounted from the UHV side, to compress the seal more equally. To further improve the homogeneity and the dosing of the force cup washers were used together with the screws. The quality of the PCB surface was improved by the manufacturer by lapping the flatness to values smaller than $50\,\mu m$ (before $< 250\,\mu m$) and polishing the surface to a remaining roughness of smaller than $0.5\,\mu m$ (before $< 5\,\mu m$) [45]. Finally, the solid aluminium rings were replaced by *Helicoflex DELTA* seals [49]. These hollow aluminium rings are spring loaded and have a ridge at each side. When the gasket is compressed, this ridge deforms plastically and is therefore adapted to the surface. Thus, a lower pressing
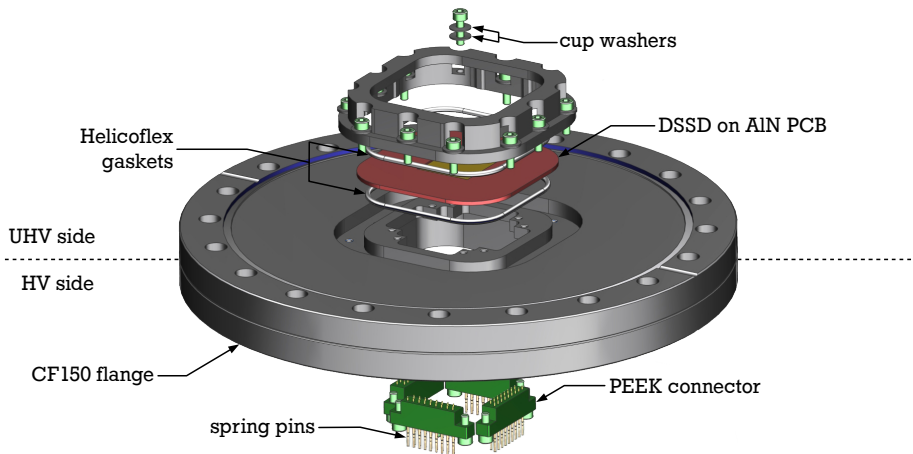
Figure 2.25.: Improved vacuum-demonstrator test-flange for the first generation 64 × 64 DSSD. (*based on technical drawings by* [50])

power is needed compared to the previous gaskets. A schematic drawing of this improved setup is shown in figure 2.25.

With the improved setup it was possible to study the dependency of the contact pressure on the efficiency of the differential pumping system with the goal to minimise the contact pressure. These tests revealed that a contact pressure of only 4.4 N/mm of seal circumference was needed to reach a sufficient vacuum in the 10^{-10} mbar region at the UHV side (see right side of figure 2.24). Nevertheless, during the E105 experiment a contact pressure of 10 N/mm was used to allow for some safety margin.

After successful tests, the improved concept of the vacuum demonstrator was adapted to be used for the second generation, full sized DSSDs. Despite the larger detector, the test assembly still fits on a CF150 flange which is shown in figure 2.26. The dimensions of the clamp, the cut-outs for the detector and the connectors are identical to the final detector head which was eventually used in the EXL experiment at the ESR (see section 3.2). Hence, it is possible to use this flange to perform the necessary UHV validation of each detector in a test stand rather than in the final scattering chamber.
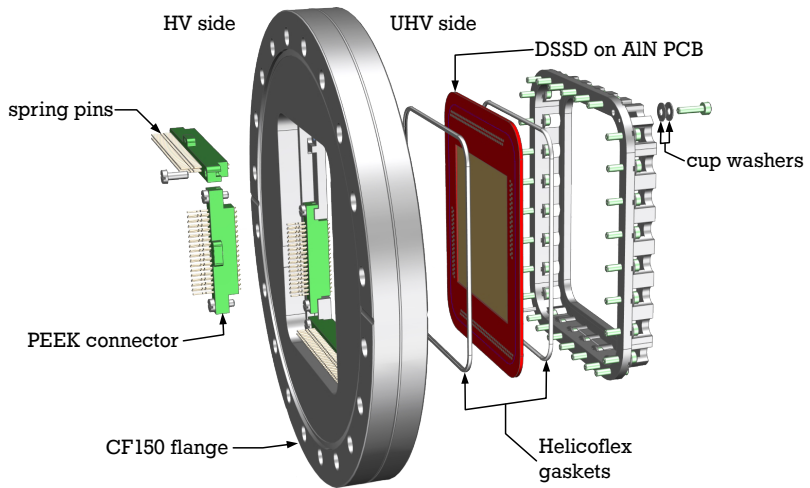
Figure 2.26.: Improved vacuum-demonstrator test-flange for the second generation 128×64 DSSD. (*based on technical drawings by* [50])

3 The EXL experiment E105 at the ESR

3.1 The GSI accelerator facility
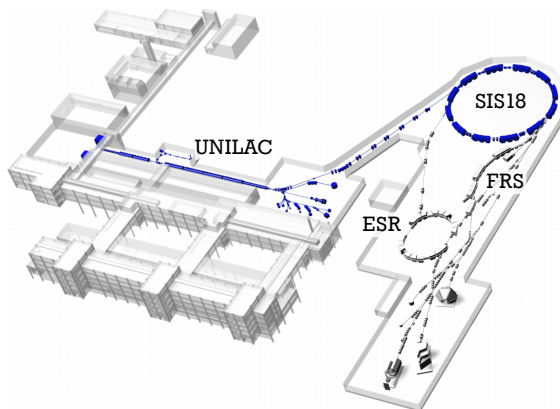
Figure 3.1.: The GSI ion accelerator facility. (*adapted from* [1])

The first EXL physics campaign with exotic beams (E105) was conducted by the EXL collaboration in October 2012 at the *GSI Helmholtzzentrum für Schwerionenforschung GmbH*[1] in Darmstadt, Germany. The GSI accelerator facility offered – at the time of this experimental campaign – the world-wide unique possibility to study radioactive nuclei in a storage ring interacting with an internal gas-jet target.

A schematic drawing of the GSI facility is shown in figure 3.1. GSI is able to provide a multitude of light- and heavy-ion beams ranging from hydrogen up to uranium. Stable-ion beams are produced in one of three sites, i. e. Terminal South, Terminal North and High Charge State Injector (HLI), by various ion sources and then accelerated in the **UNI**versal **L**inear **AC**celerator (UNILAC) to energies of up to 20 MeV/u. The UNILAC is pulsed at a frequency of 50 Hz and pulse widths of typically 5 ms, which allows a time sharing between low energy experiments and the injection into the heavy-ion synchrotron SIS18 (**S**chwer**I**onen **S**ynchrotron) [51].

---

[1]   initially founded as **G**esellschaft für **S**chwer**I**onenforschung mbH, renamed in 2008

Together with the different injectors, up to three different ion species with different energies can be accelerated in successive duty cycles [52]. For the injection into the SIS18 the ion beams are accelerated in the UNILAC up to 11.4 MeV/u. By stacking the beams, i.e. by successively injecting beams into the ring, the intensity of the ion beams can be increased. With a maximum magnetic rigidity Bρ of 18 Tm any ion species from hydrogen to uranium can be accelerated to energies up to $1 - 4.5$ GeV/u [53].

3.1.1 Radioactive beam production at the FRS
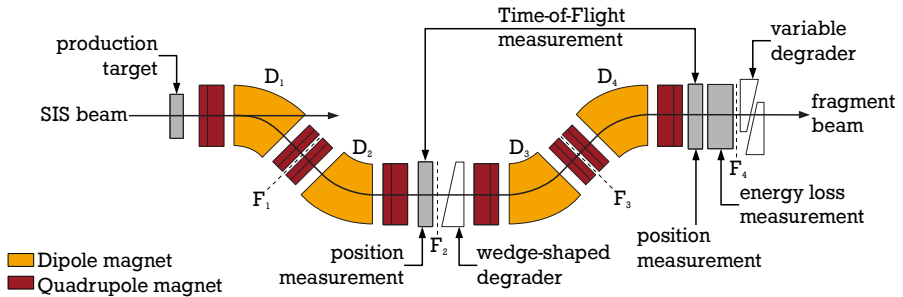
Figure 3.2.: Schematic view of the **FR**agment **S**eparator (FRS) at GSI. (*adapted from* [53, 54])

Radioactive ions are produced with the **FR**agment **S**eparator (FRS) via the so-called in-flight separation method [53]. A primary beam of stable ions at relativistic energies from the SIS18 is impinging on a production target. If a light target, like for example beryllium, is used, the exotic nuclei are predominantly created by fragmentation of the projectiles [55, 56]. The fragments are mostly fully ionised and continue with a forward peaked distribution at velocities close to the one of the initial beam. Neutron rich nuclei can be created predominantly by fission. For this purpose, a heavy beam is shot on a heavy target. The Coulomb field between the projectile and target nuclei can excite the former and induce its fission [55, 56].

To identify and select the nuclei of interest a zero-degree spectrometer is needed. However, because of the relativistic energies, a full A and Z separation is not possible by using electric and magnetic sector fields alone [53]. Instead, a combination of Bρ analysis and atomic energy-loss in matter is utilised, the so called Bρ-ΔE-Bρ-method. A first achromatic ion-optical system preselects nuclei with the same Bρ and focuses them on a profiled energy degrader that gives an additional selection criterion by exploiting the Z^2 dependence of the electronic stopping in matter. Fur-

ther purification of the secondary beam is achieved by a second Bρ analysis in a second achromatic ion-optical system similar to the first one.

A schematic drawing of the FRS at GSI is shown in figure 3.2. It consists of four independent stages with one 30° dipole magnet each that is surrounded by quadrupole as well as sextupole magnets before and after the dipole in order to fulfil first-order focussing conditions and to correct for second order aberrations, respectively. The first two dipole magnets, D_1 and D_2, accomplish a pre-selection of the fragments according to their magnetic rigidity and focus the beam on a variable wedge-shaped energy-degrader located in the focal plane F_2. Further beam purification is achieved by the remaining two dipoles D_3 and D_4 following the energy degrader. A particle identification with respect to *A* and *Z* is accomplished for individual ions by coincidence measurements of the energy loss in a **MU**ltiple-**S**ampling **I**onisation **C**hamber (MUSIC) in F_4 together with position and **T**ime-**O**f-**F**light (TOF) measurements between F_2 and F_4. Thus, the purified beam can be extracted with different beam lines leading either to experimental caves or to the **E**xperimental **S**torage **R**ing (ESR) [53].

3.1.2 The Experimental Storage Ring, ESR

The **E**xperimental **S**torage **R**ing (see schematics in figure 3.3) is constructed as a versatile storage ring for light and heavy ions from hydrogen to uranium. With its maximum magnetic rigidity of 10 Tm it is capable of storing for example U^{92+} ions with an energy of up to 560 MeV/u [59]. Six dipole magnets keep the ions on a track which is effectively 108.36 m in circumference. The resulting revolution frequency is in the order of MHz. Electron and stochastic cooling [60] are available to greatly increase the quality (emittance and momentum spread) of the ion beams. Furthermore, it is possible to re-accelerate or decelerate the stored beam using two **R**adio **F**requency (RF) cavities. The whole ring is bakeable to 300°C in order to achieve an **U**ltra-**H**igh **V**acuum (UHV) of about 10^{-11} mbar which is essential to realise long storage times. Under these conditions, the storage time of stable beams is only limited by **R**adiative **E**lectron **C**apture (REC) in the electron cooler or the internal target [61].

Primary ion beams can be injected from the SIS18 directly through a separate beam line which also contains a stripper target to ensure fully stripped ions for $Z \geq 36$ [59]. The SIS beams are cooled using the electron cooler [61] which is applicable for beam energies from 30 MeV/u to 560 MeV/u [59] over a wide range of beam intensities. By stacking subsequently injected beams, ion currents of up to 7 mA can be reached [61]. Typical and desired cooling times are in the order of a second for stable SIS18 beams. Secondary fragment-beams from the FRS,
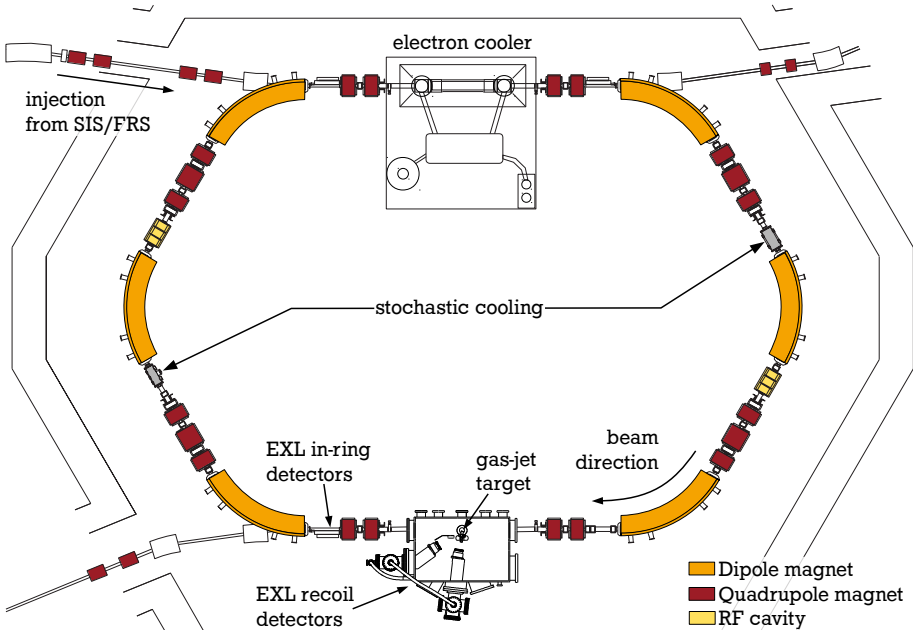
Figure 3.3.: Schematic view of the **E**xperimental **S**torage **R**ing (ESR) at GSI. (*adapted from* [57, 58])

however, have larger emittance and momentum spread resulting in too long cooling times when using the electron cooler alone. Therefore, stochastic pre-cooling can be applied to decrease emittance and momentum spread until electron cooling takes over. The stochastic cooling system was designed with an optimum cooling energy of 477 AMeV ($\beta \approx 0.75$) [62]. Typical cooling times of around a second are achieved for 10^8 particles stored in the ring [63].

3.1.3 The internal target of the ESR

The internal target is installed in the long straight section of the ring opposite of the electron cooler. It can produce target beams from a wide range of target species with intensities of up to $10^{14}\,\mathrm{cm}^{-2}$. A schematic cut through the target is shown in figure 3.4. The beams are formed by expanding the target gas through a nozzle into vacuum. Depending on the process parameters, i. e. the temperature T_0, the pressure p_0 and the diameter d_0 of the nozzle, the target gas is expanded from its
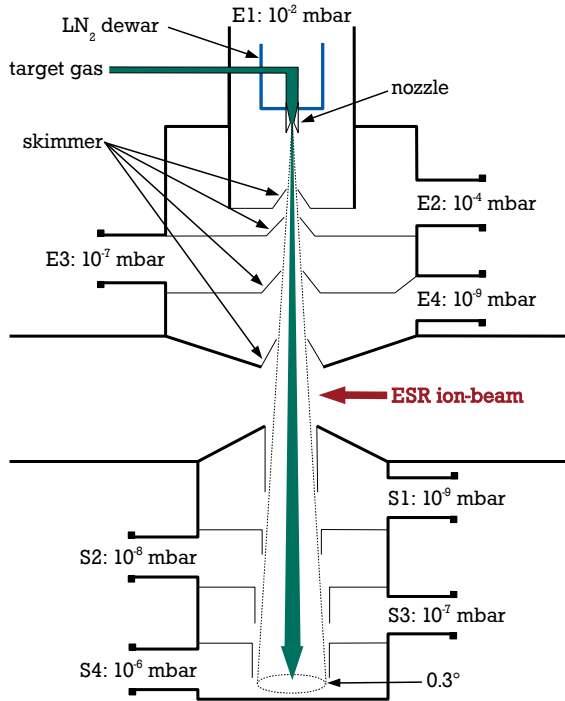
Figure 3.4.: Schematic view of the internal target of the ESR. (*adapted from* [64])

gaseous, supercritical or liquid phase leading to supersonic gas-jets, cluster beams or beams of micro droplets, respectively. After passing through a first skimmer with a diameter of 5 mm, the beam continues through four differentially pumped vacuum chambers and reaches the interaction point with the ion beam roughly 60 cm below the nozzle. After passing the interaction zone, the target beam is dumped into a four-staged differential pumping system. The speciality of this target is the operation under the UHV conditions of the ESR without limiting its geometrical acceptance by using apertures for a differential pumping system along the beam line. A more detailed description of the target can be found in [64].

3.2 Recoil detection system at the ESR
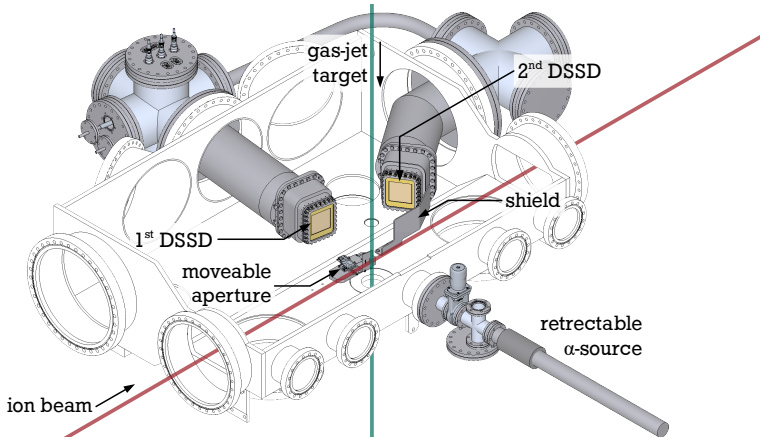
Figure 3.5.: Schematics of the EXL recoil detection system at the gas-jet target of the ESR. (*based on technical drawings by* [50])

Figure 3.5 shows a schematic drawing of the detector setup which was developed within the EXL collaboration to be used at the gas-jet target of the ESR. The first detection system centred at a mean laboratory angle of 80.5° is a detector telescope used for the investigation of elastic and inelastic scattering processes (see figure 3.6). Because of the inverse kinematics, a large dynamical range of energies needs to be covered here, i. e. starting from zero energy at 90° laboratory scattering angle up to energies of in the order of several tens of MeV. As a consequence, the system is set up as a telescope consisting of one 128×64 DSSD (see section 2.3) and two 6.5 mm thick Si(Li) detectors (see section 2.1.2). The latter were placed in the auxiliary vacuum behind the DSSD and were actively cooled during both the bake-out of the ESR and the experiment (see section 3.2.3). With a total thickness of roughly 13.3 mm of silicon the telescope stops protons with energies of up to 50 MeV.

A second, single DSSD centred at a mean forward angle of 32.5° is utilised to study different reaction channels, like for example the giant monopole resonances (GMR) using inelastic α-scattering [42]. Since the detector has an unnecessarily small segmentation for these experiments, each four strips were read out coupled together resulting in a 32×16 segmentation. To screen the detector from particles which interacted with the residual gas in the interaction chamber, a shield along the beam line was installed.
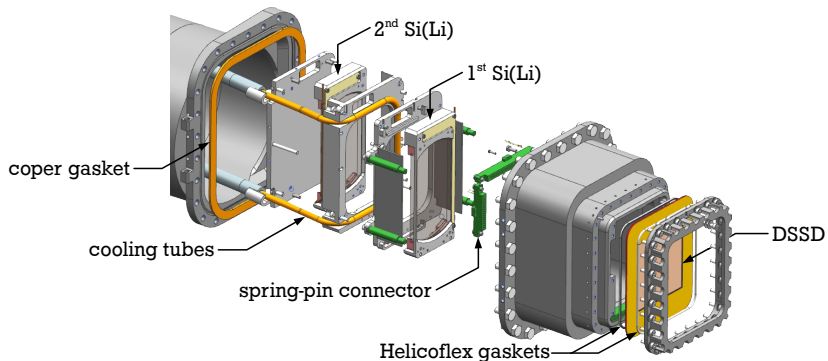
Figure 3.6.: Schematic view of the detector head containing the 90° recoil detector telescope. (*based on technical drawings by* [50])

The scattering chamber was also used in a different experiment (E087). For this experiment, two additional DSSDs were installed in a retractable pocket at the inner side of the chamber. As this system was not utilised during the E105 experiment it will not be discussed any further. Details on the E087 experiment can be found in [65].

3.2.1 Remote controllable aperture

Since the gas-jet target has a diameter of approximately 6.4 mm (see section 3.1.3), the expected angular resolution caused by the extended interaction zone is not sufficient to separate the kinematical bands for elastic and inelastic scattering. This case is illustrated by a simulation of a ^{56}Ni beam with an energy of 400 MeV/u interacting with the gas-jet target (for details on the simulation, see section 4.5.1). In figure 3.8, the kinematical bands corresponding to elastic proton scattering and inelastic scattering to the first excited state of ^{56}Ni are shown. Despite the relatively high excitation energy of 2.7 MeV [66] the two kinematical bands cannot be resolved without applying a slit.

To reach the necessary angular resolution, an aperture was placed between the target and the first detector telescope (see figure 3.7). The aperture is made of a 2 mm thick tantalum plate with two 14 mm long slits with a width of 1 mm and 2 mm. With both apertures it is possible to separate the kinematical bands of elastic and inelastic scattering as predicted by simulations shown in figure 3.8. Of course, this advantage comes at the cost of reduced angular acceptance of the detector system. For example, the solid angle coverage of the first DSSD is about 65 msr and by introducing the 1 mm slit aperture it is reduced to effectively 5 msr.
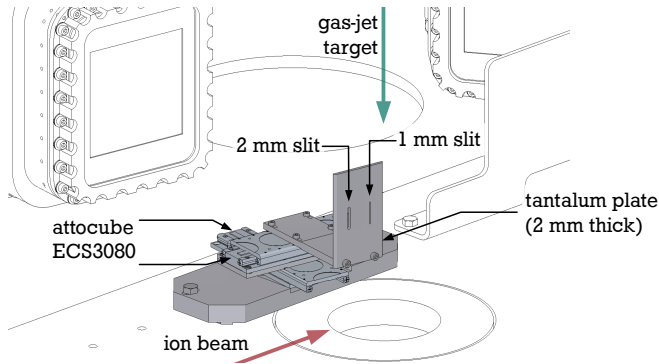
Figure 3.7.: Schematics of the remote controllable aperture for the 90° recoil detector. (*based on technical drawings by* [50])
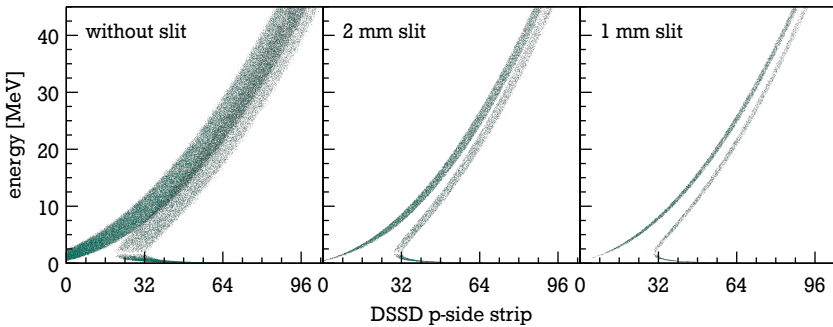
Figure 3.8.: Simulated angular correlations in the first DSSD for elastic and inelastic scattering ($E_x = 2.7$ MeV) of ^{56}Ni(p,p) at 400 MeV/u. The aperture was placed at a distance of 3 cm to the target. The discontinuity in the inelastic kinematics is an artefact by the event generator (see section 4.5.1).

The position of the aperture is adjustable transversally and longitudinally with respect to the axis of the first DSSD by two piezoelectric actuators. The two *attocube ECS3080/StSt/NUM/UHV* drives used here offer a total travel of 50 mm with an absolute precision of better than 0.01 % of the travel [67]. They are UHV compatible with a minimum reachable pressure of $5 \cdot 10^{-11}$ mbar and specified to a maximum bake-out temperature of 150 °C. The long travel of the drives makes it possible to retract the aperture during the injection cycles in order not to interfere with the ion beam and not to reduce the geometrical acceptance of the ring. It is also possible to measure without the aperture if necessary.

3.2.2 Retractable calibration source
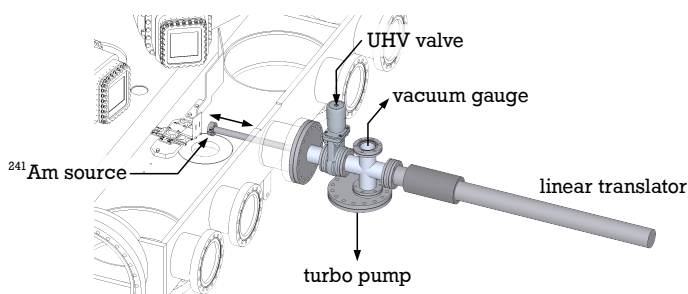
Figure 3.9.: Schematics of the retractable calibration source for the DSSDs. (*based on technical drawings by* [50])

A precise energy calibration of the recoil detection system is not just essential for the analysis in general but especially for the angular calibration of the DSSD which relies on the kinematical correlation between energy and scattering angle (see section 4.5). The maximum energy loss in the DSSD is around 6 MeV for protons which makes the use of an α-emitter such as ^{241}Am ideal. Furthermore, a source allows to perform tests of the detector mounted in place but without beam.

Because of the UHV conditions in the storage ring, it is a non trivial task to bring an α-source in front of the detector. It is also uncertain whether the typically windowless source would survive the baking procedure without contaminating the vacuum chamber. Of course, it is possible to use the source only before baking or after the experiment under worse HV conditions, but this takes away the chance to do in-situ tests of the detectors. Eventually, an ^{241}Am α-source was installed inside a small vacuum chamber at a 90° CF100 flange at the inner side of the interaction chamber (see figure 3.9). The source chamber was separated from the UHV by a valve and could be moved in and out using a linear translation mechanism. It was equipped with an independent vacuum system consisting of a scroll pump and a turbo pump. Both the interaction chamber and the source chamber were baked out together but without the source. After bake-out, the valve was closed and the actual source was installed. While this counteracted the effect of the bake-out, it was still possible to maintain a good vacuum of 10^{-7} mbar in the source chamber. Whenever the source was needed during the experiment, the valve was opened and the source was inserted using the linear translator. Experience showed that the UHV in the storage ring did not deteriorate irreversibly even after using the source for a few hours.

3.2.3 Vacuum system and bake-out procedure
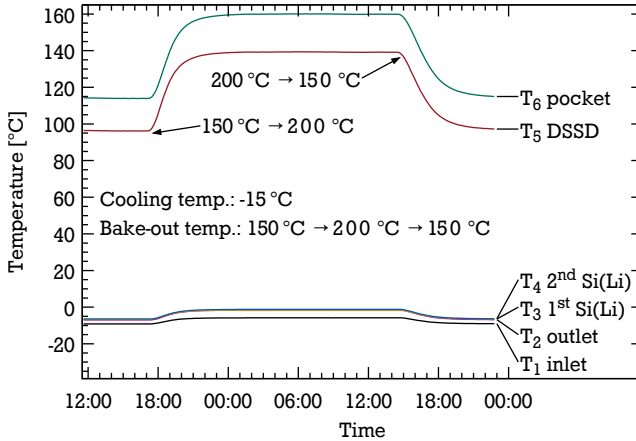
Figure 3.10.: Temperatures in the detector head measured during the bake-out test. (*data from* [29])

The vacuum concept for the two detector pockets is based on the improved vacuum-demonstrator design as described in section 2.4. With a larger EXL setup in mind, the sizes of the PCB and the clamp were already optimised for minimal dead zones in a setup of several detectors next to each other (see figure 3.6). The read-out of the detector signals was realised by custom made spring-pin connectors together with Teflon isolated ribbon-cables. The two Si(Li) detectors placed behind the first DSSD were actively cooled with a ethanol based coolant. This is not only necessary to achieve low enough leakage currents during normal operation but especially to keep the detector safe during the baking procedure. In order to prevent the lithium in the Si(Li) detectors from drifting, the temperature of the detectors should be kept below 35 °C. Hence, the cooling was viable for the experiment. To ensure that the Si(Li) detectors are kept within safe conditions at all times, a bake-out test with the Si(Li) detectors replaced by dummies made of aluminium was performed by the EXL collaboration beforehand. In this test, the vacuum chamber was baked to 200 °C and the temperatures inside the detector head were measured at several points. The test (results summarised in figure 3.10) revealed that the temperatures at the position of both Si(Li) detectors did not exceed −1.8 °C (cooling liquid: −15 °C) even at a baking temperature of 200 °C.

During the bake-out procedure, the reliability of the cooling system is crucial to guarantee the intactness of the Si(Li) detectors. A sudden loss of cooling power
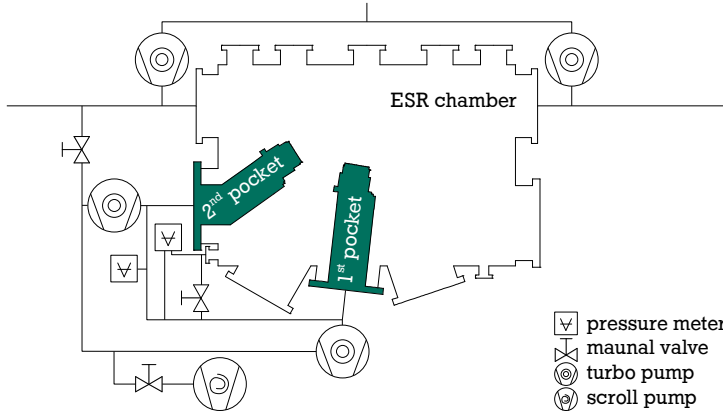
Figure 3.11.: Vacuum block-scheme for the interaction chamber during the E105 experiment [29].

during the bake-out would result in a rapid temperature increase of the Si(Li)s even if the heating could be stopped immediately. The thermal capacity of the Si(Li)s is so small compared to the whole vacuum chamber that the latter will not cool down fast enough to save the detectors. Therefore, a second cooling thermostat was kept operable as a redundant system next to the primary cooling thermostat. In case of a failure of one unit the second one can take over in a matter of minutes by manually operating two valves, only. Furthermore, to prevent the risk of power failures an **U**ninterruptible **P**ower **S**upply (UPS) was installed so that the cooling thermostat can remain operational for several hours.

The pumping scheme of the interaction chamber is illustrated in figure 3.11. The auxiliary vacuum of each of the two pockets was maintained by two independent turbo pumps coupled to the common pre-vacuum system of the ESR. The main vacuum chamber and the pockets were first coupled together by a bypass and evacuated with a common scroll pump. Especially at the beginning when pumping down from atmospheric pressure, big pressure differences between the auxiliary and the main vacuum have to be avoided. Mechanical simulations showed that the pressure difference on the DSSD must not exceed 10^{-1} mbar in order to avoid mechanical stress which could possibly break the detector. By coupling both vacua with a bypass and pumping them slowly with a common pumping system this risk is effectively minimised. Furthermore, a differential pressure gauge was installed to monitor the pressure differences. After a pre-vacuum was reached and the turbo pumps of the pockets were started, the pre-vacuum line of the turbo pumps was switched to the pre-vacuum system of the ESR and the bake-out procedure was

started. The vacuum chamber was then baked to 150 °C for about four days. After the bake-out was finished, pressures of about $2 \cdot 10^{-10}$ mbar and $8 \cdot 10^{-8}$ mbar were achieved in the interaction chamber and in the pockets, respectively.

3.3 In-ring detection systems
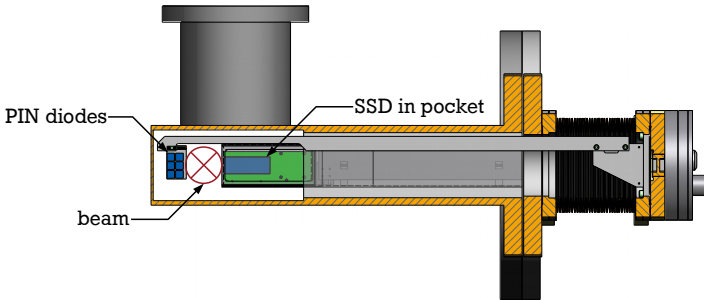
Figure 3.12.: Schematical view of the in-ring detection system for the E105 experiment. The pin-diode detector can be placed on both sides of the beam. (*based on technical drawings by* [50])

While the target-like particles can be measured in the recoil detectors around the target quite easily, measuring the beam-like particles in the ring is not. Because of the large mass difference between the projectile and the target, the projectile is deflected less in the scattering process. For example, if the recoiling proton is scattered at an laboratory angle of 88°, the corresponding ^{56}Ni ion is deflected only at an angle of 0.05°. Therefore, a particle detector has to be placed several metres downstream to detect the deflected projectiles where they are separated well enough from the primary beam. In the previous example, the ion would be displaced by about 5 mm from the nominal beam axis after at a distance of 7 m from the target. Despite the complications, measuring both participants is beneficial in order to be able to discriminate between different physical reaction channels or to drastically reduce random background by coincident measurements.

For this purpose, a vacuum chamber with two flanges exists inside the ESR about 7 m downstream of the target just before the first dipole magnet (see figure 3.3). This chamber was used to install two detection systems for the beam-like particles as illustrated in figure 3.12. One detector features an array of six silicon PIN-diodes directly placed in the UHV (figure 3.13, left) and the other one, based on a **S**ilicon **S**trip **D**etector (SSD), is installed in a vacuum pocket (figure 3.13, right). To bring

3. The EXL experiment E105 at the ESR
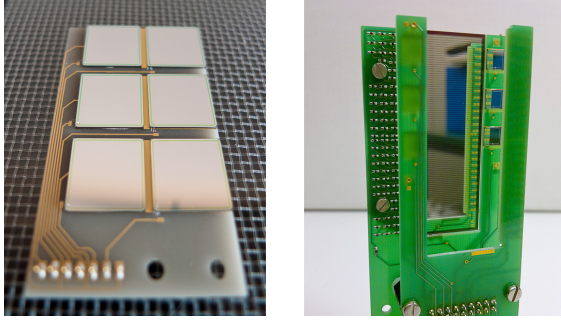
Figure 3.13.: Pictures of the two in-ring detectors. The PIN-diode detector (*left*) was placed directly in the vacuum while the SSD (*right*) was enclosed in a vacuum pocket.

the detectors close to the beam and to retract them during beam injections both detector systems are equipped with pneumatic actuators. While the SSD can be placed to the right side of the beam only, the PIN diodes can be placed on both sides of the beam. The possibility to place the PIN-diode detector at the outer side of the ring allowed to use it in coincidence with the recoil detection system of the E087 experiment which was placed at the inner side of the ring.

The first in-ring detector, which was developed by the EXL collaboration, consists of six 500 μm thick, $(1 \times 1)\,\text{cm}^2$ large PIN diodes arranged in a 2×3 configuration. In order to bring the detector as close as possible to the beam, it was placed directly in the UHV. To ensure UHV compatibility, the PIN diodes were glued to an AlN PCB and the read-out cabling was done via Kapton coated cables. The PIN diodes are biased by a common power supply to 180 V and all together showed a leakage current of about 0.6 μA.

Roughly half a meter after the PIN-diodes, a SSD, kindly provided by the TU München, is placed in a pocket with a 25 μm stainless steel window in air. The SSD is 140 μm thick, has outer dimensions of $(64 \times 23)\,\text{mm}^2$ and is divided into 96 strips on the p-side. However, the number of channels is reduced to three since the strips are read out via a resistive chain. There are two signals from the resistive chain used for the position information (E_{left}, E_{right}) and one from the common n-side used for the energy measurement (E_{total}). The relative position x of the incident particle on the SSD can then be retrieved from the two p-side signals:

$$x = \frac{E_{\text{left}} - E_{\text{right}}}{E_{\text{left}} + E_{\text{right}}}.$$

(3.1)
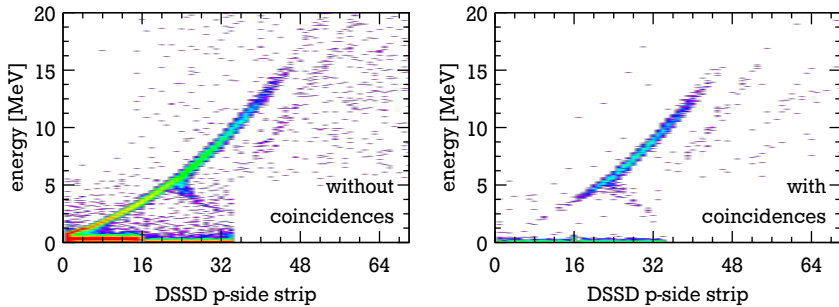
Figure 3.14.: Kinematical correlation spectrum of the recoil telescope (^{56}Ni(p,p), 1 mm slit aperture). *Left*: raw spectrum without coincidences; *right*: spectrum in coincidence with the triggers of both in-ring detectors.

During the experiment, the SSD was operated with a bias voltage of 50 V and showed a leakage current of 0.8 µA. Six additional PIN diodes were placed below and above the SSD but they were not connected during the experiment.

The benefits of a coincidence measurement between the recoil telescope and the in-ring detectors are demonstrated in figure 3.14. Although the coincident angular coverage gets much more restricted with the current in-ring detectors, an eminent reduction of background can be observed. The kinematical line corresponding to the first 2^+ state with an excitation energy of 2.7 MeV [66] is, despite the scarce statistics, well visible and separated. Nevertheless, because of the limited angular acceptance, a significant part of the cross section is missing in the coincidence spectrum in figure 3.14. Hence, the in-ring detectors were not utilised in the further analysis of the experiment.

3.4 Additional detector systems

To investigate the conditions for the detection of neutrons and gammas, the **E**uropean **L**ow **E**nergy **N**eutron **S**pectrometer (ELENS, [68]) was placed under forward angles. While ELENS used an independent data acquisition system, the analogue signals were split and fed into the data acquisition of this experiment as well. Also, the CsI scintillator used in the previous EXL demonstrator tests (see section 2.1.3) was placed outside the vacuum chamber in front of the vacuum flange under an angle of 60° [69]. However, since both detectors were not used for the present analysis, they will not be discussed any further.

3. The EXL experiment E105 at the ESR

3.5 Data acquisition system

The **d**ata **acq**uisition system (DAQ) is set up using MBS[2] (**M**ulti **B**ranch **S**ystem), a GSI developed data acquisition system based on the real-time operating system *LynxOS*. For this experiment a single branch MBS system was set up using a *CES RIO3* VME processor. Triggers from the various detector sub systems were managed by a VME trigger synchronisation module *TRIVA7*.

MBS supports 15 trigger IDs which are binary encoded via four trigger inputs of the TRIVA module (the IDs 14 and 15 are reserved for starting and stopping the acquisition). The encoding of the trigger IDs is simplified by a *VULOM3* (**V**ME **U**niversal **L**ogic **M**odule) which was configured to also provide dead-time locking of the incoming trigger signals in combination with the TRIVA module. It is possible to apply different read-out schemes in accordance to a trigger ID, which can be assigned to, for example, certain detector systems. The trigger ID is also tagged to the event and could be further used in the online/offline analysis. For the present experiment, different trigger IDs were used to differentiate events from various detector systems (see table 3.1) but for each trigger a full read-out of all VME modules was initialised.

In order to read the memory of the VME modules, several transfer modes are possible within the VME standard. The most simple, which is supported by virtually every VME module, is the D32 single-cycle access-mode where one 32 bit word can be transferred per access. The drawback of this mode is its limited throughput (about 4.6 MB/s using a *RIO3* processor [70]) caused by the overhead when transferring a larger number of data words. A higher bandwidth is achieved by the **BL**ock **T**ransfer mode BLT32 where a number of words can be transferred via a single access. While the overhead for large transfers is reduced, the initialisation of the transfer itself causes some delay which makes BLT32 rather inefficient for smaller amounts of data. Tests with the present DAQ system have revealed that BLT32 was only preferable when transferring more than about 34 data words, which corresponds to a single event from one of the ADCs used here. **M**ultiplexed **BL**ock **T**ransfer (MBLT64) works similar to BLT32 but multiplexes the address and data lines to form 64 bit address and data buses, thus increasing the throughput over BLT32. Other transfer modes like 2eVME and 2eSST allow for even higher transfer rates but are not supported by any of the VME modules used here. When many modules in the same VME crate have to be read together, the **C**hained **BL**ock **T**ransfer modes (CBLT32 and CMBLT64) can be used to group modules to a chain and read data from all of them like from a single module. Since the modules in a chain do not even need to be of the same type or from the same manufacturer,

---

[2] https://www.gsi.de/mbs/

the CBLT32/CMBLT64 modes were ideally suited for this DAQ system where in total 13 modules had to be read for every trigger. Unfortunately, because of an unresolved issue related to the *CAEN V785* ADCs it was not possible to establish a stable chained block transfer. Eventually, D32 was used instead as the total amount of data which is transferred per module and event was just at the edge where BLT32/MBLT64 could have been faster. With this configuration, a dead time of 380 μs was measured, resulting in a tolerable data rate of roughly 2.6 kHz.

The read-out of the detectors was realised with conventional analogue electronics. Most detectors were connected to *Mesytec MPR-16/-32/-64* which feature 16/32/64 channels of charge sensitive pre-amplifiers housed in a single device (the in-ring detectors, ELENS and the CsI scintillator used different types of pre-amplifiers). The differential output-signals of 16 channels were further amplified and shaped in *Mesytec MSCF-16* or *STM-16* shaping amplifiers and then digitised in either *CAEN V785* or *Mesytec MADC-32* VME-ADCs. Integrated into the *Mesytec MSCF-16* shaping amplifier is an additional timing branch with a timing amplifier and **C**onstant **F**raction **D**iscriminator (CFD) for each channel. A logical OR of all CFD output signals is used as a trigger signal for each detector. If more than one *MSCF-16* are used per detector an OR of all is created using external logic modules. The timing of the trigger signals was also recorded using two *CAEN V775* TDCs.

trigger ID	detector	remarks
01	1st DSSD || 1st Si(Li) || 2nd Si(Li)	only 1st DSSD for file IDs ≤ 14
02	2nd DSSD	rate reduced with variable reduction factors
03	in-ring PIN	
04	in-ring SSD	
05	coincidence: 01 && 03	
06	coincidence: 02 && 03	
07	ELENS	for file IDs < 55, rate reduced
	coincidence: 02 && 03	for file IDs ≥ 55
08	CsI	for file IDs < 55
	ELENS	for file IDs ≥ 55, rate reduced
09	CsI	for file IDs ≥ 55
$\vdots$		
13	scaler	2 Hz continuous trigger only active when no beam-on-target
14	—	signal for DAQ start
15	—	signal for DAQ stop

Table 3.1.: Description of the MBS trigger IDs used during the E105 experiment. For the explanation of the file IDs see table 3.3.

Besides the detector signals, additional diagnostic values were recorded using a *CAEN V830* VME scaler. These were:

- Raw and accepted rates of selected trigger

- Signal of the current transformer to determine the beam intensity (see section 4.1.2)

- Vacuum gauges of the gas-jet target for the density calculation (see section 4.1.1)

- 10 MHz reference clock

- Total dead-time (reference clock gated with the signal of the dead-time output of the *TRIVA* trigger module)

The entire analogue electronics was placed inside of the ESR cave close to the individual detection systems in order to minimise noise pick-up and signal deterioration caused by long cables routed to an outside place. This makes it of course necessary to control the modules remotely. The *Mesytec* modules offer a control bus in form of their proprietary *CBus* control bus which allows to view and manipulate all parameters of a supported module. It can be accessed either through one of the *Mesytec* VME modules or through a *CBus* to USB/RS-232 bridge, *Mesytec MRC-1*. For this experiment, both ways were implemented redundantly: One system used a *MADC-32* to configure the *CBus* devices and another one used a *MRC-1* connected to a *National Instruments cRIO* controller via RS-232 connection. The latter was used mainly during the running experiment as it could be operated independently of the main DAQ system. Online monitoring of the amplified energy or timing signals was possible through a set of monitor outputs of the *MSCF-16* shaping amplifiers which can be configured to show the signals of one of the 16 channels at a time.

Parts of the trigger logic were routed to an outside place and, together with the analogue monitoring signals, it was possible to set-up the timing of the trigger signals and the coincidence logic online without entering the ESR cave. A *TB8000 Trigger Box* was also used to easily scale down trigger rates if necessary.

3.6 Preparation of the ion beams

The experiment was conducted using stable $^{58}Ni^{28+}$ beam as well as radioactive $^{56}Ni^{28+}$ beam at an energy of approximately 400 MeV/u (see table 3.2 for exact values). In the case of ^{58}Ni beam, the ions were accelerated in the SIS18 synchrotron and then injected directly into the ESR. After a single injection from the SIS18, the data taking was started with in the order of 10^8 ions stored in the ring. The beam was continuously cooled using stochastic and electron cooling to maintain a good beam quality with low emittance and momentum spread. Electron cooling also compensated the energy loss which the beam faced in the target. The storage time of the beam was in the order of one to two hours.

For the production of ^{56}Ni, a primary $^{58}Ni^{28+}$ beam was accelerated in the SIS18 synchrotron up to an energy of 600 MeV/u. Using the fast extraction mode, the ions were directed to the fragmentation target of the FRS where $^{56}Ni^{28+}$ was created via fragmentation on a Be target with a production efficiency of roughly $1 \cdot 10^{-4}$ per primary ion [72]. The total fraction of beam contaminants like for example $^{54}Co^{27+}$ was negligibly low and was determined by Schottky mass spectrometry [56] to be in the order of $< 10^{-3}$ [72]. Because of the limited injection acceptance for secondary beams from the FRS, only about 10 % of the secondary ions could be transferred into the ESR [72]. Thus, about $8 \cdot 10^4$ ^{56}Ni ions were injected into the ESR per shot through the FRS. To increase the intensity, up to 60 injections were stacked until an intensity of well above 10^6 ions was reached. The stacking procedure which is described in detail in [72] consists of several steps. In the first step, the injected beam was pre-cooled using stochastic cooling for about 5 s before it was moved to an inner orbit of the ESR by the RF cavities. This process is illustrated by a Schottky spectrum in figure 3.15 on the left side. The deposited beam was then gradually moved towards its final orbit by electron cooling. After about 6 s of electron cooling the beam was fully merged with the existing stack as shown

	^{58}Ni	^{56}Ni
e⁻-cooler potential	219.45 kV	213.99 kV
e⁻-cooler current	400 mA	300 mA
beam energy	400.144 MeV/u	390.215 MeV/u
revolution frequency	1.98 MHz	1.96 MHz
stored ions (average)	$2 \cdot 10^8$	$3 \cdot 10^6$

Table 3.2.: Properties of the ion beams used during the E105 experiment for the determination of elastic proton-scattering cross-sections. The values for the beam energy are corrected for the space charge effects [71].
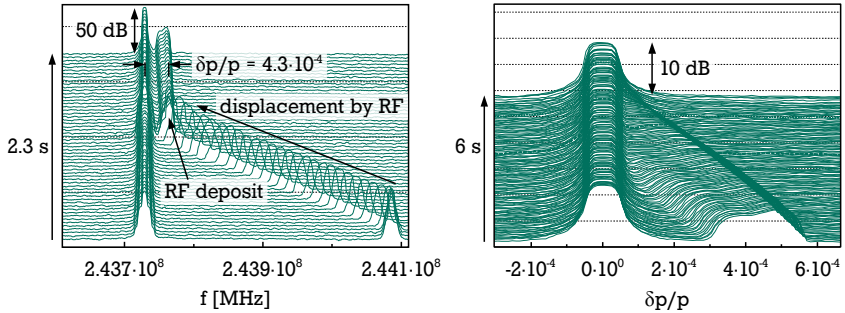
Figure 3.15.: Schottky spectra showing the procedure of ^{56}Ni beam stacking. *Left*: end of beam deposition and beginning of merging the accumulated beam with the stack; *right*: beam merging by electron cooling immediately after the RF was turned off. (*adapted from* [72])

on the right side of figure 3.15. The full injection procedure and beam stacking typically took about half an hour. As with the stable beam, electron cooling was continuously applied in order to maintain a good beam quality and to compensate for the energy loss in the target. The storage times were similar to that of stable ^{58}Ni beam and hence in the order of one to two hours.

3.7 Overview of measurements

The E105 experiment was accomplished between 16. November and 5. December 2012. As already outlined before, data were taken with stable ^{58}Ni and exotic ^{56}Ni in conjunction with H_2 and ^{4}He targets of which only the hydrogen target is relevant for this work. All experimental runs can be categorised by the exploited

ion beam	target	slit aperture	file IDs	BoT time
^{58}Ni	H_2	none	6 – 8	17 h
^{58}Ni	H_2	none	25	9 min
^{58}Ni	H_2	1 mm	14 – 16	46 min
^{56}Ni	H_2	none	59, 80	22 h
^{56}Ni	H_2	1 mm	53 – 58, 60, 62 – 65, 79	54 h
^{56}Ni	H_2	2 mm	82 – 84	16 h

Table 3.3.: Summary of the main experimental runs for the measurements of the elastic proton-scattering cross sections of ^{58}Ni/^{56}Ni.

beam/target combination and the usage of the slit aperture into six main runs. An overview of these main runs is given in table 3.3 together with the file-IDs which make up the individual data sets and the total **b**eam-**o**n-**t**arget (BoT) time of each main run. The runs with ^{58}Ni beam and without slit aperture are treated separately here since the changes in the trigger logic (see table 3.1) influenced the trigger efficiency of the detector telescope for events punching through the first DSSD so that all sub-runs cannot be combined reasonably.

3.8 Complications during the experiment

Although no major problems occurred during the whole experiment, a few complications during the measurements are worth being mentioned here.

Malfunction of one actuator of the aperture

The piezoelectric actuator which was setting the longitudinal position of the aperture relative to the normal axis of the first DSSD, i. e. the distance to the target, was defective. When moving this drive, from time to time it stopped moving at random positions and had to be moved back and forth until it eventually moved past the point. The slit was initially planned to be positioned as close as 1 cm to the target which made it mandatory to move it for a successful beam injection. With the eminent risk that the actuator could permanently fail at a position where no injection would be possible any more, it was placed at a distance of 3 cm to the target. There it could stay without interfering with the beam orbit during injections at least when no beam stacking was used. For injecting a ^{56}Ni beam, beam stacking was a necessity and thus, the slit had to be retracted to 4 cm and moved back to the 3 cm position.

Radiation damage in the 90° detector system

In the measurements with stable ^{58}Ni beam, where the luminosity was about 25 times higher than with ^{56}Ni, a gradual deterioration of detector performance was observed in the first DSSD. By the time, the maximal energy detected in the detector decreased. The issue is illustrated in figure 3.16 with two snap-shots of the kinematical correlation at the beginning of the run with file ID 14 and twelve hours later at the end of run 14. In this example, the maximum detected energy in the DSSD decreased by about 800 keV. The situation can be seen in more detail in figure 3.17 where the energy measured by three exemplary p-side strips (#16, #24
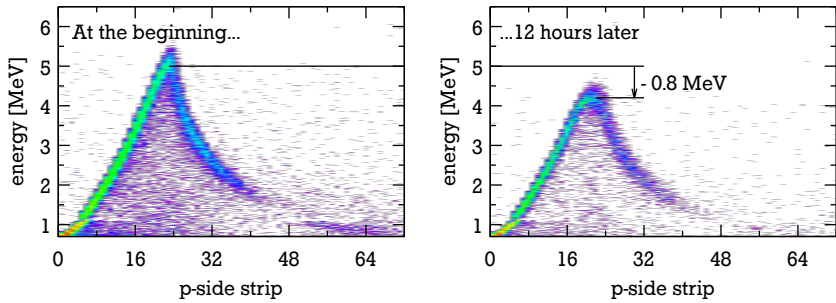
Figure 3.16.: Radiation damage observed in the first DSSD at the beginning of the ^{58}Ni run with 1 mm slit aperture (*left*) and 12 hours later (*right*).

and #32) is plotted as a function of time. While there is no apparent change in the energy response of strip #16, a steadily decreasing energy response can be seen in the other two strips where predominantly higher energy protons are detected. This behaviour could be explained by a continuously decreasing "effective" bias in the detector which results in a shrinking depletion depth. At some point, particles of a certain energy are not stopped in the depleted and hence sensitive region of the detector any more. The part of the total charge which is created in the insensitive region is then lost and a reduced energy signal is recorded. At the same time, a gradually increasing leakage current was measured during the run (see figure 3.17 at the bottom). By raising the bias voltage it was possible to restore the energy response of the detector at least temporarily. It was also noticed during the run that the current characteristics of the detector changed towards an ohmic behaviour.

The exact source of this damage is yet unverified. High fluxes of high-energy particles are not expected at the position of the DSSD and no such signals were observed with the oscilloscope either. Hence, a radiation damage of the bulk seems implausible. Instead, the issue could be caused by damages in the surface region, or more specifically in the oxide layer. If the detector was exposed to a high flux of, for example, electrons with energies below the detection threshold, these electrons would be stopped in the silicon oxide (SiO_2) at the surface of the DSSD. Since the electron mobility in SiO_2 is several orders of magnitude larger than the hole mobility, the radiation-generated electrons will diffuse out of the oxide rather fast. The holes, instead, are semi-permanently trapped in the oxide and cause a build-up of positive charge in the surface region [73]. The accumulated charge eventually counters the negative bias voltage which is applied to the p-side. Consequently, the depletion depth is reduced and the maximum energy is lowered as it was observed.
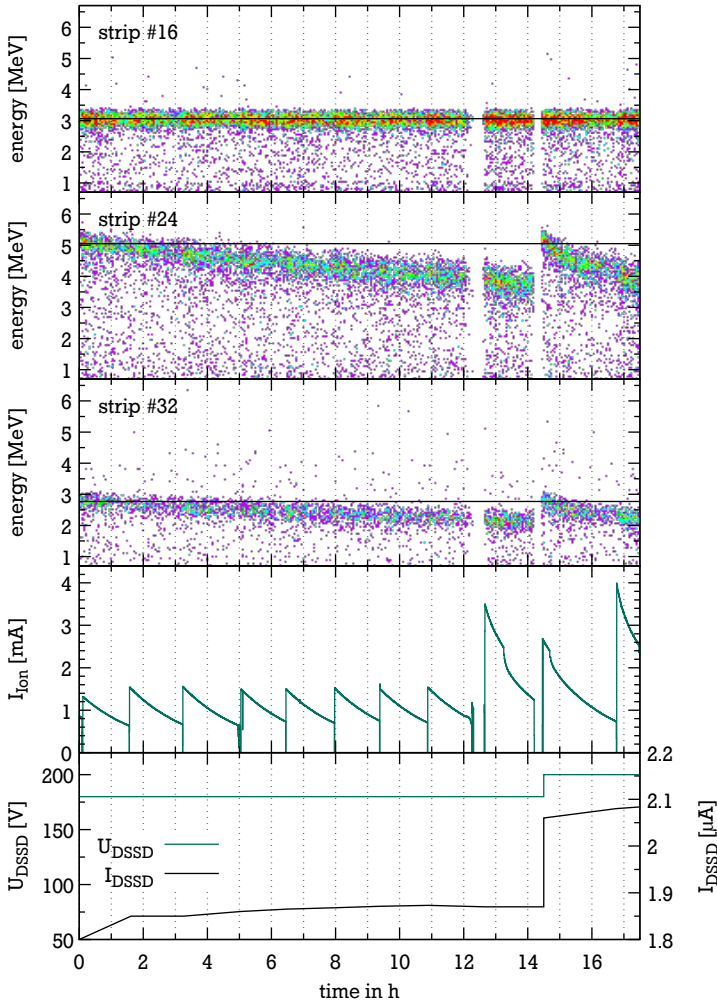
Figure 3.17.: Evolution of radiation damage in the first DSSD during the ^{58}Ni run with 1 mm slit aperture. The top three plots show the energy measured by three exemplary strips as a function of measurement time. The horizontal line indicates the expected energy in each strip. In the second plot from the bottom, the current of stored ^{58}Ni ions in the ring is displayed. At the bottom, the bias voltage and the leakage current of the DSSD are plotted.
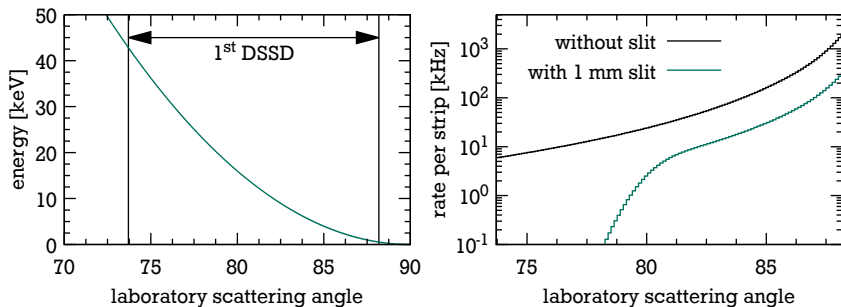
Figure 3.18.: Expected cross section and energy of delta electrons in the angular region of the first DSSD.

Raising the bias voltage would then partly compensate the effect which was the case as can be seen in figure 3.17.

The delta electrons in the angular region of the DSSD have energies below 50 keV (see figure 3.18). Especially in the first quarter of the detector close to 90° laboratory scattering angle the rates are high and the energies are even below 10 keV, which is well below the trigger thresholds. The expected rate of delta electrons, also shown in figure 3.18, was calculated using cross sections from [74] and by assuming a luminosity of 10^{28} cm^{-2} s^{-1}. The solid angles of the detector strips were estimated with the help of Monte Carlo simulations, which are described later in section 4.5. In the first strips close to 90° laboratory scattering angle the rate exceeds 1 MHz per strip and for the whole detector 21 MHz are expected. When using the 1 mm slit aperture, the total rate is considerably reduced but is still about 5 MHz in total.

Fortunately, the radiation damage posed no major complication for the analysis. The cross section for elastic proton scattering was derived from the angular distribution rather than the energy and it was still possible to discriminate the elastic scattering from the first excited state. Nevertheless, a careful study of this effect is endorsed for future experiments.

Electronics related issues

For 48 out of the 64 n-side channels of the first DSSD, the timing of the ADC gate was not adjusted properly, so that the precision of the energy measurement was worsened there considerably. The *Mesytec STM-16* shaping amplifier used for these channels lacked the possibility to monitor signals remotely. Consequently the timing of the ADC gates could not be verified for these channels from outside of the

ESR cave. As the amplifiers also had a different shaping time, one did not realise when the timing of the ADC gate was changed too much and did not cover the energy signal any more. Thus, the energy resolution in the affected channels was significantly worse and they had to be calibrated in a special procedure which is described in section 4.2.

Another issue was caused by the **B**ase-**L**ine **R**estorer (BLR) in a few of the *Mesytec MSCF-16* shaping amplifiers. By unknown reasons, neither the threshold of the BLR could be adjusted nor could it be switched off completely. Instead, the threshold appeared to be set to a very high value which caused a gap in the energy spectrum at an energy of about 1 MeV and a high non-linearity in the energy region below. The distortions were recovered to some extend by a partial calibration as described in section 4.2.

A third problem occurred in the integrity of the data stream coming from the *CAEN V830* scaler which was used mainly for the assessment of diagnostical data. The scaler was set to an event mode where the values of the scaler registers are transferred sequentially without explicitly indicating their channel ID. Occasionally, the values of the first 16 channels, i. e. the first block, were transferred in a mixed up order: the first two channels were doubled, the following 12 channels were shifted by two and the last two channels of the first block were missing completely. Fortunately, since this error provides a clear signature the affected events could be identified and corrected in the later offline analysis.

4 Data analysis

The following sections give a detailed description of the analysis procedures used to determine the cross section for elastic proton scattering on ^{58}Ni and ^{56}Ni. In a nutshell, four main steps are necessary to get there. At the very beginning, an energy calibration has to be performed (section 4.2) which then allows the reconstruction of physical events (section 4.3). Conditions are applied to select the events from elastic scattering and angular distributions as a function of detector segments are extracted. The next step is the angular calibration of these distributions. The angular calibration and correction functions for the angular acceptance of the detector system are derived using Monte Carlo simulations (section 4.5). To calculate the cross section from the angular calibration, the (integrated) luminosity has to be determined, which is discussed in the first section of this chapter. The final calculation of the cross section is documented in section 4.6.

For the analysis *Go4*[1], version 4.5.4, and *Wolfram Mathematica 9.0/10.0*[2] were used. *Go4* was used mainly to create histograms from the raw list-mode data which were then further processed using *Mathematica*. The entire fitting procedures and Monte Carlo simulations were carried out in *Mathematica* as well.

4.1 Luminosity

The luminosity $\mathscr{L}$ is a magnitude which connects the cross section σ of a physical reaction, i. e. the probability that the reaction takes place, with the event rate $\mathrm{d}N/\mathrm{d}t$ seen by the detection system:

$$\frac{\mathrm{d}N}{\mathrm{d}t} = \mathscr{L} \cdot \sigma \qquad (4.1)$$

While the cross section is a property of the physical reaction, the luminosity can be seen as a property of the experiment. It is defined as the product of the flux Φ_{beam} of incoming projectiles interacting with a target of a certain density ρ_{target}, i. e.

$$\mathscr{L} = \Phi_{\text{beam}} \cdot \rho_{\text{target}} \cdot \qquad (4.2)$$

---

[1] http://go4.gsi.de/
[2] http://www.wolfram.com/mathematica/

The luminosity is usually expressed in units of $\mathrm{cm}^{-2}\,\mathrm{s}^{-1}$. Equation (4.2) is valid for the case of a fixed target with constant density and lateral extensions larger than the distribution of the impinging projectiles. In a more general case, both the flux of incoming projectiles and the distribution of particles are not necessarily constant but may depend on the position and the time. If the density distributions of the target and the beam and their respective time dependences are known, the luminosity can be calculated by integrating them [75]:

$$\mathscr{L} = \iiiint_{-\infty}^{+\infty} \Phi_{\mathrm{beam}}(x,y,z,t)\,\rho_{\mathrm{target}}(x,y,z,t)\,\mathrm{d}x\,\mathrm{d}y\,\mathrm{d}z\,\mathrm{d}t \qquad (4.3)$$

Another approach for the determination of the luminosity is to exploit already known physical cross sections from processes that occur in coincidence with the one under investigation. In the present case, one possibility would be the measurement of **R**adioactive **E**lectron **C**apture (REC) rates. If an ion catches an electron in the target, its charge state is changed and thus, it will be shifted to a different trajectory in the dispersive section of the dipole magnet further downstream of the target. The deflected particles can then be detected in a particle detector. For known REC cross sections, the luminosity can be extracted even without knowledge of the density distribution in the interaction zone. Alternatively, a relative measurement of the luminosity can be achieved by measuring the light stemming from atomic de-excitation of the target gas which got excited in collisions with the ion beam. Technically, this can be done, for example, with a PMT pointing to the interaction zone. For this experimental campaign both techniques were prepared, but unfortunately were not usable. The particle detector showed rates which were not correlated with the ion current nor the target density. At the same time, the count rates seen by the PMT were too low to be significant. Until now, it is not clear, why the particle detector was not working as expected. However, the failing of the PMT is explainable: The well-proven PMT which is usually used for this purpose was too big to be integrated in the present experimental setup. Therefore, it had to be replaced by a smaller, hence less sensitive, one. Additionally, it had to be placed further away from the interaction point which limited the effective sensitivity even further.

Consequently, the luminosity will be calculated directly from the current of the ion beam and the density of the target. As the density distributions of both the target and the beam are not constant, the luminosity has to be calculated using equation (4.3). Throughout the experiment, the magnitudes of the ion and target beams were measured continuously. In the following two subsections it is explained how to calculate the actual beam currents from the recorded telemetry data. Since

it was not possible to determine the precise density distributions of the beams, assumptions based on other experiments were made which is laid out in the following subsections, as well.

4.1.1 Target density
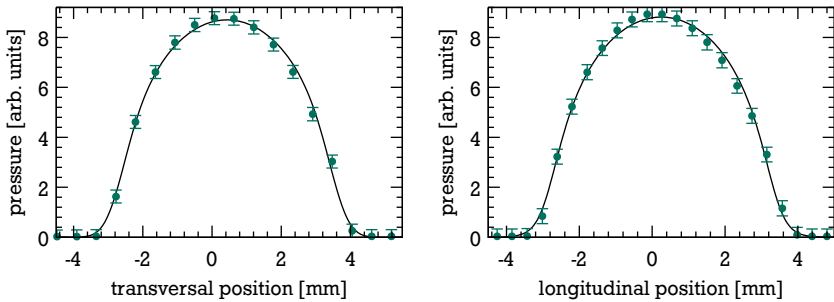
Figure 4.1.: Pressure change in the target chamber as a function of the wire position. Shown is a measurement at $19\,\mathrm{bar}$ with the wire being moved transversally (*left*) and longitudinally (*right*) with respect to the ion-beam axis. Positive values correspond to a shift to the outside of the ring and to a shift in beam direction, respectively. (*based on data from* [76])

The profile of the ESR gas-jet target was investigated thoroughly in [76] by using a mechanical gas–scatter approach. The gas jet hits a thin $0.6\,\mathrm{mm}$ constantan wire which is swept through the target. Particles hitting the wire will be scattered and thus increase the pressure in the scattering chamber which can then be detected by a mass spectrometer. The pressure increase in the target chamber at a certain wire position z is given by the line integral of the target's density distribution $\rho(x,z)$ at this position, i. e.

$$F(z) = \int_{-\infty}^{\infty} \rho(x,z)\ \mathrm{d}x\ .\qquad(4.4)$$

By scanning the target successively with the wire longitudinally and transversally to the ion-beam axis, it is possible to determine a two-dimensional target profile. Figure 4.1 shows the result of a scan transversal and longitudinal to the ion-beam axis.

To fit the data points, a certain model for the density distribution has to be assumed. In this case, a modified error function was chosen [76]:

$$\rho_{\text{target}}(x,z) = \frac{1}{2c_\rho} \left(1 + \text{erf} \left[\frac{r_{\text{target}} - \sqrt{\left(x - x_{\text{target}}\right)^2 + \left(z - z_{\text{target}}\right)^2}}{\sqrt{2}d_{\text{target}}} \right] \right) \quad (4.5)$$

Here, $\{x_{\text{target}}, z_{\text{target}}\}$ are the position coordinates, r_{target} is the radius, d_{target} the surface diffuseness of the target and c_ρ a normalisation constant. With this model it is possible to describe density distributions varying from almost Gaussian to step-like shape.

The measurements in [76] were carried out with krypton as a target gas and source pressures of 7 bar, 19 bar and 26 bar. The results of the fits with the parametrisation (4.5) are summarised in table 4.1[3]. The uncertainties given in table 4.1 are the ones from the fit and additionally, in the case of the positions, the uncertainness of the zero position (about 0.3 mm). Within these uncertainties the measurements at the three different pressures give comparable results for the position of the target. Also, the transversal and longitudinal radii are so close to each other that a cylindrical symmetry can be assumed. However, the measurement is not very sensitive on the diffuseness parameter as it fluctuates from measurement to measurement. Nevertheless, the fitted parameters allow to conclude that the target density is homogeneous in the centre and somehow diffuse at the surface.

pressure	position	radius	diffuseness
longitudinal			
p_0	x_{target}[3]	r_{target}	d_{target}
7 bar	$(0.61 \pm 0.03 \pm 0.3)$ mm	(3.64 ± 0.04) mm	(0.28 ± 0.08) mm
19 bar	$(0.25 \pm 0.03 \pm 0.3)$ mm	(3.11 ± 0.04) mm	(0.38 ± 0.07) mm
26 bar	$(0.33 \pm 0.03 \pm 0.3)$ mm	(3.42 ± 0.04) mm	(0.09 ± 0.20) mm
transversal			
p_0	z_{target}	r_{target}	d_{target}
7 bar	$(0.43 \pm 0.03 \pm 0.3)$ mm	(3.21 ± 0.04) mm	(0.37 ± 0.07) mm
19 bar	$(0.43 \pm 0.03 \pm 0.3)$ mm	(3.19 ± 0.04) mm	(0.40 ± 0.07) mm
26 bar	$(0.48 \pm 0.03 \pm 0.3)$ mm	(3.47 ± 0.03) mm	(0.18 ± 0.07) mm

Table 4.1.: Best fit parameters for the target profile as of [76].

[3]   In comparison to the original work [76], the coordinate system of the longitudinal measurement was inverted to comply with the coordinate system being used here.

Despite the use of krypton in this measurement, the results should be applicable also to other gases like hydrogen or helium [77]. For the further analysis, the position from the 19 bar measurement will be used since this measurement was performed with a pressure close to the one in the present experiment (see table 4.2). The target will be assumed to exhibit cylindrical symmetry with a radius of $r_{\text{target}} = (3.15 \pm 0.06)\,\text{mm}$, which is the mean value of both radii from the 19 bar measurement. For the diffuseness, an average of all values will be used, i. e. $d_{\text{target}} = (0.32 \pm 0.10)\,\text{mm}$.

In order to calculate the luminosity, the target profile still has to be normalised to the total number of particles N_{target} in the target. By integrating over the whole target density, the normalisation constant c_ρ can be calculated:

$$N_{\text{target}} = \iiint \frac{1}{c_\rho} \rho_{\text{target}}(x,z)\; \mathrm{d}x\, \mathrm{d}y\, \mathrm{d}z \tag{4.6}$$

Dividing equation (4.6) by $\mathrm{d}t$ gives

$$\frac{\mathrm{d}N_{\text{target}}}{\mathrm{d}t} = \iiint \frac{1}{c_\rho} \rho_{\text{target}}(x,z)\; \mathrm{d}x\, \frac{\mathrm{d}y}{\mathrm{d}t}\, \mathrm{d}z \tag{4.7}$$

$$\dot{N}_{\text{target}} = \iint \frac{v_y}{c_\rho} \rho_{\text{target}}(x,z)\; \mathrm{d}x\, \mathrm{d}z \tag{4.8}$$

$$\Rightarrow c_\rho = \frac{v_y}{\dot{N}_{\text{target}}} \iint \rho_{\text{target}}(x,z)\; \mathrm{d}x\, \mathrm{d}z \tag{4.9}$$

where v_y is the gas velocity in y-direction and $\dot{N}_{\text{target}}$ the particle flow-rate. The gas velocity can be estimated depending on the underlying physical process of the gas expansion. For an expansion of a liquid into vacuum, the Bernoulli expression for the expansion of a liquid through a pinhole orifice can be used. In this case, it is assumed that the expansion pressure p_0 is fully translated into kinetic energy and thus [78]:

$$p_0 = \frac{1}{2} \rho\, v_y^2 \tag{4.10}$$

$$\Rightarrow v_y = \sqrt{\frac{2p_0}{\rho(p_0, T_0)}}\;. \tag{4.11}$$

The liquid density $\rho(p_0, T_0)$ depends on the given source pressure p_0 and temperature T_0 at the nozzle. It can be found tabulated, for example in [79]. If, like

in the present case, the target jet was not formed by expanding from the liquid but from the gaseous state, the velocity can be estimated by assuming an isentropic flow through a nozzle [80]:

$$v_y = \sqrt{\frac{2k_B T_0}{m} \frac{\kappa}{\kappa-1} \left[1 - \left(\frac{p_2}{p_1}\right)^{(\kappa-1)/\kappa} \right]} \qquad (4.12)$$

Here, the ratio p_2/p_1 is the pressure ratio between the gas pressure inside the nozzle p_1 and the ambient pressure p_2. For an expansion into vacuum, i.e. when $p_1 \gg p_2$, the ratio is close to zero and equation (4.12) simplifies to:

$$v_y = \sqrt{\frac{2k_B T_0}{m} \frac{\kappa}{\kappa-1}} \qquad (4.13)$$

The factor κ in the equations (4.12) and (4.13) is the adiabatic index, i.e. the ratio of the heat capacity at constant pressure C_p to the heat capacity at constant volume C_V:

$$\kappa = \frac{C_p}{C_V}$$

The values for C_p and C_V can again be taken from [79]. A summary of all properties of the gas-jet target, which are necessary for the analysis, can be found in table 4.2.

property		target gas	
		H$_2$	^{4}He
pumping speed [81]	S_{dump}	1050 l/s	1320 l/s
ionisation factor [81]	$k_{\text{ioniz.}}$	2.4 (S3: 2.7)	5.9 (S3: 5.7)
temperature [82]	T_0	74 K	12 K
pressure [82]	p_0	17 bar	3.6 bar
adiabatic index [79]	$\kappa = C_p/C_V$	1.7802	1.8611

Table 4.2.: Properties of the gas-jet target during the E105 experiment.

The particle flow $\dot{N}_{\text{target}}$ can be calculated from the pressure increase in the differential pumping system of the target dump. The pressure increase which is caused by the gas load of the target jet (pressures in S1-S4, see figure 3.4) [81, 83]. Under the assumption that no significant losses of the target beam occur on the path between the interaction region and the dump, the number of particles in the target

beam has to be conserved. Therefore, the particle flow rate $\dot{N}_{\mathrm{target}}$ in the interaction region has to be equal to the $p\dot{V}$-flow through the beam-dump system. The volume change $\dot{V}$ can be replaced by the pumping speed S_{dump} of the beam-dump's pumping-system (see table 4.2). Assuming an ideal gas, this leads to:

$$p\dot{V} = p_{\mathrm{dump}}\, S_{\mathrm{dump}} = \dot{N}_{\mathrm{target}} k_{\mathrm{B}} T \tag{4.14}$$

$$\Rightarrow \dot{N}_{\mathrm{target}} = \frac{p_{\mathrm{dump}}\, S_{\mathrm{dump}}}{k_{\mathrm{B}} T} \tag{4.15}$$

To finally calculate the areal density of the gas-jet target, it is enough to measure the pressure rise p_{dump} in the target dump. For this purpose, the four pumping sections S1-S4 are equipped with vacuum gauges which are read out continuously throughout the experiment. The total pressure p_{dump} is the sum of these individual pressure readings minus an offset pressure p_{offset} which has to be measured without the target:

$$p_{\mathrm{dump}} = \sum_{i=1}^{4} p_{\mathrm{Si}} - \sum_{i=1}^{4} p_{\mathrm{offset,Si}} \tag{4.16}$$

The individual pressure readings have to be calculated from the frequency signal which was counted by the scaler. The conversion from frequency back to voltage is done via:

$$U(f) = \frac{5}{2}\left[\log_{10}(f) - 2\right] \tag{4.17}$$

Subsequently, the pressure can be calculated for the different vacuum gauges as:

$$p_{\mathrm{S1,S2}} = k_{\mathrm{ioniz.}}\, 10^{(U-7.75)/0.75}\ \mathrm{mbar} \tag{4.18}$$

$$p_{\mathrm{S3,S4}} = k_{\mathrm{ioniz.}}\, 10^{U-12}\ \mathrm{mbar} \tag{4.19}$$

Equation (4.18) is valid for the gauges at S1 and S2, while (4.19) has to be used for S3 and S4 [81]. The ionisation factor $k_{\mathrm{ioniz.}}$ introduced here is a device specific correction factor for different gas species (see table 4.2). An overview of the target density during the different experimental runs is shown in the figures 4.3 and 4.4.
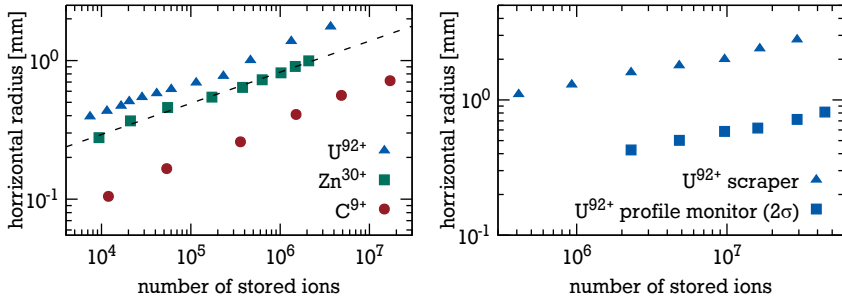
Figure 4.2.: *Left*: Horizontal beam radius measured with the scraper system for three ions (C^{6+}, Zn^{30+}, U^{92+}) at an energy of 400 MeV/u cooled by an electron current of $I_e = 0.25$ A; *right*: beam radius of a U^{92+} beam (400 MeV/u, $I_e = 0.25$ A) measured with the scraper system and σ measured with a profile monitor. (*based on data from* [61])

Since the stored ion beam was not bunched, it can be assumed to have a constant density along the z-axis. The density distribution in the $\{x, y\}$ plane, i.e. perpendicular to the beam axis, is assumed to be Gaussian [84]. For the typical beam intensities in this experiment, the transverse size of the cooled beam is dominated by intrabeam scattering. While the exact beam dimensions were not measured during the experiment, an assumption will be made from previous measurements where the dimensions were measured for different ion species and intensities [61]. There, the transverse beam size was deduced with a beam scraper system for three different ion species (C^{6+}, Zn^{30+}, U^{92+}) at an energy of 400 MeV/u as a function of the number of stored ions (see figure 4.2).

With increasing number of stored ions N_{ion}, the beam radius grows with $a \cdot N_{\text{ion}}^b$ and depends only weakly on the ion species. Hence, the data of Zn^{30+} should be applicable to the present case of Ni^{28+} in a reasonable way. The available data points were fitted and the relation between the number of stored ions and the beam radius was found to be

$$r_{\text{beam}}(N_{\text{ion}}) = 0.037 \, \text{mm} \cdot N_{\text{ion}}^{0.225} \, . \tag{4.20}$$

It is also shown in [61] that the beam radii in horizontal and vertical direction are comparable, so that a circular beam profile will be assumed here. Furthermore, the beam radius measured with the scraper corresponds to about 3.7 times the

RMS radius measured non-destructively with a beam-profile monitor as shown in figure 4.2. Ultimately, it is assumed that the beam is centred on its nominal position at $x_{\mathrm{beam}} = 0$ and $y_{\mathrm{beam}} = 0$ [71]. Taking all this into account, the beam profile can be parametrised as:

$$\Phi_{\mathrm{beam}}(x, y) = \frac{\dot{N}_{\mathrm{ion}}}{2\pi\sigma(N_{\mathrm{ion}})^2} \mathrm{e}^{-\frac{x^2+y^2}{2\sigma_{\mathrm{beam}}(N_{\mathrm{ion}})^2}} \tag{4.21}$$

with

$$\sigma_{\mathrm{beam}}(N_{\mathrm{ion}}) = 9.95 \cdot 10^{-3}\,\mathrm{mm} \cdot N_{\mathrm{ion}}^{0.225} \tag{4.22}$$

The intensity of the ion beam in the ESR is measured continuously and non-destructively by a **DC Current Transformer** (DC-CT) with an accuracy of $2\,\mu\mathrm{A}$ RMS [85, 86]. The output signal of the DC-CT is fed into a voltage-to-frequency converter in order to provide a range-independent frequency signal for the data acquisition. From the measured frequency f_{ion}, the ion-beam current I_{ion} can be calculated as

$$I_{\mathrm{ion}} = \frac{1\,\mathrm{mA}}{100\,\mathrm{kHz}}(f_{\mathrm{ion}} - f_0)\,, \tag{4.23}$$

where f_0 is an offset frequency which has to be determined in a measurement without beam. To get the number of particles per second $\dot{N}_{\mathrm{ion}}$, the current has to be divided by the elementary charge q_e times the charge Z of the ion, i. e.

$$\dot{N}_{\mathrm{ion}} = \frac{I_{\mathrm{ion}}}{q_e Z}. \tag{4.24}$$

The beam intensity as a function of time throughout the whole experiment is shown in figures 4.3 and 4.4.

4.1.3 Integrated luminosity

As stated before, knowing the luminosity allows to calculate the event rate for a given physical reaction. Therefore, it is an important information, for example, for the estimation of the rate on a detector system. The time dependent luminosity $\mathscr{L}(t)$ calculated with equation (4.3) is shown in figures 4.3 and 4.4 for ^{56}Ni and ^{58}Ni, respectively.
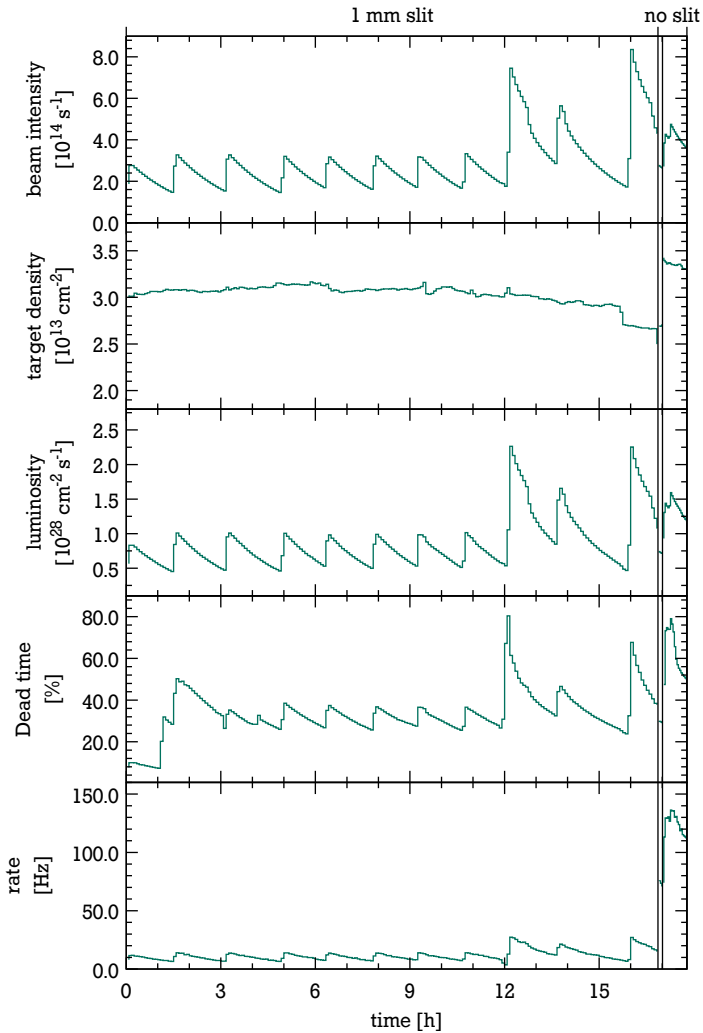
Figure 4.3.: Beam intensity, effective target density and luminosity during the runs with [58]Ni beam.
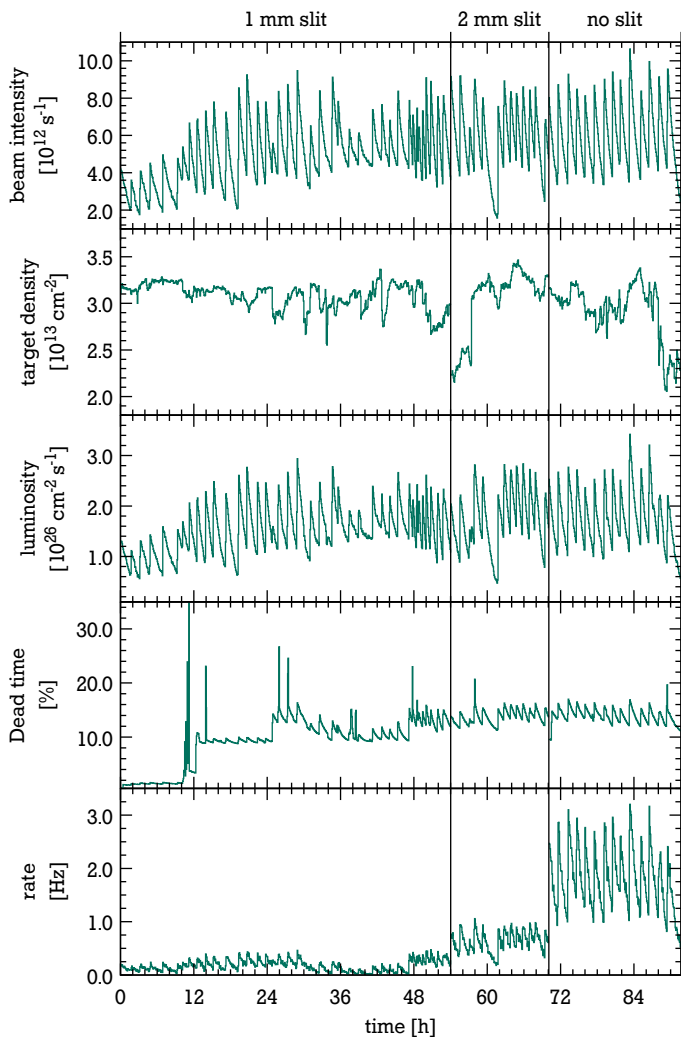
Figure 4.4.: Beam intensity, effective target density and luminosity during the runs with ^{56}Ni beam.

However, for the analysis a more important number is the integrated luminosity, as it connects the total number N of events observed throughout the experiment with the physical cross section σ. It can be calculated by integrating the time dependent luminosity $\mathscr{L}(t)$:

$$\mathscr{L}_{\text{int}} = \int_0^t \mathscr{L}(t) \, dt = \frac{N}{\sigma} \tag{4.25}$$

For practical purposes, i.e. when the luminosity was measured in time bins, the integrated luminosity can be approximated by summing over the i time bins:

$$\mathscr{L}_{\text{int}} \approx \sum_i \mathscr{L}_i \, t_{\text{live},i} = \sum_i \Phi_{\text{beam},i} \, \rho_{\text{target},i} \, t_{\text{live},i} \tag{4.26}$$

In (4.26), t_{live} is the time in which the DAQ system was not blocked. Since the dead time t_{dead} of the DAQ system was measured, t_{live} can be easily calculated and one finally gets:

$$\mathscr{L}_{\text{int}} \approx \sum_i \Phi_{\text{beam},i} \, \rho_{\text{target},i} \left(t_i - t_{\text{dead},i} \right) \tag{4.27}$$

4.2 Energy calibration

In the context of this analysis, the energy calibration of the DSSD is the most important calibration as subsequent calibrations such as the angular calibration rely on a precisely measured energy. The energy calibration is done in two steps. First, a calibration of the electronics with a pulse generator, and second, a gain match with the α-source. The necessary spectra were recorded before and after the experiment but only the latter were used for the analysis.

To calibrate the electronics, the signal from a *BNC PB-5* precision pulse generator is coupled to a test capacitance which is connected to the inputs of the pre-amplifiers (in the case of the *Mesytec MPR* pre-amplifiers, the internal test capacitance was used). By increasing the pulse height in distinctly spaced steps, a spectrum with up to ten pulser peaks was recorded for each channel (see figure 4.5). A second order polynomial of the form

$$U(k) = a + bk + ck^2 \tag{4.28}$$
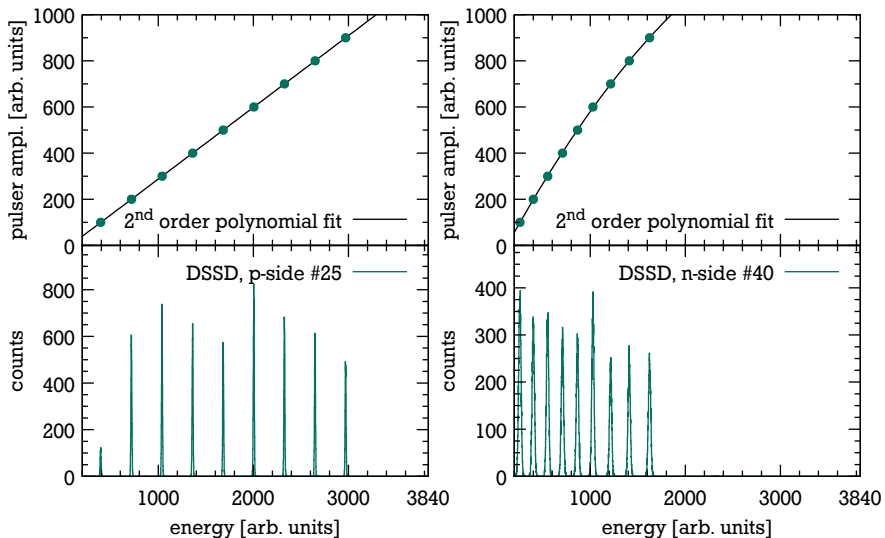
Figure 4.5.: Pulser calibration of the electronics. *Left*: DSSD, p-side channel #25; *right*: DSSD, n-side channel #40.

is then fitted to the peak positions. This yields a calibration function converting ADC channels k to a signal amplitude U (in arbitrary units proportional to the voltage). An example for two channels is shown in figure 4.5.

The calibration of the now established voltage scale to energy is still needed. Therefore, spectra with an ^{241}Am source were recorded. The spectra were converted into the voltage scale of the pulser and the position of the prominent α-lines were determined by fitting a sum of five Gaussian peaks to the data:

$$f_{^{241}\mathrm{Am}}(u) = \sum_{i=1}^{5} \frac{I_\alpha\, I_{\mathrm{rel},i}}{\sqrt{2\pi\sigma^2}}\ \exp\left[-\frac{\left(u - u_\alpha\, \mu_{\mathrm{rel},i}\right)^2}{2\sigma^2}\right] + \frac{I_{\mathrm{bg}}\, I_{\mathrm{rel},i}}{1 + \exp\left[\frac{u - u_\alpha\, \mu_{\mathrm{rel},i}}{\sigma}\right]} \quad (4.29)$$

The background is usually non-zero for energies lower than the peak energy and zero for energies above. To model this behaviour with a smooth transition, a phenomenological function in the form of a Fermi function was assumed for the background of each peak. The relative positions and intensities of the lines were fixed to their known values (see table 4.3), so that the remaining free parameters of the fit were two scaling factors I_α and I_{bg} for the peak and background, respectively, the width of the peak σ and the position of the prominent line u_α. An
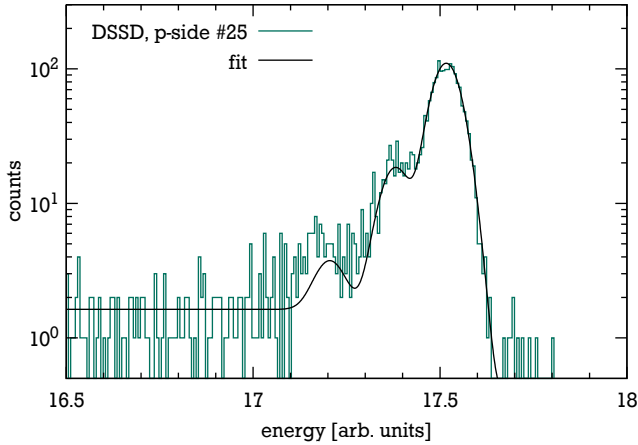
Figure 4.6.: Spectrum of an ^{241}Am α-source recorded with the p-side strip #25 of the first DSSD (*green line*) and a fit to the data (*black line*). See text for details on the fit.

i	energy E_α	intensity I_α	relative position $\mu_{\mathrm{rel},i}$	relative intensity $I_{\mathrm{rel},i}$
1	5485.56 keV	84.8 %	1	1
2	5442.8 keV	13.1 %	0.9922	0.1545
3	5388 keV	1.66 %	0.9822	0.0196
4	5544.5 keV	0.37 %	1.0107	0.0044
5	5511.5 keV	0.225 %	1.0047	0.0027

Table 4.3.: Prominent α-energies from an ^{241}Am α-source [30].

exemplary fit is shown in figure 4.6 and the energy resolutions for all p-side strips of the DSSD are summarised in figure 4.7. The average resolution of 54.3 keV (FWHM) determined after the experiment is twice as high as the average value measured before the experiment in the laboratory (see figure 2.20). On the one hand, higher electronic-noise levels inside the ESR cave already contribute with 41.8 keV FWHM to the total value (compared to 19.8 keV (FWHM) measured under laboratory conditions, before). On the other hand, also the unfolded energy resolution of 33.1 keV remains twice as high as before. A possible explanation for the difference could be the radiation damage which was described in section 3.8.
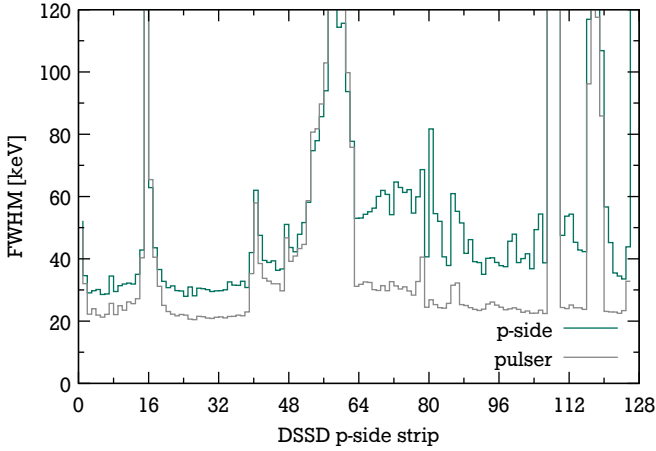
Figure 4.7.: Energy resolution (FWHM) of the p-side strips of the first DSSD for 5485.56 keV α-particles from an ^{241}Am source.

Together with equation (4.28), it is now possible to derive an equation for the energy calibration:

$$E(u) = \frac{E_\alpha}{u_\alpha} u \tag{4.30}$$

$$\Rightarrow E(k) = E(U(k)) = \frac{a E_\alpha}{u_\alpha} + \frac{b E_\alpha}{u_\alpha} k + \frac{c E_\alpha}{u_\alpha} k^2 \tag{4.31}$$

This procedure was used for all detectors involved in the present analysis. However, for some individual detector channels a different procedure or further corrections had to be applied. First, there are the 48 n-side strips of the first DSSD with the misaligned ADC gate (see section 3.8). The misalignment not only causes a drastically increased non-linear behaviour of the energy but also a lower energy is measured. While for the pulser calibration this was partly compensated by increasing the signal amplitude, the α-spectrum could not be used for calibration. Hence, after correcting the non-linearities with the pulser spectra (see figure 4.8), the gain matching was done by exploiting the correlation between the p- and n-side signals. Therefore, the energy of one n-side strip was plotted against the already calibrated energy of all p-side strips, as shown for one exemplary n-side strip in figure 4.8. Then, a line was fitted directly to the data points and the gain was determined from the fitted line for an energy of 3 MeV. However, the achieved accuracy of the energy calibration is low and together with the insufficient energy resolution, the

---
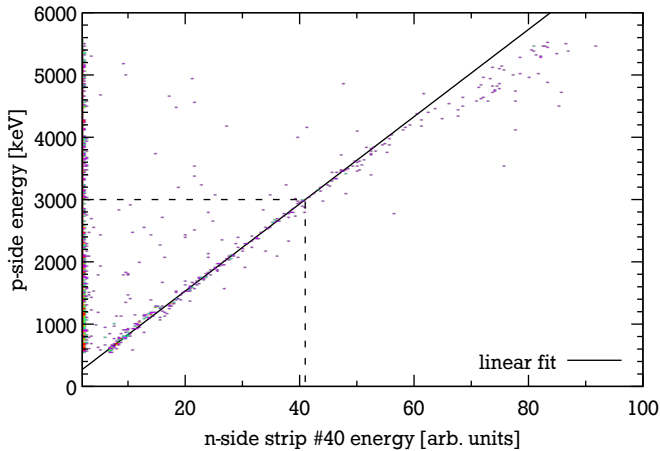
Figure 4.8.: Calibration of the DSSD n-side channels with misaligned ADC gate.

n-side channels should not be used for anything but a position measurement in this experiment.

Corrections were also needed for those channels which were affected by the flawed BLR correction of some shaping amplifiers (see section 3.8). When plotting the correlation of the affected channels of one detector side versus unaffected channels of the other side, as shown in figure 4.9, one sees that the resulting line of correlated events is intersected at lower energies. The two lines also have different slopes. Consequently, two different calibrations have to be applied above and below the threshold of the BLR, i. e. where the lines are intersected. Unfortunately it was not possible to use the correlation plots to derive the calibration parameters directly. There is not enough statistics especially in the regions where, kinematically, almost no protons of the proper energy are hitting the detector. Additionally, the energy signals from the n-side would be needed to get the correlation plots for the correction of p-side channels. However, most of the n-side channels suffer from the misaligned ADC gate and the remaining ones are affected by the faulty BLR themselves. Fortunately, at least two pulser peaks are located in the regions below the BLR threshold in all affected channels which allows a partial calibration. The region above the BLR threshold was calibrated in the way as described at the beginning of this chapter.

With this calibration, the amplitudes of the pulser peaks were re-calibrated to energy and were used to get at least a linear calibration in the region below the BLR thresholds. On the right side of figure 4.9 the calibrated energy of the first 16 p-side channels, summed together, is plotted without the corrections (*black line*)
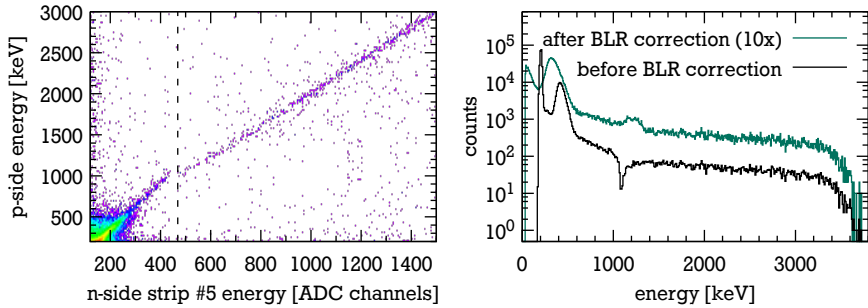
Figure 4.9.: Correction of the energy calibration for the channels with the faulty BLR: (*left*) correlation of the uncalibrated energy of n-side strip #5 of the first DSSD versus the energy of all the p-side channels not suffering from the BLR issue; the region left of the dashed line is affected by the BLR issue and calibrated separately; (*right*) sum spectra of the first 16 p-side channels of the first DSSD before and after correction.

and with the corrections applied (*green line*). While the partial calibration has improved the linearity in the low energy region, it did not resolve the distortion of the energy spectrum completely.

Calibration of the Si(Li)s

Since there was no practical possibility to illuminate the Si(Li) detectors directly with an α-source, these detectors were calibrated indirectly by connecting 16 p-side strips of the DSSD to the electronics chain of the Si(Li) detectors. In a first order approximation this yields a reasonably good calibration since the total charge created in a silicon detector does not depend so much on the structure of the detector but on the mean energy for creating an electron-hole pair, which is a physical property of silicon. However, because of the different electrical properties (mainly resistivity and capacitance) of the two kinds of detectors, their signal shapes will differ. The magnitude of this effect is expected to be in the order of a few percent. Indeed, a correction factor of 1.03 was determined by comparing the kinematical band of the elastic scattering with the expected energy. Therefore, the reconstructed energy of the telescope was used to determine the mean DSSD p-side strip per energy bin (for details on the energy reconstruction, see section 4.3). The advantage of estimating the kinematical curve this way instead of using the mean energy per strip is that the physical cross section does not change so much per energy bin and thus does not skew the result. Once the angular calibration (section 4.5) is established from the DSSD's energy, the calculated kinematical curve can be divided by the kinematical curve which was determined experimentally. The ratio between both
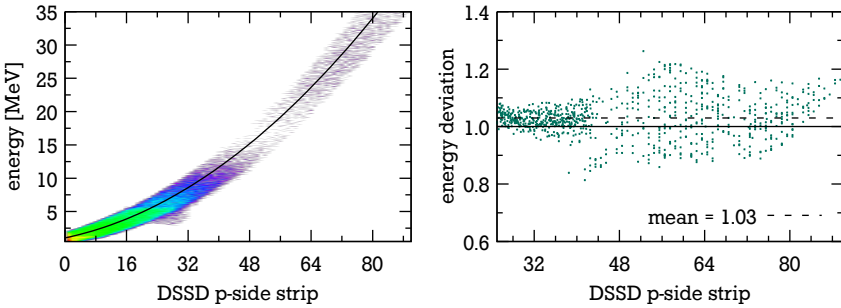
Figure 4.10.: Correction of the energy calibration of the Si(Li)s. *Left*: kinematical correlation measured with the detector telescope ([56]Ni without slit); *right*: deviation of the measured kinematical curve from the expected one (*green dots*), the dashed line indicates the mean deviation of 1.03.

is then applied to the energy calibration of the Si(Li). This procedure is shown in figure 4.10 for the case of the [56]Ni measurement without aperture.

4.3 Energy reconstruction

The DAQ was configured such that any trigger caused a read-out of all ADC channels. Since no zero suppression was used on the ADCs either, every event contains at least the noise in every channel. Therefore, a first step in the energy reconstruction is to reject the noise events. In a following step, the event in each detector is reconstructed taking into account specific properties of the detector. The procedures used here were developed benefiting from the experience gained in the previous EXL demonstrator and detector tests (see section 2). In a last step, the full energy measured by the three layers of the detector telescope can be restored.

Noise suppression

In the energy spectra of most detector channels, a prominent noise peak is visible at the lowest energies. Since the noise conditions and thus the shapes and sizes of the peaks are varying, the noise thresholds were defined channel by channel. Therefore, in each of the singles spectra the threshold was set to an energy value were the bin content first fell beneath a certain limit which was defined for each detector individually. While this procedure cannot remove every noise induced

signal, it limits the rate of noisy events to a certain acceptable level with the aim to increase the efficiency of the following reconstruction algorithms.

Energy reconstruction in the DSSDs

The main goal of the event reconstruction algorithm for the DSSD is the identification and reconstruction of interstrip events. Ideally, this should be achieved without throwing away events of interest.

After applying noise cuts, the signal multiplicity per detector side is already considerably lowered. With the chosen noise thresholds about 90 % of all events have a multiplicity of one and therefore need no further treatment. For the remaining 10 % of events, it is assumed that the channel with the highest energy contains the event of interest. All remaining entries in channels except the two neighbouring ones are considered as noise and rejected. At most three signals can remain after this procedure. In the cases where the multiplicity is two, i. e. when only one neighbouring signal exists, both energies are added and the position is assigned to the detector segment with the higher energy value. If both neighbouring channels have a signal and the multiplicity is equal to three, the event is assumed to be composed of an interstrip event in two of the channels and noise in the third. The signal which is closer to the noise threshold of the respective channel is ruled out and the remaining two signals are treated as an interstrip event like in the previous case. The n-side signals are reconstructed in the same way but, ultimately, only the position is used in the further analysis to define the azimuthal scattering angle φ.

The algorithm could be improved in future experiments by exploiting the correlation between p- and n-side signals. As both detector sides measure the same signal amplitude, an energy measured on one side with a multiplicity of one could be used as a condition for the reconstruction of an event of the other side with higher signal multiplicity. Also a detection of double hits would be possible. Unfortunately, because of the imprecise energy measurement on the n-side (see sections 3.8 and 4.2) the signals from the n-side were not usable for this purpose.

Energy reconstruction in the Si(Li)s

Similar to the DSSD also the Si(Li) detector can exhibit charge sharing between bordering segments (see also figure 2.9). The obvious difference here is that the p-side of the Si(Li) is segmented two-dimensionally so that a charge sharing may happen with any neighbouring pad. Since the unsegmented n-side of the Si(Li)s is not read-out, the full-energy signal has to be reconstructed from the p-side signals. Similar to the reconstruction of a DSSD event, the segment with the highest
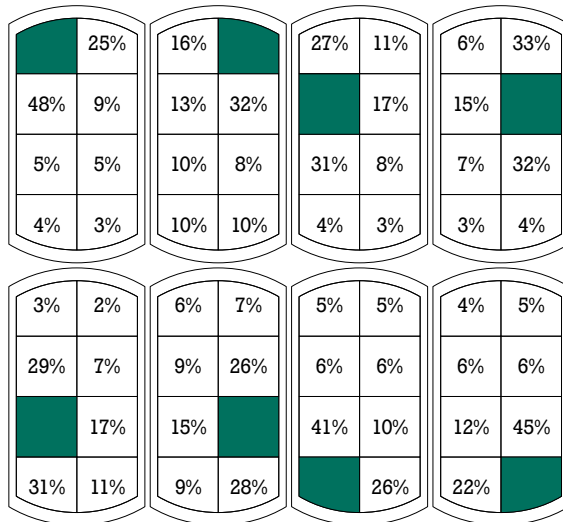
Figure 4.11.: Distribution of events in the first Si(Li) with multiplicity higher than one. For details, see text.

measured energy is chosen to be the prominent segment, i.e. the segment that was hit by the particle. Then, the signals from all adjacent segments are added up if there are any that passed the noise thresholds. The diagonal elements are ignored here, since the geometrical probability for a charge sharing should be much smaller for diagonal segments. To validate this assumption, the distribution of events with multiplicity higher than one was evaluated for the first Si(Li). For each event, a prominent segment was chosen and it was evaluated how the remaining events are distributed. The results are shown in figure 4.11. In each case, the segments which are sharing a long edge with each other, show a significantly higher probability than the diagonal ones.

Total energy reconstruction

After reconstructing the energy and position of each detector of the ΔE-E telescope, the remaining task is to reconstruct the full energy of the event. Since the dead layers of both the DSSD and the Si(Li)s were relatively thin, the energies of the individual detectors can simply be summed up without additional corrections. Because of the coarse segmentation of the Si(Li)s, a tracking is not possible and the position information can only be taken from the DSSD.
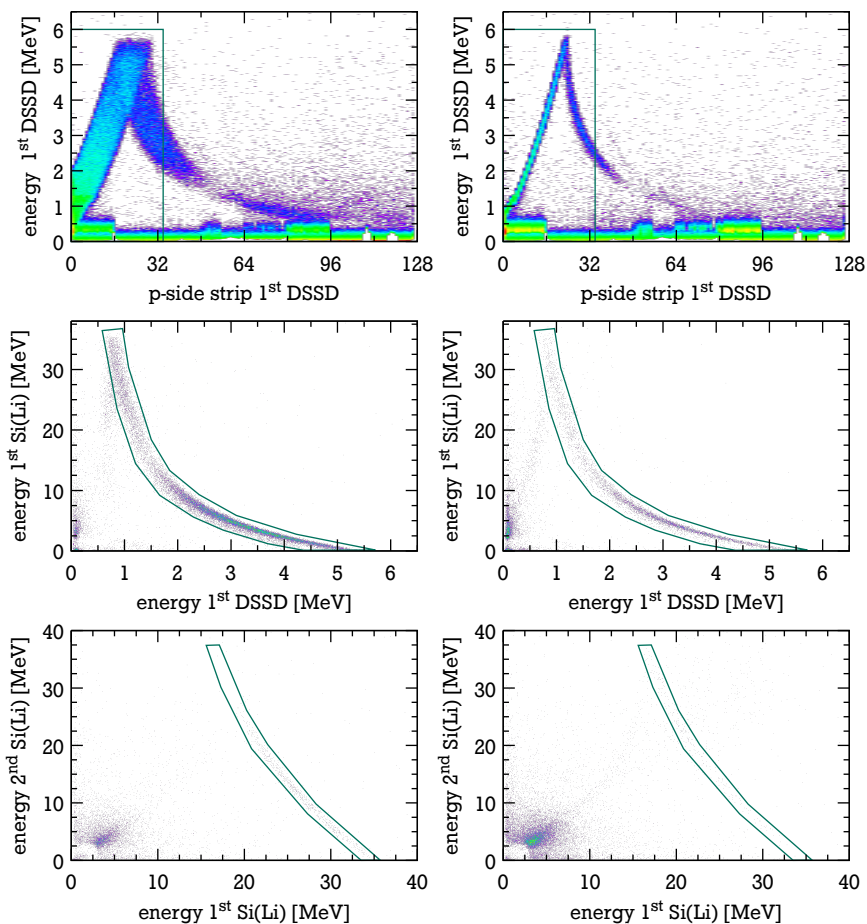
Figure 4.12.: Two dimensional cuts used for the energy reconstruction exemplary for the runs with ^{56}Ni beam without (*left*) and with 1 mm slit aperture (*right*).

To further reduce the background in the energy spectra, three two-dimensional cuts, which are illustrated in figure 4.12, were applied to different correlations in order to identify and reject background events.

Events are accepted if they are:

1. within the cut on the DSSD ($\equiv$ stopped events, no signal in subsequent detectors).

2. within the ΔE-E cut of the DSSD and the first Si(Li) (≡ events punching through the DSSD and being stopped in the first Si(Li)).

3. within the ΔE-E cut of the DSSD and the first Si(Li) and the ΔE-E cut of both Si(Li)s (≡ events punching through the DSSD and the first Si(Li) but being stopped in the second Si(Li)).

The telescope, which is effectively 13.3 mm of silicon, is able to stop protons with energies up to about 50 MeV. For the present reaction this corresponds to a laboratory scattering angle of 76.6°, which coincides with the smallest angle covered by the first Si(Li) (76.8°). Consequently, protons which punch through the second Si(Li) most probably have not passed through the first Si(Li) and are rejected by the conditions applied to the data. The effect of the conditions is demonstrated in figure 4.13 where the reconstructed energy is plotted versus the p-side segment of the DSSD with and without applying the cuts.
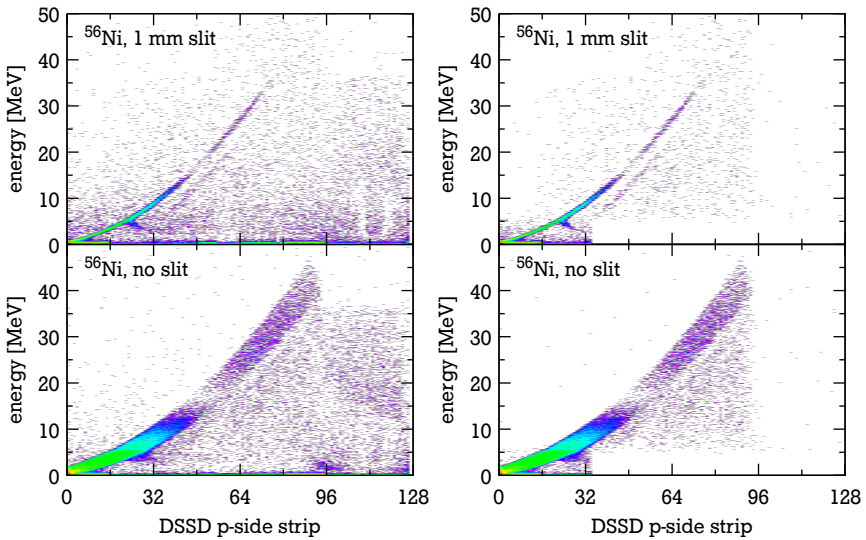
Figure 4.13.: Reconstructed energy in the recoil telescope without (*left*) and with (*right*) the two dimensional cuts as shown in figure 4.12.

4. Data analysis

4.4 Interstrip probability in the DSSD
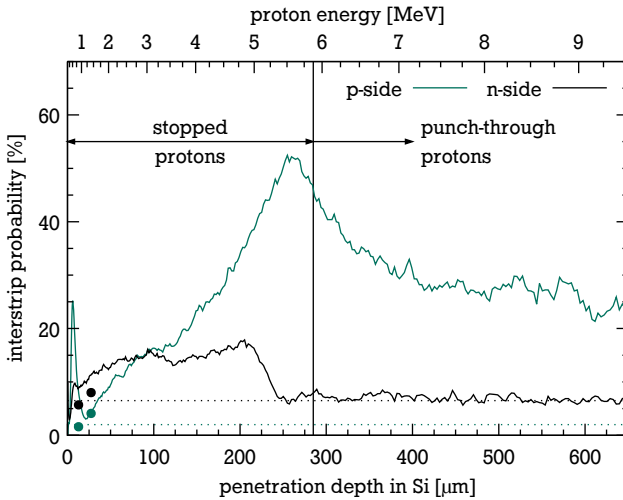
Figure 4.14.: Interstrip probability in the DSSD as a function of the penetration depth/proton energy (*solid lines*). The penetration depths were estimated using [87]. Also shown are the results from measurements with α-sources from table 2.2 (*points*) and the geometric probability (*dotted lines*).

It is expected that the probability for interstrip events, i.e. events where the created charge is being shared between two adjacent strips, depends on the penetration depth of the impinging particle and hence its energy and charge. In section 2.3, this probability was already investigated with two different α-sources at two different energies of 3182.69 keV and 5485.56 keV. The two energies correspond to penetration depths of about 13 μm and 27 μm, respectively. Hence, only the surface of the detector was probed and the resulting probabilities were – unsurprisingly – comparable with what is expected by the geometric dimensions of the strips (see table 2.2). With the continuous energy spectrum of protons which was measured during the present experiment it is now possible to determine the interstrip probability over the whole depth of the detector and even for punch-through events. Therefore, the correlation between the multiplicity of the events on one detector side and the proton energy were investigated. Instead of simply using the energy measured by the DSSD, the total energy of the telescope was used here as it automatically disentangles the stopped from the punch-through protons. Then,

the ratio between all events and interstrip events (summing multiplicities of two or three) is calculated for each energy bin. For this analysis only the runs with ^{56}Ni beam were considered as the ones with ^{58}Ni beam were affected by the continuously drifting energy caused by the radiation damage (see section 3.8). The resulting curves were then averaged and smoothed for better visibility[4] and the penetration depth of the proton was estimated from its incident energy by using the *PSTAR* databases [87]. Figure 4.14 shows the such derived interstrip probability as a function of the penetration depth (*solid lines*) together with the data points from the previous measurement with α-sources (*dots*) and the geometric probability (*dotted line*).

The analysis bears some limitations and should be interpreted rather qualitatively than quantitatively. Since the interstrip probability is effectively derived from the signal multiplicity the value depends on the noise thresholds especially at lower energies. This might explain for example the peak in the p-side curve at a penetration depth of around 10 μm which is in strong discrepancy with the results from the α-source tests. This might also explain why a higher probability was deduced for the n-side than indicated by the source tests. Nevertheless, for higher proton energies this should not be too much of an issue. There, the two curves for the p- and the n-side show a clearly different behaviour. As already indicated by the tests with α-sources, the n-side exhibits a higher probability at smaller penetration depths. While the n-side interstrip-probability grows only slightly and remains below 20 %, the probability on the p-side rises to about 50 % close to the back side of the DSSD. For punch-through events, the probability for both sides drops again and converges to a value approximately half the maximum. On the n-side this coincides well with the geometric interstrip probability.

4.5 Angular calibration

For the angular calibration of the DSSD, its position relative to the interaction point and, in the cases where it is being used, the position of the slit aperture relative to the interaction point had to be known precisely. Because of the unavoidable uncertainties in the machining processes, these positions can only be extracted from the technical drawings with certain accuracy and it was not feasible to measure them with sufficient precision during the experiment. Even if the positions were measured before or after the experiment it cannot be excluded that the vacuum chamber deforms slightly under vacuum conditions and hence, shifts the positions again. Therefore, this information was extracted from the measured

---

[4] The exponential moving average of the curve was calculated using the *Mathematica* function *ExponentialMovingAverage* with a smoothing constant of 0.2.

kinematical correlation of the recoil energy and the laboratory scattering angle in elastic scattering (see appendix A). With a Monte-Carlo simulation written in *Mathematica* both the angular calibration and the effective angular acceptance of the detector system were determined. The latter becomes very important especially when using the slit aperture.

4.5.1 Monte Carlo simulation

For the simulation, the experimental geometry is first simplified. It only consists of the first DSSD which is part of the 90° telescope, the slit aperture and the interaction zone. The latter is defined by the overlapping density distributions of the target and the ion beam (see section 4.1.1 and 4.1.2, respectively). Figure 4.15 shows a schematic drawing of the simplified geometry together with all variables which are used to define it. Their initial values together with their uncertainties and the related probability distribution functions (PDFs) are summarised in table 4.4. For the geometric quantities, the nominal values together with their tolerances were taken from the technical drawings. The tolerances which are given there define a lower and an upper limit for the possible values in accordance to the *ISO 2768-1m* norm. In this case, it is suggested by the principle of maximum entropy to describe them by an rectangular distribution with a uniform probability [88]. The quantities related to the target are based on actual measurements (see section 4.1.1) which yielded a best estimate and a standard deviation for the parameters, but the PDFs of these parameters are not known. According to the principle of maximum entropy, a Gaussian probability distribution has to be assigned in such cases [88]. In order to get the width of the ion beam, σ_{beam} is estimated from the measured beam intensities (see figures 4.3 and 4.4) as described in section 4.1.2. Additional uncertainties are not taken into account here as the fluctuations caused by the variations of the beam currents are expected to exceed them.

Event generator

The first element of the simulation is a random event generator which creates the physical events in the interaction zone of ion beam and target with respect to their individual density distributions. Since a Gaussian density distribution with radial symmetry is assumed for the ion beam, the x and y coordinates can be sampled very fast and efficiently from a bivariate normal distribution. The PDF of the remaining z coordinate depends only on the target density and is sampled via the so called *rejection method*. A random number for the z coordinate is drawn from a uniform probability distribution and, taking the previously drawn x coordinate into account, the target density $\rho_{\text{target}}(x, z)$ is calculated. Whenever $\rho_{\text{target}}(x, z)$ is
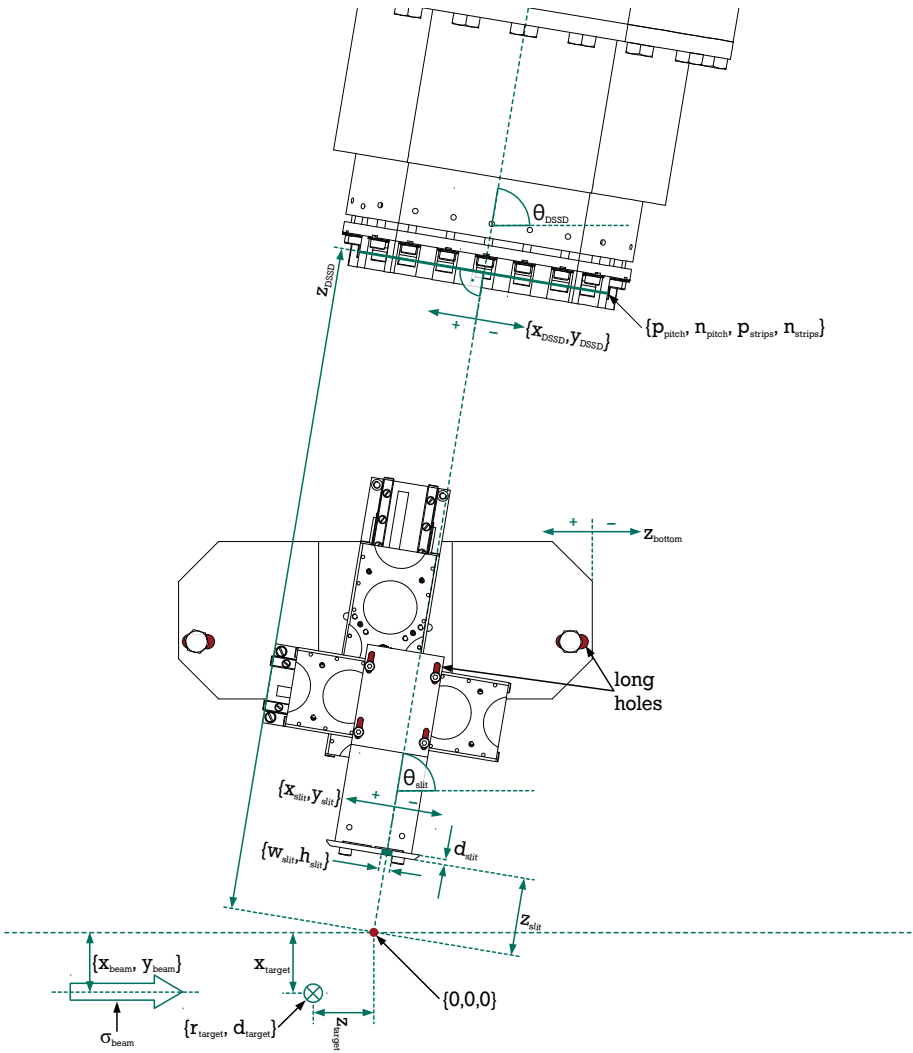
Figure 4.15.: Simplified geometry as used in the Monte-Carlo simulations for the angular calibration (not to scale). For details see text. (*based on technical drawings by* [50])

parameter	value	PDF
DSSD		
x^*_{DSSD}	$(1.6 \pm 0.8)\,\text{mm}$	see figure 4.19
y_{DSSD}	$[-1.0\,\text{mm}, 1.0\,\text{mm}]$	uniform
z_{DSSD}	$[248.9\,\text{mm}, 253.9\,\text{mm}]$	uniform
θ_{DSSD}	$[80.2°, 80.8°]$	uniform
p_{pitch}	$0.5\,\text{mm}$	—
n_{pitch}	$1.0\,\text{mm}$	—
p_{strips}	128	—
n_{strips}	64	—
aperture		
x_{slit}	$[1.6\,\text{mm}, 2.2\,\text{mm}]$	uniform
y_{slit}	$[0.7\,\text{mm}, 1.3\,\text{mm}]$	uniform
z^*_{slit}	^{56}Ni: $[25.3\,\text{mm}, 31.7\,\text{mm}]$	uniform
	^{58}Ni: $[30.8\,\text{mm}, 36.8\,\text{mm}]$	see figure 4.19
θ_{slit}	$[80.4°, 80.6°]$	uniform
w_{slit}	$1\,mm$: $[-0.9\,\text{mm}, 1.1\,\text{mm}]$	uniform
	$2\,mm$: $[-1.9\,\text{mm}, 2.1\,\text{mm}]$	uniform
h_{slit}	$[13.8\,\text{mm}, 14.2\,\text{mm}]$	uniform
d_{slit}	$[1.9\,\text{mm}, 2.1\,\text{mm}]$	uniform
z^*_{bottom}	$(0.4 \pm 0.4)\,\text{mm}$	see figure 4.19
target		
x_{target}	$(0.43 \pm 0.30)\,\text{mm}$	Gaussian
z_{target}	$(0.25 \pm 0.30)\,\text{mm}$	Gaussian
r_{target}	$(3.15 \pm 0.06)\,\text{mm}$	Gaussian
d_{target}	$(0.32 \pm 0.10)\,\text{mm}$	Gaussian
beam		
x_{beam}	$[-0.5\,\text{mm}, 0.5\,\text{mm}]$	uniform
y_{beam}	$[-0.5\,\text{mm}, 0.5\,\text{mm}]$	uniform
σ_{beam}	*individual beam current distributions*	

Table 4.4.: Initial values of the parameters used for the simulation of the experimental geometry as shown in figure 4.15. The limits and uncertainties of the initial values are extracted from the technical drawings (DSSD and aperture) or from actual measurements (target, beam). The parameters marked with a * are the results of fits to the experimental data (see section 4.5.2).
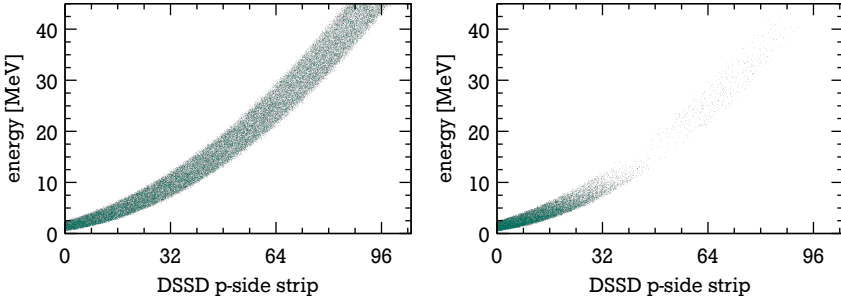
Figure 4.16.: Exemplary simulated angular correlations using a constant cross section (*left*) and a realistic cross section (*right*).

higher than an additional random number, which itself was sampled from a uniform distribution with values between zero and the maximum density, the random coordinates are taken and accumulated or rejected otherwise. For each set of random coordinates which were created this way, the physical interaction is defined by choosing polar and azimuthal laboratory scattering angles θ and φ for the recoil. In this step, a physical cross section may be used to bias the random-number generator (see figure 4.16) but for the following applications this is not necessary. Instead, the scattering angles are sampled from uniform distributions. To achieve an isotropic distribution of θ and φ in Cartesian coordinates, it is necessary to first choose two random variables u and v on an interval of $[0, 1]$ and then apply the following transformation [89]:

$$\theta = \cos^{-1}(2u - 1)$$
$$\varphi = 2\pi v \tag{4.32}$$

By using the relations for relativistic kinematics (see appendix A), the energy of the particle can be calculated from its scattering angle. For the present purpose, only elastic scattering is of interest, but it is also possible to simulate inelastic scattering with the present event generator. However, since the particles are created in the laboratory frame, the discontinuity at the maximum laboratory scattering angle (see section A) leaves a gap in the kinematical band where the two branches meet (see figure 3.8).

Particle transport and hit detection

The particle transport used in this simulation is very basic. All physical interactions of the recoils with matter are neglected in favour of increased speed as they

are not important for the intended use of the simulations. The algorithm just calculates where the particle hits the plane of the detector and checks whether the point is still on the detector. If so, the hit coordinates are converted to units of detector segments and the event together with the physical laboratory scattering angles is recorded. The slit aperture is implemented in the same way. Two planes with the dimensions of the slit ($w_{slit} \cdot h_{slit}$) are stacked behind each other at a distance of d_{slit}. These planes are then basically treated as coincidence detectors and only those events are taken which have passed through all three planes at a time.

4.5.2 Fitting the geometry

The described simulation was used to determine the angular calibration and the geometric acceptance of the recoil detector. The general idea is to vary the geometry in the simulation until the experimental data is reproduced best. Here, the experimental observable is the well-defined correlation between the laboratory scattering angle and the energy of the recoil particle, i.e. the energy-strip correlation. However, since the physical cross section changes significantly within the angular coverage of one strip, the correlation derived by the mean energy per strip depends very much on the cross section. To avoid this, the mean strip number per energy bin (typically 15 keV) is being used instead. The resulting correlation is almost independent of the underlying cross section as shown in figure 4.17. There, the energy-strip correlation was extracted in the two ways from a kinematical band which was simulated using a physical cross section (the same as of figure 4.16).
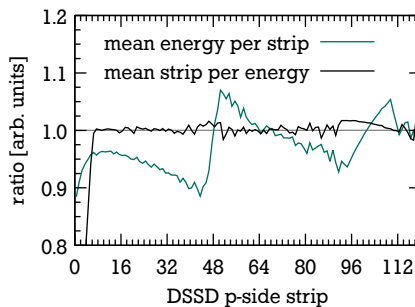
Figure 4.17.: Determination of the energy-strip correlations. Plotted is the ratio of the calculated kinematical correlation to the kinematical correlation extracted from simulations assuming realistic cross sections. It is shown that the mean detector strip per energy bin yields a kinematical correlation independent of the cross section. For details see text.

Then, the ratio to the calculated energy-strip correlation is plotted as a function of the p-side strip. The resulting ratios show identical energy-strip correlations if the mean strip per energy bin was used to calculate the correlation. It should be noted that the deviations at the first seven strips are due to the fact that the full width of the kinematical band is not completely measured by the detector any more, i.e. the edge of the detector is reached.

This way, the energy-strip correlations were extracted for the six different experimental runs (see figure 4.18). Due to the radiation damage and the drifting energy in the cases of ^{58}Ni beam, not the full statistics has been used. Since the energy calibration of the Si(Li) detectors was performed in an indirect way, the energy measurement for protons with energies above the punch-through energy of the DSSD may be less precise (see section 4.2) and hence, only the points below an energy of 5.8 MeV were used for further fits.

In the fitting procedure, these experimental correlations are then compared to the simulated ones and their χ^2 is calculated as:

$$\chi^2(p_k) = \sum_{i=1}^{N} \frac{(y_i - f(x_i, p_k))^2}{\sigma_i^2} \tag{4.33}$$

Here, y_i is the experimental value with an uncertainty of σ_i at the coordinate x_i and $f(x_i, p_k)$ is the corresponding simulated value which depends on a free parameter p_k. By varying p_k the χ^2 curve is minimised in order to determine a best p_k. The minimisation is carried out by the *Mathematica* function *FindMinimum* using the *PrincipalAxis* method.

From table 4.4 it is obvious that the geometry of the whole experimental setup, i.e. detector, slit aperture and interaction zone, is only defined up to a certain precision. As outlined before, the purpose of the fitting procedure is to adapt the geometry until the experimental observables can be best described. Since only a limited number of parameters can be fixed with the help of the experimental data, it is necessary to identify the parameters with the biggest impact on the angular calibration and the acceptance correction. First of all, this is certainly the shift of the DSSD in horizontal direction, x_{DSSD} as defined in figure 4.15. Of course, varying the polar angle of the DSSD θ_{DSSD} can yield an (almost) indistinguishable energy-strip correlation. It is also obvious that there is a correlation with z_{DSSD}, i.e. the distance between the DSSD and the point of origin. To allow for such correlations and to properly propagate the uncertainties, a Monte Carlo approach as described in [88] was applied here. The general idea behind this approach can be summarised in the following way. For independent input quantities X_i with $i = 1, \ldots, N$ and known PDFs g_{X_i} which contribute to an output quantity $Y = f(X_1, \ldots, X_n)$, the PDF of
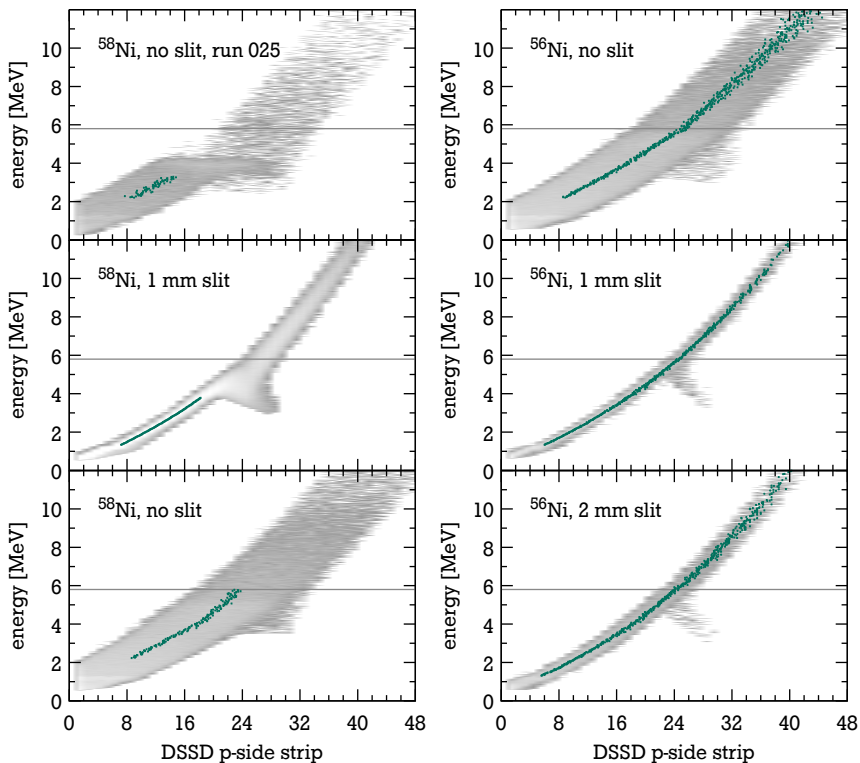
Figure 4.18.: Energy-strip correlations for the significant experimental runs (*green dots*). The horizontal grey line indicates the maximum energy stopped in the DSSD.

the output quantity g_Y can be estimated by repeatedly sampling random numbers from the input PDFs and evaluating the model $f(X_1, \ldots, X_n)$. The benefit of this approach is that it will yield a PDF for the output quantity in a straight forward way for arbitrary PDFs of the input quantities and for any model which defines the output quantity Y.

In the present case, the input quantities and their PDFs are defined in table 4.4 and the model $f(X_1, \ldots, X_n)$ is the previously described fitting procedure for the output quantity. Therefore, a random vector of 2100 elements was sampled from the definitions in table 4.4 and x_{DSSD} was determined for each of the random samples. It should be noted here that the size of the random vector and hence the maximum number of Monte Carlo trials is very much limited by the computation
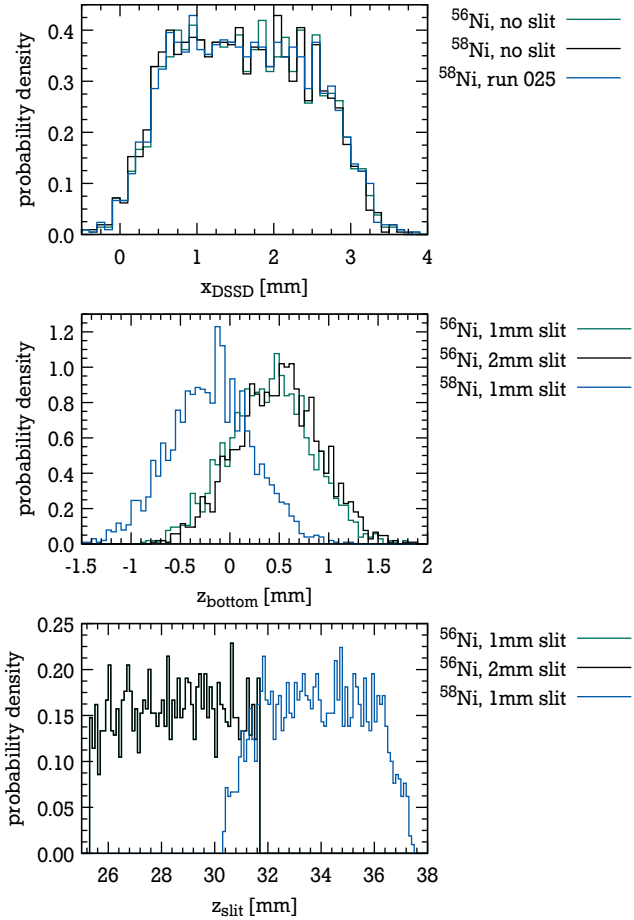
Figure 4.19.: Distribution of fit values x_{DSSD} (*top*), z_{bottom} (*middle*) and z_{slit} (*bottom*).

time. The chosen size is certainly too low to extract the full PDF of the respective output quantities, but it is expected to be still sufficient to yield a meaningful average value together with a standard deviation [88].

The procedure was repeated using the same initial random vector for each of the three measurements without the slit aperture. The resulting distributions of fitted x_{DSSD} are shown in figure 4.19. All three distributions are basically identical with a mean shift $\tilde{x}_{\mathrm{DSSD}} = 1.6\,\mathrm{mm}$ and a standard deviation of $0.8\,\mathrm{mm}$. However, for the subsequent calculations not the mean value will be used. Instead, each

sample of the initial vector is updated with the fitted value of x_{DSSD} and will be used to calculate the angular calibration and the acceptance correction. This way, the correlations between the input quantities and the fitted quantity are propagated to further steps in the analysis.

The misplacement of the DSSD corresponds roughly to an angular difference of $\Delta\theta_{DSSD} \approx 0.36°$. This is already in the same order of magnitude as the uncertainty of θ_{DSSD} which is about 0.25° (see table 4.4). The slightly shifted position of the target has an additional albeit small impact here. Taking the additional correlation of x_{DSSD} with z_{DSSD} into account, the fitted DSSD shift seems to be well within the expected tolerances. Nevertheless, it has to be kept in mind, that there is no unambiguous way to determine the actual contribution of x_{DSSD}, z_{DSSD} and θ_{DSSD} to the angular calibration. There is, in principle, the possibility to use the position sensitivity of the DSSD and the segmentation of the first Si(Li) to determine z_{DSSD} independently. However, because of the small distance between the DSSD and the Si(Li) together with the – for this case – coarse segmentation of the DSSD, the resulting uncertainties do not allow a more precise determination of z_{DSSD}.

In the cases where the slit aperture was used its position had to be determined. Before the experiment started, the position of the piezoelectric actuator which moves the slit perpendicular to the normal axis of the detector was calibrated using an optical telescope. In table 4.5 the nominal position settings for the piezo actuator are compared to the actually measured settings. The offset between both values is explainable since the telescope was aligned to the axis of the flange (83.5°) rather than the axis of the detector (80.5°). For the given distance z_{slit} of 3 cm, this measurement fixes the expected value for x_{slit} to (1.9 ± 0.3) mm.

The remaining uncertainty in the position of the slit is mainly due to two sets of long holes which affect the distance to the target, z_{slit}, and the position of the whole assembly along the beam axis, z_{bottom} (see figure 4.15). In table 4.4, the interval of possible values is given for these two parameters. Unfortunately it appeared to be infeasible to deduce both parameters from the present experimental data. Thus, it was decided to fit only z_{bottom} and leave z_{slit} randomised in the interval of possible

| distance | nominal | | measured | |
	1 mm aperture	2 mm aperture	1 mm aperture	2 mm aperture
10 mm	7 mm	22 mm	9.84 mm	24.94 mm
20 mm	7 mm	22 mm	9.44 mm	24.40 mm
30 mm	7 mm	22 mm	8.91 mm	23.91 mm

Table 4.5.: Nominal and measured positions of the piezo actuators for various distances to the target.

values. The random vector was again composed of 2100 samples but, instead of sampling a new vector from the input PDFs, it was constructed in equal parts from the three output vectors of the previous step. This way, the correlations between the original input values and the fitted values of x_{DSSD} are exactly preserved and, at the same time, the average of x_{DSSD} from the three output vectors is obtained. The resulting distributions of z_{bottom} is shown in figure 4.19 for the three different measurements with slit aperture. While the two measurements with ^{56}Ni beam yield comparable distributions with a combined mean value of $\tilde{z}_{\text{bottom}} = 0.4\,\text{mm}$ and a standard deviation of 0.4 mm, the data set with ^{58}Ni beam yields a different mean value of $\tilde{z}_{\text{bottom}} = -0.2\,\text{mm}$ and a standard deviation of 0.4 mm. In fact, it turned out during the experiment that the slit aperture was placed at a different distance for all measurements with ^{58}Ni beam. Therefore, the fitted values of z_{bottom} will be applied for the ^{58}Ni measurement, but the distance z_{slit} has to be fitted instead. Again, the input vector of random samples for this step was constructed in equal parts from the output vectors of the two ^{56}Ni data sets. The distribution of fitted distances z_{slit} is shown in figure 4.19 compared to the unaltered initial values from the fits of the ^{56}Ni data sets. The mean distance of the slit aperture during the measurements with ^{58}Ni beam was found to be $\tilde{z}_{\text{bottom}} = 33.9\,\text{mm}$ compared to the originally assumed value of 28.5 mm.

During the experiment, a set of small measurements was performed for the ^{56}Ni and ^{58}Ni beams where the slit aperture was deliberately shifted perpendicular to its normal axis in steps of 1 mm. In order to verify the geometry, x_{slit} was estimated using the corresponding output vectors from the previous fits with 1000 samples each. The resulting values are summarised in table 4.6 and reveal a very good agreement with each other within their uncertainties. Furthermore, the data can be described by a first order polynomial (see figure 4.20) with a slope close to unity. The good agreement of all individual measurements supports the correctness of the determined geometry.

slit shift	fitted slit position x_{slit}	
	^{56}Ni	^{58}Ni
−4 mm	$(5.7 \pm 0.2)\,\text{mm}$	$(5.9 \pm 0.2)\,\text{mm}$
−3 mm	$(4.9 \pm 0.2)\,\text{mm}$	—
−2 mm	$(3.9 \pm 0.2)\,\text{mm}$	$(3.9 \pm 0.2)\,\text{mm}$
−1 mm	$(2.8 \pm 0.2)\,\text{mm}$	$(3.0 \pm 0.2)\,\text{mm}$
+1 mm	$(0.9 \pm 0.2)\,\text{mm}$	$(0.9 \pm 0.2)\,\text{mm}$
+2 mm	$(-0.1 \pm 0.2)\,\text{mm}$	$(-0.1 \pm 0.1)\,\text{mm}$
+3 mm	$(-1.0 \pm 0.2)\,\text{mm}$	—

Table 4.6.: Nominal shifts of the slit aperture versus fitted x_{slit}.
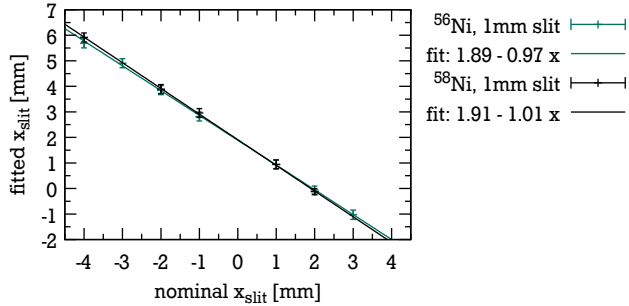
Figure 4.20.: First order polynomial fits to data of table 4.6.

Evaluation

In order to evaluate the angular calibration, the kinematical bands for elastic scattering were simulated for the different experimental runs. In each case, the geometry was defined by the mean values of the initial input parameters as well as the fitted parameters. In order to compare the simulated kinematical bands to their experimental counter parts, the simulated data was divided into bins of one strip and 50 keV and a contour of the kinematical band was created at half the maximum value in each strip. In figure 4.21 the experimental kinematical correlations are overlaid by an outline of the simulated data. In general, the kinematical bands coincide well except for the runs which suffered from the radiation damage. Especially in the cases with the slit aperture, it is important to note that the simulated correlations end approximately at the same position as the experimental correlations. Even the width of the experimental correlation is well reproduced by the simulations. This is understandable since the energy resolution of the detector system (about 50 keV (FWHM) at 5.5 MeV, figure 4.7) is small compared to the angular resolution which itself is dominated by the extended interaction zone and the width of the slit aperture.

4.5.3 Angular calibration functions

In the previous section, the experimental geometry was fitted to reproduce the measured kinematical correlation. For each of the experimental runs, vectors with random samples were kept and are used in this step to calculate the actual angular calibration and acceptance (or solid angle) of the first DSSD's p-side strips.

Effective solid angle

To properly calculate the cross section, the solid-angle coverage of each detector segment has to be known. Additionally, the acceptance of the strips is limited by

---
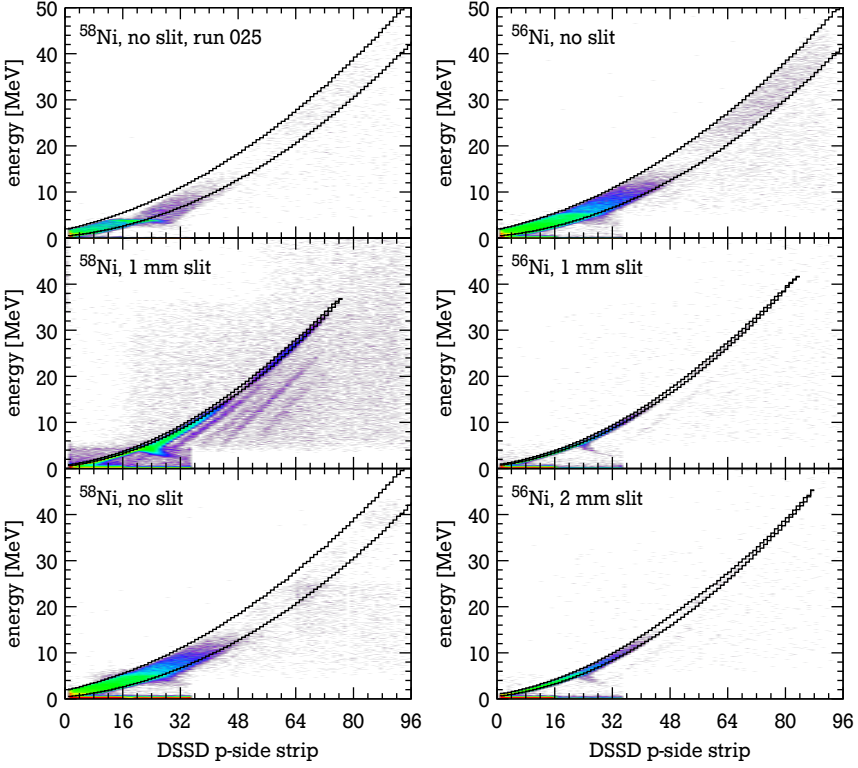
Figure 4.21.: Comparison of the experimental data (*histogram*) with simulated kinematical bands represented by a contour drawn at half maximum (*black line*).

the slit aperture. Both can be combined to an effective solid angle and estimated at the same time by performing a Monte Carlo integration. Using the same simulation module as before, $N_{\text{total}} = 10^7$ interaction coordinates were created in an angular range of $65° \leq \theta \leq 90°$ and $-10° \leq \varphi \leq 10°$. The particles hitting a detector segment $n(\text{strip})$ are accumulated and the effective solid angle per strip $\Omega_{\text{eff.}}(\text{strip})$ in units of steradian can be calculated as:

$$\Omega_{\text{eff.}}(\text{strip}) = \frac{\int_{\theta_{\min}}^{\theta_{\max}} \int_{\varphi_{\min}}^{\varphi_{\max}} \sin(\theta) \, \mathrm{d}\theta \, \mathrm{d}\varphi}{N_{\text{total}}} \left(n(\text{strip}) \pm \sqrt{n(\text{strip})} \right) \tag{4.34}$$

$$\approx 1.47522 \cdot 10^{-8} \, \text{sr} \left(n(\text{strip}) \pm \sqrt{n(\text{strip})} \right) \tag{4.35}$$

Angular calibration of p-side strips

The angular calibration for the DSSD's p-side strips is derived using the same simulation data as for the effective solid angle. Instead of just accumulating the hits per strip, the mean laboratory scattering angle per strip is extracted (as an uncertainty, the standard deviation of the mean value is used). In case of simulations with slit aperture, the vanishing acceptance does not allow to deduce the angular calibration for the whole detector. The calibration function is then extrapolated by fitting a first order polynomial to the last ten available strips. The resulting calibration functions are shown in figure 4.22.

Propagation of uncertainties

The angular calibrations and the correction functions for the effective solid angle is determined for each element of the output vectors from the previous section 4.5.2. Figure 4.22 illustrates the variations of these calibration functions which are a consequence of the uncertainties in the input quantities. The error bars related to the individual function are shown in figure 4.22 exemplary for one randomly chosen function.

In the next step, the vector of all angular calibrations and effective solid-angle functions will be used to obtain a vector of experimental cross sections. This way, the uncertainties of the whole angular calibration are effectively propagated into the cross sections.
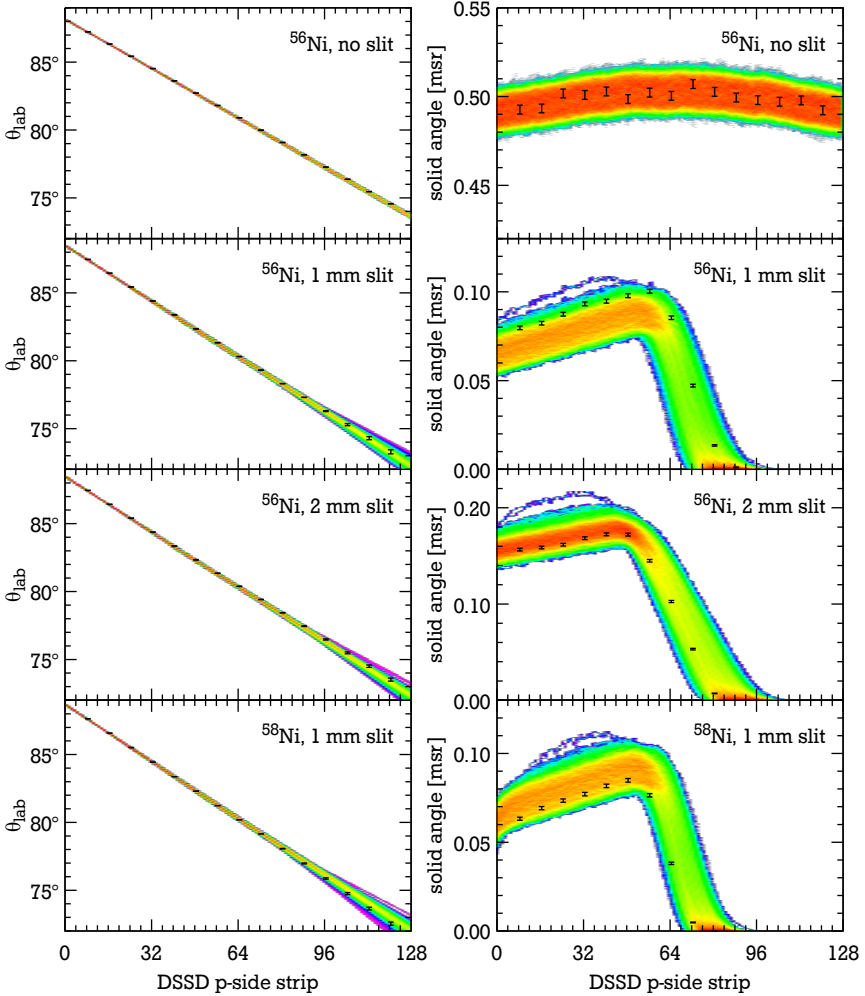
Figure 4.22.: Vector of all angular calibrations (*left*) and effective solid-angle functions (*right*) represented by histograms. The plots for ^{58}Ni beam without slit aperture are visibly indistinguishable from the case of ^{56}Ni which is shown here. The points show the error bars of a single function which was randomly chosen from the vector (a point for every eighth strip is drawn).

4.6 Experimental cross sections

The first step on the way to extract the cross section for elastic proton scatter-ing is to discriminate the elastic events from random background events and from events stemming from inelastic reaction channels. This is done by applying a two-dimensional cut to the correlation plots between the DSSD p-side strip and the reconstructed energy of the recoil proton. In figure 4.23 all correlation plots are shown together with their respective cuts on the elastic events. As already men-tioned before, without the slit aperture it is not possible to kinematically separate inelastically scattered events from elastically scattered ones. However, the data will still be further analysed as the contribution of the inelastic scattering only becomes significant in the region of the first minimum of the elastic cross section. More-over, due to the kinematics of inelastic scattering, there is no contamination below a certain momentum transfer at all (see the simulation in figure 3.8). The counts within the cuts can now be plotted either as a function of detector segment or as a function of energy. With respect to the kinematics, both distributions contain the same information and would be equivalent. However, since there is only an indi-rect energy calibration available for the Si(Li) detectors, the calibration for energies above $\approx 6\,\mathrm{MeV}$ might feature systematical deviations in the order of a few percent (see section 4.2). Additionally, the radiation damages in the DSSD caused a drift of the energy versus time in some experimental runs (see section 3.8). Therefore, the number of counts per p-side segments will be used as a basis for the experimental cross sections. The thus extracted angular distributions are plotted in figure 4.25.

It should be mentioned at this point, that the position information by the n-side strips ($\propto$ azimuthal scattering angle) was not utilised here. Because of the fairly large distance between the detector and the target together with the moderate pitch of the p-side strips, the azimuthal dependence can be neglected.

Background correction

The two-dimensional correlation plots in figure 4.23 show – besides the kine-matical bands – a background of mostly uncorrelated events. Possible sources of those events are manifold. In the region below the kinematical band of elastic scattering there is a contribution by events from inelastic scattering to higher ly-ing excited states which might not be resolved as bands any more. While this is, strictly speaking, not background, it contributes visually to it. Also, events from nu-clear reactions, like knock-out reactions (($p,2p$), (p,pn), etc.), can be found in this region. In the region above elastic scattering, a significant amount of background events is visible only in the cases where the slit aperture was used – possibly caused
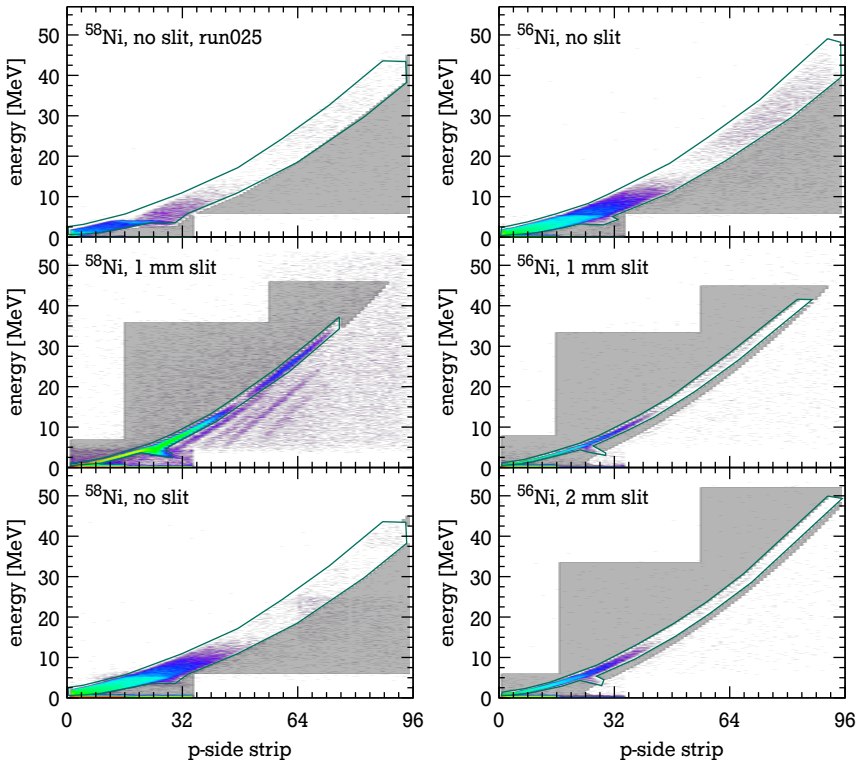
Figure 4.23.: Kinematic correlations together with two-dimensional cuts (*green*) for elastic scattering. The background was estimated from the grey area.

by small angle scattering at the slit plate. Another source, independent of the slit aperture and in comparison weaker, is due to the interaction of the ion beam with the residual gas in the interaction chamber. These events as well as events due to small angle scattering at the slit plate are expected to occur in the region below the elastic band as well.

The goal of the background correction is to estimate the number of background events contributing to the peak of interest and to subtract them from the latter. A straight forward approach to solve this problem would be to count the background events in a region nearby the peak of interest. However, since the density of background events is fairly low, large statistical fluctuations are expected. To get around this problem, a different approach was chosen. In case of measurements with slit aperture, the respective first excited states are well separated from the elastic band.
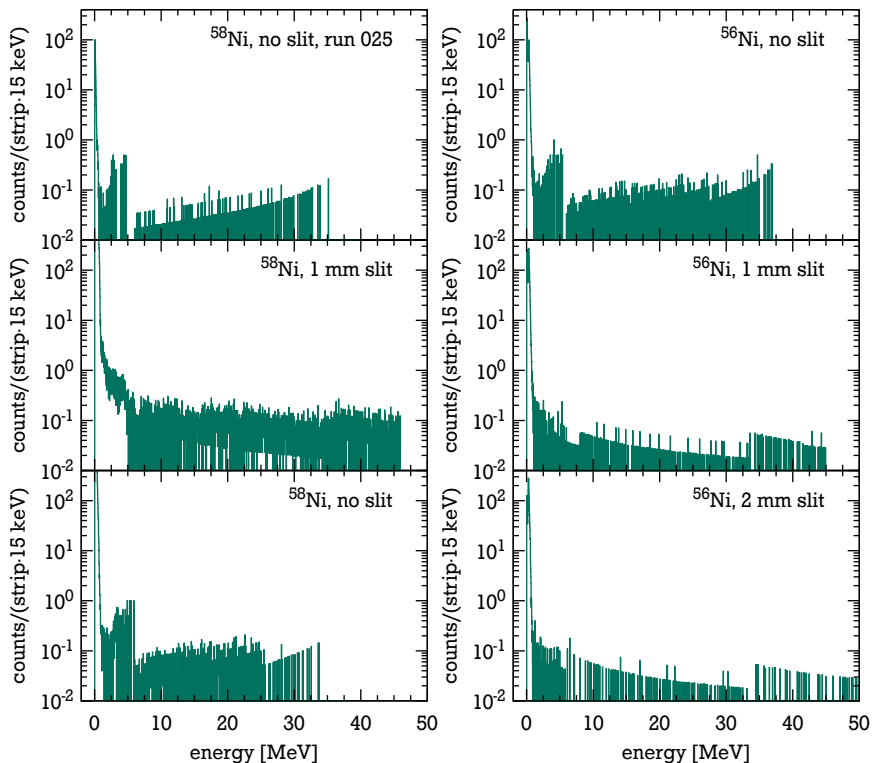
Figure 4.24.: Estimated background per strip as a function of the energy.

Hence, it can be assumed that the background contribution to the elastic band consists only of uncorrelated events caused by small angle scattering at the slit plate and scattering at the residual gas. The region was further limited by excluding the cut for the elastic band and regions where the detection system had no acceptance. The resulting background cuts are illustrated by grey areas in figure 4.23. Assuming that the statistics of the background events within the background cut depends mostly on the energy and that its angular dependence is negligible, the whole background is summed up as a function of the energy which is plotted in figure 4.24.

In the cases where the slit aperture was not used, a different procedure had to be applied. As described before, there is no significant background visible in the region above the elastic band. Since the angular resolution is not sufficient enough to resolve the kinematical band corresponding to the first excited state, the back-
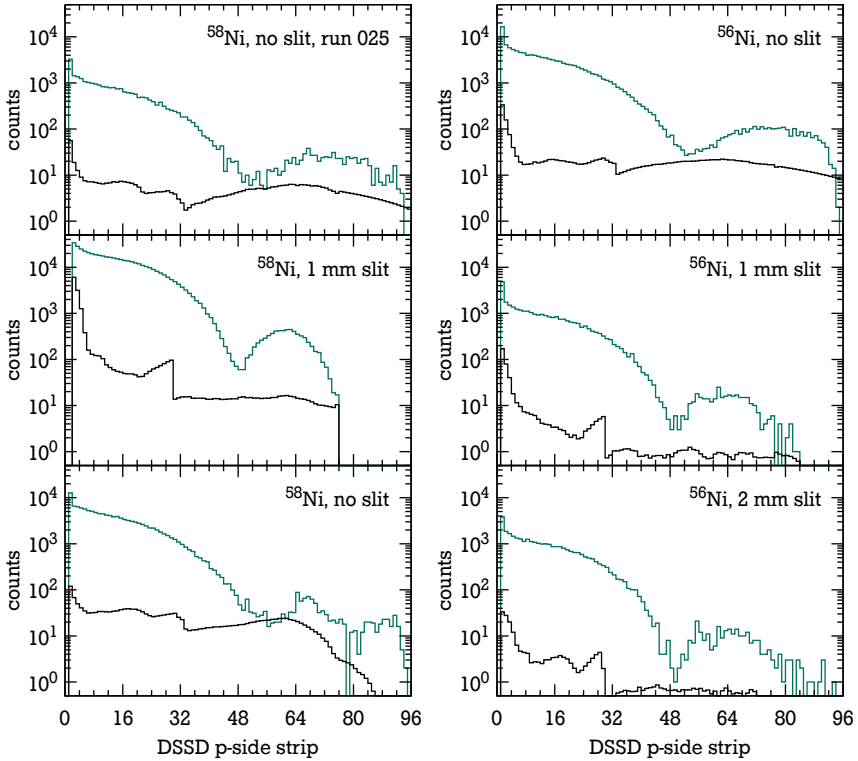
Figure 4.25.: Angular distributions for ^{58}Ni(p,p) and ^{56}Ni(p,p) as a function of the DSSD's p-side strip (*green*) together with the estimated background (*black*).

ground contribution will be estimated from the region below the elastic scattering (see the grey areas in figure 4.23 and the corresponding projections in figure 4.24). It is expected that this procedure slightly overestimates the background since the overlap between the kinematical bands of elastic and inelastic scattering to the first excited state will not be a hundred percent (see figure 3.8).

In order to get a final estimation of the number of background events per p-side strip, the background functions (figure 4.24) are integrated over the region of the elastic cut. The number of background counts as a function of the p-side strip is plotted in figure 4.25 together with the respective angular distributions. In comparison with the angular distributions, the background gives significant contributions only in the region of the minimum. Since this is only a small region, the

4. Data analysis

assumption of an angular independent background can be justified. Compared to the measurements with slit aperture, the background for the measurements without aperture seems to be slightly overestimated. Nevertheless, this only affects the angular distribution in the region of the minimum.

Calculation of the experimental cross section

With the help of equation (4.25), the experimental cross section $\mathrm{d}\sigma/\mathrm{d}\Omega$ of a detector segment with the mean angle θ can be calculated if the integrated luminosity $\mathscr{L}_{\text{int}}$ and the number of events N_i minus the background counts N_{bgr} in a given solid angle Ω_i are known, i. e.

$$\frac{\mathrm{d}\sigma}{\mathrm{d}\Omega} = \frac{N_i - N_{\text{bgr}}}{\Omega_i\,\mathscr{L}_{\text{int}}}\ . \tag{4.36}$$

For practical reasons, the cross section will be expressed as a function of the Lorentz-invariant four-momentum transfer t instead. The conversion can be done in the following way:

$$\frac{\mathrm{d}\sigma}{\mathrm{d}t} = \frac{\mathrm{d}\sigma}{\mathrm{d}\Omega}\frac{\mathrm{d}\Omega}{\mathrm{d}t}$$

Using the fact that the solid angle is given by

$$\mathrm{d}\Omega = \sin\theta\ \mathrm{d}\theta\ \mathrm{d}\varphi = -2\pi\ \mathrm{d}\cos\theta\ ,$$

one finally gets

$$\frac{\mathrm{d}\sigma}{\mathrm{d}t} = -2\pi\frac{\mathrm{d}\sigma}{\mathrm{d}\Omega}\frac{\mathrm{d}\cos\theta}{\mathrm{d}t}\ . \tag{4.37}$$

The derivative $\mathrm{d}\cos\theta/\mathrm{d}t$ can be calculated directly from equation (A.6) found in the appendix A. Combining equations (4.36) and (4.37) allows to calculate the experimental cross section:

$$\frac{\mathrm{d}\sigma}{\mathrm{d}t} = -2\pi\frac{\mathrm{d}\cos\theta}{\mathrm{d}t}\frac{N_i - N_{\text{bgr}}}{\Omega_i\,\mathscr{L}_{\text{int}}} \tag{4.38}$$

With the angular calibrations from the section 4.5, a laboratory scattering angle θ can be assigned to the p-side strip of the DSSD. Then, by using equation (A.10) (see appendix A) θ can be converted into t.

For each element from the vector of all angular calibrations (see figure 4.22), an individual cross section will be calculated using equation (4.38). The uncertain-
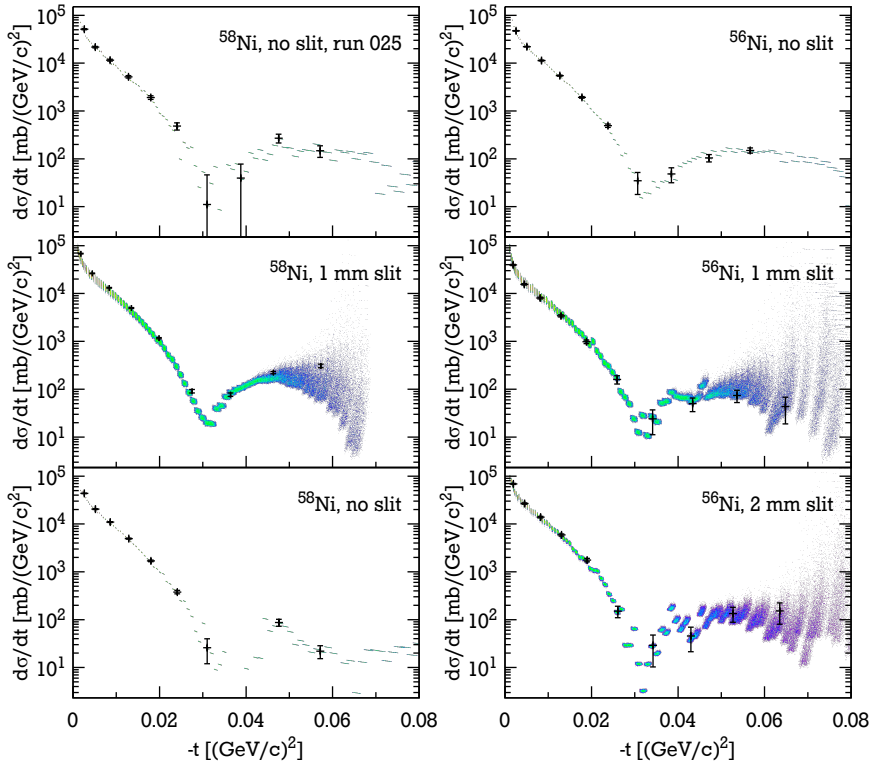
Figure 4.26.: Vector of experimental cross sections for the different experimental runs. The histograms show the variations of the cross sections which are caused by applying the vector of angular calibrations from figure 4.22 to the angular distributions from figure 4.25. The error bars are drawn for every eighth point of one cross section randomly chosen from the vector.

ties of such a single cross section are propagated in a standard Gaussian way. This covers the statistical uncertainties of the angular distribution and the background, the statistical uncertainties of the single angular calibrations and the error in the luminosity measurement. Figure 4.26 shows the full vector of cross sections (represented by histograms) and an exemplary cross section with error bars which was randomly chosen from the corresponding vector. Again, the idea is to propagate the uncertainties which are related to the experimental geometry by analysing each element of the vector individually.
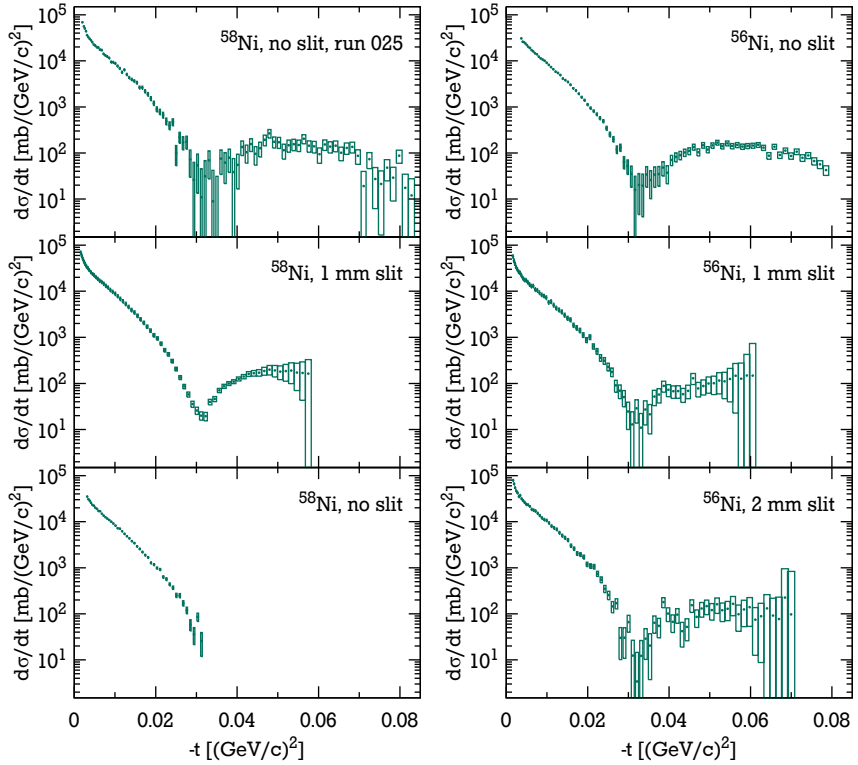
Figure 4.27.: Mean cross sections derived from the cross sections of figure 4.26. The uncertainties are represented by the length of the edges.

Additionally, a single average cross section is derived from the vectors in figure 4.26. Therefore, a sum distribution of all data points belonging to one strip is calculated by taking into account the uncertainties of the individual cross sections as well. For this sum distribution, the mean value and the standard deviation of t and $d\sigma/dt$ are calculated. Some detector strips at the end of the cross sections, i. e. towards higher momentum transfer, were removed in this step and also in the further analysis. The limits for this were set by visual judgement. In the case of the long measurement with ^{58}Ni beam and without aperture, more strips had to be removed. At the time of this measurement, the trigger thresholds were not yet properly adjusted which resulted in an insufficient trigger efficiency for the region after the diffraction minimum. The mean cross sections are plotted in figure 4.27 and can be found tabulated in appendix B.

5 Theoretical background

For the analysis of the cross sections for elastic proton scattering on ^{56}Ni and ^{58}Ni, which were presented in the previous chapter, the Glauber multiple-scattering theory will be used. It allows to extract the nuclear matter distribution from elastic proton-scattering experiments. A brief introduction into the Glauber formalism will be given in section 5.1. For the analysis it is necessary to parametrise the nuclear matter density. The models used in the present analysis will be described in section 5.2.

5.1 Glauber multiple-scattering theory
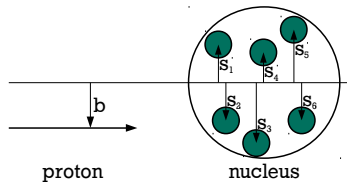
Figure 5.1.: Schematic illustration of the proton-nucleus interaction.

The Glauber multiple-scattering theory accurately describes the high-energy nucleon scattering on nuclei. Over the years it became a well established method in the analysis of proton scattering-experiments at intermediate energies ($\lesssim 1\,\text{GeV}$). In the following, a description of the key ideas of the Glauber formalism based on [2] and [3] will be given. Detailed information can be found in the two references and the references therein. A more thorough treatment of nuclear scattering theory in general can be found in [90]. It should be noted that, for reasons of simplicity, a unit system with $c = \hbar = 1$ will be used throughout this chapter.

Within the Glauber multiple-scattering theory, the nucleon-nucleus scattering amplitude is calculated in the *adiabatic approximation*. For high enough energies of the incident nucleon, it passes through the target nucleus in such a short time that the movement of the target nucleons can be neglected. Hence, the target nucleons appear mainly as stationary spectators which effectively reduces the scattering problem to a sequence of two-body interactions. It is also assumed that the trajectory of the projectile inside the nucleus can be represented by a straight line which is known as the *eikonal approximation*. This, as well, is justified for sufficiently high incident energies and small scattering angles.

Ultimately, it is assumed that the particle's total eikonal phase after passing through the nucleus at a fixed impact parameter is equal to the sum of phase shifts it would gain from scattering on individual free nucleons.

The scattering process of an incident particle with initial and final momenta $\mathbf{k}_i$ and $\mathbf{k}_f$ scattering on an A-nucleon system transforms the system from an initial state $\Psi_i(\mathbf{r}_1, \ldots, \mathbf{r}_A)$ to a final state $\Psi_f(\mathbf{r}_1, \ldots, \mathbf{r}_A)$. The corresponding scattering amplitude $F'_{fi}(\mathbf{q})$ can be written as

$$F'_{fi}(\mathbf{q}) = \frac{ik}{2\pi} \int d^2 b \, e^{i\mathbf{q}\mathbf{b}} \, \Psi_f^*(\mathbf{r}_1, \ldots, \mathbf{r}_A) \Gamma(\mathbf{b}, \mathbf{r}_1, \ldots, \mathbf{r}_A) \Psi_i(\mathbf{r}_1, \ldots, \mathbf{r}_A) \prod_{j=1}^{A} d^3 r_j . \quad (5.1)$$

In this process, a momentum $\mathbf{q} = \mathbf{k}_i - \mathbf{k}_f$ is transferred to the system. The scattering angle in the centre-of-mass system (CM) is connected through the wave number $k = |\mathbf{k}_i| = |\mathbf{k}_f|$ to the momentum transfer via $q = |\mathbf{q}| = 2k\sin(\theta/2)$ if the recoil of the target is neglected. The function $\Gamma(\mathbf{b}, \mathbf{r}_1, \ldots, \mathbf{r}_A)$ is the so-called *profile function* for the nucleon positions $\mathbf{r}_1, \ldots, \mathbf{r}_A$, i.e.

$$\Gamma(\mathbf{b}, \mathbf{r}_1, \ldots, \mathbf{r}_A) = 1 - \exp[i\chi(\mathbf{b}, \mathbf{r}_1, \ldots, \mathbf{r}_A)] \quad (5.2)$$

with the total eikonal phase χ. As mentioned before, it is expressed as the sum of phases χ_j which are due to the scattering of individual nucleons:

$$\chi(\mathbf{b}, \mathbf{r}_1, \ldots, \mathbf{r}_A) = \sum_{j=1}^{A} \chi_j(\mathbf{b} - \mathbf{s}_j) \quad (5.3)$$

The vector $\mathbf{s}_j$ is a projection of the nucleon position $\mathbf{r}_j$ onto the plane determined by the vector of the impact parameter $\mathbf{b}$ and the average momentum $\mathbf{k}_0 = (\mathbf{k}_i + \mathbf{k}_f)/2$ (see also figure 5.1):

$$\mathbf{s}_j = \mathbf{r}_j - \frac{\mathbf{k}_0}{\mathbf{k}_0^2} (\mathbf{r}_j \cdot \mathbf{k}_0) \quad (5.4)$$

The individual nucleon-nucleon phase shift χ_j is connected to the nucleon profile function $\gamma_j(\mathbf{b})$

$$\gamma_j(\mathbf{b}) = 1 - \exp[i\chi_j(\mathbf{b})] \quad (5.5)$$

by the scattering amplitude for the free nucleon-nucleon scattering

$$f_j(\mathbf{q}) = \frac{\mathrm{i}k'}{2\pi} \int \mathrm{d}^2b \, \mathrm{e}^{-\mathrm{i}\mathbf{qb}} \, \gamma_j(\mathbf{b}) \,. \tag{5.6}$$

Here, k' is the wave number in the two particle CM system. Hence, the nucleon profile function can be calculated from the nucleon-nucleon scattering amplitude by an inverse Fourier transformation, i. e.

$$\gamma_j(\mathbf{b}) = \frac{1}{2\pi\mathrm{i}k'} \int \mathrm{d}^2q \, \mathrm{e}^{\mathrm{i}\mathbf{qb}} \, f_j(\mathbf{q}) \,. \tag{5.7}$$

By assuming an independence of the spin- and isospin-amplitude, equations (5.6) and (5.7) can be re-written using the Bessel function $J_0(x)$

$$f(\mathbf{q}) = \mathrm{i}k \int_0^\infty J_0(qb) \, \gamma(b) \, b \, \mathrm{d}b \,, \tag{5.8}$$

$$\gamma(\mathbf{b}) = \frac{1}{\mathrm{i}k} \int_0^\infty J_0(q'b) \, f(q') \, q' \, \mathrm{d}q' \,. \tag{5.9}$$

With this, the nuclear profile function (5.2) can be written as

$$\Gamma(\mathbf{b}, \mathbf{r}_1, \ldots, \mathbf{r}_A) = 1 - \prod_{j=1}^A \left[1 - \gamma(\mathbf{b} - \mathbf{s}_j) \right] \,, \tag{5.10}$$

which is known as the Glauber combination law for profile functions. By expanding equation (5.10) in powers of γ, a multiple scattering series with A-terms can be created. The individual terms correspond to terms for single scattering, double scattering and so on. Terms for re-scattering, i. e. scattering on the same nucleon for more than one time, are not included. However, it is expected that they give only small contributions for high incident energies.

By introducing CM and relative coordinates

$$\mathbf{R} = \frac{1}{A} \sum_{j=1}^A \mathbf{r}_j \qquad\qquad \mathbf{S} = \frac{1}{A} \sum_{j=1}^A \mathbf{s}_j \tag{5.11}$$

$$\mathbf{r}'_j = \mathbf{r}_j - \mathbf{R} \qquad\qquad \mathbf{b}' = \mathbf{b} - \mathbf{S} \tag{5.12}$$

the scattering amplitude can be transformed into

$$F_{fi}(\mathbf{q}) = \frac{\mathrm{i}k}{2\pi} \int \mathrm{d}^2 b' \, \mathrm{e}^{\mathrm{i}\mathbf{q}\mathbf{b}'} \, \Gamma(\mathbf{b}', \mathbf{r}'_1, \ldots, \mathbf{r}'_A) \, \rho_A^{fi}(\mathbf{r}'_1, \ldots, \mathbf{r}'_A) \prod_{j=1}^{A} \mathrm{d}\mathbf{r}'_j \; . \qquad (5.13)$$

Here, ρ_A^{fi} is the nuclear many-body transition density. The scattering amplitude for elastic scattering, where the initial and the final states are identical, i. e. $f = i$, may be estimated by assuming independent particles. When all correlations between the nucleon positions are neglected, the many-body density can be expressed as a product of one-body densities

$$\rho_A^{ii}(\mathbf{r}_1, \ldots, \mathbf{r}_A) = \prod_{j=1}^{A} \rho_1(\mathbf{r}_j) \; . \qquad (5.14)$$

The nuclear many-body density ρ_A^{ii} is the probability distribution of finding the nucleons at positions $\mathbf{r}'_1, \ldots, \mathbf{r}'_A$. Summation of the scattering series then yields a simpler form of the scattering amplitude

$$F_{ii}(\mathbf{q}) = \frac{\mathrm{i}k}{2\pi} \int \mathrm{d}^2 b \, \mathrm{e}^{\mathrm{i}\mathbf{q}\mathbf{b}} \left[1 - \left(1 - \Gamma_1^{ii}(\mathbf{b}) \right)^A \right] \qquad (5.15)$$

with the corresponding profile function

$$\Gamma_1^{ii}(\mathbf{b}) = \int \gamma(\mathbf{b} - \mathbf{s}) \, \rho_1(\mathbf{r}) \, \mathrm{d}\mathbf{r} \; . \qquad (5.16)$$

Eventually, the differential cross section in the CM frame can be calculated using

$$\frac{\mathrm{d}\sigma}{\mathrm{d}\Omega} = |F_{ii}(\mathbf{q})|^2 \; . \qquad (5.17)$$

Hence, for a given one-body density distribution, only the scattering amplitudes for free nucleon-nucleon scattering are needed to calculate the differential cross section. They can be expressed in a parametrised form which will be discussed in section 5.1.1.

Coulomb interaction
So far the nucleons were only interacting via the strong force with each other. However, the Coulomb interaction of charged particles plays an important role, too.

Especially at low momentum transfer, where the strong and the electromagnetic force interfere coherently, the contribution of the Coulomb interaction has to be taken into account in order to describe the elastic proton-scattering cross sections.

Therefore, the phase shift for proton-proton scattering χ_p is considered as the sum of phase shifts χ_p^S from pure strong interaction and χ_p^C from pure Coulomb interaction, i. e.

$$\chi_p(\mathbf{b}) = \chi_p^S(\mathbf{b}) + \chi_p^C(\mathbf{b}) \; . \tag{5.18}$$

The scattering amplitude for proton-nucleus scattering can then be calculated by assuming that the total nuclear phase shift is caused by the sum of the phase shift due to the strong interaction and the phase shift which occurs from the interaction with an averaged Coulomb field.

Centre-of-mass correlations

In the previous derivation of the elastic scattering cross section, correlations between the target nucleons were neglected. To take these correlations into account, correction terms may be applied in the calculation of the cross section. Besides correlations which arise from the separation of nucleons into shells and from the antisymmetrisation procedure due to the Pauli principle, short-range correlations and clustering correlations due to α-clustering of the nuclear matter and eventually the *centre-of-mass correlations* are important. While the former correction terms give mostly minor contributions, the latter has sizeable effects on the cross section. It is especially important for light nuclei but the effects do not vanish even for heavy nuclei like ^{208}Pb.

The corrections for the centre-of-mass motion in the nucleus may be applied by multiplying the nuclear scattering amplitude (5.15) by a correction factor

$$H_{CM}(\mathbf{q}) = \mathrm{e}^{\frac{\mathbf{q}^2 r_m^2}{6(A-1)}} \; . \tag{5.19}$$

Here, $r_m \equiv \left\langle r_m^2 \right\rangle^{1/2}$ is the nuclear **R**oot-**M**ean-**S**quare (RMS) radius. It is defined as the second momentum of the matter-density distribution $\rho(\mathbf{r})$ [91]. If the density distribution is normalised to unity and spherical symmetry is assumed, i. e.

$$\int \rho(\mathbf{r}) \, \mathrm{d}^3 r = 4\pi \int_0^\infty r^2 \rho(r) \, \mathrm{d}r \equiv 1 \; , \tag{5.20}$$

the second momentum can be calculated with

$$\left\langle r_m^2 \right\rangle^{1/2} = \sqrt{\int r^2 \rho(\mathbf{r}) \, \mathrm{d}^3 r} = \sqrt{4\pi \int_0^\infty r^4 \rho(r) \, \mathrm{d}r} \; . \qquad (5.21)$$

The correction (5.19) gives exact results for Gaussian density distributions, only. For non-Gaussian density distributions, the correction is still relatively accurate up to the second diffraction maximum of the proton-nucleus differential cross section.

5.1.1 The free nucleon-nucleon scattering amplitudes

It was shown in the description of the Glauber multiple-scattering theory, that the free nucleon-nucleon scattering amplitudes are needed for the calculation of the p-nucleus cross section.

The free pp and pn (short: pN) scattering amplitudes consist of a central part, i. e. the scalar part stemming from the strong interaction, and a vector part, which describes the influence of spin-orbit and spin-spin interaction. Especially the latter part is experimentally uncertain [2]. However, it has been shown in [2] that the contributions of the vector part at an incident energy of 1 GeV are rather small. Neglecting the vector part, the pN scattering amplitude can be parametrised in the usual form using the central part, only:

$$f_{pN}(\mathbf{q}) = \frac{k\sigma_{pN}}{4\pi} \left(\epsilon_{pN} + \mathrm{i} \right) \mathrm{e}^{-\frac{\mathbf{q}^2 \beta_{pN}}{2}} \qquad (5.22)$$

The parameters in equation (5.22) can be extracted from nucleon-nucleon scattering experiments. The total cross sections σ_{pp} and σ_{pn} are experimentally well determined. In figure 5.2, the experimental data in the intermediate energy range are shown. A parametrisation of the data was achieved by fitting a polynomial to the experimental data points. The error bands were estimated by fitting the experimental data points with their individual uncertainties added and subtracted.

The parameter ϵ_{pN} corresponds to the ratio between the real and the imaginary part of the scattering amplitude. The experimental values for ϵ_{pp} are taken from [92] while the values for ϵ_{pn} came from [4]. The latter are obtained with the help of dispersion relations. In both cases, the points were parametrised by fitting a polynomial to the data. This time, however, the error band was estimated from the error band of the fit at a 1σ level (see figure 5.3).

For the *slope parameter* β_{pN} only scarce data are available. Moreover, values determined by analysing the shape of the differential cross sections and values from
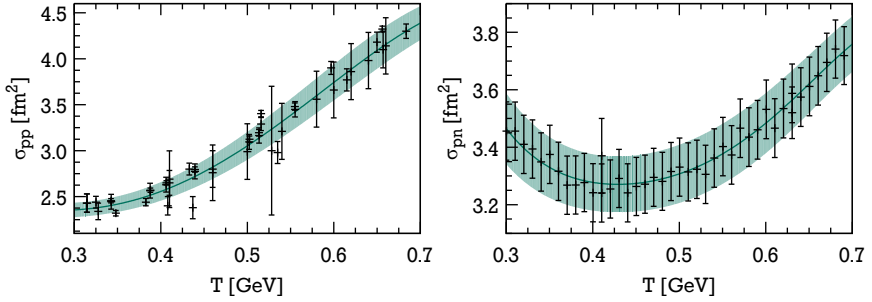
Figure 5.2.: Total cross sections σ_{pN} for free nucleon-nucleon scattering as a function of the total kinetic energy T [92].
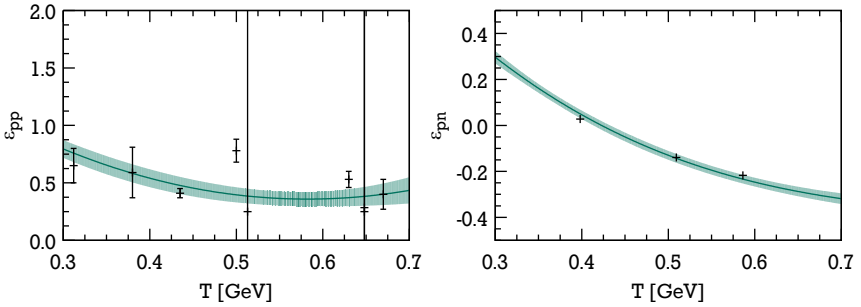
Figure 5.3.: Ratio between the real and the imaginary part of the nucleon-nucleon scattering amplitude (ϵ_{pp} from [92], ϵ_{pn} from [4]) as a function of the total kinetic energy T. For ϵ_{pn} no error bars are given in [4].
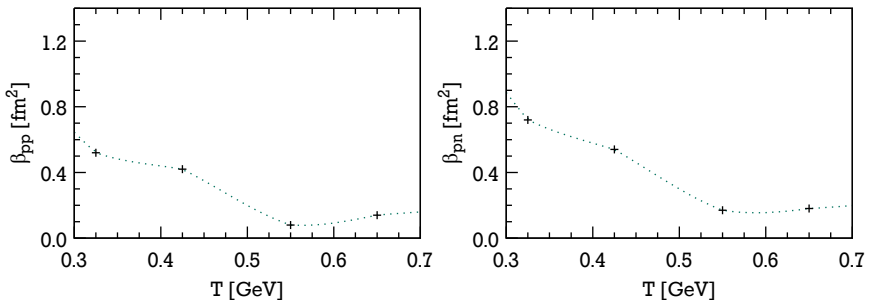
Figure 5.4.: Slope parameter β_{pN} of the nucleon-nucleon scattering amplitude as a function of the total kinetic energy T [93]. The lines are to guide the eye.

phase shift analyses differ from each other. This is the case especially for energies below 1 GeV where the contribution from the spin terms is larger [2]. The data shown in figure 5.4 are just for reference purpose and has not been used during the analysis. Instead, an effective value for β_{pN} was extracted from the measured cross section for elastic proton scattering on ^{58}Ni (see sections 5.1.2 and 6.1).

5.1.2 Software implementation

For the analysis of the present experiment, an existing software implementation of the Glauber multiple-scattering formalism was used. The code was originally written for the analysis of elastic proton-scattering experiments with light-ions at energies of 700 MeV [4, 5, 6]. The cross section is calculated as a function of the Lorentz-invariant four-momentum transfer $t = -\mathbf{q}^2$ given in units of $(\text{GeV}/c)^2$. Consequently, the differential cross section is given as $\mathrm{d}\sigma/\mathrm{d}t$ with the unit $\text{mb}/(\text{GeV}/c)^2$. The conversion from laboratory or centre-of-mass frame is explained in the appendix A.

With this software, information about the radial matter density can be extracted from the experimental cross section by varying the free parameters of a phenomenological density distribution until the calculated cross sections describe the experimental ones best. The calculation of the cross sections considers the Coulomb interaction and CM corrections like previously described. Via different settings in the programme, either the point density (assuming point-like nucleons) or the folded density (taking into account the size of the nucleon) can be extracted.

As a consequence of its original purpose, the programme implemented mostly density-distribution models suitable for light nuclei. The sum-of-Gaussians method (see section 5.2.3) was not implemented. Therefore, the original code, written in *Fortran*, was translated into *Mathematica* in order to allow an easy implementation of the missing functionality. Thereby, the subroutines which calculate the differential cross section were not altered. However, the original code used Riemann sums to numerically calculate the integrals on an equidistant grid. For reasons of speed, the latter was not changed but the higher order *Boole's rule* is now used for a more precise numerical integration [94]. The original libraries used for the fitting were replaced by Mathematica's *NonlinearModelFit* routines.

Another consequence of the software's heritage is that only the scalar part of the free nucleon-nucleon scattering amplitude is considered and the contributions from the vector part, i.e. spin-orbit and spin-spin interactions, are neglected (see section 5.1.1). While this can be justified for incident energies close to 1 GeV used in the earlier experiments, the vector part has an effect at the lower energies used now [2]. However, it is suggested in [4] that the use of effective values for the slope

　　　　　　　　　　　　　　　　　5. Theoretical background

parameter β_{pN} may take the neglected spin effects into account. This effective value is estimated by fitting the experimental proton-nucleus cross section for a nucleus with an already known matter density distribution (see section 6.1).

5.2 Parametrisations of the nuclear matter density

The nuclear matter distribution $\rho(r)$ is connected to the elastic p-nucleus cross section via a Fourier transformation and hence, the full information about $\rho(r)$ can only be extracted from a cross section which was measured from zero to infinite momentum transfer q. In a realistic scenario where the cross section is deduced within a finite interval of $[q_{min}, q_{max}]$, only the amplitudes of the Fourier components of $\rho(r)$ within the interval of wavelengths of $[2\pi/q_{min}, 2\pi/q_{max}]$ can be extracted from the data [95]. This makes it necessary to describe the radial density distribution by a phenomenological model. The model effectively imposes assumptions about the Fourier components of $\rho(r)$ which are not accessible in the experiment.

An example of such a phenomenological model, suitable for a wide range of medium to heavy nuclei, is the well known two-parameter Fermi function. Often, the traditional Fermi function is extended by a third parameter. A detailed description of these models is given in sections 5.2.1 and 5.2.2 for the two-parameter and the three-parameter form, respectively.

It has to be kept in mind that a density distribution which has been deduced with a certain phenomenological model contains a systematic error due to implicit assumptions of the model about the amplitudes of the Fourier components of $\rho(r)$ which are experimentally missing. A way to estimate these uncertainties could be to use many different model descriptions and to derive the error bars as an envelope around the individual errors like it was done in [6]. However, the limitation can only be fully avoided by a model independent analysis. If the experimental cross section was measured over a large enough q range, for example a **S**um-**O**f-**G**aussians (SOG) description of the nuclear density can be used [96]. While the SOG model is not fully model independent either, it is transparent in its assumptions and the shape of the radial density is not a priori defined. The method is discussed in more detail in section 5.2.3.

5.2.1 Symmetrised Fermi distribution
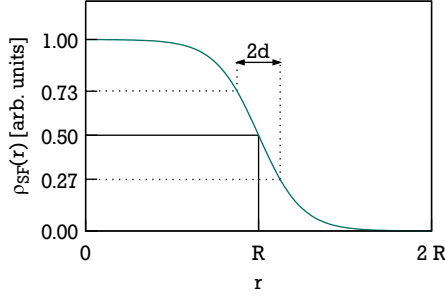
Figure 5.5.: Symmetrised Fermi distribution.

The general properties of the radial density distribution of nuclear matter can be described by a two-parameter Fermi distribution (2pF):

$$\rho_{2pF}(r) = \rho_0 \frac{1}{1 + \exp\left(\frac{r-R}{d}\right)} \tag{5.23}$$

It features a flat central part with a half-density radius of R and a diffuse but somewhat narrow surface of which the thickness is controlled by the diffuseness parameter d. The model however comes with the disadvantage, that its derivative is not zero for $r = 0$. This causes the radial density to have a cusp in the centre. While it is not exactly crucial for heavier nuclei where $R \gg d$, it can be completely avoided by using the so-called symmetrised Fermi function (SF):

$$\rho_{SF}(r) = \rho_0 \frac{\sinh\left(\frac{R}{d}\right)}{\cosh\left(\frac{r}{d}\right) + \cosh\left(\frac{R}{d}\right)} \tag{5.24}$$

For more information on mathematical properties and the history of the symmetrised Fermi function see [97] and references therein. The meaning and interpretation of the two parameters R and d is identical at least for $R \gg d$.

The normalisation factor ρ_0 can be determined with the condition:

$$\iiint \rho(r)\, r^2 \sin\theta \; d\theta \; d\varphi \; dr = 4\pi \int_0^\infty \rho(r)\, r^2 \; dr \equiv 1 \tag{5.25}$$

Alternatively, the density can be normalised to the number of nucleons A, the number of protons Z or the number of neutrons N depending on whether it is a matter, charge or neutron density. In this work, however, all densities will be normalised to unity.

5.2.2 Three-parameter Fermi distribution
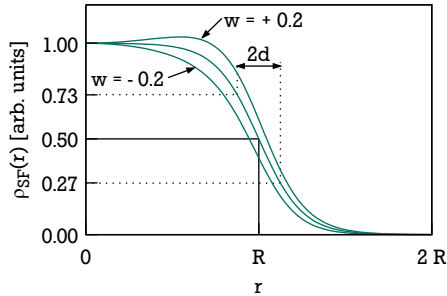
Figure 5.6.: Three-parameter Fermi distribution.

The two-parameter Fermi distribution is often extended by a third parameter w to the so-called three-parameter Fermi distribution (3pF):

$$\rho_{3pF}(r) = \rho_0 \frac{1 + w\frac{r^2}{R^2}}{1 + \exp\left(\frac{r-R}{d}\right)} \tag{5.26}$$

Because of the way the third parameter affects the shape of the distribution it is sometimes referred to as *wine-bottle parameter* [95]. With the parameter w, a relative lowering or enhancement of the central density can be achieved (see figure 5.6). However, the function of the parameter is not unambiguous since it also has a big influence on the density for larger radii $r > R$. For example, it is not clear whether a factor $w > 0$ is needed in the analysis to lower the density in the centre or to raise it at larger radii [96].

5.2.3 Sum-of-Gaussians distribution
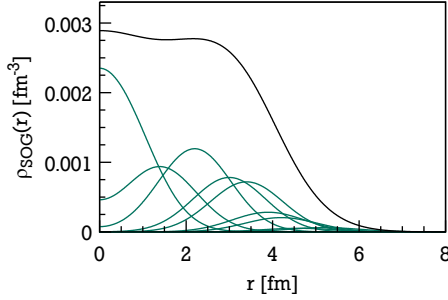
Figure 5.7.: Example for a **S**um-**O**f-**G**aussians (SOG) charge density distribution of ^{58}Ni (*black*) together with the individual Gaussians (*green*). (*based on data from* [95])

The **S**um-**o**f-**G**aussians (SOG) method was originally presented in [96] as a model independent method to derive charge distributions from cross sections of elastic electron scattering but was also successfully applied in conjunction with proton elastic scattering to derive matter density distributions [6].

In a strict formal interpretation, a model independent determination of the density distribution – may it be charge, neutron or total matter – is only possible if the respective cross section is measured over an infinite range of momentum transfer and hence, all amplitudes of the Fourier components of $\rho(r)$ are available. Since no such measurement exists, generality has to be restricted by some assumptions. These assumptions should be, however, transparent and based on physical argumentation. Hence, it is reasonable to assume that no structure in the density distribution is smaller than a certain limit. At the same time, the density at different radii should be decoupled from each other as much as possible. A way to fulfil both considerations is to represent the density distribution as a sum of independent Gaussians with a common width γ, i. e.

$$\rho_{SOG}(r) = \frac{1}{2\pi^{3/2}\gamma^3} \sum_{i=1}^{N} \frac{Q_i}{1+2R_i^2/\gamma^2} \left(e^{-(r-R_i)^2/\gamma^2} + e^{-(r+R_i)^2/\gamma^2} \right). \tag{5.27}$$

The amplitudes Q_i have to meet the conditions

$$Q_i \geq 0 \ \text{ and } \ \sum_{i=1}^{N} Q_i = 1 \tag{5.28}$$

5. Theoretical background

to ensure that $\rho(r) \geq 0$ and that $\rho(r)$ is normalised. It also guarantees that no arbitrarily small structures are obtained by interferences between different Gaussians. At the same time, the fact that the Gaussian function drops quite rapidly for increasing $|R_i - r|$ allows for the decoupling of neighbouring radii. The remaining model dependence lies in the width γ. Hence, the value should be physically justified. The most rigorous argument is probably that γ should be connected to the size of a single nucleon as no structure in the density is expected to be narrower than that. Another way would be to relate γ to the minimal widths of the peaks observed in the radial wave functions of the nucleus under investigation (an example is given in [96]).

The choice of the R_i could also introduce some model dependence. To avoid this, the R_i are chosen randomly and only the corresponding Q_i are fitted to reproduce the data. The procedure is then repeated for new sets of randomly chosen R_i. All fits which yield a reduced χ^2 of $\tilde{\chi}^2 \geq \tilde{\chi}^2_{\min} + 1$ are rejected and the remaining SOG densities are considered as possible density distributions. The superposition of these densities defines the density together with its uncertainties. For practical purposes, it is expected that about 100 fits, which meet the previous condition, are needed to derive the error band [96]. It is one of the virtues of the SOG method, that the error band is expected to cover the results of possible future experiments spanning a larger range of momentum transfer [96].

6 Nuclear matter densities and radii

In this chapter, the analysis of the cross section for elastic proton scattering on ^{56}Ni will be presented. The nuclear matter density and the matter radius will be extracted from the cross section using the Glauber multiple-scattering theory as described in chapter 5.1. First, it is necessary to determine effective values for the slope parameters β_{pp} and β_{pn} (short: β_{pN}) of the free nucleon-nucleon scattering amplitudes (see section 6.1). Once these values are known, the density distribution of ^{56}Ni can be determined in a model dependent way using the symmetrised Fermi (SF) parametrisation. The model independent Sum-of-Gaussians (SOG) parametrisation will then be used to estimate the systematic uncertainties in the extraction of the density distribution.

Throughout the whole work, the size of the nucleon was taken into account and hence, folded density distributions and matter radii are presented.

6.1 Determination of β_{pN}

As already outlined in section 5.1.1, data for the slope parameters β_{pp} and β_{pn} of the free nucleon-nucleon scattering amplitudes is very scarce. Therefore, the value for the slope parameters will be fitted to reproduce the experimental cross section of ^{58}Ni using an already known matter density distribution [4]. As outlined in section 5.1.2, using effective values for the slope parameters may also account for the spin effects which were neglected in the parametrisation of the nucleon-nucleon scattering amplitudes.

However, instead of using the radial matter density of ^{58}Ni, the SOG charge density from [95] will be used as reference. The reason for this choice is that the nuclear charge distributions are well known from model independent analyses of electron scattering data. Measurements of the neutron distributions of ^{58}Ni suggest that the difference between both is very small [10]. Also, the difference between the RMS charge and neutron radii is just 0.01 fm [9]. As will be shown later, this difference is well below what can be resolved in this experiment.

In accordance with [4], a common value β_{pN} will be derived by setting $\beta_{pp} \equiv \beta_{pn}$. Using the known density distribution, the cross section is calculated and fitted to the experimental cross section by varying β_{pN}. For the fit, the experimental cross section measured with the 1 mm slit was used. The uncertainties arising from the angular calibration are considered by fitting β_{pN} to each element of the vector of cross sections (see figure 4.26). To take into account also the
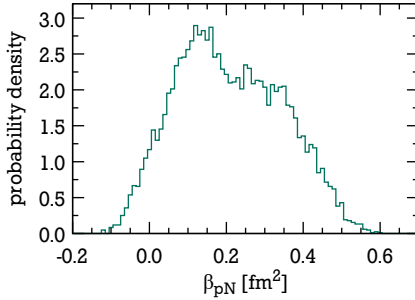
Figure 6.1.: Distribution of fitted β_{pN}. For details see text.

uncertainties of the remaining parameters of the free nucleon-nucleon scattering amplitude, these parameters were randomised for each individual fit according to their respective uncertainty (see section 5.1.1). Each cross section was therefore fitted four times with the parameters for the free nucleon-nucleon scattering amplitude randomised for every fit. This cumulated in about 8400 fits altogether which yielded a mean value of $\beta_{pN} = (0.21 \pm 0.14)\,\mathrm{fm}^2$ (figure 6.1). The covariance matrix of the five parameters was calculated in order to create a multivariate normal distribution which allows to sample correlated random numbers to be used in the later fits. The parameters which will be used in the further analysis are listed in table 6.1.

Since the ^{58}Ni cross section was used to fix β_{pN} here, the further analysis of this cross section should yield the matter density which was already put into the fit. Nevertheless, the analysis of the measured ^{58}Ni cross section will be carried out in parallel to ^{56}Ni.

	^{58}Ni	^{56}Ni
σ_{pp}	$(2.57 \pm 0.10)\,\mathrm{fm}^2$	$(2.53 \pm 0.10)\,\mathrm{fm}^2$
σ_{pn}	$(3.28 \pm 0.10)\,\mathrm{fm}^2$	$(3.28 \pm 0.10)\,\mathrm{fm}^2$
ϵ_{pp}	(0.53 ± 0.07)	(0.55 ± 0.08)
ϵ_{pn}	(0.04 ± 0.02)	(0.06 ± 0.02)
$\beta_{pp} = \beta_{pn}$	$(0.21 \pm 0.14)\,\mathrm{fm}^2$	$(0.21 \pm 0.14)\,\mathrm{fm}^2$

Table 6.1.: Parameters of the nucleon-nucleon scattering amplitude used in the analysis.

6.2 Model-dependent analysis – Symmetrised Fermi

The radial matter-density distributions of ^{56}Ni and ^{58}Ni were determined for each of the six experimental runs using the symmetrised Fermi density-parametrisation. The cross section which is calculated using the Glauber multiple-scattering theory is fitted to the experimental data by varying the two free parameters of the density distribution. An additional third parameter is needed for a global normalisation of the cross section. In figure 6.3, the results of fits to the mean cross sections (see figure 4.27) are shown. The corresponding best fit parameters are listed in table 6.2 (*single SF-fit*). The uncertainty of this fit reflects mostly the statistical uncertainty of the experimental cross section. In the following, this uncertainty will be referred to as the statistical uncertainty $\Delta_{\text{stat.}}$.

Because of the small number of free parameters, the fits are computed rather fast which allows to fit all 2100 cross sections from the vectors in figure 4.26. Hence it is possible to propagate the uncertainties of the angular calibration to the matter density. Another source of uncertainty are the parameters for the nucleon-nucleon scattering amplitude. Their contribution to the total uncertainty can also be estimated in a Monte Carlo approach. Therefore, the vector of cross sections is fitted three times, whereby the parameters for the nucleon-nucleon scattering amplitude are randomised for the fit of each individual cross section. Altogether, this leads to 6300 fits of which the results are listed in table 6.2 (*angular calibration and NN amplitude parameters*). In figure 6.3 the fitted density distributions are illustrated as histograms to give an impression of the possible variations caused by the uncertainties of the input variables. An average density and an error band is derived from the histograms by calculating the mean and the standard deviation at distinct radii r.

The uncertainties Δ_{SF} derived from the last fits reflect all known uncertainties except the systematic uncertainty from the model dependence of the density parametrisation. Under the assumption that the statistical uncertainties $\Delta_{\text{stat.}}$, the uncertainties from the angular calibration $\Delta_{\text{geom.}}$ and the uncertainties due to the nucleon-nucleon scattering-amplitude $\Delta_{\text{NNamp.}}$ are all independent of each other, the individual contributions can be unfolded from Δ_{SF}, i. e.

$$\Delta_{\text{SF}} \approx \sqrt{\Delta_{\text{stat.}}^2 + \Delta_{\text{geom.}}^2 + \Delta_{\text{NNampl.}}^2} \, . \tag{6.1}$$

Therefore, the cross sections were analysed again by firstly fitting the vector of cross sections with constant parameters for the nucleon-nucleon scattering amplitude and secondly fitting the mean cross section with randomised parameters for the nucleon-nucleon scattering amplitude. The best fit parameters are included

single SF-fit

measurement		normalisation	R [fm]	d [fm]	$\left\langle r_m^2 \right\rangle^{1/2}$ [fm]
^{56}Ni	no slit	0.82 ± 0.01	3.94 ± 0.02	0.59 ± 0.01	3.76 ± 0.01
^{56}Ni	1 mm slit	0.61 ± 0.01	3.97 ± 0.05	0.58 ± 0.03	3.76 ± 0.03
^{56}Ni	2 mm slit	0.90 ± 0.01	3.88 ± 0.05	0.63 ± 0.02	3.81 ± 0.02
^{58}Ni	no slit	0.80 ± 0.01	3.43 ± 0.08	0.76 ± 0.02	3.88 ± 0.02
^{58}Ni	no slit, run 025	0.80 ± 0.01	4.00 ± 0.05	0.60 ± 0.02	3.81 ± 0.02
^{58}Ni	1 mm slit	0.75 ± 0.01	4.23 ± 0.02	0.50 ± 0.02	3.77 ± 0.02

Monte Carlo SF-fits: angular calibration

measurement		normalisation	R [fm]	d [fm]	$\left\langle r_m^2 \right\rangle^{1/2}$ [fm]
^{56}Ni	no slit	0.82 ± 0.01	3.94 ± 0.03	0.59 ± 0.01	3.77 ± 0.02
^{56}Ni	1 mm slit	0.61 ± 0.05	3.94 ± 0.12	0.59 ± 0.06	3.76 ± 0.06
^{56}Ni	2 mm slit	0.90 ± 0.05	3.88 ± 0.12	0.62 ± 0.06	3.79 ± 0.06
^{58}Ni	no slit	0.80 ± 0.01	3.42 ± 0.08	0.76 ± 0.02	3.88 ± 0.02
^{58}Ni	no slit, run 025	0.80 ± 0.01	4.00 ± 0.06	0.60 ± 0.02	3.82 ± 0.02
^{58}Ni	1 mm slit	0.75 ± 0.07	4.18 ± 0.10	0.52 ± 0.06	3.79 ± 0.06

Monte Carlo SF-fits: NN amplitude parameters

measurement		normalisation	R [fm]	d [fm]	$\left\langle r_m^2 \right\rangle^{1/2}$ [fm]
^{56}Ni	no slit	0.82 ± 0.02	3.94 ± 0.04	0.59 ± 0.04	3.76 ± 0.07
^{56}Ni	1 mm slit	0.61 ± 0.02	3.97 ± 0.06	0.58 ± 0.04	3.76 ± 0.07
^{56}Ni	2 mm slit	0.90 ± 0.02	3.88 ± 0.07	0.63 ± 0.04	3.81 ± 0.07
^{58}Ni	no slit	0.80 ± 0.02	3.43 ± 0.16	0.76 ± 0.04	3.88 ± 0.06
^{58}Ni	no slit, run 025	0.80 ± 0.02	4.00 ± 0.06	0.60 ± 0.04	3.81 ± 0.07
^{58}Ni	1 mm slit	0.75 ± 0.02	4.24 ± 0.04	0.50 ± 0.04	3.77 ± 0.06

Monte Carlo SF-fits: angular calibration and NN amplitude parameters

measurement		normalisation	R [fm]	d [fm]	$\left\langle r_m^2 \right\rangle^{1/2}$ [fm]
^{56}Ni	no slit	0.82 ± 0.02	3.94 ± 0.05	0.59 ± 0.04	3.77 ± 0.07
^{56}Ni	1 mm slit	0.61 ± 0.06	3.94 ± 0.13	0.59 ± 0.07	3.76 ± 0.08
^{56}Ni	2 mm slit	0.90 ± 0.05	3.88 ± 0.13	0.62 ± 0.07	3.79 ± 0.09
^{58}Ni	no slit	0.80 ± 0.02	3.42 ± 0.16	0.76 ± 0.04	3.88 ± 0.06
^{58}Ni	no slit, run 025	0.80 ± 0.02	4.00 ± 0.07	0.60 ± 0.04	3.82 ± 0.07
^{58}Ni	1 mm slit	0.75 ± 0.07	4.18 ± 0.11	0.52 ± 0.08	3.79 ± 0.09

Table 6.2.: Overview of best fit parameters of SF density parametrisation of the radial matter density of ^{56}Ni/^{58}Ni.
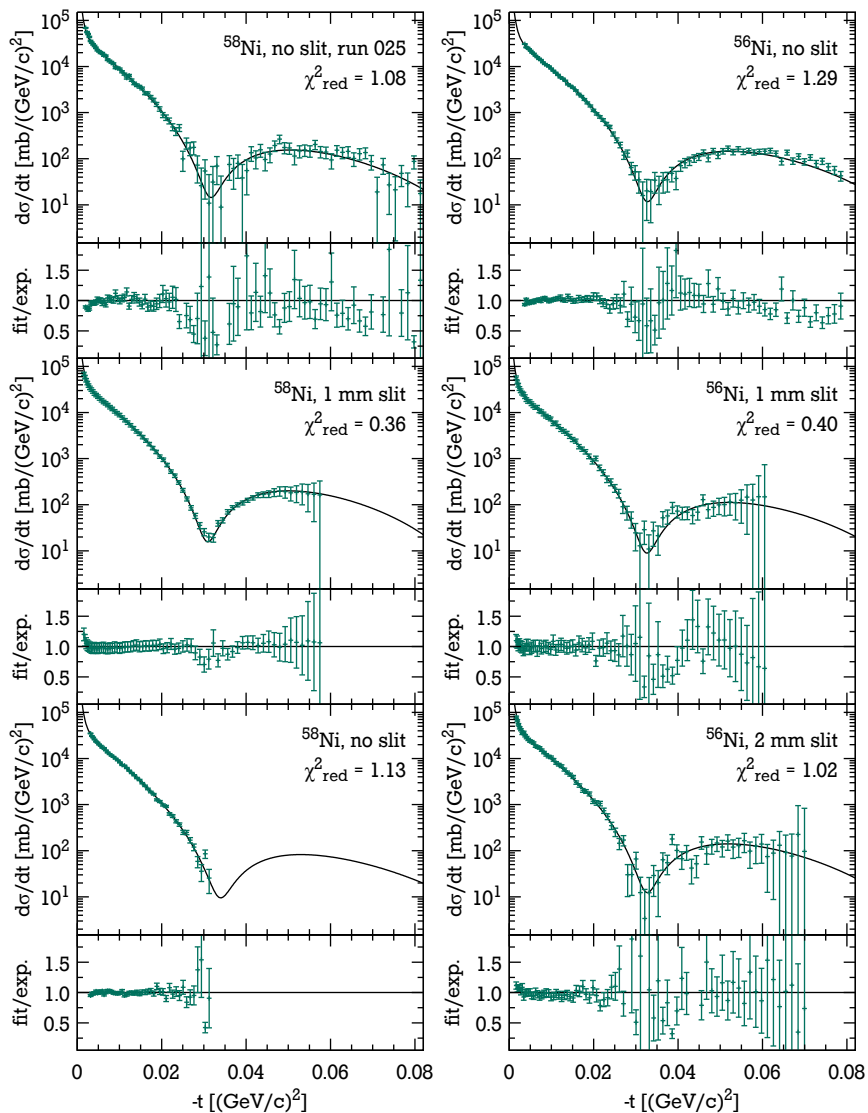
Figure 6.2.: Overview of fits to mean cross sections using the SF density parametrisation.
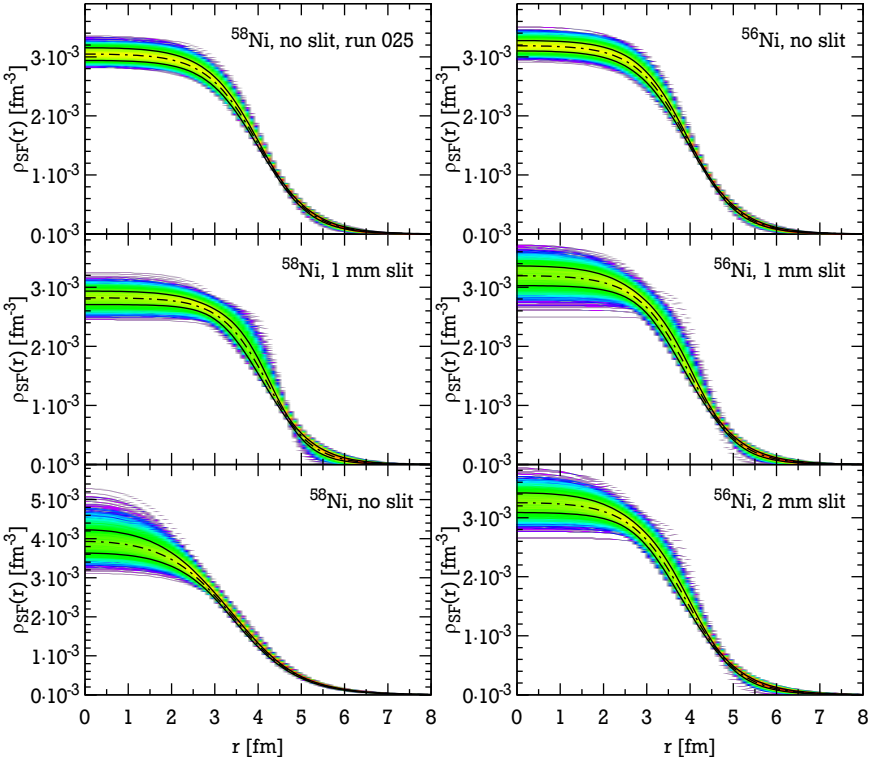
Figure 6.3.: Histogram of all fitted SF densities together with the mean density (*dashed line*) and the 1σ error bands (*solid line*).

in table 6.2 (*angular calibration* and *NN amplitude parameters*). By unfolding the statistical uncertainties, the individual contributions from $\Delta_{geom.}$ and $\Delta_{NNamp.}$ can now be estimated. However, because of the way β_{pN} was determined taking into account also the geometric uncertainties (see section 6.1), $\Delta_{NNamp.}$ itself contains a contribution by $\Delta_{geom.}$.

6.3 Model-independent analysis – Sum-of-Gaussians

As outlined before, the main advantage of a model-independent determination of the radial matter distribution is the possibility to derive realistic error bars reflecting the actual range of momentum transfer for which the cross section was measured. For this purpose the SOG method (see section 5.2.3) was used to analyse
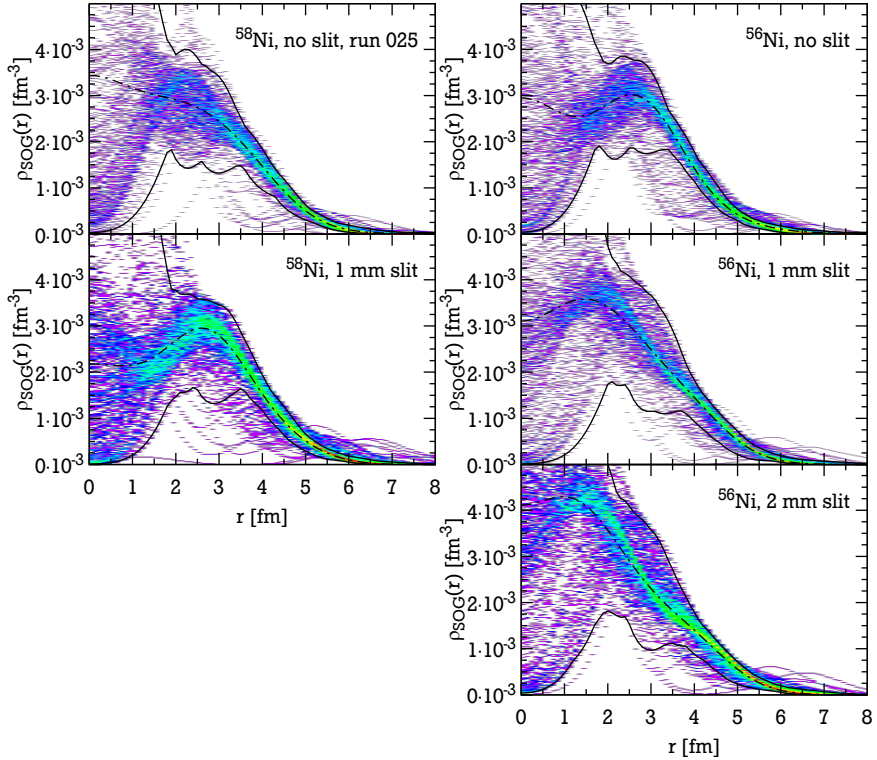
Figure 6.4.: Histogram of all fitted SOG densities. The error band represented by the solid lines are the superposition of all densities which yielded a good fit with $\tilde{\chi}^2 \leq \tilde{\chi}^2_{\min} + 1$. The dashed line corresponds to the mean value weighted by $\tilde{\chi}^{-2}$ of the good densities.

the measured cross sections. For all data sets $N = 12$ Gaussians are considered with positions R_i chosen in an interval of $[0\,\text{fm}, 9\,\text{fm}]$. The width of the Gaussians γ was set to value of $\gamma = 1.18$. These conditions were chosen in accordance with the recommendations in [96] and taken from the parameters for the SOG charge density in [95].

Since a single SOG fit takes about fifty times longer than a fit with a SF density parametrisation, it was not feasible to use the Monte Carlo approach for the propagation of the uncertainties from the angular calibration and the parameters for the nucleon-nucleon scattering amplitude. Instead, only the mean cross sections (figure 4.27) were used and fitted with 300 iterations. The long measurement

measurement		$\tilde{\chi}^2_{\min}$	$\langle r_m^2 \rangle^{1/2}$ [fm]
^{56}Ni	no slit	0.76	3.96 ± 0.05
^{56}Ni	1 mm slit	0.43	3.71 ± 0.04
^{56}Ni	2 mm slit	1.00	3.72 ± 0.04
^{58}Ni	no slit	—	—
^{58}Ni	no slit, run 025	1.10	4.04 ± 0.08
^{58}Ni	1 mm slit	0.20	3.79 ± 0.02

Table 6.3.: Overview of RMS matter-radii deduced with the SOG method.

"^{58}Ni, no slit" was not used in this part of the analysis as the experimental cross section was deduced in a too narrow interval of momentum transfer to give meaningful results.

The results are summarised in figure 6.4 where the fitted SOG densities are depicted as two-dimensional histograms. The error bands (*solid line*) were derived as described in section 5.2.3. Additionally, an average density (*dashed line*) is plotted which was calculated as the mean density weighted by $\tilde{\chi}^{-2}$ taking into account only the good fits for which $\tilde{\chi}^2 \leq \tilde{\chi}^2_{\min} + 1$. The RMS matter radii extracted from the good SOG fits are listed in table 6.3 together with their uncertainties. Like in the previous cases it will be assumed that the uncertainty of the SOG fits Δ_{SOG} is independent from the statistical uncertainty $\Delta_{\text{stat.}}$. The remaining contribution to Δ_{SOG} can then be interpreted as an estimate for the systematic uncertainty in the previous model dependent analysis. Hence, it is assumed that

$$\Delta_{\text{SOG}} \approx \sqrt{\Delta_{\text{stat.}}^2 + \Delta_{\text{model}}^2} \,. \tag{6.2}$$

6. Nuclear matter densities and radii

6.4 Summary
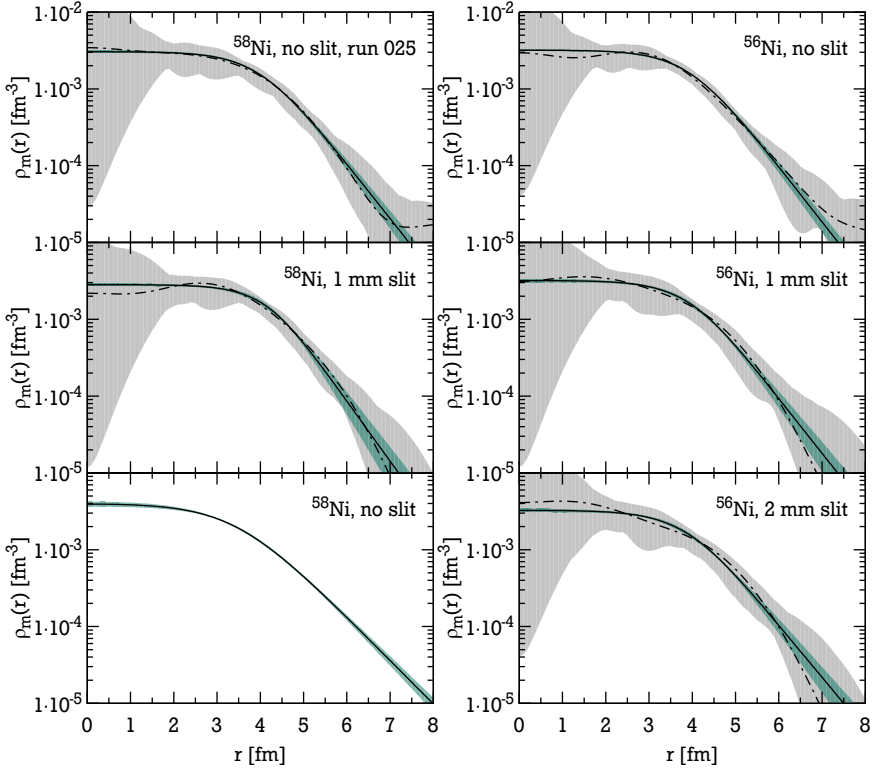
Figure 6.5.: Nuclear matter densities of ^{56}Ni and ^{58}Ni deduced with a SF density parametrisation (*solid line, green band*) and in a model-independent way using the SOG method (*dashed line, grey band*).

In order to compare the results from the model-dependent analysis (SF) with the results from the model-independent analysis (SOG), the corresponding matter distributions are plotted together in figure 6.5. A logarithmic y-scale is used in order to be able to evaluate the density in the surface region of the nucleus better. The RMS matter radii from both analyses are summarised in table 6.4 together with the estimated uncertainties. Following the previously made assumptions about independent sources of uncertainty, the total uncertainty can be estimated by:

$$\Delta_{\text{total}} \approx \sqrt{\Delta_{\text{stat.}}^2 + \Delta_{\text{geom.}}^2 + \Delta_{\text{NNampl.}}^2 + \Delta_{\text{model}}^2} \tag{6.3}$$

By using (6.1) and (6.2), the above equation can be re-written to

$$\Delta_{\text{total}} \approx \sqrt{\Delta_{\text{SF}}^2 + \Delta_{\text{SOG}}^2 - \Delta_{\text{stat.}}^2} \,, \tag{6.4}$$

which is then used to calculate the total uncertainty given in table 6.4.

measurement		$\langle r_m^2 \rangle^{1/2}$ [fm]		uncertainties [fm]				
		SF	SOG	$\Delta_{\text{stat.}}$	$\Delta_{\text{geom.}}$	$\Delta_{\text{NNampl.}}$	Δ_{model}	Δ_{total}
^{56}Ni	no slit	3.765	3.961	0.009	0.013	0.067	0.045	0.081
^{56}Ni	1 mm slit	3.756	3.708	0.028	0.049	0.063	0.024	0.083
^{56}Ni	2 mm slit	3.793	3.724	0.022	0.057	0.063	0.034	0.092
^{58}Ni	no slit	3.878	—	0.018	0.009	0.062	—	—
^{58}Ni	no slit, run 025	3.817	4.037	0.019	0.015	0.067	0.073	0.099
^{58}Ni	1 mm slit	3.789	3.785	0.016	0.059	0.063	0.017	0.087

Table 6.4.: Overview of RMS matter radii of ^{56}Ni and ^{58}Ni deduced in this work.

7 Discussion

7.1 Experimental cross sections
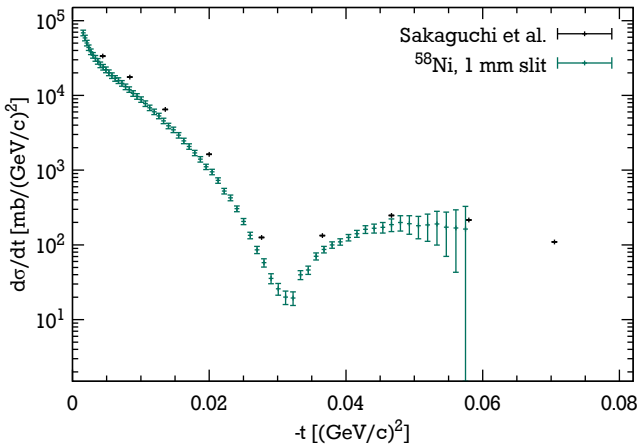
Figure 7.1.: Differential cross section for ^{58}Ni(p,p) measured in this experiment (*green*) compared to a measurement by Sakaguchi et al. (*black*) [10].

Cross section for p-^{58}Ni scattering

A recent measurement of the differential cross section for elastic proton scattering on ^{58}Ni in normal kinematics was published by Sakaguchi et al. in [10]. The measurement was performed at the *Research Center for Nuclear Physics* (RCNP) in Osaka, Japan. A 400 MeV proton beam impinged on a solid ^{58}Ni target and the scattered protons were detected with the *Grand Raiden* spectrometer. In the ^{58}Ni experiment of this work, the equivalent proton energy for normal kinematics would be 403 MeV which allows a direct comparison of the cross sections measured in both experiments. In figure 7.1 the cross section for ^{58}Ni with 1 mm slit is compared to a subset of the data from [10]. In order to estimate the difference between both cross sections better, the ratio between the two is evaluated in figure 7.2. For this, it was necessary to interpolate linearly between the data points of this work's cross sections. Besides an offset factor of about 0.65 (1 mm slit aperture) and 0.71 (without slit aperture), the cross sections measured in this experiment are in
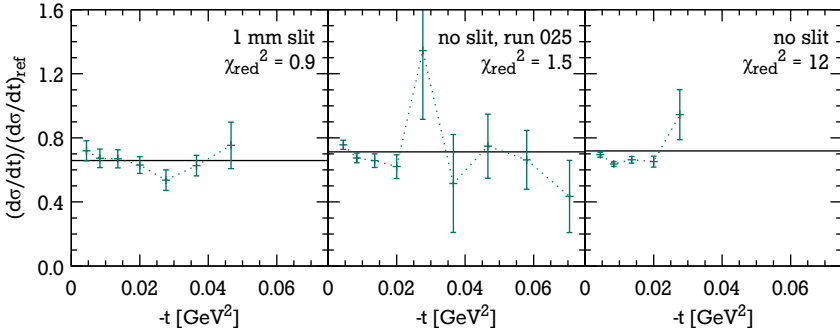
Figure 7.2.: Ratio of ^{58}Ni(p,p) cross sections from this experiment to a reference cross section by Sakaguchi et al. [10]. The reduced χ^2 was calculated relative to the average ratio (*horizontal line*).

good agreement with the literature data. Especially the data-set measured with the 1 mm slit aperture shows a good agreement with a $\tilde{\chi}^2 = 0.9$ which gives confidence in the correctness of the angular calibration and correction of the effective solid angle. A reason for the somewhat worse accordance of the measurements without slit aperture could be due to the background correction, in which the contribution of inelastic scattering may be overestimated (see section 4.6). Another possible issue could be the way the angular distribution was calculated by using the angular information from the p-side strips (see figure 4.17). The effect of the latter is minimal for the measurements where the slit aperture was used since the width of the kinematic band is significantly smaller.

The comparison of both experiments also reveals the superior angular resolution achieved with the EXL principle. In the present work, the cross section was determined with an average spacing of the data points of $\Delta t \approx 9 \cdot 10^{-4}\,\text{GeV}^2$ and thus, a factor of 20 finer than it was resolved with the Grand Raiden spectrometer.

Cross section for p-^{56}Ni scattering

Since the cross section for ^{56}Ni(p,p) was measured for the first time, a comparison with previous data is not possible. What remains, is a comparison of the cross sections from the different experimental runs relative to each other. Therefore, the cross section measured with the 1 mm slit aperture was used as a reference and the ratio of the two remaining ^{56}Ni cross sections to this reference were calculated (see figure 7.3). On this relative basis, the ^{56}Ni cross sections agree well with each other except for a global normalisation.
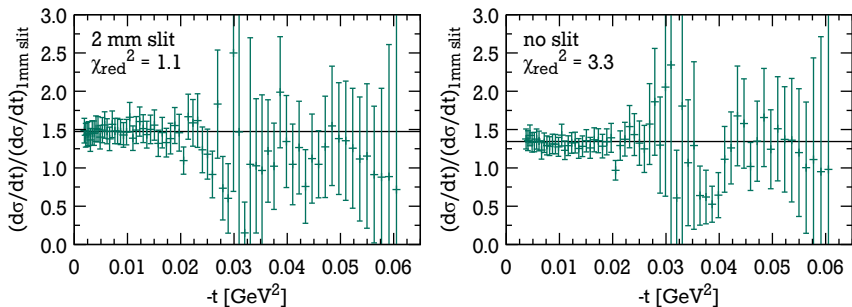
Figure 7.3.: Ratio of ^{56}Ni(p,p) cross sections to the cross section measured with 1 mm slit aperture. The reduced χ^2 was calculated relative to the ratio of the normalisation factors (*horizontal line*).

Absolute normalisation

The normalisation factor which was introduced as a free parameter for the fits of the cross sections (see section 6.2) is predominantly determined from the data points towards zero momentum transfer. Here, the density of data points is higher and their relative uncertainty is smaller. At the same time, the Glauber formalism in its current implementation ought to be accurate and reliable in this region. Hence, the normalisation factor can be interpreted as a measure for the absolute normalisation of the experimental cross sections. A value close to unity would indicate that the differential cross section was measured absolutely.

The factors obtained in the model dependent analysis (see section 7.1) are summarised in table 7.1. While the cross sections, which were measured without the slit aperture basically yield the same normalisation values, the factors differ significantly in the other cases in which the aperture was used. Moreover, with the

measurement		normalisation
^{56}Ni	no slit	0.82 ± 0.02
^{56}Ni	1 mm slit	0.61 ± 0.06
^{56}Ni	2 mm slit	0.90 ± 0.05
^{58}Ni	no slit	0.80 ± 0.02
^{58}Ni	no slit, run 025	0.80 ± 0.02
^{58}Ni	1 mm slit	0.75 ± 0.07

Table 7.1.: Overview of normalisation factors for the cross sections. For details, see section 6.2.

exception of the ^{56}Ni cross section determined with the 2 mm aperture, these normalisations are further away from unity.

The reasons for these deviations are not fully understood yet. In cases where the slit aperture was used, the deviation might indicate that the experimental geometry and especially the position of the aperture was not determined properly. Hence, the effective solid angle which was obtained based on this geometry (see section 4.5) could be inaccurate and therefore responsible for the differences. However, this should yield an equal deviation for all three measurements with slit aperture which is not the case. Also, a different position of the slit aperture in the simulation would influence the shape of the cross section. The previous evaluation of the cross sections has not revealed significant discrepancies (see figures 7.2 and 7.3). Altogether, it is unlikely that the deviations are caused by the correction of the effective solid angle. In the measurements without slit, the normalisation deviates by 20 % from unity. Technically, this could be explained by an inaccurately assumed DSSD position (z_{DSSD}). But again, for a factor of 0.8 the relative distance between the target and the DSSD had to be wrong by roughly 10 % which would correspond to about 25 mm. While it cannot be fully excluded that the distance was assumed slightly wrong, it certainly cannot be taken as a sole explanation. Another possible explanation could be a systematic deviation in the determination of the luminosity. At present, however, this can neither be verified nor ruled out.

7.2 Nuclear matter densities and radii

7.2.1 Validation of the Glauber code

Since the software for the calculation of the p-nucleus cross sections was re-implemented using another programming language (see section 5.1.2), it needed to be verified again. Therefore, a cross section for elastic proton scattering on ^{58}Ni which was obtained for an energy of 1.047 GeV [7, 98] was re-analysed with the new software. In order to avoid the limitations introduced by the centre-of-mass correction (see section 5.1), the cross section was analysed up to the second diffraction maximum, only. The fit was performed using a SF density parametrisation and with the same parameters for the nucleon-nucleon scattering amplitude as given in [98]. While the fit fails to reproduce the data in the minima, as shown in figure 7.4, the overall agreement is still good. However, a similar trend was already apparent in the original analysis [98]. The situation improved slightly by taking into account the spin-orbit interaction in the nucleon-nucleon scattering amplitude [7].
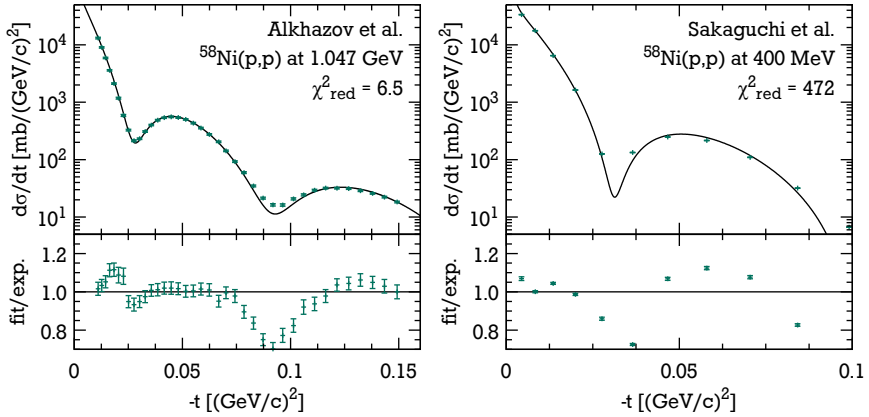
Figure 7.4.: Re-analysis of the ^{58}Ni(p,p) differential cross section at 1.047 GeV [7, 98] (*left*) and ^{58}Ni(p,p) differential cross section at 400 MeV [10] (*right*). For the fit, the nuclear density was parametrised by a SF distribution.

The comparison of the radial matter densities from this analysis and the densities determined in the original analyses reveals a good agreement especially in the surface region of the nucleus (see figure 7.5). Particularly, the 2pF density by Lombard et al. [7] is almost identical to the result obtained in the present analysis. The deduced RMS matter radii are summarised in table 7.2. The evaluation of the radii is complicated by the fact that no uncertainties for the total matter radius are given in [98]. An uncertainty of 0.03 fm is given for the radius of the neutron distribution, only. However, even when assuming this as a lower limit, all measurements including the new analysis are in good agreement and hence, verify the correctness of the re-implemented Glauber code.

As another benchmark, the previously mentioned differential cross section by Sakaguchi et al. [10] was analysed. Therefore, the cross section was limited to a range of momentum transfer comparable to the one of the present experiment and fitted using a SF density parametrisation. Since the cross section was measured at the same equivalent energy as in the present experiment, the same parameters for the nucleon-nucleon scattering amplitude were chosen. The resulting fit is shown on the right side of figure 7.4. Although the fit does not reproduce the experimental cross section well, the fitted density distribution (figure 7.5) and the corresponding RMS matter radius (table 7.2) are almost indistinguishable from the previously shown case. Despite the good agreement, it became apparent that the fit results depend very much on the range of data points which was selected for the fit. While
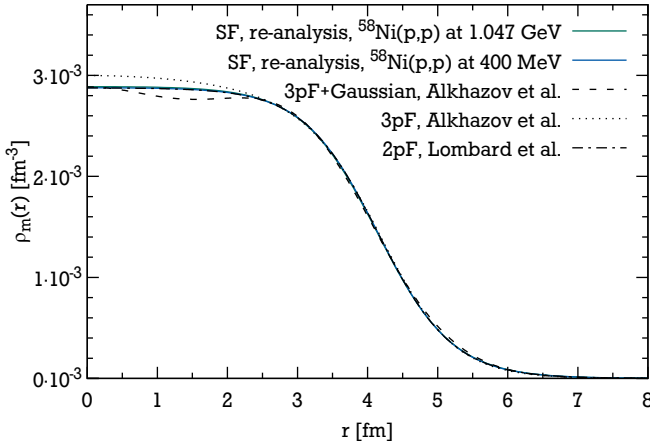
Figure 7.5.: Radial matter distribution $\rho_m(r)$ of ^{58}Ni determined from the ^{58}Ni(p,p) differential cross sections at 1.047 GeV [7, 98] and at 400 MeV [10].

analysis	energy	model	$\left\langle r_m^2 \right\rangle^{1/2}$
Alkhazov et al. [98]	1.047 GeV	3pF	3.74 fm
	1.047 GeV	3pF + Gaussian	3.77 fm
Lombard et al. [7]	1.047 GeV	3pF	3.75 ± 0.10 fm
	1.047 GeV	2pF	3.78 ± 0.10 fm
Re-analysis of [7, 98]	1.047 GeV	SF	3.776 ± 0.004 fm
Re-analysis of [10]	400 MeV	SF	3.770 ± 0.002 fm

Table 7.2.: RMS matter radii $\left\langle r_m^2 \right\rangle^{1/2}$ of ^{58}Ni from a re-analysis of differential cross sections from [7, 98] and [10]. In [98], no uncertainty for the total matter radius was stated. The uncertainties of the re-analysed matter radii is based on the statistical uncertainty of the fit.

this could be simply an effect of the widely spaced data points, it could also indicate that the presently used Glauber code and the assumptions therein may not be perfectly applicable at these lower energies anymore (see sections 5.1.1 and 5.1.2).

7.2.2 Nuclear matter density of ^{58}Ni
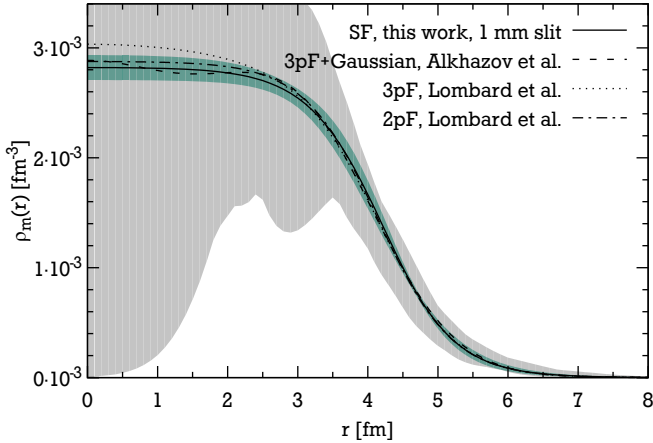
Figure 7.6.: Radial matter distribution $\rho_m(r)$ of ^{58}Ni measured in this work compared to results from Alkhazov et al. [98] and Lombard et al. [7]. The error bands from the model dependent analysis (SF) and the model-independent analysis (SOG) are represented by the green and the grey band respectively.

Since the radial matter density of ^{58}Ni was already put into the fit of the slope parameter β_{pN} (see section 6.1), the analysis of the ^{58}Ni cross section should not yield radial densities which differ much from what was put into. In fact, as shown in figure 7.6, the radial matter density measured with the 1 mm slit aperture matches the distributions from the literature already within the uncertainty of the model-dependent analysis. The only exception is the 3pF density obtained by Lombard et al. [7] which lies slightly above the others in the central region. Since the SF function cannot reproduce this particular shape, it could be an effect of the model dependence. However, the error bars from the model-independent analysis clearly reveal that the present experiment is not sensitive on the density distribution in the centre of the nucleus and hence, does not allow to conclude on the shape in this region.

When comparing the ^{58}Ni density distribution measured with the 1 mm slit to the distributions obtained from the measurements without slit, larger differences become visible (see figure 7.7). While the three curves lie within the limits of the uncertainties from the model-independent analysis, they hardly match within the error bands of the model-dependent analysis. Consequently, the parameters
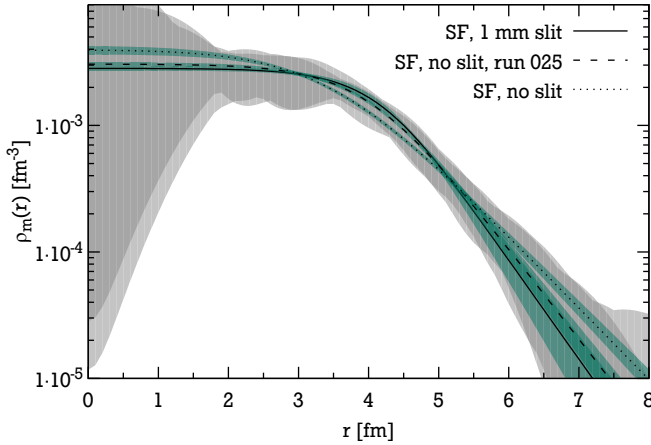
Figure 7.7.: Radial matter distribution $\rho_m(r)$ of ^{58}Ni as determined in this experiment. The error bands from the model dependent analysis (SF) and the model-independent analysis (SOG) are represented by the green and the grey bands, respectively.

of the SF distributions (see table 6.2) differ as well. These deviations might be explainable partly by the fact that the kinematical band of elastic scattering was not separated from inelastic scattering (see section 4.6) and partly by considering the way the angular distribution was deduced using the angular information of the p-side strips (see section 4.5.2 and especially figure 4.17). Both issues supposedly skewed the cross section and thus affect the density distributions. Additionally, the cross section extracted from the "^{58}Ni, no slit" measurement only reaches up to the beginning of the first diffraction minimum (see figure 4.27) which is too limited to determine the shape of the density distribution properly.

The RMS matter radius obtained from the SOG analysis of the ^{58}Ni cross section of run 025 is about 0.2 fm larger than the radius determined with a SF density parametrisation. It is also larger than both radii from the measurement with the slit aperture where identical SF and SOG radii are determined. The reason for this issue becomes visible when comparing the average SOG densities of the two measurements (see figure 7.8). At larger radii, the average SOG density features an artificial bump which increases the RMS radius. The reasons for this bump are not yet clear but the same issue can be observed in the case of ^{56}Ni. Therefore, it is presumably connected to a particular deviation in the cross sections which were measured without the slit aperture. Nevertheless, the problem also demonstrates the benefit of the model-independent density distribution and especially the decou-
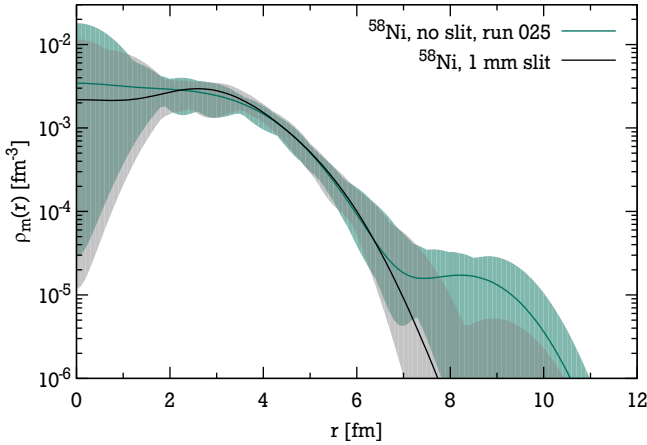
Figure 7.8.: Comparison between the mean SOG densities of ^{58}Ni from run 025 without slit aperture (*green*) and the measurement with 1 mm slit (*black/grey*). The artificial bump around 8.5 fm causes the higher RMS radius of the measurement without slit aperture.

pling of the density at different radii. Despite the disagreement of the two results towards larger radii, both cross sections give identical results in the region of the surface (between 3 fm and 6 fm) where also the uncertainties are the smallest. As a consequence, only the results from the measurement with slit aperture will be considered in the further discussion in section 7.3.

Nuclear matter density of ^{56}Ni

In this work, the radial matter density of ^{56}Ni was determined for the first time. The analysis with a SF density parametrisation revealed a very good agreement of the three experimental runs with 1 mm, 2 mm and without slit aperture. The fitted parameters are identical within their uncertainties (see table 6.2) and, consequently, the density distributions are in good agreement as well (see figure 7.9). However, as it was already noticed previously for the case of ^{58}Ni, the SOG densities obtained from the measurements without slit yield a too large RMS radius. Again, the deviation is caused by an artificial bump in the density distribution at a radius of about 9 fm. Therefore, the measurement without slit aperture will be excluded from the further discussion.

In figure 7.10 the experimental point-matter density from the measurement with 1 mm slit is compared to two theoretical predictions. The first one is the
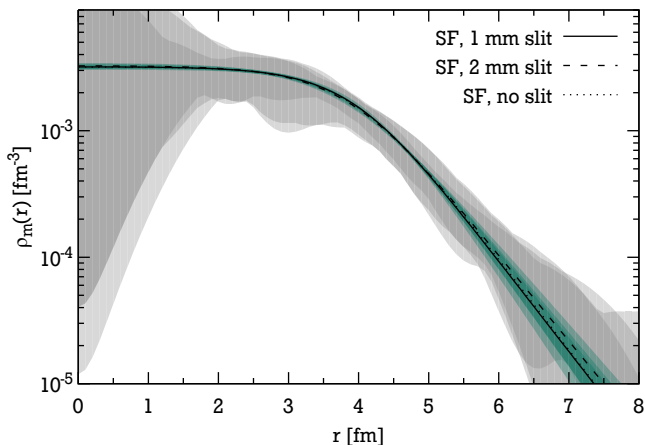
Figure 7.9.: Radial matter distribution $\rho_m(r)$ of ^{56}Ni as determined in this experiment. The error bands from the model-dependent analysis (SF) and the model-independent analysis (SOG) are represented by the green and the grey bands, respectively.
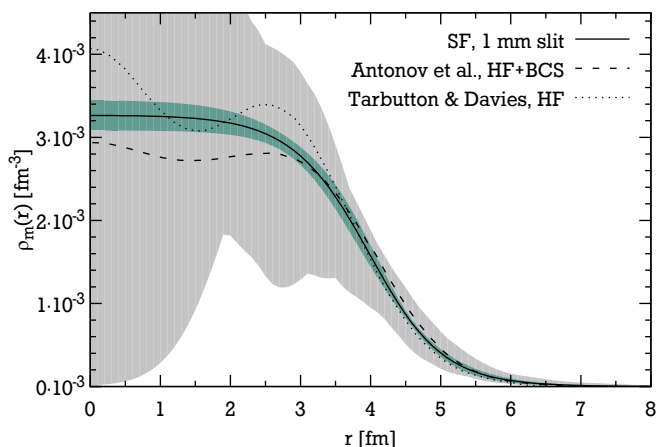
Figure 7.10.: Point-matter distribution of ^{56}Ni compared to theoretical predictions of the point-proton [99] and point-matter distribution [100]. The experimental uncertainties from the model dependent analysis (SF) and the model independent analysis (SOG) are represented by the green and the grey bands respectively.

point-matter density calculated using Hartree-Fock (HF) approximations [100], and the second one is the point-proton distribution calculated in the deformed self-consistent mean-field Skyrme HF+BCS method [99]. The proton distribution was included into the figure since the differences to the matter distribution are expected to be relatively small. The difference between the RMS proton and matter radii is predicted to be $r_p - r_m = -0.029$ fm [99]). For ^{58}Ni, in the same source, a difference of -0.012 is calculated which is in agreement with experimental findings [7, 9, 98, 101].

7.3 Systematics of RMS matter radii

| experiment | model | RMS matter radius $\left\langle r_m^2 \right\rangle^{1/2}$ | |
		^{56}Ni	^{58}Ni
this work, 1 mm slit	SF	(3.76 ± 0.08) fm	(3.79 ± 0.09) fm
this work, 2 mm slit	SF	(3.79 ± 0.09) fm	—
Alkhazov et al. [98]	3pF	—	3.74 fm
	3pF + Gaussian	—	3.77 fm
Lombard et al. [7]	3pF	—	(3.75 ± 0.10) fm
	2pF	—	(3.78 ± 0.10) fm
Blanpied et al. [101]	3pF	—	(3.79 ± 0.03) fm
Ray et al. [102]	3pF	—	(3.77 ± 0.04) fm
theory		^{56}Ni	^{58}Ni
Antonov et al. [99]	HF+BCS	3.799 fm	3.809 fm
Lenske & Kienle [18]	HFB	3.770 fm	3.816 fm
Tarbutton & Davies [100]	HF	3.609 fm	—

Table 7.3.: Measured RMS matter radii $\left\langle r_m^2 \right\rangle^{1/2}$ of ^{56}Ni and ^{58}Ni compared to literature values and theoretical predictions.

The RMS matter radii for ^{58}Ni and ^{56}Ni are summarised in table 7.3 and figure 7.11 together with previous experimental results and theoretical predictions. As mentioned before, the results for ^{58}Ni are in good agreement with previous experiments which gives strong confidence in the results for ^{56}Ni. The RMS matter radius of ^{56}Ni obtained here for the first time, supports the predicted matter radii by Antonov et al. [99] as well as by Lenske & Kienle [18]. However, the precision of the now established experimental value does not allow to favour one over the other. The calculations by Tarbutton & Davies [100], on the other hand, can be disregarded using the experimental results.
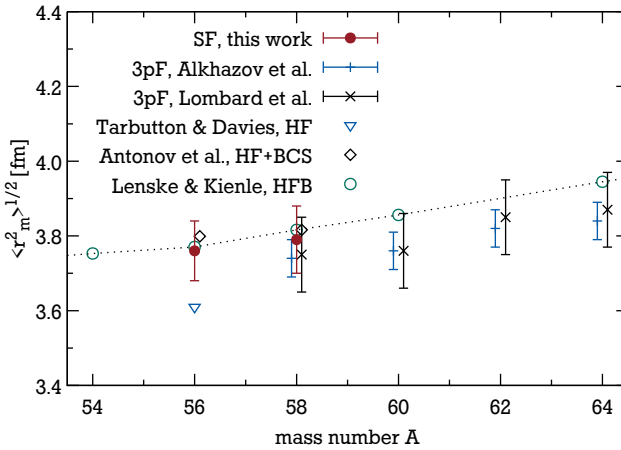
Figure 7.11.: Measured RMS matter radii of ^{56}Ni and ^{58}Ni compared to literature values from Lombard et al. [7], Alkhazov et al. [98] and theoretical predictions by Tarbutton & Davies [100], Antonov et al. [99] and Lenske & Kienle [18]. The line serves as a guide to the eye.

Encouraged by these experimental results, coupled-cluster calculations (L-CCSD(T)) were initiated by [103, 104] in order to calculate the RMS matter radius of ^{56}Ni. Results are in preparation, but at the time of writing no convergence has been reached yet.

8 Outlook

In the previous chapters the analysis and the results of the EXL-E105 experiment were presented. The measurement of the differential cross section for elastic proton scattering on ^{58}Ni is in good agreement with previous measurements in normal kinematics [10]. Also, the matter distribution and RMS matter radius of ^{58}Ni, which were extracted from this cross section, reproduce the established literature values well. This gives strong confidence in the correctness of the analysis and also proves that the novel experimental setup is well understood. Furthermore, with the measurement of the cross section of the elastic proton scattering on ^{56}Ni, a nuclear reaction with a stored radioactive beam was investigated for the first time ever. In the subsequent analysis, a matter density distribution was extracted and the RMS matter radius of ^{56}Ni was determined to be (3.76 ± 0.08) fm.

From a technical point of view, the experiment proved that the whole concept of EXL is feasible. The principle of using a DSSD as an active vacuum window separating the UHV of the storage ring from an auxiliary vacuum was successfully demonstrated. It shows that a detector system consisting of partly non-UHV compatible components, like for example Si(Li) detectors, can be operated in a UHV environment without sacrificing a low energy threshold by using pockets.

Being the first experiment of the EXL physics program, the experimental campaign and the analysis gave a valuable amount of experience for the improvement of future experiments. It was shown in the analysis that the uncertainty of the geometry had a larger contribution to the total uncertainty than the statistical uncertainties. Hence, it is worthwhile to investigate possibilities to define the geometry when the detectors are already mounted in the interaction chamber. Moreover, since the slope parameter of the nucleon-nucleon scattering amplitude β_{pN} was fitted to reproduce the measured cross section of ^{58}Ni, more precise knowledge about the geometry would also lower the uncertainty related to β_{pN}. Following the same argumentation, it is advisable to measure the position and the shape of the interaction zone continuously throughout the experiment. This could be achieved by measuring the light from atomic de-excitation of the target gas with a set of appropriate cameras (an example is given in figure 8.1) [83]. By having more precise information about the dimensions of the interaction zone, the absolute normalisation of the cross section could be improved, too. Nevertheless, the implementation of independent methods for measuring the luminosity should be envisaged.

The experience gained from the in-ring detection system (see section 3.3) opens up the opportunity to place the DSSD of the recoil detector completely into the UHV. An obvious difference between the two detection systems is the number of
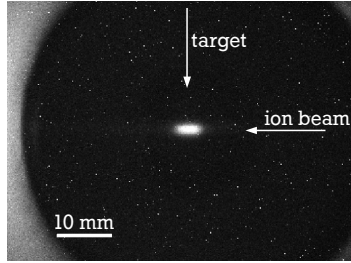
Figure 8.1.: Image of the overlap region of a hydrogen target with a 150 MeV/u Xe[54+] ion beam, recorded with an EM-CCD camera. (*adapted from* [83])

channels and hence, the amount of readout cabling. However, first vacuum tests with the components necessary for the read-out of a full DSSD have not revealed general limitations. Also, the use of thick silicon detectors with a thickness of more than 1 mm could possibly replace the Si(Li) detectors currently used. Since these silicon detectors can be baked, they can be placed directly in the UHV as well. Nevertheless, they would still need to be cooled down during operation which makes the development of a UHV compatible cooling system necessary. A possible setup of such a detector telescope is shown in figure 8.2. Placing the detectors directly inside the chamber also allows to increase the solid angle coverage by stacking detectors on top of each other, which is technically much easier than with the present pocket geometry (see figure 8.2).

This way, the existing 90° detector telescope could be extended by an additional DSSD in front of it. With this DSSD it is possible to employ particle tracking and hence improve the angular resolution of the telescope. In figure 8.3, the result of a simulation for proton elastic scattering on ^{56}Ni and inleastic scattering to the first excited state of ^{56}Ni (2.7 MeV) is shown. For energies above 6 MeV, i. e. when the protons punch trough the first 300 μm thick DSSD, the tracking enables to separate the elastic and the inelastic bands. The tracking would also allow to determine the cross section in an angular region where the recoils punch through the detectors.

Another way to improve the angular resolution is to reduce the diameter of the target. At present, the size of the target is defined by the diameter of the first skimmer downstream of the nozzle (see figure 3.4). In a new inlet chamber, which is intended to replace the current one soon, it will be possible to exchange the skimmer by smaller ones remotely. The reduction of interaction length, of course, comes at the expense of a reduced target density [77]. While this will be available soon, the ultimate aim for future EXL experiments is to have target beams of liquid droplets. For ^{4}He the expected target density of such a droplet beam is in the order
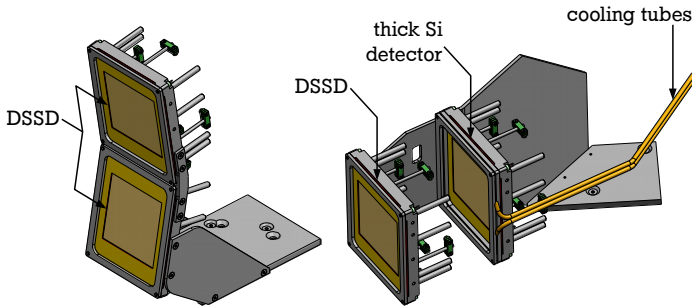
Figure 8.2.: Schematic view of a vertical array of two DSSDs (*right*) and a detector telescope (*left*) for the operation directly in the UHV. (*based on technical drawings by* [50])

of $10^{16}\,\mathrm{cm}^{-2}$ with an interaction length much smaller than $1\,\mathrm{mm}$ [83]. However, with such high densities the energy loss of the ions in the target might be too large to be still compensated by the electron cooler [105].

Ultimately, the tracking and the reduced target diameter will make the slit aperture obsolete. Without the aperture, the factor gained in count rate might offset the loss of target density due to a smaller skimmer. However, without the aperture, the foremost detector will also be exposed to a higher rate of delta electrons (see section 3.8). Hence, it has to be investigated whether the DSSD can be hardened against the surface damage imposed by the high flux of low-energy electrons. An improved detector design is supposed to address this issue [28]. The new detectors are already available, but still need to be tested.

Concerning the analysis of the differential cross sections one would clearly benefit from extending the measurements to higher momentum transfers. Technically, this could be achieved by exploiting the previously mentioned tracking which would allow to use the full solid angle covered by detectors. Another possibility, which could be applied in addition, is to extend the dynamic range of the telescope to higher energies by placing additional detectors like for example CsI crystals in the auxiliary vacuum.

Especially with respect to the model-independent SOG method, data points at higher momentum transfer are needed to reduce the uncertainties towards the central region of the density distribution. It would also be worthwhile to improve the implementation of the Glauber formalism, which was used for the analysis of the present experiment. As already mentioned in section 5.1.2, the current code was intended for elastic proton-scattering experiments of light ions at energies close to $1\,\mathrm{GeV}$. Hence, the approximations made in this code may not be perfectly valid to describe the scattering on heavier nuclei at energies around $400\,\mathrm{MeV}$. While the
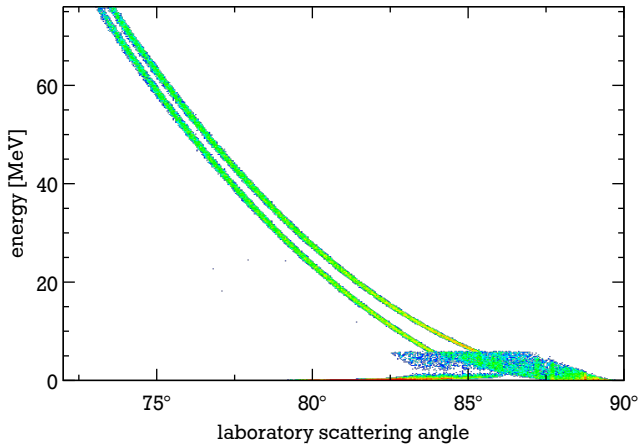
Figure 8.3.: Benefit of tracking demonstrated for the existing $90°$ detector telescope. Simulation of a second DSSD positioned $13\,\text{cm}$ in front of the telescope. The same simulation routines as in section 4.5.1 were used to simulate proton elastic scattering on ^{56}Ni as well as inleastic scattering to the first excited state of ^{56}Ni at $2.7\,\text{MeV}$.

analysis of the present experiment has revealed that the experimental cross sections are still very well described by the code, the re-analysis of the ^{58}Ni(p,p) differential cross section measured at $400\,\text{MeV}$ by Sakaguchi et al. indicates some inaccuracies at higher momentum transfer.

The future of EXL and in-ring nuclear reaction studies

Despite the fact that the origin of the EXL project was the **N**ew **E**xperimental **S**torage **R**ing (NESR) of the FAIR facility, it is not bound to this particular storage ring. The latest EXL campaign and the analysis of this work demonstrated the feasibility of EXL experiments at the present ESR. Until the NESR becomes available the ESR will allow to continue not only with the development of the EXL detector system but also to conduct further physics experiments. Thereby, the ESR will benefit from the intensity upgrades of the UNILAC and the SIS18 which are envisaged in preparation of the upcoming FAIR facility. In the mid-term future, i. e. when the SuperFRS will be available, a transfer line might connect the SuperFRS with the ESR. Technically, it is also possible to place EXL in the **H**igh **E**nergy **S**torage **R**ing (HESR).

In the near future, EXL-like experiments can be conducted at the **H**eavy **I**on **R**esearch **F**acility in **L**anzhou (HIRFL), China [106]. The HIRFL-CSR (**C**ooler-

Storage-Ring) facility features the experimental storage ring CSRe, which provides stored exotic beams with maximum energies between 400 MeV/u (U^{90+}) and 600 MeV/u (C^{6+}). The ring is equipped with an electron cooler as well as an internal gas-jet target and is therefore well suited for EXL experiments. Another facility, currently being planned in China, is the **H**igh **I**ntensity heavy ion **A**ccelerator **F**acility (HIAF) [107]. The design is not yet finished but the facility will take advantage of several storage rings to allow for a broad field of research.

In the course of upgrading the ISOLDE (**I**sotope **S**eparator **O**n **L**ine **DE**vice) facility at CERN to HIE-ISOLDE (**H**igh **I**ntensity and **E**nergy ISOLDE), it is envisaged to include the low-energy ring TSR (**T**est **S**torage **R**ing) which was constructed and operated at the Max-Planck-Institut für Kernphysik in Heidelberg [108]. The ring will provide cooled beams of exotic nuclei at energies of up to 10 MeV/u [109]. While these energies are too low to perform elastic scattering experiments like in the present work, there will be the possibility to study transfer reactions induced by an internal gas-jet target [109]. The same kind of experiments will also be possible with the **L**ow energy **S**torage **R**ing (LSR) at the FAIR facility. The LSR is an evolution of the CRYRING [110] and will offer cooled beams of exotic nuclei at energies of around 14 MeV/u as well as an internal gas-jet target. It is currently being installed at the present GSI facility and it is planned to be employed in conjunction with the ESR. The two rings will not only work as a test bench for FAIR experiments but also allow experiments with decelerated beams of exotic nuclei [111].

A Relativistic kinematics

A thorough review of relativistic particle kinematics is given for example in [112] which also serves as a basis for the following brief description. Consequently, throughout this chapter a unit system with $c = 1$ will be used. In the following, $\mathbf{p}$ will be used for the four-momentum vector and $\vec{p}$ to indicate the three-momentum. The absolute values of the four- and three-momentum is denoted by p and P, respectively.

Assuming the scattering of two particles with four-momenta $\mathbf{p}_a$ and $\mathbf{p}_b$ and masses m_a and m_b to two particles with momenta $\mathbf{p}_1$ and $\mathbf{p}_2$ and masses m_1 and m_2, i.e.

$$\mathbf{p}_a + \mathbf{p}_b \rightarrow \mathbf{p}_1 + \mathbf{p}_2 \ . \tag{A.1}$$

The corresponding scattering angles are illustrated in figure A.1 for the laboratory frame (LAB) as well as the centre-of-mass frame (CM).
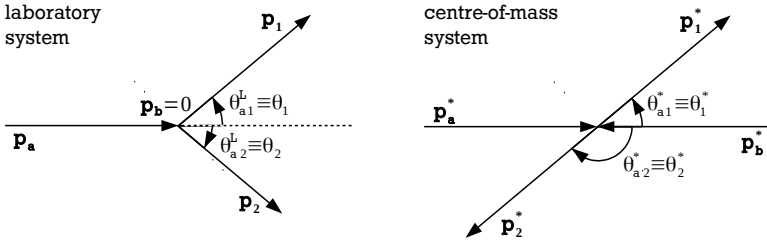
Figure A.1.: Particle scattering kinematics in the laboratory system (*left*) and in the centre of mass system (*right*).

The laboratory system is defined as the reference frame in which the detector is located and all energies and momenta are actually measured. Furthermore, it will be assumed that the particle b is at rest and hence $\vec{p}_b = 0$. The centre-of-mass frame is defined as the coordinates system in which

$$\vec{p}_a^* + \vec{p}_b^* = \vec{p}_1^* + \vec{p}_2^* = 0 \ .$$

As a direct consequence, the two scattering angles in the centre-of-mass frame are related to one another by

$$\theta_1^* = \pi - \theta_2^* \ .$$

An elegant way to describe the relativistic scattering process is by introducing the Lorentz invariant *Mandelstam variables s, t* and *u*:

$$
\begin{aligned}
s &= (p_a + p_b)^2 = (p_1 + p_2)^2 \\
t &= (p_a - p_1)^2 = (p_b - p_2)^2 \\
u &= (p_a - p_2)^2 = (p_b - p_1)^2
\end{aligned}
\tag{A.2}
$$

Since the three Mandelstam variables depend only on two independent variables, it can be shown that

$$
s + t + u = m_a^2 + m_b^2 + m_1^2 + m_2^2 .
\tag{A.3}
$$

Hereby, *s* is commonly interpreted as the *two particle invariant mass squared* and *t* as the *invariant momentum transfer squared*. By expanding the binomials in (A.2) one can find the following useful relations:

$$
\begin{aligned}
s &= m_a^2 + m_b^2 + 2m_b E_a^L \\
t &= m_a^2 + m_1^2 - 2E_a E_1 + 2P_a P_1 \cos\theta_1 \quad \text{(LAB and CM)} \\
&= m_b^2 + m_2^2 + 2m_b E_2^L \\
u &= m_a^2 + m_2^2 - 2E_a E_2 + 2P_a P_2 \cos\theta_2 \quad \text{(LAB and CM)} \\
&= m_b^2 + m_1^2 + 2m_b E_1^L
\end{aligned}
\tag{A.4}
$$

With the help of (A.3) and (A.4) it is now possible to derive relations between the Mandelstam variables and the LAB as well as the CM quantities. A few of them, which are of importance for this work, will be listed in the following.

Laboratory scattering angles

The laboratory scattering angles θ_1 and θ_2 are related to the Mandelstam variables by

$$
\cos\theta_1 = \frac{\left(s - m_a^2 - m_b^2\right)\left(m_b^2 + m_1^2 - u\right) + 2m_b^2\left(t - m_a^2 - m_1^2\right)}{\lambda^{1/2}\left(s, m_a^2, m_b^2\right)\lambda^{1/2}\left(u, m_b^2, m_1^2\right)}
\tag{A.5}
$$

and

$$\cos\theta_2 = \frac{\left(s - m_a^2 - m_b^2\right)\left(m_b^2 + m_2^2 - t\right) + 2m_b^2\left(u - m_a^2 - m_2^2\right)}{\lambda^{1/2}\left(s, m_a^2, m_b^2\right)\lambda^{1/2}\left(u, m_b^2, m_2^2\right)} \ . \qquad \text{(A.6)}$$

Here, the kinematical function λ was introduced, i. e.

$$\lambda(x, y, z) = (x - y - z)^2 - 4yz \ . \qquad \text{(A.7)}$$

In order to calculate the relation between the scattering angle and the kinetic energy of the recoil for elastic scattering with $m_a \equiv m_1$ and $m_b \equiv m_2$, one has to employ (A.3) in order to replace u by s and t in (A.5). Then, after applying the relations from (A.2) to replace s and t and introducing the kinetic energy $T = E - m$, one gets two equations of which the one with the positive solution gives the physical result:

$$T_2(\theta_2) = \frac{\sqrt{m_b^2 T_a^2 \cos^4(\theta_2)(2m_a + T_a)^2} + m_b T_a \cos^2(\theta_2)(2m_a + T_a)}{(m_a + m_b + T_a)^2 - T_a \cos^2(\theta_2)(2m_a + T_a)} \qquad \text{(A.8)}$$

For the case of inelastic scattering, the derivation is similar but the masses m_1 and m_2 have to be replaced by $m_1 = m_a + Ex_1$ and $m_2 = m_b + Ex_2$ whereas Ex is the excitation energy of the respective particle. Then, both resulting equations have to be taken into account as they yield a low energy branch and a high energy branch of the kinematics with a discontinuity where both meet.

Centre-of-mass scattering angles

The scattering angles in the centre-of-mass frame θ_1^* and θ_2^* are related to the Mandelstam variables by

$$\cos\theta_1^* = -\cos\theta_2^* = \frac{s\,(t - u) + \left(m_a^2 - m_b^2\right)\left(m_1^2 - m_2^2\right)}{\lambda^{1/2}\left(s, m_a^2, m_b^2\right)\lambda^{1/2}\left(s, m_1^2, m_2^2\right)} \ . \qquad \text{(A.9)}$$

The derivation of the relation between the scattering angle and the particle's energy is then equal to the previous case.

Conversion from laboratory system to Mandelstam variables

The cross sections in the present experiment were presented as a function of t. The conversion of the laboratory scattering angle can be derived in the same way as

equation (A.8), but without replacing t in the process. Assuming elastic scattering, one finds:

$$\cos\theta_2(t) = \frac{m_b \left[m_a(4m_b T_a + t) + m_b \left(t + 2T_a^2 \right) + t T_a \right]}{\sqrt{m_b^2 T_a(2m_a + T_a)(2m_b T_a + t)(4m_a m_b + 2m_b T_a + t)}} \qquad \text{(A.10)}$$

B Differential cross sections

**Differential cross section for p-^{56}Ni elastic scattering
(with 1 mm slit aperture)**

$-t$ $\left[(\text{GeV}/c)^2\right]$	Δt $\left[(\text{GeV}/c)^2\right]$	$\frac{d\sigma}{dt}$ $\left[\text{mb}/(\text{GeV}/c)^2\right]$	$\Delta\frac{d\sigma}{dt}$ $\left[\text{mb}/(\text{GeV}/c)^2\right]$
$1.647 \cdot 10^{-3}$	$2.602 \cdot 10^{-5}$	56645.2	5280.91
$1.892 \cdot 10^{-3}$	$2.523 \cdot 10^{-5}$	45860.6	4309.70
$2.154 \cdot 10^{-3}$	$2.409 \cdot 10^{-5}$	39346.5	3691.08
$2.433 \cdot 10^{-3}$	$2.257 \cdot 10^{-5}$	33187.9	3118.66
$2.729 \cdot 10^{-3}$	$2.087 \cdot 10^{-5}$	29597.1	2760.82
$3.042 \cdot 10^{-3}$	$1.872 \cdot 10^{-5}$	26535.3	2478.24
$3.373 \cdot 10^{-3}$	$1.639 \cdot 10^{-5}$	25137.1	2354.79
$3.721 \cdot 10^{-3}$	$1.370 \cdot 10^{-5}$	22164.7	2061.40
$4.086 \cdot 10^{-3}$	$1.082 \cdot 10^{-5}$	19125.1	1791.56
$4.468 \cdot 10^{-3}$	$8.093 \cdot 10^{-6}$	17539.9	1635.78
$4.867 \cdot 10^{-3}$	$6.386 \cdot 10^{-6}$	17303.2	1603.71
$5.284 \cdot 10^{-3}$	$7.076 \cdot 10^{-6}$	15595.0	1451.33
$5.719 \cdot 10^{-3}$	$1.016 \cdot 10^{-5}$	14030.3	1303.90
$6.170 \cdot 10^{-3}$	$1.448 \cdot 10^{-5}$	12902.2	1197.52
$6.640 \cdot 10^{-3}$	$1.967 \cdot 10^{-5}$	12974.3	1203.39
$7.127 \cdot 10^{-3}$	$2.514 \cdot 10^{-5}$	10931.9	1016.39
$7.630 \cdot 10^{-3}$	$3.137 \cdot 10^{-5}$	10463.5	965.833
$8.152 \cdot 10^{-3}$	$3.771 \cdot 10^{-5}$	9301.66	862.897
$8.690 \cdot 10^{-3}$	$4.460 \cdot 10^{-5}$	8358.22	777.155
$9.246 \cdot 10^{-3}$	$5.218 \cdot 10^{-5}$	7846.71	729.405
$9.822 \cdot 10^{-3}$	$5.955 \cdot 10^{-5}$	7285.17	681.452
$1.041 \cdot 10^{-2}$	$6.788 \cdot 10^{-5}$	5758.87	551.970
$1.102 \cdot 10^{-2}$	$7.606 \cdot 10^{-5}$	5943.85	558.994
$1.165 \cdot 10^{-2}$	$8.535 \cdot 10^{-5}$	4997.11	478.819
$1.229 \cdot 10^{-2}$	$9.431 \cdot 10^{-5}$	4300.84	416.885
$1.296 \cdot 10^{-2}$	$1.036 \cdot 10^{-4}$	3926.87	381.518
$1.364 \cdot 10^{-2}$	$1.135 \cdot 10^{-4}$	3562.98	348.532
$1.433 \cdot 10^{-2}$	$1.238 \cdot 10^{-4}$	3036.65	301.929
$1.505 \cdot 10^{-2}$	$1.350 \cdot 10^{-4}$	2607.57	264.486
$1.578 \cdot 10^{-2}$	$1.457 \cdot 10^{-4}$	2407.43	244.356
$1.653 \cdot 10^{-2}$	$1.569 \cdot 10^{-4}$	1829.17	195.811
$1.730 \cdot 10^{-2}$	$1.689 \cdot 10^{-4}$	1609.35	174.487
$1.808 \cdot 10^{-2}$	$1.813 \cdot 10^{-4}$	1414.28	157.639
$1.889 \cdot 10^{-2}$	$1.939 \cdot 10^{-4}$	1125.66	131.950
$1.971 \cdot 10^{-2}$	$2.067 \cdot 10^{-4}$	874.895	109.210

continued from previous page

$-t \left[(\text{GeV}/c)^2\right]$	$\Delta t \left[(\text{GeV}/c)^2\right]$	$\frac{\mathrm{d}\sigma}{\mathrm{d}t} \left[\text{mb}/(\text{GeV}/c)^2\right]$	$\Delta\frac{\mathrm{d}\sigma}{\mathrm{d}t} \left[\text{mb}/(\text{GeV}/c)^2\right]$
$2.055 \cdot 10^{-2}$	$2.204 \cdot 10^{-4}$	1013.15	119.841
$2.141 \cdot 10^{-2}$	$2.340 \cdot 10^{-4}$	637.569	86.2220
$2.228 \cdot 10^{-2}$	$2.483 \cdot 10^{-4}$	499.854	72.5437
$2.317 \cdot 10^{-2}$	$2.624 \cdot 10^{-4}$	361.083	58.5857
$2.408 \cdot 10^{-2}$	$2.778 \cdot 10^{-4}$	311.002	53.0721
$2.501 \cdot 10^{-2}$	$2.926 \cdot 10^{-4}$	229.988	43.9541
$2.596 \cdot 10^{-2}$	$3.076 \cdot 10^{-4}$	178.144	37.6791
$2.692 \cdot 10^{-2}$	$3.237 \cdot 10^{-4}$	90.6799	26.3205
$2.790 \cdot 10^{-2}$	$3.397 \cdot 10^{-4}$	69.6753	22.9584
$2.890 \cdot 10^{-2}$	$3.566 \cdot 10^{-4}$	50.4774	19.4071
$2.992 \cdot 10^{-2}$	$3.737 \cdot 10^{-4}$	24.6142	14.5835
$3.095 \cdot 10^{-2}$	$3.910 \cdot 10^{-4}$	12.8991	11.4264
$3.201 \cdot 10^{-2}$	$4.079 \cdot 10^{-4}$	28.9341	15.1845
$3.307 \cdot 10^{-2}$	$4.239 \cdot 10^{-4}$	10.9867	11.2633
$3.416 \cdot 10^{-2}$	$4.426 \cdot 10^{-4}$	27.2503	14.7179
$3.527 \cdot 10^{-2}$	$4.598 \cdot 10^{-4}$	21.4286	13.3764
$3.639 \cdot 10^{-2}$	$4.759 \cdot 10^{-4}$	52.0878	18.9736
$3.752 \cdot 10^{-2}$	$4.913 \cdot 10^{-4}$	57.2586	19.4712
$3.868 \cdot 10^{-2}$	$5.081 \cdot 10^{-4}$	88.2176	23.6353
$3.985 \cdot 10^{-2}$	$5.222 \cdot 10^{-4}$	72.8120	21.3809
$4.103 \cdot 10^{-2}$	$5.335 \cdot 10^{-4}$	67.8957	20.6090
$4.223 \cdot 10^{-2}$	$5.460 \cdot 10^{-4}$	68.3880	20.8809
$4.344 \cdot 10^{-2}$	$5.560 \cdot 10^{-4}$	58.4466	19.7311
$4.466 \cdot 10^{-2}$	$5.662 \cdot 10^{-4}$	68.9959	22.4565
$4.590 \cdot 10^{-2}$	$5.738 \cdot 10^{-4}$	129.357	34.6462
$4.715 \cdot 10^{-2}$	$5.828 \cdot 10^{-4}$	78.1653	27.1011
$4.841 \cdot 10^{-2}$	$5.944 \cdot 10^{-4}$	87.8873	31.7746
$4.970 \cdot 10^{-2}$	$6.066 \cdot 10^{-4}$	99.5724	38.3604
$5.099 \cdot 10^{-2}$	$6.196 \cdot 10^{-4}$	100.775	43.4169
$5.231 \cdot 10^{-2}$	$6.325 \cdot 10^{-4}$	115.183	55.8513
$5.363 \cdot 10^{-2}$	$6.479 \cdot 10^{-4}$	110.855	64.0544
$5.497 \cdot 10^{-2}$	$6.651 \cdot 10^{-4}$	125.527	85.7646
$5.633 \cdot 10^{-2}$	$6.850 \cdot 10^{-4}$	146.487	123.694
$5.771 \cdot 10^{-2}$	$7.068 \cdot 10^{-4}$	126.581	150.398
$5.910 \cdot 10^{-2}$	$7.308 \cdot 10^{-4}$	149.301	275.961
$6.052 \cdot 10^{-2}$	$7.564 \cdot 10^{-4}$	148.005	588.568

Differential cross section for p-^{56}Ni elastic scattering
(with 2 mm slit aperture)

$-t$ $\left[(\text{GeV}/c)^2\right]$	Δt $\left[(\text{GeV}/c)^2\right]$	$\frac{\mathrm{d}\sigma}{\mathrm{d}t}$ $\left[\text{mb}/(\text{GeV}/c)^2\right]$	$\Delta\frac{\mathrm{d}\sigma}{\mathrm{d}t}$ $\left[\text{mb}/(\text{GeV}/c)^2\right]$
$1.688 \cdot 10^{-3}$	$2.657 \cdot 10^{-5}$	78878.7	4186.83
$1.935 \cdot 10^{-3}$	$2.595 \cdot 10^{-5}$	65897.0	3552.52
$2.200 \cdot 10^{-3}$	$2.482 \cdot 10^{-5}$	54078.9	2960.49
$2.482 \cdot 10^{-3}$	$2.338 \cdot 10^{-5}$	46369.6	2578.88
$2.780 \cdot 10^{-3}$	$2.172 \cdot 10^{-5}$	42095.5	2357.88
$3.096 \cdot 10^{-3}$	$1.972 \cdot 10^{-5}$	35015.0	2017.36
$3.430 \cdot 10^{-3}$	$1.747 \cdot 10^{-5}$	36911.0	2097.04
$3.781 \cdot 10^{-3}$	$1.494 \cdot 10^{-5}$	31213.5	1810.88
$4.148 \cdot 10^{-3}$	$1.214 \cdot 10^{-5}$	28429.4	1654.55
$4.533 \cdot 10^{-3}$	$9.665 \cdot 10^{-6}$	25979.2	1523.81
$4.935 \cdot 10^{-3}$	$8.116 \cdot 10^{-6}$	23889.5	1412.56
$5.355 \cdot 10^{-3}$	$8.424 \cdot 10^{-6}$	23171.8	1366.14
$5.793 \cdot 10^{-3}$	$1.111 \cdot 10^{-5}$	21638.0	1287.97
$6.248 \cdot 10^{-3}$	$1.526 \cdot 10^{-5}$	18549.8	1125.42
$6.721 \cdot 10^{-3}$	$1.986 \cdot 10^{-5}$	17749.9	1076.07
$7.211 \cdot 10^{-3}$	$2.532 \cdot 10^{-5}$	17018.3	1030.07
$7.717 \cdot 10^{-3}$	$3.150 \cdot 10^{-5}$	15186.0	933.544
$8.241 \cdot 10^{-3}$	$3.770 \cdot 10^{-5}$	13505.5	839.615
$8.782 \cdot 10^{-3}$	$4.497 \cdot 10^{-5}$	12026.6	758.997
$9.341 \cdot 10^{-3}$	$5.186 \cdot 10^{-5}$	11053.1	708.201
$9.920 \cdot 10^{-3}$	$5.997 \cdot 10^{-5}$	10612.9	679.680
$1.051 \cdot 10^{-2}$	$6.730 \cdot 10^{-5}$	9355.48	612.005
$1.113 \cdot 10^{-2}$	$7.602 \cdot 10^{-5}$	8019.68	539.284
$1.175 \cdot 10^{-2}$	$8.495 \cdot 10^{-5}$	7351.16	500.584
$1.240 \cdot 10^{-2}$	$9.405 \cdot 10^{-5}$	6808.59	469.949
$1.307 \cdot 10^{-2}$	$1.035 \cdot 10^{-4}$	5759.54	411.783
$1.375 \cdot 10^{-2}$	$1.134 \cdot 10^{-4}$	4977.36	365.795
$1.445 \cdot 10^{-2}$	$1.237 \cdot 10^{-4}$	4475.97	333.873
$1.517 \cdot 10^{-2}$	$1.348 \cdot 10^{-4}$	3980.96	304.840
$1.591 \cdot 10^{-2}$	$1.453 \cdot 10^{-4}$	3011.57	247.810
$1.666 \cdot 10^{-2}$	$1.563 \cdot 10^{-4}$	2601.65	222.229
$1.743 \cdot 10^{-2}$	$1.686 \cdot 10^{-4}$	2045.48	188.142
$1.822 \cdot 10^{-2}$	$1.812 \cdot 10^{-4}$	1937.58	180.315
$1.903 \cdot 10^{-2}$	$1.935 \cdot 10^{-4}$	1709.02	164.801
$1.985 \cdot 10^{-2}$	$2.059 \cdot 10^{-4}$	1187.62	130.356
$2.069 \cdot 10^{-2}$	$2.196 \cdot 10^{-4}$	1093.54	122.591
$2.155 \cdot 10^{-2}$	$2.327 \cdot 10^{-4}$	1057.38	119.131
$2.243 \cdot 10^{-2}$	$2.463 \cdot 10^{-4}$	740.686	96.0346
$2.332 \cdot 10^{-2}$	$2.602 \cdot 10^{-4}$	552.835	80.6919
$2.423 \cdot 10^{-2}$	$2.748 \cdot 10^{-4}$	351.075	62.7850

continued from previous page

$-t\ \left[(\mathrm{GeV}/c)^2\right]$	$\Delta t\ \left[(\mathrm{GeV}/c)^2\right]$	$\frac{\mathrm{d}\sigma}{\mathrm{d}t}\ \left[\mathrm{mb}/(\mathrm{GeV}/c)^2\right]$	$\Delta\frac{\mathrm{d}\sigma}{\mathrm{d}t}\ \left[\mathrm{mb}/(\mathrm{GeV}/c)^2\right]$
$2.516\cdot10^{-2}$	$2.881\cdot10^{-4}$	255.689	52.8387
$2.611\cdot10^{-2}$	$3.022\cdot10^{-4}$	145.193	39.7501
$2.707\cdot10^{-2}$	$3.155\cdot10^{-4}$	170.124	42.5030
$2.805\cdot10^{-2}$	$3.281\cdot10^{-4}$	30.2173	20.0749
$2.904\cdot10^{-2}$	$3.406\cdot10^{-4}$	30.3958	19.6339
$3.005\cdot10^{-2}$	$3.527\cdot10^{-4}$	66.3445	26.4136
$3.108\cdot10^{-2}$	$3.625\cdot10^{-4}$	12.4120	14.2688
$3.212\cdot10^{-2}$	$3.699\cdot10^{-4}$	3.41184	11.1235
$3.316\cdot10^{-2}$	$3.781\cdot10^{-4}$	12.2598	14.0321
$3.423\cdot10^{-2}$	$3.849\cdot10^{-4}$	29.0228	18.7990
$3.530\cdot10^{-2}$	$3.921\cdot10^{-4}$	20.4077	16.6621
$3.639\cdot10^{-2}$	$3.972\cdot10^{-4}$	63.8634	26.0535
$3.749\cdot10^{-2}$	$4.036\cdot10^{-4}$	55.0381	24.8235
$3.861\cdot10^{-2}$	$4.114\cdot10^{-4}$	180.135	43.9982
$3.974\cdot10^{-2}$	$4.178\cdot10^{-4}$	101.248	33.5027
$4.087\cdot10^{-2}$	$4.246\cdot10^{-4}$	67.1342	27.7819
$4.202\cdot10^{-2}$	$4.345\cdot10^{-4}$	95.8136	33.6884
$4.319\cdot10^{-2}$	$4.465\cdot10^{-4}$	42.1598	23.1058
$4.437\cdot10^{-2}$	$4.574\cdot10^{-4}$	52.1506	26.1906
$4.556\cdot10^{-2}$	$4.706\cdot10^{-4}$	154.654	46.8195
$4.677\cdot10^{-2}$	$4.836\cdot10^{-4}$	85.8955	35.0877
$4.800\cdot10^{-2}$	$4.993\cdot10^{-4}$	130.324	45.9134
$4.924\cdot10^{-2}$	$5.168\cdot10^{-4}$	147.404	51.0901
$5.050\cdot10^{-2}$	$5.344\cdot10^{-4}$	120.434	47.0847
$5.178\cdot10^{-2}$	$5.520\cdot10^{-4}$	161.987	59.7883
$5.307\cdot10^{-2}$	$5.691\cdot10^{-4}$	119.888	52.0006
$5.438\cdot10^{-2}$	$5.887\cdot10^{-4}$	128.714	57.4330
$5.570\cdot10^{-2}$	$6.097\cdot10^{-4}$	164.838	73.7171
$5.705\cdot10^{-2}$	$6.312\cdot10^{-4}$	98.3491	56.6178
$5.841\cdot10^{-2}$	$6.531\cdot10^{-4}$	124.856	72.2554
$5.979\cdot10^{-2}$	$6.771\cdot10^{-4}$	139.926	86.3798
$6.119\cdot10^{-2}$	$6.986\cdot10^{-4}$	74.8124	62.2242
$6.261\cdot10^{-2}$	$7.264\cdot10^{-4}$	88.9081	80.1421
$6.404\cdot10^{-2}$	$7.547\cdot10^{-4}$	131.298	130.360
$6.550\cdot10^{-2}$	$7.836\cdot10^{-4}$	92.0134	125.870
$6.697\cdot10^{-2}$	$8.104\cdot10^{-4}$	76.8724	153.980
$6.846\cdot10^{-2}$	$8.423\cdot10^{-4}$	225.806	726.069
$6.997\cdot10^{-2}$	$8.776\cdot10^{-4}$	97.1599	733.353

Differential cross section for p-^{56}Ni elastic scattering (without slit aperture)

$-t$ $\left[(\text{GeV}/c)^2\right]$	Δt $\left[(\text{GeV}/c)^2\right]$	$\frac{d\sigma}{dt}$ $\left[\text{mb}/(\text{GeV}/c)^2\right]$	$\Delta \frac{d\sigma}{dt}$ $\left[\text{mb}/(\text{GeV}/c)^2\right]$
$3.711 \cdot 10^{-3}$	$1.765 \cdot 10^{-5}$	30659.0	603.519
$4.032 \cdot 10^{-3}$	$1.688 \cdot 10^{-5}$	26015.1	534.982
$4.365 \cdot 10^{-3}$	$1.593 \cdot 10^{-5}$	25427.6	522.639
$4.713 \cdot 10^{-3}$	$1.506 \cdot 10^{-5}$	23887.1	498.089
$5.074 \cdot 10^{-3}$	$1.431 \cdot 10^{-5}$	21962.7	469.405
$5.449 \cdot 10^{-3}$	$1.337 \cdot 10^{-5}$	19987.7	436.124
$5.836 \cdot 10^{-3}$	$1.295 \cdot 10^{-5}$	19009.8	416.546
$6.239 \cdot 10^{-3}$	$1.287 \cdot 10^{-5}$	17114.0	387.194
$6.654 \cdot 10^{-3}$	$1.263 \cdot 10^{-5}$	15957.2	367.162
$7.083 \cdot 10^{-3}$	$1.309 \cdot 10^{-5}$	14592.0	343.253
$7.526 \cdot 10^{-3}$	$1.445 \cdot 10^{-5}$	13891.9	330.388
$7.982 \cdot 10^{-3}$	$1.583 \cdot 10^{-5}$	12319.6	302.063
$8.451 \cdot 10^{-3}$	$1.760 \cdot 10^{-5}$	11280.2	281.952
$8.933 \cdot 10^{-3}$	$1.982 \cdot 10^{-5}$	10663.5	270.761
$9.429 \cdot 10^{-3}$	$2.266 \cdot 10^{-5}$	10048.2	257.565
$9.939 \cdot 10^{-3}$	$2.549 \cdot 10^{-5}$	9055.37	238.714
$1.046 \cdot 10^{-2}$	$2.871 \cdot 10^{-5}$	8139.29	221.016
$1.100 \cdot 10^{-2}$	$3.216 \cdot 10^{-5}$	7335.92	204.959
$1.155 \cdot 10^{-2}$	$3.605 \cdot 10^{-5}$	6577.33	190.433
$1.212 \cdot 10^{-2}$	$3.968 \cdot 10^{-5}$	5808.24	174.724
$1.270 \cdot 10^{-2}$	$4.402 \cdot 10^{-5}$	5454.80	167.169
$1.329 \cdot 10^{-2}$	$4.803 \cdot 10^{-5}$	4916.87	155.162
$1.390 \cdot 10^{-2}$	$5.248 \cdot 10^{-5}$	4118.01	138.032
$1.452 \cdot 10^{-2}$	$5.648 \cdot 10^{-5}$	3797.78	130.456
$1.515 \cdot 10^{-2}$	$6.099 \cdot 10^{-5}$	3479.33	122.765
$1.580 \cdot 10^{-2}$	$6.624 \cdot 10^{-5}$	3024.22	112.004
$1.646 \cdot 10^{-2}$	$7.153 \cdot 10^{-5}$	2529.54	99.5356
$1.713 \cdot 10^{-2}$	$7.664 \cdot 10^{-5}$	2260.27	92.6901
$1.782 \cdot 10^{-2}$	$8.232 \cdot 10^{-5}$	1928.78	84.1745
$1.852 \cdot 10^{-2}$	$8.822 \cdot 10^{-5}$	1627.66	76.2710
$1.924 \cdot 10^{-2}$	$9.336 \cdot 10^{-5}$	1394.38	69.6235
$1.997 \cdot 10^{-2}$	$9.971 \cdot 10^{-5}$	1121.70	61.6839
$2.071 \cdot 10^{-2}$	$1.057 \cdot 10^{-4}$	941.277	56.0187
$2.147 \cdot 10^{-2}$	$1.123 \cdot 10^{-4}$	811.509	51.6815
$2.225 \cdot 10^{-2}$	$1.187 \cdot 10^{-4}$	692.007	47.4538
$2.303 \cdot 10^{-2}$	$1.251 \cdot 10^{-4}$	569.183	42.9315
$2.383 \cdot 10^{-2}$	$1.316 \cdot 10^{-4}$	491.174	39.8875
$2.465 \cdot 10^{-2}$	$1.392 \cdot 10^{-4}$	345.295	33.9531
$2.547 \cdot 10^{-2}$	$1.460 \cdot 10^{-4}$	252.802	29.6860
$2.631 \cdot 10^{-2}$	$1.534 \cdot 10^{-4}$	200.059	27.0368
$2.717 \cdot 10^{-2}$	$1.612 \cdot 10^{-4}$	119.372	22.7371

continued from previous page

$-t\ \left[(\mathrm{GeV}/c)^2\right]$	$\Delta t\ \left[(\mathrm{GeV}/c)^2\right]$	$\frac{\mathrm{d}\sigma}{\mathrm{d}t}\ \left[\mathrm{mb}/(\mathrm{GeV}/c)^2\right]$	$\Delta\frac{\mathrm{d}\sigma}{\mathrm{d}t}\ \left[\mathrm{mb}/(\mathrm{GeV}/c)^2\right]$
$2.804\cdot10^{-2}$	$1.686\cdot10^{-4}$	131.669	23.1563
$2.892\cdot10^{-2}$	$1.758\cdot10^{-4}$	64.1337	19.1538
$2.981\cdot10^{-2}$	$1.835\cdot10^{-4}$	52.5525	18.3320
$3.072\cdot10^{-2}$	$1.919\cdot10^{-4}$	35.0035	17.0259
$3.165\cdot10^{-2}$	$2.005\cdot10^{-4}$	15.9109	15.5205
$3.258\cdot10^{-2}$	$2.089\cdot10^{-4}$	20.1997	15.6138
$3.354\cdot10^{-2}$	$2.178\cdot10^{-4}$	19.5291	15.4172
$3.450\cdot10^{-2}$	$2.265\cdot10^{-4}$	34.2856	16.2587
$3.548\cdot10^{-2}$	$2.362\cdot10^{-4}$	25.2380	15.6935
$3.647\cdot10^{-2}$	$2.448\cdot10^{-4}$	33.9888	16.0300
$3.748\cdot10^{-2}$	$2.547\cdot10^{-4}$	34.9371	15.9850
$3.851\cdot10^{-2}$	$2.643\cdot10^{-4}$	48.2131	16.7196
$3.954\cdot10^{-2}$	$2.745\cdot10^{-4}$	37.2886	15.8680
$4.059\cdot10^{-2}$	$2.835\cdot10^{-4}$	70.8981	17.7013
$4.166\cdot10^{-2}$	$2.927\cdot10^{-4}$	82.2236	18.3252
$4.274\cdot10^{-2}$	$3.037\cdot10^{-4}$	89.7770	18.4624
$4.383\cdot10^{-2}$	$3.135\cdot10^{-4}$	102.774	18.8937
$4.494\cdot10^{-2}$	$3.238\cdot10^{-4}$	110.916	19.1301
$4.605\cdot10^{-2}$	$3.341\cdot10^{-4}$	135.039	20.0370
$4.719\cdot10^{-2}$	$3.458\cdot10^{-4}$	104.402	18.2641
$4.833\cdot10^{-2}$	$3.563\cdot10^{-4}$	147.614	20.1606
$4.949\cdot10^{-2}$	$3.666\cdot10^{-4}$	119.188	18.5853
$5.067\cdot10^{-2}$	$3.775\cdot10^{-4}$	146.225	19.5823
$5.186\cdot10^{-2}$	$3.885\cdot10^{-4}$	168.408	20.3648
$5.306\cdot10^{-2}$	$4.013\cdot10^{-4}$	140.815	18.8979
$5.427\cdot10^{-2}$	$4.143\cdot10^{-4}$	162.157	19.7014
$5.550\cdot10^{-2}$	$4.248\cdot10^{-4}$	141.938	18.5918
$5.675\cdot10^{-2}$	$4.375\cdot10^{-4}$	149.430	18.7444
$5.800\cdot10^{-2}$	$4.499\cdot10^{-4}$	137.777	18.0589
$5.928\cdot10^{-2}$	$4.633\cdot10^{-4}$	142.591	17.8845
$6.057\cdot10^{-2}$	$4.756\cdot10^{-4}$	145.239	17.9400
$6.187\cdot10^{-2}$	$4.884\cdot10^{-4}$	150.747	18.0217
$6.319\cdot10^{-2}$	$5.023\cdot10^{-4}$	130.771	16.8860
$6.451\cdot10^{-2}$	$5.144\cdot10^{-4}$	87.7071	14.4450
$6.586\cdot10^{-2}$	$5.259\cdot10^{-4}$	137.020	16.8509
$6.721\cdot10^{-2}$	$5.391\cdot10^{-4}$	90.2076	14.2452
$6.857\cdot10^{-2}$	$5.517\cdot10^{-4}$	112.682	15.2975
$6.995\cdot10^{-2}$	$5.664\cdot10^{-4}$	86.6578	13.7260
$7.135\cdot10^{-2}$	$5.807\cdot10^{-4}$	107.254	14.7043
$7.276\cdot10^{-2}$	$5.967\cdot10^{-4}$	78.8038	12.9664
$7.418\cdot10^{-2}$	$6.104\cdot10^{-4}$	88.8423	13.3931
$7.562\cdot10^{-2}$	$6.260\cdot10^{-4}$	66.8929	11.9402
$7.707\cdot10^{-2}$	$6.409\cdot10^{-4}$	56.8656	11.1543
$7.854\cdot10^{-2}$	$6.555\cdot10^{-4}$	42.7364	10.0326

B. Differential cross sections

Differential cross section for p-^{58}Ni elastic scattering
(with 1 mm slit aperture)

$-t \left[(\mathrm{GeV}/c)^2\right]$	$\Delta t \left[(\mathrm{GeV}/c)^2\right]$	$\frac{\mathrm{d}\sigma}{\mathrm{d}t} \left[\mathrm{mb}/(\mathrm{GeV}/c)^2\right]$	$\Delta\frac{\mathrm{d}\sigma}{\mathrm{d}t} \left[\mathrm{mb}/(\mathrm{GeV}/c)^2\right]$
$1.589 \cdot 10^{-3}$	$2.210 \cdot 10^{-5}$	68728.0	5979.70
$1.837 \cdot 10^{-3}$	$2.119 \cdot 10^{-5}$	58721.1	5041.50
$2.103 \cdot 10^{-3}$	$1.993 \cdot 10^{-5}$	50208.2	4313.48
$2.387 \cdot 10^{-3}$	$1.829 \cdot 10^{-5}$	43649.9	3725.23
$2.690 \cdot 10^{-3}$	$1.640 \cdot 10^{-5}$	38418.8	3307.55
$3.011 \cdot 10^{-3}$	$1.401 \cdot 10^{-5}$	34408.6	2960.25
$3.350 \cdot 10^{-3}$	$1.156 \cdot 10^{-5}$	31390.9	2715.83
$3.709 \cdot 10^{-3}$	$8.813 \cdot 10^{-6}$	28606.0	2464.35
$4.085 \cdot 10^{-3}$	$6.542 \cdot 10^{-6}$	25755.0	2234.62
$4.479 \cdot 10^{-3}$	$5.969 \cdot 10^{-6}$	23936.3	2060.49
$4.893 \cdot 10^{-3}$	$8.194 \cdot 10^{-6}$	22077.2	1922.39
$5.324 \cdot 10^{-3}$	$1.224 \cdot 10^{-5}$	20147.6	1740.16
$5.775 \cdot 10^{-3}$	$1.691 \cdot 10^{-5}$	18468.0	1594.79
$6.243 \cdot 10^{-3}$	$2.237 \cdot 10^{-5}$	16915.9	1453.03
$6.732 \cdot 10^{-3}$	$2.832 \cdot 10^{-5}$	15815.1	1371.71
$7.237 \cdot 10^{-3}$	$3.459 \cdot 10^{-5}$	14541.8	1254.44
$7.762 \cdot 10^{-3}$	$4.135 \cdot 10^{-5}$	13067.7	1116.79
$8.306 \cdot 10^{-3}$	$4.859 \cdot 10^{-5}$	12004.3	1026.43
$8.867 \cdot 10^{-3}$	$5.574 \cdot 10^{-5}$	10623.6	905.962
$9.448 \cdot 10^{-3}$	$6.450 \cdot 10^{-5}$	9710.15	830.846
$1.005 \cdot 10^{-2}$	$7.235 \cdot 10^{-5}$	8822.88	749.362
$1.067 \cdot 10^{-2}$	$8.166 \cdot 10^{-5}$	7787.31	666.587
$1.130 \cdot 10^{-2}$	$9.046 \cdot 10^{-5}$	6836.75	574.930
$1.196 \cdot 10^{-2}$	$1.001 \cdot 10^{-4}$	6045.34	510.591
$1.263 \cdot 10^{-2}$	$1.102 \cdot 10^{-4}$	5311.62	446.067
$1.333 \cdot 10^{-2}$	$1.208 \cdot 10^{-4}$	4566.32	384.702
$1.404 \cdot 10^{-2}$	$1.316 \cdot 10^{-4}$	3912.15	328.946
$1.477 \cdot 10^{-2}$	$1.429 \cdot 10^{-4}$	3464.93	290.414
$1.552 \cdot 10^{-2}$	$1.544 \cdot 10^{-4}$	2935.58	246.615
$1.629 \cdot 10^{-2}$	$1.666 \cdot 10^{-4}$	2464.21	206.118
$1.708 \cdot 10^{-2}$	$1.783 \cdot 10^{-4}$	2074.75	172.719
$1.788 \cdot 10^{-2}$	$1.917 \cdot 10^{-4}$	1701.88	140.946
$1.871 \cdot 10^{-2}$	$2.054 \cdot 10^{-4}$	1401.06	117.280
$1.955 \cdot 10^{-2}$	$2.185 \cdot 10^{-4}$	1109.72	92.6179
$2.041 \cdot 10^{-2}$	$2.327 \cdot 10^{-4}$	948.649	79.3258
$2.130 \cdot 10^{-2}$	$2.473 \cdot 10^{-4}$	729.052	61.6865
$2.220 \cdot 10^{-2}$	$2.625 \cdot 10^{-4}$	525.232	44.9110
$2.312 \cdot 10^{-2}$	$2.764 \cdot 10^{-4}$	426.895	37.0234
$2.406 \cdot 10^{-2}$	$2.934 \cdot 10^{-4}$	305.025	27.1296
$2.502 \cdot 10^{-2}$	$3.095 \cdot 10^{-4}$	206.241	19.2386

$-t$ $\left[(\text{GeV}/c)^2\right]$	Δt $\left[(\text{GeV}/c)^2\right]$	$\frac{d\sigma}{dt}$ $\left[\text{mb}/(\text{GeV}/c)^2\right]$	$\Delta\frac{d\sigma}{dt}$ $\left[\text{mb}/(\text{GeV}/c)^2\right]$
$2.599 \cdot 10^{-2}$	$3.256 \cdot 10^{-4}$	134.307	13.4707
$2.699 \cdot 10^{-2}$	$3.423 \cdot 10^{-4}$	85.9642	9.56504
$2.800 \cdot 10^{-2}$	$3.588 \cdot 10^{-4}$	57.8155	7.26897
$2.904 \cdot 10^{-2}$	$3.767 \cdot 10^{-4}$	35.6431	5.45677
$3.009 \cdot 10^{-2}$	$3.945 \cdot 10^{-4}$	25.8611	4.60047
$3.116 \cdot 10^{-2}$	$4.125 \cdot 10^{-4}$	20.0446	4.11587
$3.225 \cdot 10^{-2}$	$4.306 \cdot 10^{-4}$	19.4853	4.02686
$3.336 \cdot 10^{-2}$	$4.475 \cdot 10^{-4}$	39.7910	5.50502
$3.449 \cdot 10^{-2}$	$4.668 \cdot 10^{-4}$	46.1525	5.91275
$3.563 \cdot 10^{-2}$	$4.849 \cdot 10^{-4}$	70.4842	7.61851
$3.680 \cdot 10^{-2}$	$5.019 \cdot 10^{-4}$	86.9536	8.76191
$3.797 \cdot 10^{-2}$	$5.181 \cdot 10^{-4}$	99.9823	9.72749
$3.917 \cdot 10^{-2}$	$5.349 \cdot 10^{-4}$	109.830	10.6987
$4.039 \cdot 10^{-2}$	$5.506 \cdot 10^{-4}$	125.567	12.4270
$4.161 \cdot 10^{-2}$	$5.618 \cdot 10^{-4}$	141.128	14.9992
$4.286 \cdot 10^{-2}$	$5.745 \cdot 10^{-4}$	161.475	19.2574
$4.411 \cdot 10^{-2}$	$5.836 \cdot 10^{-4}$	166.876	22.8963
$4.538 \cdot 10^{-2}$	$5.928 \cdot 10^{-4}$	171.721	27.8837
$4.667 \cdot 10^{-2}$	$6.010 \cdot 10^{-4}$	186.984	36.1763
$4.796 \cdot 10^{-2}$	$6.096 \cdot 10^{-4}$	199.263	46.0675
$4.927 \cdot 10^{-2}$	$6.211 \cdot 10^{-4}$	192.050	53.3451
$5.060 \cdot 10^{-2}$	$6.346 \cdot 10^{-4}$	180.755	59.8598
$5.194 \cdot 10^{-2}$	$6.488 \cdot 10^{-4}$	185.077	73.3174
$5.331 \cdot 10^{-2}$	$6.633 \cdot 10^{-4}$	190.199	90.7837
$5.468 \cdot 10^{-2}$	$6.824 \cdot 10^{-4}$	172.530	102.339
$5.608 \cdot 10^{-2}$	$7.022 \cdot 10^{-4}$	168.719	125.623
$5.749 \cdot 10^{-2}$	$7.269 \cdot 10^{-4}$	163.193	164.927

Differential cross section for p-^{58}Ni elastic scattering (without slit aperture)

$-t$ $\left[(\text{GeV}/c)^2\right]$	Δt $\left[(\text{GeV}/c)^2\right]$	$\frac{d\sigma}{dt}$ $\left[\text{mb}/(\text{GeV}/c)^2\right]$	$\Delta\frac{d\sigma}{dt}$ $\left[\text{mb}/(\text{GeV}/c)^2\right]$
$3.173 \cdot 10^{-3}$	$1.849 \cdot 10^{-5}$	34971.3	617.394
$3.472 \cdot 10^{-3}$	$1.781 \cdot 10^{-5}$	30718.9	562.673
$3.784 \cdot 10^{-3}$	$1.704 \cdot 10^{-5}$	28455.5	531.138
$4.110 \cdot 10^{-3}$	$1.631 \cdot 10^{-5}$	25778.9	492.556
$4.450 \cdot 10^{-3}$	$1.544 \cdot 10^{-5}$	23212.1	456.859
$4.803 \cdot 10^{-3}$	$1.464 \cdot 10^{-5}$	22162.2	440.433
$5.171 \cdot 10^{-3}$	$1.375 \cdot 10^{-5}$	20027.1	406.653
$5.552 \cdot 10^{-3}$	$1.279 \cdot 10^{-5}$	18939.8	391.942

B. Differential cross sections

continued from previous page

$-t\ \left[(\mathrm{GeV}/c)^2\right]$	$\Delta t\ \left[(\mathrm{GeV}/c)^2\right]$	$\frac{\mathrm{d}\sigma}{\mathrm{d}t}\ \left[\mathrm{mb}/(\mathrm{GeV}/c)^2\right]$	$\Delta\frac{\mathrm{d}\sigma}{\mathrm{d}t}\ \left[\mathrm{mb}/(\mathrm{GeV}/c)^2\right]$
$5.947 \cdot 10^{-3}$	$1.243 \cdot 10^{-5}$	17112.8	361.817
$6.357 \cdot 10^{-3}$	$1.256 \cdot 10^{-5}$	16853.1	357.631
$6.779 \cdot 10^{-3}$	$1.282 \cdot 10^{-5}$	14977.3	326.991
$7.215 \cdot 10^{-3}$	$1.345 \cdot 10^{-5}$	13495.2	301.460
$7.665 \cdot 10^{-3}$	$1.479 \cdot 10^{-5}$	12460.5	284.724
$8.130 \cdot 10^{-3}$	$1.644 \cdot 10^{-5}$	11605.9	268.189
$8.606 \cdot 10^{-3}$	$1.876 \cdot 10^{-5}$	10828.2	255.815
$9.098 \cdot 10^{-3}$	$2.092 \cdot 10^{-5}$	9953.44	238.997
$9.602 \cdot 10^{-3}$	$2.380 \cdot 10^{-5}$	9121.36	225.346
$1.012 \cdot 10^{-2}$	$2.697 \cdot 10^{-5}$	8220.38	208.519
$1.065 \cdot 10^{-2}$	$3.038 \cdot 10^{-5}$	7245.07	190.019
$1.120 \cdot 10^{-2}$	$3.374 \cdot 10^{-5}$	7018.09	184.280
$1.176 \cdot 10^{-2}$	$3.745 \cdot 10^{-5}$	6217.40	169.426
$1.234 \cdot 10^{-2}$	$4.160 \cdot 10^{-5}$	5441.24	154.530
$1.293 \cdot 10^{-2}$	$4.531 \cdot 10^{-5}$	4838.72	142.600
$1.353 \cdot 10^{-2}$	$4.996 \cdot 10^{-5}$	4339.65	132.611
$1.415 \cdot 10^{-2}$	$5.398 \cdot 10^{-5}$	3775.67	120.955
$1.478 \cdot 10^{-2}$	$5.907 \cdot 10^{-5}$	3415.24	113.410
$1.542 \cdot 10^{-2}$	$6.335 \cdot 10^{-5}$	2914.17	102.133
$1.608 \cdot 10^{-2}$	$6.850 \cdot 10^{-5}$	2555.76	93.5837
$1.675 \cdot 10^{-2}$	$7.395 \cdot 10^{-5}$	2189.49	84.5011
$1.743 \cdot 10^{-2}$	$7.914 \cdot 10^{-5}$	1873.98	76.6020
$1.813 \cdot 10^{-2}$	$8.532 \cdot 10^{-5}$	1676.58	71.6059
$1.885 \cdot 10^{-2}$	$9.085 \cdot 10^{-5}$	1273.78	61.1091
$1.958 \cdot 10^{-2}$	$9.683 \cdot 10^{-5}$	1165.13	57.7910
$2.032 \cdot 10^{-2}$	$1.030 \cdot 10^{-4}$	982.539	52.4022
$2.108 \cdot 10^{-2}$	$1.096 \cdot 10^{-4}$	916.348	50.1946
$2.185 \cdot 10^{-2}$	$1.161 \cdot 10^{-4}$	628.724	41.2730
$2.264 \cdot 10^{-2}$	$1.225 \cdot 10^{-4}$	566.470	38.9753
$2.344 \cdot 10^{-2}$	$1.285 \cdot 10^{-4}$	436.549	34.2215
$2.425 \cdot 10^{-2}$	$1.358 \cdot 10^{-4}$	369.634	31.4581
$2.508 \cdot 10^{-2}$	$1.429 \cdot 10^{-4}$	251.786	26.4983
$2.592 \cdot 10^{-2}$	$1.495 \cdot 10^{-4}$	248.851	26.1563
$2.677 \cdot 10^{-2}$	$1.576 \cdot 10^{-4}$	169.658	22.3877
$2.764 \cdot 10^{-2}$	$1.659 \cdot 10^{-4}$	119.910	19.6554
$2.852 \cdot 10^{-2}$	$1.727 \cdot 10^{-4}$	58.7368	16.0711
$2.942 \cdot 10^{-2}$	$1.809 \cdot 10^{-4}$	35.8653	14.4123
$3.033 \cdot 10^{-2}$	$1.885 \cdot 10^{-4}$	85.8301	17.5172
$3.126 \cdot 10^{-2}$	$1.972 \cdot 10^{-4}$	25.6322	13.8033
$3.220 \cdot 10^{-2}$	$2.054 \cdot 10^{-4}$	20.6059	13.3915

Differential cross section for p-^{58}Ni elastic scattering (without slit aperture, run 025)

$-t\ \left[(\text{GeV}/c)^2\right]$	$\Delta t\ \left[(\text{GeV}/c)^2\right]$	$\frac{\mathrm{d}\sigma}{\mathrm{d}t}\ \left[\text{mb}/(\text{GeV}/c)^2\right]$	$\Delta\frac{\mathrm{d}\sigma}{\mathrm{d}t}\ \left[\text{mb}/(\text{GeV}/c)^2\right]$
$3.767 \cdot 10^{-3}$	$1.366 \cdot 10^{-5}$	30269.5	1049.68
$4.092 \cdot 10^{-3}$	$1.342 \cdot 10^{-5}$	27933.1	986.851
$4.431 \cdot 10^{-3}$	$1.331 \cdot 10^{-5}$	25445.1	923.057
$4.784 \cdot 10^{-3}$	$1.339 \cdot 10^{-5}$	22589.4	850.371
$5.151 \cdot 10^{-3}$	$1.364 \cdot 10^{-5}$	21435.5	815.319
$5.532 \cdot 10^{-3}$	$1.482 \cdot 10^{-5}$	19796.3	767.987
$5.926 \cdot 10^{-3}$	$1.530 \cdot 10^{-5}$	19417.6	749.726
$6.334 \cdot 10^{-3}$	$1.691 \cdot 10^{-5}$	17375.1	693.672
$6.755 \cdot 10^{-3}$	$1.867 \cdot 10^{-5}$	17108.6	679.769
$7.191 \cdot 10^{-3}$	$2.066 \cdot 10^{-5}$	14103.1	602.168
$7.641 \cdot 10^{-3}$	$2.310 \cdot 10^{-5}$	13161.6	572.061
$8.105 \cdot 10^{-3}$	$2.583 \cdot 10^{-5}$	12355.2	544.989
$8.581 \cdot 10^{-3}$	$2.855 \cdot 10^{-5}$	11499.0	518.507
$9.071 \cdot 10^{-3}$	$3.177 \cdot 10^{-5}$	9429.50	459.735
$9.574 \cdot 10^{-3}$	$3.505 \cdot 10^{-5}$	9328.98	449.933
$1.009 \cdot 10^{-2}$	$3.904 \cdot 10^{-5}$	8821.88	431.261
$1.062 \cdot 10^{-2}$	$4.240 \cdot 10^{-5}$	7696.97	396.035
$1.117 \cdot 10^{-2}$	$4.670 \cdot 10^{-5}$	6843.18	367.779
$1.173 \cdot 10^{-2}$	$5.057 \cdot 10^{-5}$	5662.65	329.238
$1.231 \cdot 10^{-2}$	$5.481 \cdot 10^{-5}$	6370.78	346.437
$1.290 \cdot 10^{-2}$	$5.939 \cdot 10^{-5}$	5060.23	303.384
$1.350 \cdot 10^{-2}$	$6.363 \cdot 10^{-5}$	4308.77	276.440
$1.411 \cdot 10^{-2}$	$6.847 \cdot 10^{-5}$	3933.22	260.422
$1.474 \cdot 10^{-2}$	$7.327 \cdot 10^{-5}$	3650.06	247.633
$1.539 \cdot 10^{-2}$	$7.908 \cdot 10^{-5}$	3342.82	233.555
$1.604 \cdot 10^{-2}$	$8.370 \cdot 10^{-5}$	2645.38	204.557
$1.671 \cdot 10^{-2}$	$8.922 \cdot 10^{-5}$	2615.33	200.601
$1.740 \cdot 10^{-2}$	$9.574 \cdot 10^{-5}$	2177.13	181.113
$1.810 \cdot 10^{-2}$	$1.017 \cdot 10^{-4}$	1879.11	166.802
$1.881 \cdot 10^{-2}$	$1.076 \cdot 10^{-4}$	1514.11	148.467
$1.954 \cdot 10^{-2}$	$1.144 \cdot 10^{-4}$	1204.70	131.517
$2.028 \cdot 10^{-2}$	$1.200 \cdot 10^{-4}$	892.913	112.978
$2.104 \cdot 10^{-2}$	$1.272 \cdot 10^{-4}$	783.324	105.581
$2.181 \cdot 10^{-2}$	$1.339 \cdot 10^{-4}$	665.806	97.3080
$2.260 \cdot 10^{-2}$	$1.405 \cdot 10^{-4}$	490.186	84.4652
$2.339 \cdot 10^{-2}$	$1.472 \cdot 10^{-4}$	395.834	76.3884
$2.421 \cdot 10^{-2}$	$1.545 \cdot 10^{-4}$	471.187	81.5431
$2.503 \cdot 10^{-2}$	$1.617 \cdot 10^{-4}$	99.2243	46.1450
$2.587 \cdot 10^{-2}$	$1.695 \cdot 10^{-4}$	221.807	59.5789
$2.672 \cdot 10^{-2}$	$1.781 \cdot 10^{-4}$	170.725	54.2005

continued on next page

continued from previous page

$-t$ $\left[(\text{GeV}/c)^2\right]$	Δt $\left[(\text{GeV}/c)^2\right]$	$\frac{\mathrm{d}\sigma}{\mathrm{d}t}$ $\left[\text{mb}/(\text{GeV}/c)^2\right]$	$\Delta\frac{\mathrm{d}\sigma}{\mathrm{d}t}$ $\left[\text{mb}/(\text{GeV}/c)^2\right]$
$2.759 \cdot 10^{-2}$	$1.855 \cdot 10^{-4}$	176.445	54.7060
$2.848 \cdot 10^{-2}$	$1.937 \cdot 10^{-4}$	72.6677	42.8863
$2.937 \cdot 10^{-2}$	$2.015 \cdot 10^{-4}$	26.1112	36.6184
$3.028 \cdot 10^{-2}$	$2.098 \cdot 10^{-4}$	54.2104	40.8786
$3.121 \cdot 10^{-2}$	$2.182 \cdot 10^{-4}$	10.9356	34.5100
$3.215 \cdot 10^{-2}$	$2.273 \cdot 10^{-4}$	31.2963	36.9710
$3.310 \cdot 10^{-2}$	$2.361 \cdot 10^{-4}$	69.3736	41.9151
$3.406 \cdot 10^{-2}$	$2.455 \cdot 10^{-4}$	8.92699	33.2394
$3.504 \cdot 10^{-2}$	$2.549 \cdot 10^{-4}$	0.16460	31.0642
$3.604 \cdot 10^{-2}$	$2.641 \cdot 10^{-4}$	75.4663	41.3636
$3.705 \cdot 10^{-2}$	$2.740 \cdot 10^{-4}$	61.7583	40.0170
$3.807 \cdot 10^{-2}$	$2.847 \cdot 10^{-4}$	79.4038	41.6849
$3.911 \cdot 10^{-2}$	$2.944 \cdot 10^{-4}$	38.4914	36.9957
$4.017 \cdot 10^{-2}$	$3.049 \cdot 10^{-4}$	55.3424	38.8536
$4.124 \cdot 10^{-2}$	$3.146 \cdot 10^{-4}$	135.030	47.1019
$4.232 \cdot 10^{-2}$	$3.249 \cdot 10^{-4}$	104.250	44.0219
$4.341 \cdot 10^{-2}$	$3.349 \cdot 10^{-4}$	156.136	48.5084
$4.452 \cdot 10^{-2}$	$3.455 \cdot 10^{-4}$	96.2744	41.6332
$4.565 \cdot 10^{-2}$	$3.575 \cdot 10^{-4}$	126.788	44.7825
$4.678 \cdot 10^{-2}$	$3.679 \cdot 10^{-4}$	193.403	50.2901
$4.793 \cdot 10^{-2}$	$3.797 \cdot 10^{-4}$	266.890	55.6338
$4.910 \cdot 10^{-2}$	$3.907 \cdot 10^{-4}$	175.102	47.3085
$5.028 \cdot 10^{-2}$	$4.020 \cdot 10^{-4}$	171.950	46.8216
$5.147 \cdot 10^{-2}$	$4.129 \cdot 10^{-4}$	114.721	40.8763
$5.268 \cdot 10^{-2}$	$4.243 \cdot 10^{-4}$	147.598	43.2278
$5.390 \cdot 10^{-2}$	$4.384 \cdot 10^{-4}$	155.483	43.2933
$5.513 \cdot 10^{-2}$	$4.513 \cdot 10^{-4}$	149.547	41.7427
$5.639 \cdot 10^{-2}$	$4.627 \cdot 10^{-4}$	203.913	45.8553
$5.765 \cdot 10^{-2}$	$4.750 \cdot 10^{-4}$	143.892	39.5542
$5.893 \cdot 10^{-2}$	$4.892 \cdot 10^{-4}$	139.387	39.3851
$6.022 \cdot 10^{-2}$	$5.027 \cdot 10^{-4}$	94.3173	34.2814
$6.153 \cdot 10^{-2}$	$5.160 \cdot 10^{-4}$	152.964	39.7147
$6.285 \cdot 10^{-2}$	$5.288 \cdot 10^{-4}$	137.778	37.8054
$6.419 \cdot 10^{-2}$	$5.428 \cdot 10^{-4}$	144.441	37.9958
$6.554 \cdot 10^{-2}$	$5.558 \cdot 10^{-4}$	101.258	33.1692
$6.691 \cdot 10^{-2}$	$5.680 \cdot 10^{-4}$	129.214	35.6262
$6.828 \cdot 10^{-2}$	$5.809 \cdot 10^{-4}$	135.774	35.8516
$6.967 \cdot 10^{-2}$	$5.954 \cdot 10^{-4}$	87.1763	30.2996
$7.107 \cdot 10^{-2}$	$6.099 \cdot 10^{-4}$	19.1126	20.6620
$7.249 \cdot 10^{-2}$	$6.251 \cdot 10^{-4}$	73.8158	27.8986
$7.392 \cdot 10^{-2}$	$6.415 \cdot 10^{-4}$	27.2504	21.0520
$7.537 \cdot 10^{-2}$	$6.557 \cdot 10^{-4}$	21.2618	19.6036
$7.683 \cdot 10^{-2}$	$6.721 \cdot 10^{-4}$	48.1437	23.3078

continued from previous page

$-t\ \left[(\text{GeV}/c)^2\right]$	$\Delta t\ \left[(\text{GeV}/c)^2\right]$	$\frac{\mathrm{d}\sigma}{\mathrm{d}t}\ \left[\text{mb}/(\text{GeV}/c)^2\right]$	$\Delta\frac{\mathrm{d}\sigma}{\mathrm{d}t}\ \left[\text{mb}/(\text{GeV}/c)^2\right]$
$7.831\cdot10^{-2}$	$6.875\cdot10^{-4}$	29.1156	20.0130
$7.980\cdot10^{-2}$	$7.019\cdot10^{-4}$	87.5003	27.5779
$8.131\cdot10^{-2}$	$7.199\cdot10^{-4}$	17.5787	17.1252
$8.283\cdot10^{-2}$	$7.346\cdot10^{-4}$	11.9696	15.5708

B. Differential cross sections

Bibliography

[1] H.H. Gutbrod et al. (Eds.). FAIR - Baseline technical report, volume 4, experiment proposals on nuclear structure and astro physics (NUSTAR). 2006. http://www.fair-center.eu/fileadmin/fair/publications_FAIR/FAIR_BTR_4.pdf.

[2] G.D. Alkhazov, S.L. Belostotsky, and A.A. Vorobyov. Scattering of 1 GeV protons on nuclei. *Phys. Rep.*, 42(2):89, 1978. http://dx.doi.org/10.1016/0370-1573(78)90083-2.

[3] J. Saudinos and C. Wilkin. Proton-nucleus scattering at medium energies. *Annu. Rev. Nucl. Part. Sci.*, 24(1):341, 1974. http://dx.doi.org/10.1146/annurev.ns.24.120174.002013.

[4] G.D. Alkhazov et al. Nuclear matter distributions in the ^{6}He and ^{8}He nuclei from differential cross sections for small-angle proton elastic scattering at intermediate energy. *Nucl. Phys. A*, 712(3–4):269, 2002. http://dx.doi.org/10.1016/S0375-9474(02)01273-3.

[5] A.V. Dobrovolsky et al. Study of the nuclear matter distribution in neutron-rich Li isotopes. *Nucl. Phys. A*, 766(0):1, 2006. http://dx.doi.org/10.1016/j.nuclphysa.2005.11.016.

[6] S. Ilieva et al. Nuclear-matter density distribution in the neutron-rich nuclei ^{12,14}Be from proton elastic scattering in inverse kinematics. *Nucl. Phys. A*, 875(0):8, 2012. http://dx.doi.org/10.1016/j.nuclphysa.2011.11.010.

[7] R.M. Lombard, G.D. Alkhazov, and O.A. Domchenkov. Intermediate energy proton scattering and nuclear transition densities in nickel isotopes. *Nucl. Phys. A*, 360(2):233, 1981. http://dx.doi.org/10.1016/0375-9474(81)90145-7.

[8] A. Chaumeaux, V. Layly, and R. Schaeffer. Neutron densities from 1 GeV proton scattering. *Phys. Lett. B*, 72(1):33, 1977. http://dx.doi.org/10.1016/0370-2693(77)90056-9.

[9] L. Ray. Neutron isotopic density differences deduced from 0.8 GeV polarized proton elastic scattering. *Phys. Rev. C*, 19:1855, 1979. http://link.aps.org/doi/10.1103/PhysRevC.19.1855.

[10] H. Sakaguchi et al. Elastic scattering of polarized protons from ^{58}Ni at $E_p =$ 192, 295, and 400 MeV. *Phys. Rev. C*, 57:1749, 1998. `http://link.aps.org/doi/10.1103/PhysRevC.57.1749`.

[11] D.T. Yordanov et al. Nuclear charge radii of $^{21\text{-}32}$Mg. *Phys. Rev. Lett.*, 108:042504, 2012. `http://link.aps.org/doi/10.1103/PhysRevLett.108.042504`.

[12] T. Suzuki et al. Neutron skin of Na isotopes studied via their interaction cross sections. *Phys. Rev. Lett.*, 75:3241, 1995. `http://link.aps.org/doi/10.1103/PhysRevLett.75.3241`.

[13] A. Krasznahorkay et al. Excitation of isovector spin-dipole resonances and neutron skin of nuclei. *Phys. Rev. Lett.*, 82:3216, 1999. `http://link.aps.org/doi/10.1103/PhysRevLett.82.3216`.

[14] P. Schrock. *The Electric Dipole Response of* ^{132}*Sn*. PhD thesis, Technische Universität Darmstadt, Darmstadt, 2015. `https://hds.hebis.de/ulbda/Record/HEB362272972`.

[15] A. Trzcińska et al. Neutron density distributions deduced from antiprotonic atoms. *Phys. Rev. Lett.*, 87:082501, 2001. `http://link.aps.org/doi/10.1103/PhysRevLett.87.082501`.

[16] M. Wada and Y. Yamazaki. Technical developments toward antiprotonic atoms for nuclear structure studies of radioactive nuclei. *Nucl. Instrum. Methods Phys. Res., Sect. B*, 214(0):196, 2004. `http://dx.doi.org/10.1016/j.nimb.2003.08.019`.

[17] P. Kienle. Medium energy antiproton absorption, a tool to study neutron halo nuclei. *Nucl. Instrum. Methods Phys. Res., Sect. B*, 214(0):191, 2004. `http://dx.doi.org/10.1016/S0168-583X(03)01776-2`.

[18] H. Lenske and P. Kienle. Probing matter radii of neutron-rich nuclei by antiproton scattering. *Phys. Lett. B*, 647(2–3):82, 2007. `http://dx.doi.org/10.1016/j.physletb.2007.02.009`.

[19] S. Abrahamyan et al. Measurement of the neutron radius of ^{208}Pb through parity violation in electron scattering. *Phys. Rev. Lett.*, 108:112502, 2012. `http://link.aps.org/doi/10.1103/PhysRevLett.108.112502`.

[20] C.M. Tarbert et al. Neutron skin of ^{208}Pb from coherent pion photoproduction. *Phys. Rev. Lett.*, 112:242502, 2014. `http://link.aps.org/doi/10.1103/PhysRevLett.112.242502`.

[21] H. Moeini et al. First feasibility experiment for the EXL project with proto-type detectors at the ESR storage ring. *Nucl. Instrum. Methods Phys. Res., Sect. A*, 634(1):77, 2011. `http://dx.doi.org/10.1016/j.nima.2011.01.036`.

[22] S. Ilieva et al. Feasibility studies of the EXL setup for FAIR using the GSI storage ring ESR. *Eur. Phys. J. Spec. Top.*, 150:357, 2007. `http://dx.doi.org/10.1140/epjst/e2007-00345-x`.

[23] K. Yue et al. Feasibility studies for the EXL project at FAIR. *PoS*, STORI11:14, 2011. `http://pos.sissa.it/archive/conferences/150/014/STORI11_014.pdf`.

[24] N. Kalantar for the EXL collaboration. Start up of part of the EXL physics program with ^{56}Ni. Experiment proposal, 2010.

[25] B. Cheal et al. High-resolution laser spectroscopy of nickel isotopes. Technical Report CERN-INTC-2013-007. INTC-P-373, CERN, Geneva, 2013. `https://cds.cern.ch/record/1551733`.

[26] P.J. Börger et al. *In-beam EXL demonstrator tests*, volume 2010-1 of *GSI Report*, page 36. GSI Helmholtzzentrum für Schwerionenforschung, Darmstadt, 2010. `http://repository.gsi.de/record/53522`.

[27] Le Xuan Chung et al. Prototyping of DSSDs for particle tracking and spectroscopy within the EXL project at FAIR. *Communications in Physics*, 22(3), 2012. `http://vjs.ac.vn/index.php/cip/article/view/2525`.

[28] V. Eremin. private communication. Vladimir.Eremin@cern.ch.

[29] B. Streicher. private communication. b.streicher@gsi.de.

[30] M.S. Basunia. Nuclear data sheets for A = 237. *Nuclear Data Sheets*, 107(8):2323, 2006. `http://dx.doi.org/10.1016/j.nds.2006.07.001`.

[31] V. Eremin. DSSD's and thick Si detectors for EXL. Presentation at the EXL/ELISe Collaboration Meeting on Technical Issues, 2009.

[32] M. von Schmid et al. First application of pulse-shape analysis to silicon micro-strip detectors. *Nucl. Instrum. Methods Phys. Res., Sect. A*, 629(1):197, 2011. `http://dx.doi.org/10.1016/j.nima.2010.10.096`.

[33] M. von Schmid. Pulse shape discrimination with silicon microstrip detectors. Master's thesis, TU Darmstadt, 2009. unpublished.

[34] *Si(Li)-detectors for the MUST2-experiment*. Semikon Detector GmbH, Karl-Heinz-Beckurts-Straße 13, D-52428 Jülich, 2012. `http://www.semikon-detector.de/uploads/media/1D_SiLi_MUST2_29022012.pdf`.

[35] E. Pollacco et al. MUST2: A new generation array for direct reaction studies. *Eur. Phys. J. A*, 25(1):287, 2005. `http://dx.doi.org/10.1140/epjad/i2005-06-162-5`.

[36] D. Protić et al. *Position-Sensitive Si(Li) Transmission Detectors for the EXL-Experiments at GSI-Darmstadt*, volume 2007-1 of *GSI Report*, page 33. GSI Helmholtzzentrum für Schwerionenforschung, Darmstadt, 2007. `http://repository.gsi.de/record/53525`.

[37] D. Protić and T. Krings. Development of transmission Si(Li) detectors. *IEEE Trans. Nucl. Sci.*, 50(4):1008, 2003. `http://dx.doi.org/10.1109/TNS.2003.815106`.

[38] J. Peyré. R&D on calorimeters. Presentation at the EXL/ELISe Collaboration Meeting on Technical Issues, 2009.

[39] D. Cortina-Gil et al. CALIFA, a dedicated calorimeter for the R^3B/FAIR. *Nuclear Data Sheets*, 120(0):99, 2014. `http://dx.doi.org/10.1016/j.nds.2014.07.017`.

[40] CALIFA/R^3B Collaboration. Technical report for the design, construction and commissioning of the CALIFA barrel. Technical report, 2011. `http://www.fair-center.de/fileadmin/fair/publications_exp/CALIFA_BARREL_TDR_web.pdf`.

[41] O.B. Tarasov and D. Bazin. LISE++: Radioactive beam production with in-flight separators. *Nucl. Instrum. Methods Phys. Res., Sect. B*, 266(19–20):4657, 2008. `http://dx.doi.org/10.1016/j.nimb.2008.05.110`.

[42] J.C. Zamora Cardona. *Nuclear Reaction Studies using Stored Ion Beams at ESR with EXL*. PhD thesis, Technische Universität Darmstadt, in preparation.

[43] A. Rytz. Recommended energy and intensity values of alpha particles from radioactive decay. *At. Data Nucl. Data Tables*, 47(2):205, 1991. `http://dx.doi.org/10.1016/0092-640X(91)90002-L`.

[44] M. Mutterer. Integration of the Si-array – A new proposal for recoil detector ESPA. Presentation at the R^3B/EXL/ELISe Joint Collaboration Meeting, 2008.

[45] B. Streicher et al. Application of a double-sided silicon-strip detector as a differential pumping barrier for NESR experiments at FAIR. *Nucl. Instrum. Methods Phys. Res., Sect. A*, 654(1):604, 2011. `http://dx.doi.org/10.1016/j.nima.2011.06.075`.

[46] *EPO-TEK H77 Technical Data Sheet*. Epoxy Technology, Inc. `http://www.epotek.com/site/administrator/components/com_products/assets/files/Style_Uploads/H77.pdf`.

[47] D. Parker et al. *Polymers, High-Temperature*. Wiley-VCH Verlag GmbH & Co. KGaA, 2000. `http://dx.doi.org/10.1002/14356007.a21_449.pub4`.

[48] M. Dommach. Specification: UHV Guidelines for X-Ray Beam Transport Systems. *Technical Note*, 2011. `http://bib-pubdb1.desy.de/record/88939`.

[49] *DELTA, Spring Energized Metal Seals*. Technetics Group. `http://www.techneticsgroup.com/bin/Delta.pdf`.

[50] M. Lindemulder. private communication. m.f.lindemulder@rug.nl.

[51] K. Blasche et al. The SIS heavy ion synchrotron project. *IEEE Trans.Nucl.Sci.*, 32:2657, 1985. `http://dx.doi.org/10.1109/TNS.1985.4334010`.

[52] J. Glatz. The unilac as a fast switching, variable ion and energy accelerator. *Proceedings of LINAC86, Stanford*, page 321, 1986. `http://slac.stanford.edu/pubs/slacreports/reports05/slac-r-303.pdf`.

[53] H. Geissel et al. The GSI projectile fragment separator (FRS): a versatile magnetic system for relativistic heavy ions. *Nucl. Instrum. Methods Phys. Res., Sect. B*, 70(1):286 – 297, 1992. `http://dx.doi.org/10.1016/0168-583X(92)95944-M`.

[54] GSI. Relativistische Strahlen exotischer Kerne. GSI-Nachrichten 03-1997, 1997. `https://www-alt.gsi.de/documents/DOC-2003-Jun-35-2.pdf`.

[55] G. Münzenberg. The separation techniques for secondary beams. *Nucl. Instrum. Methods Phys. Res., Sect. B*, 70(1–4):265, 1992. `http://dx.doi.org/10.1016/0168-583X(92)95942-K`.

[56] B. Franzke et al. Mass and lifetime measurements of exotic nuclei in storage rings. *Mass Spectrom. Rev.*, 27(5):428, 2008. `http://dx.doi.org/10.1002/mas.20173`.

[57] B. Franzke. The heavy ion storage and cooler ring project ESR at GSI. *Nucl. Instrum. Methods Phys. Res., Sect. B*, 24–25, Part 1(0):18, 1987. `http://dx.doi.org/10.1016/0168-583X(87)90583-0`.

[58] A. Gumberidze. *Experimental studies of the ground state QED corrections in H- and He-like Uranium*. PhD thesis, Johann Wolfgang Goethe-Universität, Frankfurt am Main, 2003. `http://publikationen.ub.uni-frankfurt.de/frontdoor/index/index/docId/5301`.

[59] B. Franzke et al. Heavy ion beam accumulation, cooling, and experiments at the ESR. In *Particle Accelerator Conference, 1993., Proceedings of the 1993*, page 1645 vol.3, 1993. `http://dx.doi.org/10.1109/PAC.1993.309087`.

[60] S. van der Meer. Stochastic damping of betatron oscillations in the ISR. Technical Report CERN-ISR-PO-72-31. ISR-PO-72-31, CERN, Geneva, 1972. `https://cds.cern.ch/record/312939`.

[61] M. Steck et al. Electron cooling experiments at the ESR. *Nucl. Instrum. Methods Phys. Res., Sect. A*, 532(1–2):357, 2004. `http://dx.doi.org/10.1016/j.nima.2004.06.065`.

[62] F. Nolden et al. First experiments on stochastic cooling of heavy ion beams at the ESR. *Proceedings of the Sixth European Particle Accelerator Conference, Stockholm*, page 1052, 1998. `http://www.cern.ch/accelconf/e98/PAPERS/THP39G.PDF`.

[63] F. Nolden et al. Stochastic cooling at the ESR. *Nucl. Instrum. Methods Phys. Res., Sect. A*, 441(1–2):219, 2000. `http://dx.doi.org/10.1016/S0168-9002(99)01136-5`.

[64] H. Reich et al. The ESR internal target. *Nucl. Phys. A*, 626(1–2):417, 1997. `http://dx.doi.org/10.1016/S0375-9474(97)00564-2`.

[65] D. Doherty et al. Nuclear transfer reaction measurements at the ESR - for the investigation of the astrophysical $^{15}O(\alpha,\gamma)^{19}Ne$ reaction. *Phys. Scripta T*, 2015. to be published.

[66] Huo Junde, Huo Su, and Yang Dong. Nuclear data sheets for A = 56. *Nuclear Data Sheets*, 112(6):1513, 2011. `http://dx.doi.org/10.1016/j.nds.2011.04.004`.

[67] *ECS3080, nanoprecise open loop stepper positioner for linear, horizontal motion*. attocube systems AG, 2014/5 edition, 2014. `http://www.attocube.com/attomotion/industrial-line/ecs3080/`.

[68] L. Stuhl et al. A neutron spectrometer for studying giant resonances with (p,n) reactions in inverse kinematics. *Nucl. Instrum. Methods Phys. Res., Sect. A,* 736(0):1, 2014. `http://dx.doi.org/10.1016/j.nima.2013.10.038`.

[69] M. Kuilman. Start-up experiment of the EXL project. Master thesis, Rijksuniversiteit Groningen, Netherlands, 2013.

[70] N. Kurz. *GSI Data Acquisition System MBS Release Notes V5.0.* GSI, Gesellschaft für Schwerionenforschung mbH, 2006. `https://www.gsi.de/fileadmin/EE/MBS/gm_mbs_rel_50.pdf`.

[71] S. Litvinov. private communication. S.Litvinov@gsi.de.

[72] F. Nolden et al. Radioactive beam accumulation for a storage ring experiment with an internal target. *Proceedings of IPAC2013, Shanghai, China*, page 91, 2013. `http://accelconf.web.cern.ch/accelconf/IPAC2013/papers/mopea013.pdf`.

[73] G. Lutz. *Semiconductor Radiation Detectors*. Oxford University Press, Oxford, 2005.

[74] F. Salvat A. Jablonski and C.J. Powell. *NIST Electron Elastic-Scattering Cross-Section Database - Version 3.2.* 2010. `http://www.nist.gov/srd/nist64.cfm`.

[75] W. Herr and B. Muratori. Concept of luminosity. Technical report, CERN, 2006. `http://cds.cern.ch/record/603056/files/CERN-2006-002.pdf?version=1`.

[76] T. Gassner and H. Beyer. Spatial characterisation of the internal gas target at the ESR for the FOCAL experiment. Internal report, unpublished, 2013.

[77] N. Petridis. private communication. n.petridis@gsi.de.

[78] R.E. Grisenti et al. Cryogenic microjet source for orthotropic beams of ultralarge superfluid helium droplets. *Phys. Rev. Lett.*, 90:234501, 2003. `http://link.aps.org/doi/10.1103/PhysRevLett.90.234501`.

[79] M.O. McLinden E.W. Lemmon and D.G. Friend. Thermophysical properties of fluid systems. `http://webbook.nist.gov`. Accessed: 30.05.2015.

[80] G.P. Sutton. *Rocket Propulsion Elements: An Introduction to the Engineering of Rockets*. A Wiley-Interscience publication. Wiley, 1992.

[81] M. Kühnel. Entwicklung einer kryogenen cluster- und tröpfchenquelle als internes target am experimentierspeicherring ESR. Diploma thesis, Johann Wolfgang Goethe-Universität Frankfurt am Main, 2009.

[82] U. Popp. private communication. u.popp@gsi.de.

[83] M. Kühnel et al. Low- internal target from a cryogenically cooled liquid microjet source. *Nucl. Instrum. Methods Phys. Res., Sect. A*, 602(2):311, 2009. `http://dx.doi.org/10.1016/j.nima.2008.12.212`.

[84] V. Gostishchev et al. Comparison of measurements and simulations of internal target effects in the ESR storage ring. *Nucl. Instrum. Methods Phys. Res., Sect. A*, 641(1):12, 2011. `http://dx.doi.org/10.1016/j.nima.2011.03.047`.

[85] H. Reeg et al. Current transformers for GSI's keV/u to GeV/u ion beams - an overview. *5th European Workshop on Diagnostics and Beam Instrumentation*, DIPAC 2001:108, 2001.

[86] H. Reeg et al. *The beam current transformers at SIS and ESR*, volume 1991-1 of *GSI Report*, page 392. GSI Helmholtzzentrum für Schwerionenforschung, Darmstadt, 1991. `http://repository.gsi.de/record/53541`.

[87] M.J. Berger et al. ESTAR, PSTAR, and ASTAR: Computer programs for calculating stopping-power and range tables for electrons, protons, and helium ions (version 1.2.3). `http://physics.nist.gov/Star`, 2005. Accessed: 20.06.2013.

[88] JCGM. Evaluation of measurement data – Supplement 1 to the "Guide to the expression of uncertainty in measurement" – Propagation of distributions using a Monte Carlo method. In *Guide to the Expression of Uncertainty in Measurement (GUM)*. Joint Committee for Guides in Metrology, 2008. `http://www.bipm.org/en/publications/guides/gum.html`.

[89] E.W. Weisstein. Sphere point picking. MathWorld–A Wolfram Web Resource. `http://mathworld.wolfram.com/SpherePointPicking.html`. Accessed: 10.04.2015.

[90] C.A. Bertulani and P. Danielewicz. *Introduction to Nuclear Reactions*. Graduate Student Series in Physics. Taylor & Francis, 2004.

[91] G.D. Alkhazov, I.S. Novikov, and Yu.M. Shabelski. Nuclear radii of unstable nuclei. *Int. J. Mod. Phys. E*, 20(03):583, 2011. `http://www.worldscientific.com/doi/pdf/10.1142/S0218301311018101`.

[92] K.A. Olive and Particle Data Group. Review of particle physics. *Chinese Physics C*, 38(9):090001, 2014. `http://pdg.lbl.gov/`.

[93] L. Ray. Proton-nucleus total cross sections in the intermediate energy range. *Phys. Rev. C*, 20:1857, 1979. `http://link.aps.org/doi/10.1103/PhysRevC.20.1857`.

[94] E.W. Weisstein. Boole's rule. MathWorld–A Wolfram Web Resource. `http://mathworld.wolfram.com/BoolesRule.html`. Accessed: 04.07.2015.

[95] H. De Vries, C.W. De Jager, and C. De Vries. Nuclear charge-density-distribution parameters from elastic electron scattering. *At. Data Nucl. Data Tables*, 36(3):495, 1987. `http://dx.doi.org/10.1016/0092-640X(87)90013-1`.

[96] I. Sick. Model-independent nuclear charge densities from elastic electron scattering. *Nucl. Phys. A*, 218(3):509, 1974. `http://dx.doi.org/10.1016/0375-9474(74)90039-6`.

[97] D.W.L. Sprung and J. Martorell. The symmetrized fermi function and its transforms. *J. Phys. A: Math. Gen.*, 30(18):6525, 1997. `http://stacks.iop.org/0305-4470/30/i=18/a=026`.

[98] G.D. Alkhazov et al. Neutron matter densities in the even Ni isotopes. *Phys. Lett. B*, 67(4):402, 1977. `http://dx.doi.org/10.1016/0370-2693(77)90430-0`.

[99] A.N. Antonov et al. Charge and matter distributions and form factors of light, medium, and heavy neutron-rich nuclei. *Phys. Rev. C*, 72:044307, 2005. `http://link.aps.org/doi/10.1103/PhysRevC.72.044307`.

[100] R.M. Tarbutton and K.T.R. Davies. Further studies of the Hartree-Fock approximation in finite nuclei. *Nucl. Phys. A*, 120(1):1, 1968. `http://dx.doi.org/10.1016/0375-9474(68)90057-2`.

[101] G.S. Blanpied et al. Elastic scattering of 0.8 GeV protons from ^{12}C, ^{58}Ni, and ^{208}Pb. *Phys. Rev. Lett.*, 39:1447, 1977. `http://link.aps.org/doi/10.1103/PhysRevLett.39.1447`.

[102] L. Ray et al. Analysis of 0.8-GeV polarized-proton elastic scattering from ^{208}Pb, ^{90}Zr, ^{58}Ni, and ^{12}C. *Phys. Rev. C*, 18:1756, 1978. `http://link.aps.org/doi/10.1103/PhysRevC.18.1756`.

[103] G. Hagen. private communication. hageng@ornl.gov.

[104] A. Ekström. private communication. ekstrom@utk.edu.

[105] N. Petridis et al. Energy loss and cooling of relativistic highly charged uranium ions interacting with an internal hydrogen droplet target beam. *Nucl. Instrum. Methods Phys. Res., Sect. A*, 656(1):1, 2011. `http://dx.doi.org/10.1016/j.nima.2011.07.035`.

[106] J.W. Xia et al. The heavy ion cooler-storage-ring project (HIRFL-CSR) at Lanzhou. *Nucl. Instrum. Methods Phys. Res., Sect. A*, 488(1–2):11, 2002. `http://dx.doi.org/10.1016/S0168-9002(02)00475-8`.

[107] J.C. Yang et al. High Intensity heavy ion Accelerator Facility (HIAF) in China. *Nucl. Instrum. Methods Phys. Res., Sect. B*, 317, Part B(0):263, 2013. `http://dx.doi.org/10.1016/j.nimb.2013.08.046`.

[108] D. Krämer et al. One year of operation at the heidelberg TSR. *Nucl. Instrum. Methods Phys. Res., Sect. A*, 287(1–2):268, 1990. `http://dx.doi.org/10.1016/0168-9002(90)91806-M`.

[109] M. Grieser et al. Storage ring at HIE-ISOLDE. *Eur. Phys. J. Spec. Top.*, 207(1):1, 2012. `http://dx.doi.org/10.1140/epjst/e2012-01599-9`.

[110] K. Abrahamsson et al. CRYRING — a synchrotron, cooler and storage ring. *Nucl. Instrum. Methods Phys. Res., Sect. B*, 79(1–4):269, 1993. `http://dx.doi.org/10.1016/0168-583X(93)95341-2`.

[111] M. Lestinsky et al. CRYRING@ESR: A study group report. Technical report, GSI Helmholtzzentrum für Schwerionenforschung, 2012. `https://www.gsi.de/fileadmin/SPARC/documents/Cryring/ReportCryring_40ESR.PDF`.

[112] E. Byckling and K. Kajantie. *Particle kinematics*. A Wiley-Interscience publication. Wiley, 1972.

Curriculum vitae

Personal information

Name:	Mirko von Schmid
Address:	Robert-Bosch-Straße 10 64293 Darmstadt
Date of Birth:	3. April 1983
Place of Birth:	Fulda, Germany
Nationality:	German
Parents:	Angela von Schmid, née Steube Siegmar von Schmid

Education

Since October 2009	**PhD student in physics** Technische Universität Darmstadt, Germany Supervisor: Prof. Dr. Thorsten Kröll
June 2007 – August 2009	**Master student in physics** Technische Universität Darmstadt, Germany Degree: Master of Science (July 2009) Title of the master thesis: "*Pulse Shape Discrimination with Silicon Microstrip Detectors*" Supervisor: Prof. Dr. Dr. h.c. Norbert Pietralla
October 2003 – May 2007	**Bachelor student in physics** Technische Universität Darmstadt, Germany Degree: Bachelor of Science (May 2007)

	Title of the bachelor thesis: *"Design and development of segmented detectors from solar cells for the detection of ionized particles"* Supervisor: Prof. Dr. Dr. h.c. Norbert Pietralla
August 2002 – August 2003	**Civillian service**: Rettungshelfer Arbeitsgemeinschaft Rettungsdienst DRK Kreisverband Alsfeld und Lauterbach
August 1999 – June 2002	**Gymnasium** Alexander-von-Humboldt-Schule, Lauterbach (Hessen), Germany Degree: Abitur
September 1993 – June 1999	**Comprehensive school** Gesamtschule Schlitz, Germany
August 1989 – July 1993	**Primary School** Dieffenbach-Schule, Schlitz, Germany

Conferences and workshops

13. – 17. October 2014	*FAIR2014 – International Conference on Science and Technology for FAIR in Europe 2014*, Worms, Germany **Invited talk**: *"Status of EXL"*
28. September – 3. October 2014	STORI'14 – *9th International Conference on Nuclear Physics at Storage Rings*, Sankt Goar, Germany **Best poster award**: *"Investigation of the Nuclear Matter Distribution of ^{56}Ni by Elastic Proton Scattering in Inverse Kinematics"*
30. June – 4. July 2014	*DREB2014 – Direct Reactions with Exotic Beams*, Darmstadt, Germany
19. – 22. February 2014	*2nd Topical Workshop on Modern Aspects in Nuclear Structure*, Bormio, Italy

2. – 7. June 2013	*25th International Nuclear Physics Conference (INPC 2013)*, Firenze, Italy
25. – 26. March 2013	*3rd HIC for FAIR Detector Systems Networking Workshop*, Darmstadt, Germany
25. February – 3. March 2013	*NUSTAR Annual Meeting 2013*, Darmstadt, Germany
14. – 18. January 2013	*513. WE-Heraeus-Seminar on Astrophysics with ion storage rings*, Bad Honnef, Germany
17. – 21. October 2011	*NUSTAR Week 2011*, Bucharest, Romania
13. July 2011	*PSI Institutsseminar E12*, TU München, Garching, Germany **Invited talk**: *"The EXL project at FAIR - Status and perspectives"*
9. – 10. February 2011	*HIC for FAIR Detector Systems Networking Workshop*, Darmstadt, Germany
4. – 8. October 2010	*NUSTAR Week 2010*, Lund, Sweden
9. – 10. February 2010	*HIC for FAIR Detector Systems Networking Workshop*, Darmstadt, Germany

Publications

- M. von Schmid et al. Investigation of the nuclear matter distribution of ^{56}Ni by elastic proton scattering in inverse kinematics. *Physica Scripta T*, 2015. In print.

- J.C. Zamora Cardona et al. Isoscalar giant resonance studies in a stored-beam experiment within EXL. *Physica Scripta T*, 2015. In print.

- M. Mutterer et al. Experimental techniques for in-ring reaction experiments. *Physica Scripta T*, 2015. In print.

- D. Doherty et al. Nuclear transfer reaction measurements at the ESR - For the investigation of the astrophysical ^{15}O$(\alpha,\gamma)^{19}$Ne reaction. *Physica Scripta T*, 2015. In print.

- P. Egelhof et al. First nuclear reaction experiment with stored radioactive ^{56}Ni beam and internal hydrogen and helium targets. *JPS Conf. Proc.* 6:020049, 2015. http://dx.doi.org/10.7566/JPSCP.6.020049.

- M. Scheck et al. Do nuclei go pear-shaped? Coulomb excitation of ^{220}Rn and ^{224}Ra at REX-ISOLDE (CERN). *EPJ Web of Conferences* 93:01038, 2015. http://dx.doi.org/10.1051/epjconf/20159301038.

- R. Orlandi et al. Single-neutron orbits near 78Ni: Spectroscopy of the isotope ^{79}Zn. *Phys. Lett. B*, 740(0):298, 2015. http://dx.doi.org/10.1016/j.physletb.2014.12.006.

- D. Cortina-Gil et al. CALIFA, a dedicated calorimeter for the R^{3}B/FAIR. *Nuclear Data Sheets*, 120(0):99, 2014. http://dx.doi.org/10.1016/j.nds.2014.07.017.

- M. von Schmid et al. First EXL experiment with stored radioactive beam: Proton scattering on ^{56}Ni. *EPJ Web of Conferences* 66:03093, 2014. http://dx.doi.org/10.1051/epjconf/20146603093.

- S. Bönig et al. Quadrupole collectivity in neutron-rich Cd isotopes. *EPJ Web of Conferences* 66:02012, 2014. http://dx.doi.org/10.1051/epjconf/20146602012.

- L.P. Gaffney et al. Studies of pear-shaped nuclei using accelerated radioactive beams. *Nature* **497**:199, (2013). http://dx.doi.org/10.1038/nature12073.

- B. Streicher et al. Application of a double-sided silicon-strip detector as a differential pumping barrier for NESR experiments at FAIR. *Nucl. Instrum. Methods Phys. Res., Sect. A*, 654(1):604, 2011. http://dx.doi.org/10.1016/j.nima.2011.06.075.

- M. von Schmid et al. First application of pulse-shape analysis to silicon micro-strip detectors. *Nucl. Instrum. Methods Phys. Res., Sect. A*, 629(1):197, 2011. http://dx.doi.org/10.1016/j.nima.2010.10.096

- K.-H. Speidel et al. First g-factor measurements on semi-magic 36S and their implications for the rigidity of the shell closure. *Phys. Lett. B*, 659(1-2):101, 2008. http://dx.doi.org/10.1016/j.physletb.2007.11.049.